Fall 12-20-2013

Ultra-low Temperature Measurements of London Penetration Depth in Iron Selenide Telluride Superconductors

Andrei Diaconu
University of New Orleans, adiaconu@uno.edu

Ultra-low Temperature Measurements of London Penetration Depth in Iron Selenide Telluride Superconductors

A Dissertation

Submitted to the Graduate Faculty of the
University of New Orleans
in partial fulfillment of the
requirements for the degree of

Doctor of Philosophy
in
Engineering and Applied Science
Physics

by

Andrei Diaconu

B.S. "Alexandru Ioan Cuza" University, Iasi, Romania, 2006
M.S. "Alexandru Ioan Cuza" University, Iasi, Romania, 2008
M.S. University of New Orleans, New Orleans, USA, 2012

December, 2013

Dedication

To my loving parents, Romeo and Maria.

Acknowledgment

I am deeply thankful to my advisor, Prof. Dr. Leonard Spinu, for his valuable guidance and constant support throughout my research here at University of New Orleans. Working under his supervision for the past years has been an amazing opportunity. I have learned a great deal about being a man of science from him and I am grateful for that. He has been an amazing teacher and a tremendous help in so many ways, professionally and personally. It has been an honor to be his student.

I would like to thank our collaborators at Tulane University, Prof. Dr. Zhiqiang Mao and his students, Jin Hu and T.J. Liu for their extensive support, advice and assistance throughout the years. Their continuous help has made this work possible.

To all my colleagues and friends at AMRI, whom I have had the pleasure of knowing and working with, I would like to extend my thanks for all their help and valued friendship.

I would also like to thank my professors at UNO for their essential contribution to my scientific knowledge and laboratory skills.

I am profoundly grateful to Dr. Vladimir Shvarts from Janis Research Company for his indispensable support and assistance in operating the dilution refrigerator and deeper understanding of the fascinating field of cryogenics.

To my closest friends Kyle, Denny and Westly, I am extremely grateful for making my life in the United States a pleasurable and memorable experience.

I want to express my deepest gratitude to Dr. Catalin Martin for his extensive support and essential contribution. This work would not have been possible without his invaluable assistance.

Table of Contents

List of Figures

List of Tables

Abstract

The newly discovered iron based superconductors have captivated the attention of the scientific community due to the unusual mechanism behind their superconductivity and their promise as the next generation high temperature superconductors. After a century of superconductor research, the physical mechanism behind high temperature superconductivity is still not understood. These new materials bring renewed hope in elucidating the origin behind the pairing mechanism in high transition temperature (HTC) superconductors and achieving the ultimate goal of the field, room temperature superconductivity. Consequently, a deeper understanding of the intriguing properties of iron based materials is essential.

A great deal about the pairing mechanism of Cooper electron pairs can be inferred from the symmetry of their pairing wave function or order parameter. One of the most involved probes for studying the pairing symmetry is the London penetration depth. The low temperature behavior of London penetration depth in superconductors is directly related to the density of states and provides a powerful tool for investigating low-lying quasiparticle energy and, for this very reason, can give valuable hints on superconducting gap function symmetry.

The work presented focuses on investigating the pairing symmetry in the $Fe_{1+y}(Te_{1-x}Se_x)$ iron chalcogenide using a radio-frequency tunnel diode oscillator (TDO) technique for precise measurements of the temperature dependence of their in-plane penetration depth. The TDO technique, based on an original concept involving the use of planar inductors in an novel configuration, was implemented on a dilution refrigerator to investigate a significant number of single crystal samples, with nominal Se concentrations of 36%, 40%, 43% and 45% respectively, down to temperatures as low as 50 mK.

A systematic study together with a comprehensive analysis regarding the order parameter symmetry in the $Fe_{1+y}(Te_{1-x}Se_x)$ system is presented. In many cases we found that London penetration depth shows an upturn below at low temperatures, indicative of a paramagnetic-type contribution. Also the low-temperature behavior of penetration depth is best described by a quadratic power law with no systematic dependence on the Se concentration. Most importantly, in the limit of $T \rightarrow 0$, in some samples we observed a narrow region of linear temperature dependence, suggestive of nodes in the superconducting gap of $Fe_{1+y}(Te_{1-x}Se_x)$.

Keywords: *tunnel diode oscillator, planar inductors, dilution refrigerator, ultra-low temperature measurements, Meissner effect, London penetration depth, iron based superconductors, iron chalcogenides, iron selenide telluride, FeSeTe.*

Introduction

Since its discovery in 1911, superconductivity has been the subject of intensive research due to its intriguing properties and remarkable potential for technical applications [1, 2]. Although a satisfactory theoretical explanation emerged half a century late, the significance of the experimental discovery was immediately recognized by the scientific community and brought Heike K. Onnes the Nobel Prize in 1913. In the subsequent decades, this phenomenon has been observed in several materials and it seemed to be limited by a critical temperature of 30 K according to the interpretations of the microscopic theory proposed by Bardeen, Cooper and Schrieffer (Nobel Prize in 1972) in the late 1950's. Consequently, the 1986 discovery of a cuprate superconductors by Bednorz and Müller (Nobel Prize in 1987) [3] with a transition temperature of 35 K came as a surprise and the fundamental understanding of the unconventional mechanism behind high temperature superconductivity has since posed a major challenge for theoretical physics. Many other superconductors have been discovered thereafter, reaching critical temperatures as high as 138 K at ambient pressure and even 164 K under high pressure [4-6].

For a very long time, ferromagnetism and superconductivity have long been thought to be competing phenomena thus mutually exclusive. Hence the uncovering of superconductivity in the ferromagnetic UGe_2 in 2000 was unexpected [7]. Moreover, the recent discovery of high temperature superconductivity in iron based materials came as a huge surprise and has opened a new era in superconductor research [8]. Five years later, this seminal paper has been cited by almost 5000 times and numerous research groups are now focused on the study of iron-based superconductors. This tremendous interest is driven by the scientific curiosity in the coexistence of superconductivity and magnetism and the hope to finally uncover the underlying principles behind high temperature superconductivity.

Although the superconductive materials known as cuprates still hold the record for highest critical temperature (-139˚C) since their discovery in 1986, their ceramic texture and high manufacturing cost makes them impractical for a large number of technological applications [9]. As a consequence, superconductors for high-field application are still based on low-temperature superconductors. However, this year (2013) critical currents of an order of magnitude higher than typical superconductors have been reported in thin films of iron based superconductors [10]. Also, Fe based superconductors currently hold the record for highest critical field [11]. Their superior advantage over other materials makes them a genuine alternative in the production of high magnetic fields. From a theoretical perspective they could hold the key for the search of room temperature superconductors, an idea long believed to be impossible, which if brought to life, would revolutionize the technological world.

The pairing mechanism responsible with the high critical temperature of iron based materials is a highly controversial topic and like in the case of cuprates, its origin is still unknown. The conventional phonon mediated mechanism was quickly ruled out [12] although it is believed that phonon-electron coupling may play at least a partial role in the superconductivity of some iron based superconductors [13, 14]. Most of the experimental evidence to date favors an unconventional pairing mechanism closely tied to magnetism. A variety of microscopic pairing models have been proposed [15, 16] most of them based on magnetic fluctuations thus, an important steps towards understanding the mechanism responsible for high T_C superconductors is investigating the superconductive order parameter symmetry from which different microscopic pairing models can be tested based on their association with different symmetry states. Although in cuprates the gap symmetry has been pin-pointed to d-wave type [17], the order parameter symmetry in iron based superconductors is a largely debated topic. This is a very dynamic research field considering the experimental complexity of phase measurements and especially since there seems to be a non-universal symmetry describing iron based materials.

There are over 50 different superconductive Fe based compounds discovered to date. Despite exhibiting different behavior and properties they share common structural properties. They all share a layered structure based upon a planar layer of Fe atoms joined by tetrahedral coordinated pnictogens (P, As) or chalcogens (S, Se, Te) anions arranged in a stacked sequence separated by alkali, alkaline earth or rare earth and oxygen/fluorine "blocking layers". This work focuses on the iron chalcogenide $Fe_{1+y}(Te_{1-x}Se_x)$, an important ferrous superconducting system representing a special class of Fe based superconductors.

One of the most involved probes for studying $Fe_{1+y}(Te_{1-x}Se_x)$ superconductors is the London penetration depth λ. Temperature dependent measurements of $\lambda(T)$ can provide direct information about the density of states and provide a powerful tool for investigating low-lying quasiparticle energy and, for this very reason, can give valuable hints on superconducting gap function symmetry. Muon-spin rotation spectrometry (μ-SR) [18, 19] and microwave cavity studies [20] showed that superfluid density in $Fe_{1+y}(Te_{1-x}Se_x)$ for $x = 0.50$ and 0.41, respectively, is consistent with two gaps with $s\pm$ symmetry. The microwave measurements also found that at low temperature, $\lambda(T)$ has a nearly quadratic behavior. Similar power-law temperature dependence T^n, with exponent $n \approx 2$, was also reported from radio-frequency tunnel diode oscillator (TDO) data by several groups [21-24].

In this work we implemented a tunnel diode oscillator technique to study the superconducting properties of materials and specifically the ultra-low temperature dependence of London penetration depth. For the $Fe_{1+y}(Te_{1-x}Se_x)$ system H. Kim *et al.* [21] used the TDO method to probe the temperature dependence of the in-plane penetration depth in $Fe_{1.03}(Te_{0.63}Se_{0.37})$ single crystals down to 0.5 K reporting a power law behavior of $\Delta\lambda_{ab}(T)$ at low temperatures with an exponent $n \approx 2.1$. A similar power law

behavior with $n \approx 2.2$ was reported for $Fe_{1.0}(Te_{0.56}Se_{0.44})$ using the same method by A. Serafin *et al.* [22] down to a temperature of 0.2 K. T. Klein *et al.* [23] used a tunnel diode oscillator to measure the temperature dependence of λ_{ab} and λ_c in $Fe_{1.05}(Te_{0.55}Se_{0.44})$ and found the same quadratic temperature dependence for both crystallographic directions. K. Cho *et al.* [24] reported TDO measurements of $\Delta\lambda_{ab}(T)$ in optimally-doped single crystals of $Fe_{1.0}(Te_{0.58}Se_{0.42})$ focusing on the effects of sample size, shape and surface roughness and reporting on a $n \approx 2.3$ power law variation for a number of different samples indicating an intrinsic behavior.

Most previous TDO studies, however, focus on one particular Se concentration, especially close to the optimal doping of the $Fe_{1+y}(Te_{1-x}Se_x)$ system, and there seem to be relatively large variations in the magnitude of $\lambda(T)$ between different measurements. Moreover, most reported penetration depth studies are limited to temperatures above 0.5 K with only one TDO study conducted at lower temperatures down to 0.2 K, performed only on $Fe_{1.0}Te_{0.44(4)}Se_{0.56(4)}$ samples [22]. Since variations of $\lambda(T)$ represent the spectrum of the low-lying quasiparticles it is only at very low temperatures that it is possible to have valuable hints on the gap function symmetry. Consequently, the temperature investigation of the London penetration depth is appropriate in determining the pairing symmetry of iron based superconductors provided that very low temperatures can be achieved. For higher temperatures thermal effects can make it difficult or even impossible to distinguish different symmetries.

We present a systematic study of the temperature dependence of the in-plane penetration depth $\lambda_{ab}(T)$ in $Fe_{1+y}(Te_{1-x}Se_x)$.We measured a significant number of single crystals, with different Se concentrations within the bulk superconductive region, and our measurements were extended down to 50mK in order to better understand the pairing symmetry of this system and its evolution with doping. We will also show the importance of extending the temperature range to the lowest possible value and the effect that ultra-low temperature region measurements can have on the interpretation of results.

A more specific outline of the dissertation format is given below:

Chapter I, *Overview of Superconductivity*, begins with a historical timeline of major developments and key players in the field of superconductivity, from its discovery to present day. What follows is a concentrated mathematical description of some of the more relevant theories in the field, namely the London theory and the microscopic BCS theory. Relevant concepts emerging from theories, such as London penetration depth and energy gap, are introduced and discussed. An overview of different symmetry states of the order parameter (energy gap) in unconventional superconductors, including the multi-gap scenario of superconductivity, is given concluding with a brief recount of some of the experimental methods implemented in studying the superconductive gap structure.

Chapter II, *The London Penetration Depth in Superconductors,* begins by describing the magnetic penetration depth as derived from London theory of Meissner state. The London equations are solved for some theoretically relevant geometries and the relation between the measurable magnetic susceptibility and London penetration depth is derived. The derivation for a more practical geometry, namely rectangular slab shaped samples, is discussed. In the last part of the chapter we elaborate on the connection between the temperature dependence of the London penetration depth and the order parameter and how $\lambda(T)$ measurements can be used to obtain information about the superconductive gap structure.

Chapter III, *The Tunnel Diode Oscillator Technique,* introduces the TDO method and gives a brief historical review of its applications. A detailed analysis of the principles and theory behind the method is presented together with numerical simulations and experimental investigations. The issues regarding practical implementation of the TDO circuit are described with extensive focus on temperature effects. A comprehensive theoretical analysis is presented regarding the use and limitations of the method in investigating the London penetration depth in superconductive samples. In this chapter we introduce a novel inductor geometry based on parallel planar coils and outline the advantages over other inductors supported by theoretical calculations and numerical simulations. Lastly, we detail the practical setup for ultra-low temperature in-plane penetration depth measurements using the TDO technique in a dilution refrigerator.

Chapter IV, *Iron Based Superconductors,* starts with an overview if iron based superconductors, their classification and relevance in research. A detailed description of the superconductive properties of the iron chalcogenide $Fe_{1+y}(Te_{1-x}Se_x)$ is presented together with a literature survey regarding penetration depth temperature measurements. Details about crystalline sample growth and standard characterization techniques are given, followed by a primary characterization of the samples using techniques other than the TDO.

Chapter V, *London Penetration Depth in $Fe_{1+y}(Te_{1-x}Se_x)$ Single Crystals,* discusses the results regarding the $\lambda(T)$ dependence in $Fe_{1+y}(Te_{1-x}Se_x)$ single crystals obtained using the TDO technique. The low temperature dependence of London penetration depth as well as the full range temperature variation of the corresponding superfluid density is interpreted and conclusions about the superconductive properties of the material are presented and compared to literature reports. Based on our results, we indicate the evidence for different pairing symmetries and suggest our own scenario.

Chapter 1

Overview of Superconductivity

1.1. History of superconductivity

In 1908, Heike Kamerlingh Onnes, a Dutch scientist working on refrigeration techniques in his laboratory in Leiden, became the first person ever to liquefy helium. By using helium as a refrigerant he was able to reach a groundbreaking low temperature of 1.5 K initiating the field of low temperature physics. Investigating the electrical properties of pure metals, three years later he found that, below 4.15 K, the dc resistance of mercury completely vanished. The new phenomenon received the name of "supraconductivity" (later the superconductivity term was adopted) and its discovery is considered as the genesis of the field of superconductivity. In 1912 he found that applying a magnetic field would cause the dissolution of superconductivity and a year later observed the same superconductive properties below 7.2 K in lead. For his *"investigations on the properties of matter at low temperatures which led, inter alia, to the production of liquid helium"* H. K. Onnes received the Noble Prize in Physics 1913.

In 1933 German physicists Walther Meissner and Robert Ochsenfeld discovered that, in addition to magnetic fields being excluded from superconductive materials, a magnetic field flux applied in the normal state of a superconductive sample will be expelled as the temperature is decreased below its transition temperature. At very low temperatures, the superconductive samples exhibited perfect diamagnetism as the magnetic flux was entirely expelled from the sample volume. This phenomenon later became known as the Meissner- Ochsenfeld effect. Although perfect conductivity could explain the exclusion of magnetic flux from a zero field cooled superconductive material, upon cooling the material from its normal state to its superconductive state in a previously applied magnetic field perfect conductivity would cause the flux to become trapped within the volume of the superconductor thus the expulsion of the field proved that superconductors are more than just perfect conductors.

The discovery of the Meissner effect and its inexplicable origin compelled German brothers Heinz and Fritz London in 1935 [25] to propose a phenomenological theory to account for flux expulsion in superconductors. Based on a two-fluid picture where the electric field accelerates only the superconductive frictionless electrons which short circuit the normal electrons they proposed two equations in addition to Maxwell's equations to account for the observable electromagnetic properties of superconductors. The success of the theory relies in its ability to explain the Meissner-Ochsenfeld effect as well as in the prediction that the magnetic field is not completely expelled near the surface of the

superconductor but its magnitude is exponentially attenuated as the field penetrates the volume over a characteristic length called magnetic London penetration depth.

A major breakthrough in the theoretical advancement of superconductivity came in 1950 when Russian scientists Vitaly Lazarevich Ginzburg and Lev Davidovich Landau formulated a theory to explain the macroscopic properties of superconductors [26]. The phenomenological theory, based on Landau's generalized theory of second order phase transitions, introduced the concept of an order parameter to describe the normal-superconductive phase transition. The superconductive order parameter was introduced as a thermodynamic variable, in the form of a pseudo-wave function. It is zero above the critical temperature and non-zero in the superconductive state with a value directly related to the density of superconductive electrons. The theory introduces another important parameter in superconductivity namely the coherence length, a characteristic length which defines the distance over witch the density of superconductive electrons does not vary significantly. Besides being able to provide a derivation of London equations, the Ginzburg-Landau theory was able to describe the thermodynamic properties of superconductors. Although not generally appreciated at first mostly by the western scientific community, mainly because of its simple assumptions and phenomenological approach, its success in predicting so many properties of superconductors and its extensive current use as a powerful formalism in treating the unique phenomena behind applied superconductivity, make it one of the greatest theories today in superconductivity. L. Landau received the Nobel Prize in Physics in 1962 for his development of mathematical theory of super-fluidity and was later followed by V. L. Ginzburg in 2003 for his pioneering contribution to the theory of superconductors.

The radical development in the field of superconductivity came in 1957 [27, 28] when, after more than half a century since its discovery, the first successful microscopic theory of superconductivity was proposed by American scientists John Bardeen and his students Leon Neil Cooper and John Robert Schrieffer. The BCS formalism is now the theoretical basis of our understanding of the nature of superconductivity. With the prediction made by H. Frohlich in 1950 [29] that the superconductive transition temperature would decrease as the mass of the nuclei in the ionic system would increase (isotope effect), which later that year was observed experimentally in mercury by two different groups i.e. Emanuel Maxwell [30] and C. A. Reynolds *et al.* [31], it became clear that lattice vibrations play an important role in the physics behind superconductivity. One year before the publication of the BCS formalism, L. N. Cooper [32] demonstrated that an attractive potential between electrons, however weak, will lower the energy of an electron gas below the Fermi level due to the formation of bound electron pairs. The coupled fermions, now referred as Cooper pairs, can take the character of bosons and condense into a ground state resembling a Bose-Einstein condensate with lower energy. Using the idea of Cooper pairs, correlated due to Pauli's exclusion principle, and assuming a phonon mediated electron pairing

interaction, advocated by the isotope effect, the BCS theory proposes a model for the attractive interaction and a symmetric wave function to describe the Cooper pairs to solve for the Hamiltonian describing the many-electron state. The theory showed how a superconductive state forms when coherent electron pairs condense below the Fermi level leaving an energy gap. The BCS formalism predicts the temperature dependence of the superconductive gap magnitude forming just below the critical temperature and reaching a maximum value at lowest temperatures. It also manages to relate the critical superconductive temperature to microscopic properties of materials. In addition to providing a quantitative theoretical explanation of so many experimentally observed properties of superconductors it also provided a microscopic justification for the rather successful phenomenological two-fluid model of superconductivity, consistent with London's description of the Meissner effect. Besides, F. London suggested in 1947 [33] that London equations may be consequences of the coherence of a quantum state. In 1953, Brian Pippard [34] proposed that this would modify the London equations via a new scale parameter called the coherence length followed by J. Bardeen [35] who, in 1955, argued that such a modification will occur naturally in a theory with an energy gap). The successes of the BCS theory were immediately recognized and in 1972 Bardeen, Copper and Schrieffer received the Noble Prize in Physics *"for their jointly developed theory of superconductivity, usually called the BCS-theory"*.

Only two years after the development of the BCS formalism Lev Gor'kov, a Russian physicist, published his microscopic derivation of the Ginzburg-Landau equations [36] in the BCS theory of superconductivity providing the first solid theoretical foundation to the phenomenological Ginzburg-Landau (G-L) theory. Gor'kov showed that, at least near the critical temperature, this simple theory proposed on symmetry grounds alone and postulating the existence of a macroscopic wave function, equivalent to an order parameter, was able to provide exact solutions to superconductive phenomena and explain many of the unique properties of superconductors. It was the discovery of Gor'kov that provided the Ginzburg-Landau theory and its architects the much deserved worldwide attention and appreciation. The London equations follow naturally from the G-L theory and its application nowadays is essential for applied superconductivity.

The same year in which the BCS theory came to be, the Russian physicist Alexei Alexeyevich Abrikosov, a former student of Lev D. Landau, published his results based on the Ginzburg-Landau formalism on the magnetic properties of type II superconductors [37]. He demonstrated that it is possible for some superconductors to develop a mixed superconductive-normal state in the presence of high magnetic fields. He introduced the concept of type II superconductors in 1952 when he showed that, in materials with coherence length smaller than a certain value, the transition from superconducting to the normal state happens gradually in increasing field with two limiting critical fields. Although Landau did not initially approve of his findings, in 1957 he showed that in a type II superconductor, it is energetically

favorable to have the creation of normal domains within the superconductive bulk surrounded by super-current whirlpools called vortices, dispensed in a periodic lattice structure, through witch magnetic flux can penetrate in discrete quanta. The discovery did not attract attention, in spite of an English translation, and only after the discovery in the beginning of the 1960s of superconducting alloys and compounds with high critical magnetic fields there appeared an interest in his work. Even after that experimentalists did not believe in the possibility of existence of a vortex lattice incommensurable with the crystalline lattice. Only after the vortex lattice was experimentally observed ten years later, first by neutron diffraction [38] and then by bitter decoration [39], Abrikosov's theory on the mixed state in type II superconductors received its rightful consideration. The fact that most superconductors discovered from here on out are type II and considering that Abrikosov vortices are responsible for most of the electromagnetic behavior of applied superconductivity today, it is no surprise that A. A. Abrikosov received the Nobel Prize in Physics in 2003 together with V. L. Ginzburg and Anthony J. Leggett *"for pioneering contributions to the theory of superconductors and superfluids"*.

By the late 1970s superconductivity seemed to be a more or less closed subject. The nature of superconductivity in most elements and alloys discovered since has been successfully explained by the BCS theory. It was understood that electrons would pair up to form Cooper pairs with a total spin S = 0 (singlet pairing) and a total orbital momentum $L = 0$ due to a week attractive interaction caused by a virtual exchange of phonons and the screened Coulomb repulsion. The pairing was described by an isotropic wave function (s-wave) and below the transition temperature a macroscopic quantum state is formed by the bosonic condensate. However, in 1979, Steglich *et al.* [40] reported on the superconductivity of $CeCu_2Si_2$, a heavy-fermion compound characterized by immensely enhanced effective mass of the quasi-particles (Cooper pairs) with unusual superconductive properties and a coexistence with anti-ferromagnetic order. This came as a surprise since magnetism and superconductivity were believed to be antagonistic phenomena. Later several Uranium based heavy electron compounds were discovered to show signs of unconventional superconductivity, described by a non-phonon mediated pairing mechanism, like UBe_{13} (H. R. Ott *et al.* in 1983) [41], UPt_3 (G. R. Stewart *et al.* in 1984) [42] and many more after. The Cooper pairing in these materials seems to be of the $L = 1$ (p-wave) type however, the mechanism behind the coupling of the electrons remained elusive. The fact that a generalized BCS theory to account for unconventional superconductivity, introduced by P. Morel and P. W. Anderson in 1961 [43] together with R. Balian and N. Werthamer in 1963 [44], was able to explain the superconductivity of heavy fermion compounds emphasizes the brilliance, universality and importance of the concepts introduced by the BCS theory.

A milestone in the field of superconductivity is represented by the events in 1986 when Swiss scientist Karl Alex Müller and German physicist Johannes Georg Bednorz, researchers at IBM, reported

their results on the superconductivity of a barium-doped compound of lanthanum and copper oxide with a high critical temperature of 35 K [3]. The importance of the discovery lies in the fact that the BCS theory, although able to explain the nature of superconductivity in previously discovered superconductors, predicted a limit to the critical temperature of ~30 K, thus the origin of the unconventional superconductivity in this layer copper oxide was unknown. When the article appeared in print it was initially met with skepticism as high-Tc superconductivity has been sporadically reported over the previous years but always failed to show the required diamagnetic response. When a Japanese group (S. Tanaka *et al.* [45]) confirmed, at the end of 1986, that diamagnetism is indeed present above 30 K in Ba-doped $LaCuO_3$ followed shortly by the report of American group of P. Chu [46] reproducing the original results, it was obvious that the historical limit of the transition temperature has been crossed and sparked the attention of the international scientific community resulting in a flurry of activity which lead to a rapid rise of recorded transition temperature. The discovery of J. G. Bednorz and K. A. Müller is considered as the starting point of a new era in superconductivity and marks the beginning of high-temperature superconductivity field. *"For their important break-through in the discovery of superconductivity in ceramic materials"* its originators received the Nobel Prize in Physics in 1987.

It was only a year later that the American group led by Paul Chu discovered superconductivity in Yttrium Barium Copper Oxide (YBCO) at 93 K [47], the first material to show superconductivity above the 77 K boiling point temperature of liquid nitrogen and, although its application are limited and many more superconductors with superior performances have been discovered since, it is currently one of the most famous superconductive materials known, partly because of its wide use in educational demonstrations. The Bismuth Strontium Calcium Copper Oxide (BSCCO) family of superconductors, discovered in 1988 by H. Maeda and coworkers in Japan [48], reached critical temperatures as high as 110 K and were the first superconductors to be used in the manufacturing of superconductive wires. The critical temperature range has since continuously increased. The discovery of Thallium based HTC superconductive oxides ($Tl_2Ca_2Ba_2Cu_3O_{10+\delta}$ by Hazen *et al.* in 1988 [49]) with critical temperatures above 120 K and the discovery of Mercury based HTSC cuprate oxides ($HgBa_2CuO_{4+\delta}$ by Putilin *et al.* [50] and $HgBa_2Ca_2Cu_3O_{1+x}$ by Schilling *et al.* in 1993 [51]) with transition temperatures above 130 K are some of the major breakthroughs. The continual increase in critical temperature culminated in 1993 when A. Schilling et al. reported on ambient pressure superconductivity of $HgBa_2Ca_2Cu_3O_8$ with transition temperature of 133 K, a record that still holds to this day, and a transition temperature of 164 K under 45GPa in the same compound reported in 1994 by L. Gao *et al.* [6].

The discovery of cuprates initiated the development of high temperature superconductivity and was a milestone in the technological implementation of superconductors. From a theoretical perspective, their unconventional superconducting nature has led to a better understanding of the whole field and has

had a huge impact on the development of concepts behind superconductivity. During the subsequent years following their discovery, a tremendous amount of research has been focused towards uncovering the underlying principles of superconductivity in copper oxides. Over 100.000 scientific papers have been published since their discovery thus far and, although the microscopic mechanism responsible for pairing is still unclear, the pairing symmetry is unambiguously assigned to be of d-wave type for most of them.

For a long time, the coexistence of magnetism and superconductivity was inconceivable considering they were believed to be competing forms of electronic order. The study of the interplay between superconductivity and magnetism started with the cuprates and the antiferromagnetic correlations with the superconductive phase which led many researchers to suggest that the origin of the superconductivity in the cuprates is magnetic. With the recent uncovering of superconductivity in the ferromagnetic UGe_2 reported by S .S. Saxena *et al*. in 2000 [7] together with the discovery of superconducting URhGe by D. Aoki *et al.* in 2001 [52], ferromagnetic superconductors have sparked considerable interest in the scientific community and a great deal of effort has been focused towards the understanding of their unconventional superconductivity and intrinsic coexistence of superconductivity with ferromagnetism.

Perhaps the most significant advancement after the cuprate superconductors came with the discovery of superconductivity of magnesium diboride MgB_2 in 2001 with a transition temperature of 39 K by the Japanese group of J. Nagamatsu *at al.* [53]. Although its remarkably high transition temperature would suggest unconventional superconductivity, the boron isotope effect observed in the material reported by American research group at AMES Laboratory of S. L. Bud'ko *et al.* [54] showed that it was consisted with conventional phonon-mediated BCS superconductivity. The fact that it is a simple compound of two abundant inexpensive elements together with relatively high critical temperature makes MgB_2 a strong candidate for practical applications. It's rather unusual, given conventional superconductivity, makes it also one of the most theoretically interesting materials. The understanding of its superconductive properties has been full of surprises, and it seems the nature of superconductivity in MgB_2 can be explained by the concept of the simultaneous existence of two superconducting energy gaps.

The most recent radical development in the field of superconductivity occurred after 2006 when the Japanese group of Hideo Hosono announced superconductivity in the iron-based layered oxy-pnictide material LaOFeP around 4 K [55]. Although the finding did not received interest at first, due to the low transition temperature value, a second publication by the same group two years later (Y. Kamihara et al. in 2008 [56]) , reporting on a superconductive transition temperature of 26 K in fluorine doped $LaO_{1-x}F_xFeAs$, caught the immediate attention of the international scientific community and marked the beginning of a new era in superconductor research. The cuprate age had been replaced by the new era of iron-based superconductors as all the research and funding shifted from the study of cuprates to the new

superconductors. As a result, a multitude of superconductors containing iron have since been discovered with critical temperatures as high as 55 K (in $Sm[O_{1-x}F_x]FeAs$ reported by Z. A. Ren *et al.* in 2008 [57]). The fact that the ferromagnetic iron is present in a superconducting structure was clear evidence that the nature of superconductivity in these new materials is unconventional and has led researchers into an active investigation of their intriguing properties. In only 5 years since their discovery, the seminal paper has been cited over 5.000 times and the mechanism behind the superconductivity in iron based materials is considered, as of 2010, one of the major unsolved problems of theoretical condensed matter physics. Their exotic properties revolving around the coexistence of superconductivity and magnetism together with the large variety of compounds with relatively simple structures for research could hold the key towards resolving the mystery behind the mechanism of high temperature superconductivity. Apart from the theoretical interest, more and more studies about their potential for technological applications seem to point to iron based superconductors as the new materials in applied superconductivity.

For over a century now superconductivity has been a field of continuous development and high controversy, plentifully bestrewn with ground breaking discoveries and theoretical advancements. Today its usage in a large variety of science fields is indispensable and its applications are countless. The technological and socio-economic reasons for carrying out further research on superconductors go far beyond what we can see now as practical applications: electric generators, super-strong magnets for particle accelerators and MRI, levitating trains, spintronics, SQUID magnetometers, electronic devices, cryogenic applications etc. The ultimate goal of this field to develop room-temperature superconductors will more likely revolutionize our society by enabling a truly global energy supply and ultra-high performance Information and Communication Technology (ITC) devices. As mentioned in [58], the Saharan sun could power Europe via superconductor cables of thousands of kilometers with losses of only a few percent while the superconducting quantum computers could solve problems thousands of times faster than the most powerful conventional supercomputers [59, 60].

1.2. Theories and concepts in superconductivity

Two decades after H. K. Onnes made the discovery of zero resistance in mercury below 4.15 K [4] and below 7.2 K in lead [5] W. Meissner and R. Ochsenfeld conducted an experiment to investigate the magnetic susceptibility of superconductors in an applied magnetic field. The tests were performed for elongated single crystal cylinders of lead and tin in a small applied field of 5 Gauss and revealed that on cooling below the transition temperature the field line pattern in the region outside the superconductor changes almost to that which would be expected if the materials had perfect diamagnetism. According to Maxwell's theory for a perfect conductor, the field lines should be excluded from a superconductive

material upon applying an external field. However, the theory could not account for the observed field expulsion effect upon cooling the superconductors from their normal state in an existing applied field (Fig. 1.1). It thus became obvious that superconductors are more than just perfect conductors and that there is another fundamental characteristic of these materials manifested in the expelling of magnetic flux from their interior upon transitioning from a normal state to a superconductive state which later became known as the Meissner-Ochsenfeld effect (Meissner effect).

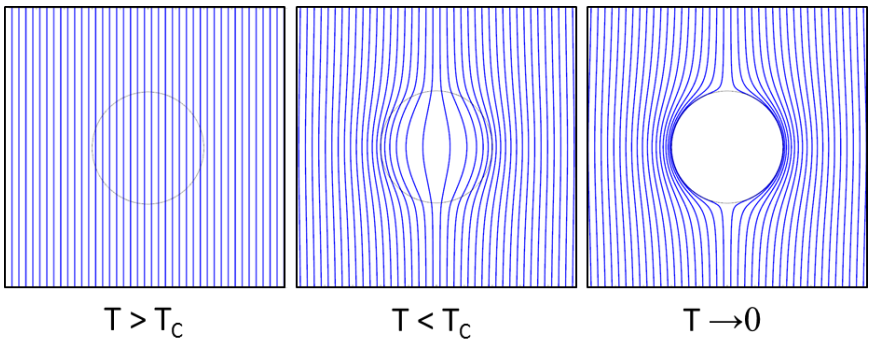

Figure 1.1 Magnetic flux expulsion from a superconductive sphere

Many theories have been proposed to describe the zero resistance of superconductors since their discovery although none could explain this newly discovered effect. In order to account for this fascinating phenomenon, in 1935 German brothers Heinz and Fritz London proposed a set of equations derived from phenomenological observations regarding the electromagnetic behavior of superconductors. It is important to notice that using Drude's model for resistivity proposed in 1900, the Ohm's law is given by

$$\boldsymbol{j} = \frac{e^2 n}{m} \tau \, \boldsymbol{E} \qquad (1.1)$$

where $\boldsymbol{j}$ is the electric current density with electron charge e , mass m , density n and τ average scattering time in an applied electric field $\boldsymbol{E}$. This resulted in a frequently proposed view that the scattering rate should be infinite in superconductors which Landau did not agree with, as mentioned in his 1933 publication [61], where he argued that it is highly implausible that all interactions are suddenly switched off at the transition temperature. The classical equation of motion of electrons is given by

$$m\frac{d\boldsymbol{v}}{dt} = e\boldsymbol{E} - \frac{m\boldsymbol{v}}{\tau} \qquad (1.2)$$

where $\boldsymbol{v}$ is the average drift velocity. Since superconductors exhibit a permanent current even in the absence of an electric field, the proportionality between the current and electric field, as it is the case in Ohm's law, could not be applied to superconducting currents. As a replacement Becker, Sauter and Heller [62] proposed in 1933 an acceleration equation of the form:

$$\frac{d\boldsymbol{j}}{dt} = \frac{e^2 n}{m}\,\boldsymbol{E} \qquad (1.3)$$

which in the absence of a field ($\boldsymbol{E} = \boldsymbol{0}$) would lead to a stationary current $\boldsymbol{j} = const$ which is the case for a perfect conductor in an electric field.

The London brothers, following the proposal of Gorter and Casimir [63], started their approach assuming that currents in a superconductor are the sum of a normal electrons component whose behavior is described by Ohm's law (Eq. 1.1) and a superconducting component which is accelerated by $\boldsymbol{E}$ (Eq. 1.3). Considering Faraday's law:

$$\nabla \times \boldsymbol{E} = -\frac{\partial \boldsymbol{B}}{\partial t} \qquad (1.4)$$

it would mean that in a perfect conductor

$$\nabla \times \frac{\partial \boldsymbol{j}}{\partial t} = -\frac{e^2 n}{m}\frac{\partial \boldsymbol{B}}{\partial t} \qquad (1.5)$$

From Ampere's law $\nabla \times \boldsymbol{B} = \mu_0 \boldsymbol{j}$, considering quasi-static electric fields, Eq. 1.5 implies that the magnetic field $\boldsymbol{B}$ inside a superconductor would decay with a length scale given by:

$$\lambda = \sqrt{\frac{m}{\mu_0 e^2 n}} \qquad (1.6)$$

In addition, the London brothers concluded that the initial field would have to remain unchanged inside the superconductor through its transition from normal state if superconductors are treated as perfect conductors.

Given the new experimental discovery of Meissner and Ochsenfeld it was obvious that the acceleration equation alone could not explain the expulsion effect of the magnetic field from superconductors upon cooling down. H. London and F. London realized that superconductors cannot be treated in the frame of perfect electric conduction and that the history dependence of the magnetic flux is a direct consequence of the presence of time derivatives on both sides of Eq. 1.5. Consequently, they postulate that in a superconductor the time dependence in Eq. 1.5 can be dropped and suggest the Ohm's law for supercurrents be replaced by:

$$\nabla \times \boldsymbol{j} = -\frac{e^2 n}{m}\boldsymbol{B} \qquad (1.7)$$

Most of the previous theories trying to explain superconductive transport phenomena seemed to relate the supercurrents density to the external electric fields or time varying magnetic fields by some relation as it was inconceivable that electron motion would be caused by anything else. London's fundamental contribution was to make it unambiguously clear that supercurrents inside a superconductor are supported by magnetic fields and not by electric fields [64]. It is important to mention that Eq. 1.7 was not directly derived from the electromagnetic theory but was suggested as an additional condition to

Maxwell's equations to account for the experimental behavior of superconductors in magnetic field. Using the substitution from Eq. 1.6 we can rewrite Eq. 1.3 and Eq. 1.7 as:

$$\frac{d\boldsymbol{j}}{dt} = \frac{\boldsymbol{E}}{\mu_0 \lambda^2} \tag{1.8}$$

and

$$\nabla \times \boldsymbol{j} = -\frac{\boldsymbol{B}}{\mu_0 \lambda^2} \tag{1.9}$$

Historically, these last two equations became known as the first and second London equation, respectively and, although without any microscopic grounds at the time of their conception, they provided the first satisfactory theory to account for the unique electromagnetic properties observed in superconductors.

Adopting the new model for supercurrents H. and F. London suggested that Meissner effect can be explained considering that the supercurrents would short-circuit the normal electrons current thus no energy dissipation occurs inside the material bulk and that the production of heat occurs on the surface where normal currents still exist. Considering Maxwell's equation for slow time varying electric fields $\nabla \times \boldsymbol{B} = \mu_0 \boldsymbol{j}$, the second London equation can be expressed as

$$\nabla^2 \boldsymbol{B} = -\frac{\boldsymbol{B}}{\lambda^2} \tag{1.10}$$

and it characterizes the magnetic flux density inside a superconductor. The same Helmholtz type differential equation can also be used to analyze the spatial dependence of supercurrents density. Indeed, by applying the curl operator to Eq. 1.9, we arrive at the alternative expression for London's second equation in respect to current density:

$$\nabla^2 \boldsymbol{j} = -\frac{\boldsymbol{j}}{\lambda^2} \tag{1.11}$$

The same equation can be used to describe the electric field inside a superconductor. Considering Faraday's law (Eq. 1.4) for the current density in second London equation we arrive at:

$$\nabla^2 \boldsymbol{E} = -\frac{\boldsymbol{E}}{\lambda^2} \tag{1.12}$$

If we consider the magnetic flux density **B** as being derived from a vector potential **A** defined by

$$\boldsymbol{B} = \nabla \times \boldsymbol{A} \tag{1.13}$$

since $\boldsymbol{A}$ is essentially derived from $\boldsymbol{B}$ via integration, this definition is not complete. It is easy to see that adding the gradient of a scalar function to the magnetic vector potential $\boldsymbol{A} = \boldsymbol{A} + \nabla \mathrm{k}$ will give the same result for $\boldsymbol{B}$. A simple fix for the problem is adding a gauge for the potential to simply the resulting equation. The choice of gauge in London's theory is the Coulomb gauge:

$$\nabla \cdot \boldsymbol{A} = 0 \tag{1.14}$$

Consequently, we can write the second London equation (Eq. 1.9) as:

$$\boldsymbol{j} = -\frac{\boldsymbol{A}}{\mu_0 \lambda^2} \tag{1.15}$$

Considering that charge conservation requires $\nabla \cdot \boldsymbol{j} = 0$, the vector potential $\boldsymbol{A}$ must be transverse thus the choice of gauge is appropriate. In superconductivity the condition expressed in Eq. 1.14 is also known as the London gauge and is the necessary condition for which Eq. 1.15 is valid.

Similarly, a scalar potential V can be used for the electric field $\boldsymbol{E}$ of the form $\boldsymbol{E} = -\nabla V$. Considering the contribution from time varying magnetic fields, the electric field can be expressed as:

$$\boldsymbol{E} = -\nabla V - \frac{\partial \boldsymbol{A}}{\partial t} \tag{1.16}$$

Using the expression for $\boldsymbol{E}$ in the first London equation, one arrives at:

$$\frac{\partial \boldsymbol{j}}{\partial t} = \frac{1}{\mu_0 \lambda^2}\left(-\nabla V - \frac{\partial \boldsymbol{A}}{\partial t}\right) \tag{1.17}$$

which, in the London gauge, leads to the same expression in Eq. 1.3. Therefore, both London equations can be merged into one of the form, expressed in Eq. 1.15, whereas the electric potential can be transformed to verify the equation

$$V \rightarrow V - \frac{\partial k}{\partial t} \tag{1.18}$$

with k being the same scalar function used for the magnetic vector potential $\boldsymbol{A}$.

As we will show in Chapter II, the solutions to the London equations substantiate the fact that electromagnetic fields in Meissner state superconductors are exponentially attenuated over a length scale λ, as they enter the superconducting domain, vanishing deep inside the bulk of the superconductor. The length λ is characteristic to each material and is a fundamental parameter in superconductors known as the London penetration depth.

From Eq. 1.6 it is transparent that the penetration depth is a function of the electron density. The two-fluid model proposed by Gorter and Casimir [63] based of experimental observations leads to a temperature dependence of the density of superconducting electrons n_S of the form

$$n_S = n\left[1 - \left(\frac{T}{T_c}\right)^4\right] \tag{1.19}$$

where n is the total density of conduction electrons and T_c the critical temperature. Consequently the magnetic penetration depth λ is expected to have a temperature behavior of the form

$$\lambda(T) = \lambda(0) \Big/ \sqrt{1 - \left(\frac{T}{T_c}\right)^4} \tag{1.20}$$

The experimental confirmation of the partial penetration law of magnetic fields inside a superconductor proposed by the London brothers was made five years later by D. Schoenberg [65]. Measuring the magnetic susceptibility in a colloidal suspension of small mercury particles as a function of temperature he was able to give the first experimental verification of the theory and the first curves representing the temperature variation of the London penetration depth.

While the theory proposed by the London brothers provides a remarkable phenomenological account of the Meissner effect, a microscopic confirmation of its concepts was missing. A considerable number of distinguished scientists of the period took an interest in formulating a theory of superconductivity. Werner Heisenberg, one of the creators of modern quantum mechanics, as well as Max Born together with K. C. Chen published their microscopic explanation for superconductivity in 1948 [66, 67] which F. London strongly disagreed with. As a result, in the same year, F. London proposed his own microscopic theory. In his publication [33] he pointed out the flaws of the previously proposed theories and gave a quantum motivation for the London equations based on the exchange interactions of electrons that can lead to an *"attraction in momentum space"*. He also emphasized the use of the vector potential $\boldsymbol{A}$ and although vague, his ideas clearly indicate that a superconductor is a macroscopic object in a coherent quantum state. The density of electrons n_S participating in this rigid ground state at temperatures close to zero will result in the ideal theoretical limit for the London penetration depth:

$$\lambda(0) = \sqrt{\frac{m}{\mu_0 e^2 n_S}} \qquad (1.21)$$

However, subsequent temperature measurements of the radio-frequency penetration depth above and below the critical temperature seem to always yield higher values for the London penetration depth λ even if the temperature dependence was extrapolated to zero to give $\lambda(0)$.

In 1953 Sir Alfred Brian Pippard gave a quantitative explanation of this observed excess penetration depth considering that the electrons have a long range influence on each other [34]. Working on a non-local generalization of London's equations, inspired by the non-local generalization of Ohm's law proposed by R. G. Chambers, he argued that, similarly to the mean free path of the electrons in Ohm's law, the superconducting wave function should have an analogous characteristic length scale which he called coherence range (length). He used the uncertainty principle to argue that only the electrons with energies within $\sim k_B T_C$ of the Fermi level can play a contribution in a phenomenon which sets in at T_C. Accordingly:

$$\Delta x \gtrsim \frac{\hbar}{\Delta p} \approx \frac{\hbar v_F}{k_B T_C} \qquad (1.22)$$

leads to an expression for the coherence length ξ of the form:

$$\xi \sim \frac{\hbar v_F}{k_B T_C} \qquad (1.23)$$

These ideas inspired Pippard to propose a non-local variant of London's equation (Eq. 1.15) and conclude that there is a length scale ξ over which the supercurrents density will not vary significantly in a spatially varying magnetic field, namely the coherence length. The value of this characteristic length is much larger than the London penetration depth in elemental superconductors and plays a similar role as the mean free path in non-local electrodynamics in the sense that it is dependent on the degree of material purity. Because in elemental metals $\xi \gg \lambda$ and the vector potential $\boldsymbol{A}$ is expected to decrease exponentially with λ over a region on the scale of ξ, the supercurrents magnitude is weakened which increases field penetration therefore justifying the experimentally observed excess in magnetic penetration depth values.

In 1950 V. L. Ginzburg and L. D. Landau used the notions of penetration depth, coherence length and the idea of a superconductive wave-function introduced by London, to propose their own phenomenological theory of superconductivity. Although generally ignored at first due to its lack of a microscopic foundation and simple assumptions, as its legitimacy was later confirmed, its usefulness was widely recognized and continues to be one of the most valuable theories in superconductor physics. In their approach, Ginzburg and Landau introduce a complex pseudo-wave function ψ as an order parameter, within Landau's theory of second order phase transition, to describe the superconducting electrons, with the density (the same defined for London equations) given by:

$$n_S = |\psi(x)|^2 \qquad (1.24)$$

They used a variational principle and assumed a series expansion of the free energy to arrive at the following differential equation for the order parameter:

$$\alpha\psi + \beta\psi|\psi|^2 - \frac{1}{2m^*}(i\hbar\nabla + q^*\boldsymbol{A})^2\psi = 0 \qquad (1.25)$$

where α, β are the expansion coefficients and the corresponding equation for the supercurrents density:

$$\boldsymbol{j} = \frac{i\hbar q^*}{2m^*}(\psi\nabla\psi^* - \psi^*\nabla\psi) - \frac{{q^*}^2}{m^*}|\psi|^2\boldsymbol{A} = 0 \qquad (1.26)$$

where m^* and q^* are the mass and charge of the superconducting particles. The formalism also introduces a characteristic length which features the distance over which the wave function ψ can vary without undue energy increase now called the Ginzburg-Landau (GL) coherence length:

$$\xi(T) \sim \frac{\hbar}{\sqrt{|2m^*\alpha(T)|}} \qquad (1.27)$$

which is related to the one introduced by Pippard but distinct. The theory also introduces a parameter, trait of material, defined as the ratio between the two characteristic lengths (GL parameter) $\kappa = \lambda/\xi$.

The London equations arise naturally from the GL theory. Additionally, the success of the formalism consists in its ability to treat situations when the density of superconducting electrons n_S has a spatial variation as well as nonlinear effects of magnetic fields strong enough to change its magnitude, details which London formalism could not handle. One of such situations is the intermediate state of superconductors. It was established that a strong enough magnetic field, known as the critical field, will destroy the superconductive state. However, for a finite size superconducting sample in an applied field below the critical value, the demagnetizing effects will create regions within the sample in which the internal field value is larger than the critical value thus returning the region to a normal state. The critical field will also induce an associated critical current density. As the GL theory can show, the normal regions can coexist with the superconductive ones in an energetically favorable state called intermediate state. The Ginzburg-Landau theory managed to provide quantitative descriptions for the observed temperature dependence of the London penetration depth, critical current density and critical magnetic field and proved extremely useful in explaining and treating the intermediate state of superconductors. For most superconductors known at the time the GL parameter $\kappa \ll 1$ and Ginzburg and Landau showed that the energy associated with the formation of a boundary between the normal and superconductive domains is positive. As a consequence, an intermediate state is energetically favored, with normal domains, of dimensions comparable with microscopic length ξ, forming in the superconductor.

A. A. Abrikosov, trying to experimentally confirm the predictions of the theory developed by Ginzburg and Landau, observed that superconductive thin films exhibit two thermodynamic critical fields. He then proceeded to investigate what would happen in GL theory if the parameter κ was large instead of small i.e. $\lambda > \xi$. He concluded that there exists a breaking point between two very different behavioral regimes of superconductors in magnetic fields defined by a value of the Ginzburg-Landau parameter $\kappa = 1/\sqrt{2}$. In his 1957 publication he introduced the concept of superconductors of second type (type II superconductors) described by a GL parameter value $\kappa > 1/\sqrt{2}$ for which he found a continuous increase in flux penetration starting at lower critical field H_{C1} and reaching the maximum value at an upper critical field H_{C2}. This behavior was attributed to the formation of normal domains surrounded by whirlpools of supercurrents. He described the normal domains as magnetic vortices, through which quanta of magnetic flux can penetrate, forming a lattice within the superconductive domain which he called the mixed state. This situation is different than that of Type I superconductors, characterized by $\kappa < 1/\sqrt{2}$, in which an intermediate state can arise with a thermodynamic critical field H_C. In both cases the Meissner state will be present for a magnetic field value below H_C for type I and H_{C1} for type II materials. The situation is described in Fig. 1.2 which depicts the thermodynamic critical fields as a function of temperature for both superconductor types.

Since Abrikosov's discovery, many superconducting materials have been found to be of type II which is in fact the case for most superconductors known today. Moreover, since the upper critical field values can reach extremely high values, their application in generating high magnetic fields is crucial. The microscopic vortex structures play a key role in the complex electromagnetic behavior of applied superconductors. The same vortices that stabilize a superconductor in magnetic fields give it the ability of carrying electrical current with no resistance. Vortex movement is responsible for dissipating energy and destroying the zero-resistance. Finding a way of pinning the vortices in type-II superconductors, to ensure zero electrical power losses, has been one of the central problems for their application. Motivated by this quest, vortex physics has been the subject of extensive experimental and theoretical studies.

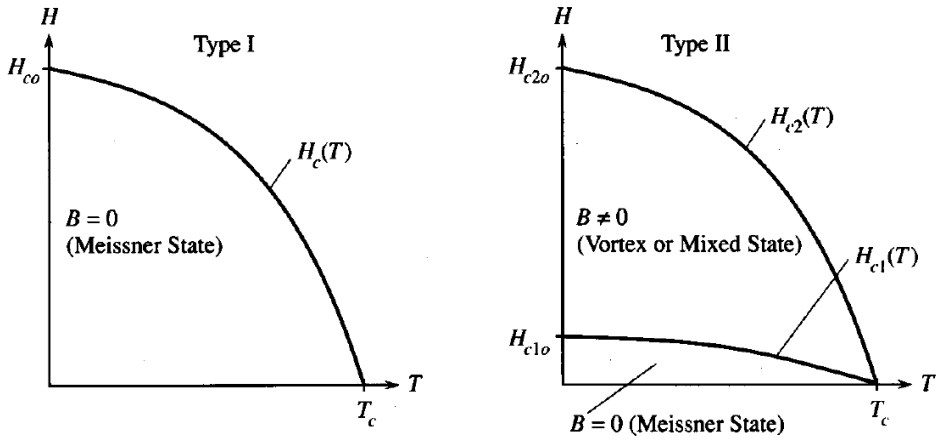

Figure 1.2 Thermodynamic critical field diagram for Type I (left) and Type II (right) superconductors

The same year Abrikosov published his findings Barden, Cooper and Schrieffer introduced their theory of superconductivity, the first microscopic theory to give an accurate description of the unique properties of superconductors and continues to remain the most successful theory to this day. It was observed that in most superconductors the transition temperature T_C often decreased with increasing isotope mass M according to a relation of the form $M^{\alpha}T_C = const$ where $\alpha \approx 1/2$. It became obvious that lattice vibrations play a key role in the mechanism behind superconductivity. The isotope effect together with the findings of Cooper, who showed that a non-interacting Fermi sea is unstable towards the formation of a single pair of electrons due to a weak attractive interaction, provided the necessary ingredients for the conception of the BCS formalism.

The formation of Cooper pairs can be thought of as arising from deformations of the ionic lattice. As one electron moves through it, the Coulomb attraction will cause a slight local deformation of the ionic system characterized by a net positive charge density. Considering that a typical electron close to

the Fermi surface moves with velocity $v_F = k_F/m$, which is much larger than the velocity of the ions $v_I = E_F m/M$, by the time ($\tau \sim 2\pi/\omega_D \sim 0.1ps$) the ions have polarized themselves, the electron would have traveled a distance ~ 1000Å. A second electron can happen to pass by and feel the attraction of the positive charge before the ionic fluctuation relaxes away. This gives rise to an effective attraction between the two electrons which can lead to the formation of boson like pairs. As shown by the BCS theory, the formation of electronic bound states is necessary but not sufficient. The theory started by constructing the wave-function of such a bound pair assuming that spins have opposite magnetic moments and symmetric orbital parts (singlet spin state). The wave function is symmetric (s-wave) and a total wave function can be built by the product of individual wave-functions. Considering an effective Hamiltonian Bardeen, Cooper and Schrieffer were able to find the quantum-mechanical state of the system and conclude that the Copper pairs will condense into a ground state characterized by a BCS wave-function where the phases of all bound pairs are coherent. Although BCS formalism can be applied regardless of the origin of the attractive interaction, phonon-mediated attractive potential will give rise to the formation of Cooper pairs with s-wave symmetry. Since superconductivity arises from the formation of bound Cooper pairs, a finite amount of energy is needed to break these pairs. This implies there must be an energy gap near the Fermi level which is highest at low temperatures but vanishes at the transition temperature when superconductivity ceases to exist. By supplying an amount of energy equal to the value of the energy gap, the Cooper pairs will break into what are known as Bogoliubov quasi-particles. If we consider $\xi_k = \epsilon_k - \mu$ as the energy of single particle energy relative to Fermi level, where μ is the chemical potential and ϵ_k the Fermi energy, the BCS formalism can be used to derive the equation for the elementary excitation energy of the Bogoliubov quasi-particles:

$$E_k = \sqrt{{\xi_k}^2 + {\Delta_k}^2} \qquad (1.28)$$

It is obvious that Δ_k plays the role of the energy gap considering that even at the Fermi surface, where $\xi_k = 0$, the excitation energy of a fermion quasi-particle is positive.

One of the greatest triumphs of the BCS theory was its ability to provide a quantitative description of the temperature dependence of the energy gap. The probability of exciting a quasi-particle of energy E_k is described by the Fermi distribution thus by employing the BCS formalism an equation of the form can be derived:

$$\Delta_k = \sum_{k'} V_{kk'} \frac{\Delta_{k'}}{2E_{k'}} \tanh \frac{E_{k'}}{2k_B T} \qquad (1.29)$$

This last equation is known as the BCS gap equation where $V_{kk'}$ describes the attractive potential responsible with Cooper pair formation. In the original formulation of the BCS theory, the attractive potential was treated as being zero if $|\xi_k| \geq \hbar\omega_c$ and constant $-V$ otherwise, resulting in $\Delta_k = \Delta$ for

$|\xi_k| < \hbar\omega_c$ and $\Delta_k = 0$ for $|\xi_k|$ larger than the cutoff energy $\hbar\omega_c$ (where for phonon mediated interactions $\hbar\omega_c = \hbar\omega_D$). Therefore, the gap equation can be expressed in an integral form, where N_0 is the number of quasi-particles at zero temperature, given by:

$$\frac{1}{N_0 V} = \int_0^{\hbar\omega_D} \frac{1}{\left({\xi_k}^2 + \Delta^2\right)^{1/2}} \tanh \frac{\left({\xi_k}^2 + \Delta^2\right)^{1/2}}{2k_B T} d\xi_k \qquad (1.30)$$

The critical temperature T_C is defined as the temperature at which the order parameter vanishes. Near T_C the gap value $\Delta \to 0$ meaning $E_k \to |\xi_k|$. The gap equation, in its integral form (Eq. 1.30), can be approximated by:

$$\frac{1}{N_0 V} = \int_0^{\hbar\omega_D} \frac{1}{\xi_k} \tanh \frac{\xi_k}{2k_B T_C} d\xi_k \qquad (1.31)$$

This integral is divergent so the existence of a cutoff frequency (ω_D for phonon mediated interaction) is crucial. It can be evaluated to give:

$$\frac{1}{N_0 V} \approx \ln\left(1.13 \frac{\hbar\omega_D}{k_B T_C}\right) \Rightarrow T_C \approx 1.13 \frac{\hbar\omega_D}{k_B} e^{-1/N_0 V} \qquad (1.32)$$

In the model assumed by Cooper for the formation of a bound pair, he found a similar dependence for the energy gap Δ. For weak interactions, also known as the weak-coupling limit, $N_0 V \ll 1$ meaning $\hbar\omega_c / k_B T_C \gg 1$. Cooper showed that the pair binding energy is:

$$\Delta(T = 0) = \Delta_0 \cong 2\hbar\omega_C e^{-1/N_0 V} \qquad (1.33)$$

although, at the time, he did not know that the cutoff frequency ω_C can be identified as the phonon frequency ω_D. Comparing Eq. 1.32 and Eq. 1.33 we find that, in the weak-coupling limit,

$$\Delta(0) = \frac{2}{1.13} k_B T_C = 1.764\, k_B T_C \qquad (1.34)$$

The factor 1.764 has been experimentally tested and found to be very close to the predicted value for a large number of low T_C superconductors. Moreover, for weak interactions, expanding Eq. 1.30 near T_C we can find that the temperature dependence of the energy gap can be expressed as:

$$\frac{\Delta(T)}{\Delta(0)} \approx 1.74 \sqrt{1 - \frac{T}{T_C}} \qquad (1.35)$$

The ratio $\Delta(T)/\Delta(0)$ will reach the zero value at T_C and is expected to monotonically increase towards a maximum value of 1 at low temperatures. Since near $T = 0$ the temperature dependence is exponentially slow, the hyperbolic tangent in Eq. 1.30 is close to unity therefore $\Delta(T)$ will be constant. Alternatively, we can say that increasing the temperature from its minimum value, the energy gap has a value of unity $\Delta(T) = 1$ and will remain constant at least until a significant number of quasi-particles are excited.

In principle, the energy gap values can be found for any temperature by numerically solving the gap equation expressed in Eq. 1.29 or Eq. 1.30, although, at the time, numerical analysis was extremely laborious. B. Muhlschlegl [68] took it upon himself to carefully calculate and compile a table for $\Delta(T)$ and compare it with experimentally derived values. Fig. 1.3 depicts the experimental results obtained by P. Townsend and J. Sutton [69] by electron tunneling for the superconducting energy gap in a few materials. The fact that the experimental values are in close agreement with the predictions of the BCS theory attests to the competence of the formalism and its acclaim.

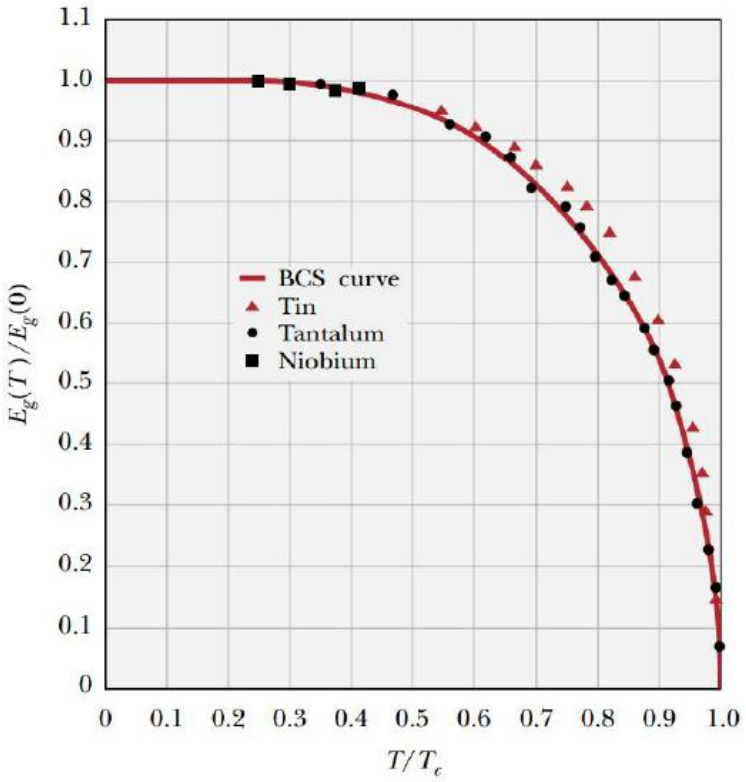

Figure 1.3 Energy gap temperature dependence for conventional superconductors

If we consider the electronic specific heat of superconductive materials, the BCS formalism yields an exponential dependence of temperature and shows how the superconductive transition gives rise to a discontinuity at T_C

$$\Delta C = (C_{es} - C_{en})_{T_C} = N_0 \left(\frac{d\Delta^2}{dT} \right) \qquad (1.36)$$

where C_{es} is the specific heat of the superconductive state and C_{en} the normal-state specific heat:

$$C_{en} = \frac{2\pi^2}{3} N_0 {k_B}^2 T = \gamma T \qquad (1.37)$$

The temperature dependence of the specific heat from BCS theory is depicted in Fig. 1.4. Using the approximate form of Eq. 1.35, the normalized magnitude value of the discontinuity is:

$$\frac{\Delta C}{C_{en}} = 1.43 \qquad (1.38)$$

The normalized specific heat jump is another ratio that the BSC theory was able to predict which helped confirm the theory in classic superconductors.

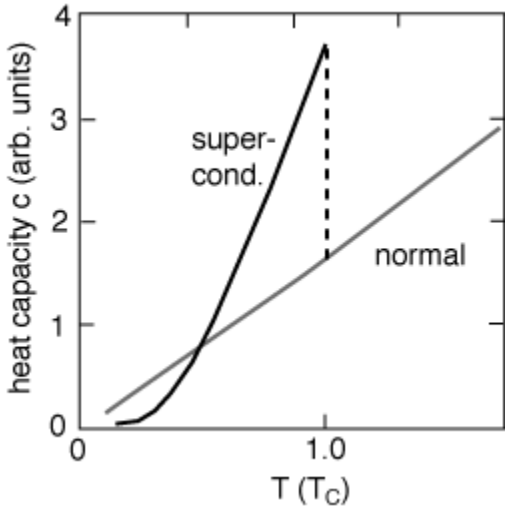

Figure 1.4 Heat capacity temperature dependence in superconductors

1.3. Unconventional superconductivity

Although the BCS theory proved to be a great tool in justifying so many of the observed properties of most known superconductors at the time, with the discovery of high temperature cuprate superconductors, heavy-fermion, ferromagnetic and, more recently, iron-based superconductors, it was clear that the standard phonon mediated picture is not universal. In the original form of the BCS theory, the formation of Cooper pairs was considered to be mediated by electron-phonon interactions. At low temperatures, pair formation becomes energetically favorable resulting in superconducting ground state. Relative to the normal state, the condensation energy (energy gap) can be calculated from the BCS theory in the form of the energy gap equation 1.29. For conventional superconductors the theory correctly

predicts the variation of this gap with temperature as shown in Fig. 1.3. It also gives an expression which shows how the gap grows with the strength of the attractive interaction and the (normal phase) single particle density of states at the Fermi energy. Furthermore, it describes how the density of states is changed on entering the superconducting state, where there are no electronic states any more at the Fermi energy.

An alternative, more modern, method of finding the ground state energy involves canonical transformations where the pair formation in momentum space can be described by a pairing amplitude given by [70]:

$$g_{\boldsymbol{k}\sigma_1\sigma_2} = \langle \hat{c}_{-\boldsymbol{k}\sigma_1} \hat{c}_{\boldsymbol{k}\sigma_2} \rangle \quad (1.39)$$

Here $\boldsymbol{k}$ is the relative momentum of the pair and $\hat{c}_{-\boldsymbol{k}\sigma_1}$ and $\hat{c}_{\boldsymbol{k}\sigma_2}$ are the creation operators of a fermion with spin σ in the quantum states $\{-\boldsymbol{k}, \sigma_1\}$ and $\{\boldsymbol{k}, \sigma_2\}$. The Pauli principle requires that the pair amplitude is asymmetric under spin and momentum exchange:

$$g_{-\boldsymbol{k}\sigma_1\sigma_2} = -g_{\boldsymbol{k}\sigma_1\sigma_2} \quad (1.40)$$

This allows for a classification of superconductors in respect to symmetry of the spin and spatial parity. If the total spin of the pair is zero we have singlet pairing with pair amplitude given by:

$$g_{\boldsymbol{k}\sigma_2\sigma_1} = \begin{pmatrix} 0 & g_{\boldsymbol{k}} \\ -g_{\boldsymbol{k}} & 0 \end{pmatrix}_{\sigma_1\sigma_2} = g_{\boldsymbol{k}} (i\sigma^2)_{\sigma_1\sigma_2} \quad (1.41)$$

where $g_{\boldsymbol{k}} = \frac{1}{2}[g_{\boldsymbol{k}\downarrow\uparrow} - g_{\boldsymbol{k}\uparrow\downarrow}]$ and σ^2 is one of the Pauli matrices. According to Pauli principle, expressed in Eq. 1.40, $g_{\boldsymbol{k}}$ must have even parity with respect to $\boldsymbol{k}$, meaning that $g_{-\boldsymbol{k}} = g_{\boldsymbol{k}}$.

It is well-known that the spatial dependence of $g_{\boldsymbol{k}}$ can be expressed as a sum over spherical functions in which the spherical harmonics are described by the orbital angular momentum l and its projection on z-axis m. Consequently, for isotropic Fermi surfaces, the pairing can be classified based on the orbital quantum number l. For singlet states ($s = 0$) the quantum number l can take the values $0, 2, 4, \ldots$ for which the states are labeled as $s, l, d, \ldots$ .If $l = 0$ the paring is referred to as s-wave pairing. For $l = 2$ we have d-wave type pairing and so on.

For triplet pairing ($s = 1$) the pairing amplitude can be expressed as [70]:

$$g_{\boldsymbol{k}\sigma_2\sigma_1} = \begin{pmatrix} g_{\boldsymbol{k}\uparrow\uparrow} & g_{\boldsymbol{k}} \\ g_{\boldsymbol{k}} & g_{\boldsymbol{k}\downarrow\downarrow} \end{pmatrix}_{\sigma_1\sigma_2} = \boldsymbol{g}_{\boldsymbol{k}} (\boldsymbol{\sigma} i\sigma)_{\sigma_1\sigma_2} \quad (1.42)$$

where the triplet components of $\boldsymbol{g}_{\boldsymbol{k}}$ corresponding to the magnetic quantum numbers $m = -1,0,1$ can be written as $g_{\boldsymbol{k}_x} = \frac{1}{2}[g_{\boldsymbol{k}\downarrow\downarrow} - g_{\boldsymbol{k}\uparrow\uparrow}]$, $g_{\boldsymbol{k}_y} = \frac{1}{2}[g_{\boldsymbol{k}\downarrow\downarrow} + g_{\boldsymbol{k}\uparrow\uparrow}]$, and $g_{\boldsymbol{k}_z} = \frac{1}{2}[g_{\boldsymbol{k}\downarrow\uparrow} + g_{\boldsymbol{k}\uparrow\downarrow}]$ and have odd parity with respect to $\boldsymbol{k}$, i.e. $g_{-\boldsymbol{k}} = -g_{\boldsymbol{k}}$. For triplet state states ($s = 1$) the quantum number l can take the values $1, 3, 5, \ldots$ for which the pairing is referred to as p-wave pairing ($l = 1$), f-wave pairing ($l = 3$), etc.

For singlet states, considering that Cooper pairing is a result of an attractive potential $V_{\boldsymbol{kp}}$, the pair potential can thus be expressed as an averaged pairing amplitude over all the pairs:

$$\Delta_{\boldsymbol{k}} = \sum_{p} V_{\boldsymbol{kp}} g_p \qquad (1.43)$$

From BCS theory, it can be shown that the pair amplitude in thermal equilibrium is given by:

$$g_k = \frac{\Delta_k}{2E_k} \tanh \frac{E_k}{2k_B T} \qquad (1.44)$$

which, introduced in the sum of Eq. 1.43 leads to the same expression as for the energy gap equation 1.29. Consequently, the pair potential plays the role of the energy gap in the spectrum of elementary excitations of the Bogoliubov quasi-particles ξ_k. The pairing amplitude is temperature dependent vanishing above the superconductive critical temperature. Consequently the pair potential (energy gap) $\Delta_{\boldsymbol{k}}$ can be divided into in a temperature dependent magnitude $\Delta_0(T)$ and a momentum $\boldsymbol{k}$ orbital part $f(\boldsymbol{k})$ of the form (for the spin singlet states):

$$\Delta_{\boldsymbol{k}} = \Delta(\boldsymbol{k}) = \Delta_0(T) f(\boldsymbol{k}) \qquad (1.45)$$

Gor'kov showed that the BCS gap has the same significance as the order parameter defined by Ginzburg-Landau theory. Consequently, the pair potential (energy gap) in Eq. 1.45 can be thought-out as the order parameter of superconductivity which is a temperature dependent complex function of orientation in momentum k-space.

Fermi systems are classified based on the symmetry of the pair potential. Comparing the symmetry of the orbital part in energy gap (order parameter in Eq. 1.45) to the symmetry of the Fermi surface leads to a classification of superconductors based on the symmetry. **Superconductors where both symmetries are the same are labeled as conventional. In unconventional superconductors the orbital part of the pair potential (Eq. 1.45) has a lower symmetry than the one of the Fermi surface.**

In conventional superconductors, the pairing is mediated by phonon-electron interactions. This results in a symmetric pairing attraction which leads to a symmetric orbital component of the order parameter. Then, for s-wave pairing we can write:

$$f_s(\boldsymbol{k}) = 1 \Rightarrow \Delta(\boldsymbol{k}) = \Delta_0(T) \qquad (1.46)$$

which, for spherical Fermi surfaces, means that the superconductor is fully gapped with isotropic energy gap magnitude. This is the conventional BCS type gap structure of phonon mediated superconductors. The situation is illustrated in Fig. 1.5 where, in the left side, we show a 2D k-space representation of the amplitude of the order parameter (magnitude of energy gap) at a fixed temperature.

With the discovery of high critical temperature superconductors it was clear that standard phonon mediated scenario no longer applies. Growing experimental evidence seemed to point to other interactions, such as antiferromagnetic or ferromagnetic spin fluctuations, which could favor anisotropic

pairing. Investigations of the complex superconductive order parameter can be used to test the concept suggesting spin mediated pairing mechanism. By examining the symmetry of the energy gap (order parameter) in momentum space different pairing mechanisms can be tested.

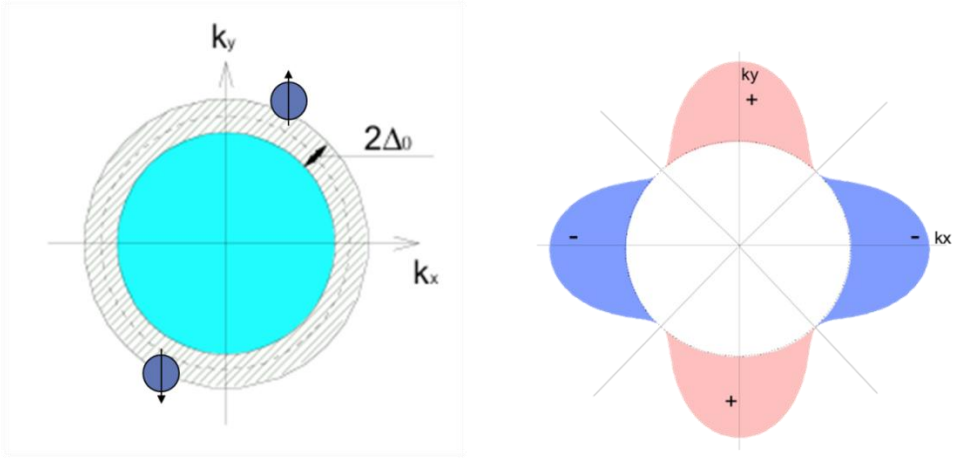

Figure 1.5 Order parameter symmetry for s-wave (left) and d-wave (right)

In high T_C cuprates is it now widely accepted that the order parameter has d-wave symmetry. The Fermi surface of cuprates is cylindrical in k-space. Consequently, the d-wave symmetry in cuprates is also referred to as $d_{x^2-y^2}$ symmetry. In this case, the order parameter can be expressed as:

$$f_{d_{x^2-y^2}}(\boldsymbol{k}) = \cos(2\varphi) \Rightarrow \Delta(\boldsymbol{k}) = \Delta_0(T)\cos(2\varphi) \qquad (1.47)$$

This situation is depicted in Fig. 1.5 (right side). The order parameter magnitude changes signs at four points on the Fermi surface meaning that the energy gap amplitude must go through zero. The points of the Fermi surface where the energy gap is zero are known as nodes. Consequently, cuprates are characterized by unconventional (non-BCS) anisotropic superconductivity with nodal gaps. Because of the proximity of the superconducting phase in these materials to a magnetic state in the doping phase diagram, it is widely believed that spin fluctuations may play a similar role for pair mediation to phonons in the case of s-wave superconductors. However, some reports support the d-wave symmetry while some experimental results suggest different symmetries. Determining whether the pairing wave function has d-wave type symmetry is essential to test the spin fluctuation mechanism. If non d-wave symmetry is involved then a spin mediated pairing mechanism can be ruled out. The ambiguity of reported experimental results regarding the pairing symmetry in cuprates makes the mechanism responsible for their superconductivity still under discussion.

As it turns out, most superconductors known today and especially HTC materials are unconventional. There is evidence that in some, notably heavy fermion superconductors [71] and in $SrRuO_4$ [72], triplet p-wave superconductivity may be involved. Moreover, some superconductors can be more complex for which it was suggested that mixtures of different symmetries might be involved, with proposed wave types such as $s + g$ or $d_{x^2-y^2} + id_{xy}$ and many others [73].

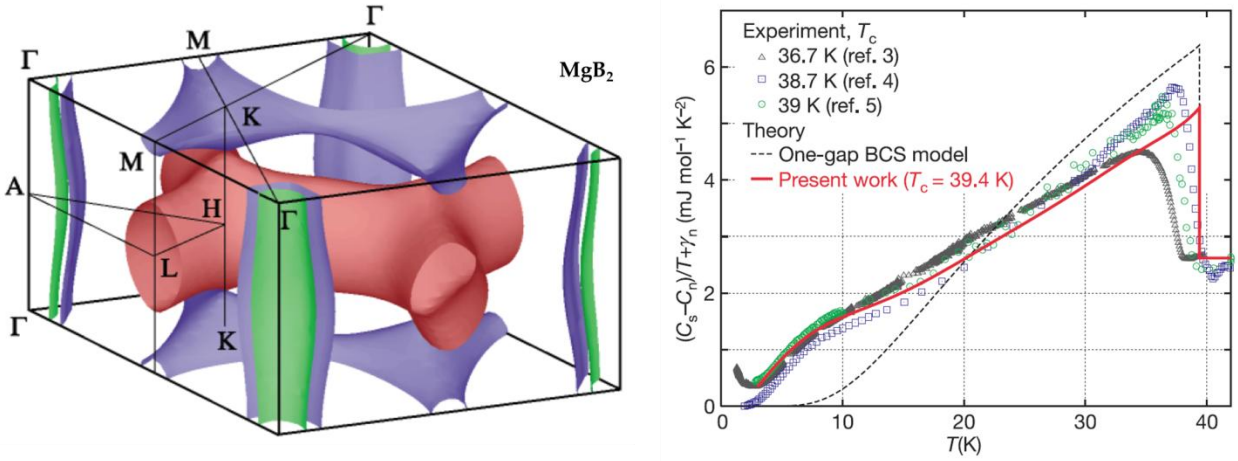

Figure 1.6 Left: Fermi surfaces topology in MgB_2 [74]. Right: Anomalous temperature dependence of specific heat in MgB_2 [75].

In materials characterized by multiple Fermi surfaces, superconducting gaps may develop at more than one surface resulting in multigap superconductivity. Strong candidates for the multigap scenario are the MgB_2 [76] (left side of Fig. 1.6) and V_3Si [77] including the more recent iron based superconductors.

The high transition temperature MgB_2 seemed unconventional in nature. The heat capacity data (left side of Fig. 1.6) clearly revealed a non-BCS type behavior. However, the boron isotope effect discovered in MgB_2 [54] suggested a standard phonon mediated BCS behavior. There is now compelling evidence that in MgB_2 superconductivity is characterized by two distinct energy gaps, both exhibiting conventional s-wave symmetry [75, 76]. The situation is illustrated in Fig. 1.7(a) where a simplified representation of two gap s-wave scenario is shown. At the center and corners of the Brillion zone there are separate isotropic gaps forming with the same phase. In iron based superconductors, a strong candidate is the so called s± wave symmetry, for which a similar picture exists except the different gap magnitudes have opposite signs at electron and hole Fermi surface pockets (Fig. 1.7(b)).

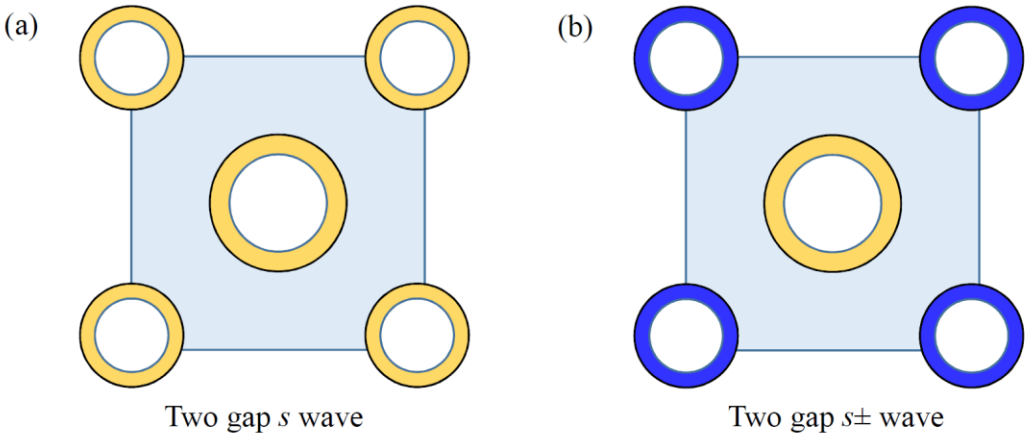

Figure 1.7 A simplified representation of the Fermi surface topology and energy gap symmetry for multigap superconductors exhibiting: two gap s-wave pairing (a) and s± wave symmetry (b).

As suggested by Eq. 1.45, the amplitude of the order parameter (the superconducting gap function) is temperature dependent, vanishing at values higher than the critical temperature. In principle, by solving the self-consistent gap equation (Eq. 1.29), the temperature variation of $\Delta_0(T)$ can be calculated for any symmetry. Since the gap equation involves a Fermi surface average of the orbital part $f(\boldsymbol{k})$, the temperature function $\Delta_0(T)$ is expected to be dependent on pairing symmetry. For the weak coupling limit, a useful approximate expression was given by Gross *et al.* [78] :

$$\Delta_0(T) \approx \Delta_0(0)\tanh\left(\frac{\pi T_C}{\Delta_0(0)}\sqrt{a\left(\frac{T}{T_C}-1\right)}\right) \qquad (1.48)$$

where $\Delta_0(0)$ is the zero temperature gap magnitude and a is a parameter dependent on the pairing symmetry. In Fig. 1.8 we illustrate the comparison with exact solutions obtained from the gap equation carried out by R Prozorov and R. W. Giannetta [17] for a number of different symmetries. It is easy to see that, at least for the weak-coupling limit, the expression in Eq. 1.48 proves adequate in describing the temperature dependence of the superconducting gap. Moreover, the magnitude is relatively saturated at temperatures below $0.3\ T_C$. As we will later show, this is relevant when trying to extract information about the symmetry of the gap from low temperature measurements of the London penetration depth.

It is important to mention that, for a symmetry characterized by nodes on the Fermi surface (e.g. d-wave symmetry), even at $T = 0$, the energy gap goes to zero at the nodal points. Consequently, as the temperature is increased, normal quasiparticle states can become occupied even at lowest temperatures. The situation is different than fully gaped superconductors, where finite temperatures must be achieved before pairs are broken. Since the population of these low energy normal states can significantly alter the

temperature dependence of quantities dependent on the electronic density of states, the presence of nodes can be experimentally detected from low temperature measurements.

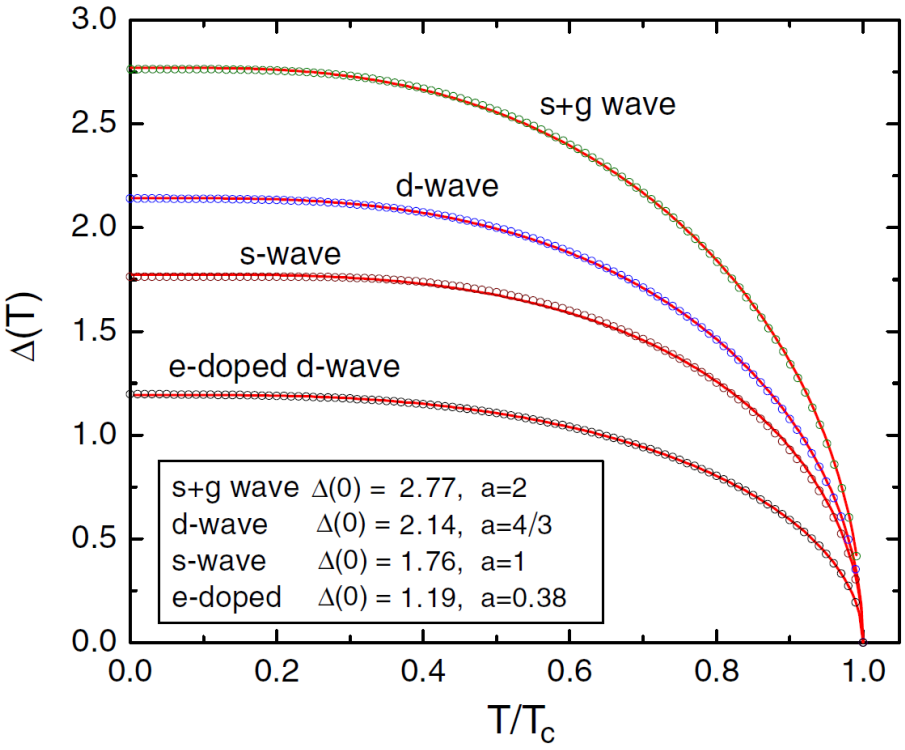

Figure 1.8 Temperature dependence of superconductive gap for different pairing symmetries as evaluated from the gap equation (Eq. 1.29) (symbols) and the fit using the approximate expression in Eq. 1.47 (lines). Image taken from [17].

The microscopic origin of the mechanism responsible with pair formation in unconventional superconductors is still unclear. Information about the superconductive gap structure is essential in confirming or disproving various proposed theoretical models. Consequently, a wide range of experimental methods have been established to investigate the superconductive energy gap.

In order to fully characterize the order parameter of superconducting materials one needs information regarding the parity and spin state, the magnitude and the nodal structure of the energy gap, and the macroscopic superconductive phase [70]. Each property can be experimentally accessed by different methods.

The parity and spin state can be investigated through measurements in a magnetic field due to the different response of the pairs with $s = 0$ and $s = 1$, respectively. Such measurements include upper

critical field Hc_2 investigations [79], nuclear magnetic resonance (NMR) [80, 81] and the muon spin rotation (μSR) investigations [81-83].

The most direct method for probing the energy gap magnitude is through spectroscopy measurements. By projecting photons, neutrons or electrons, with a known energy and momentum, direct information regarding basic excitations in the system can be inferred from the absorption and emission of a well-known amount of energy [84]. Such tools include planar tunneling spectroscopy [85], scanning tunneling spectroscopy [86] and point-contact Andreev reflection spectroscopy [87, 88]. A high energy and angular resolution technique is the angle-resolved photoemission spectroscopy (ARPES), a widely used tool for studying the Fermiology of superconductors as it directly measures the occupied part of the single-particle spectral function in momentum space. The technique has been instrumental in revealing the d-wave superconducting gap of cuprates [89-91].

Phase probing measurements are usually based on the Josephson effect [92] which involves pair tunneling. Phase information in unconventional materials can also be provided via quasiparticle tunneling. A sign change of the superconductive phase leads to the formation of an Andreev bound state which can be probed by the tunneling effect [93].

The nodal structure in unconventional superconductors can be tested by measurements of the temperature and magnetic field dependence of thermodynamic and transport properties, by instigating the angular dependence of thermal properties, like heat capacity and thermal conductivity [94-97], or by studying the directional dependence of current–voltage characteristics in point-contact and tunneling measurements [70].

One of the most involved probes in studying the superconducting gap structure is based on temperature dependent London penetration depth measurements. Since investigating $\lambda(T)$ is the main focus of our research, the method will be discussed in greater detail throughout this text. Important information about order parameter symmetry can be inferred from low temperature measurements of $\lambda(T)$. Being directly related to the superfluid density it is useful in observing effects correlated with the anisotropy of the superconducting gap as well as those associated with multigap superconductivity.

Our study of the pairing symmetry in iron based superconductors is based on temperature measurements of London penetration depth. We derive in the next chapter the formal connection between the temperature dependent penetration depth $\lambda(T)$ and the structure of the superconductive gap $\Delta(\boldsymbol{k}, T)$. We will show how the London penetration depth can be experimentally probed from magnetic susceptibility measurements of the Meissner state in superconductors and how information about the symmetry of the order parameter can be extracted from $\lambda(T)$ measurements.

Chapter 2

The London Penetration Depth in Superconductors

2.1. Magnetic fields in the Meissner state

As previously mentioned, a superconductive material in a weak applied magnetic field cooled below its transition temperature will enter a diamagnetic state called Meissner state. At low enough temperatures the Meissner state is characterized by the total expulsion of magnetic fields from the bulk of the superconductive domain.

Let's consider the simple situation illustrated Fig. 2.1 where a magnetic field of intensity $B = B_z = B_0$ is applied parallel to the surface of a superconductive infinite domain extended in the half space defined by $x > 0$.

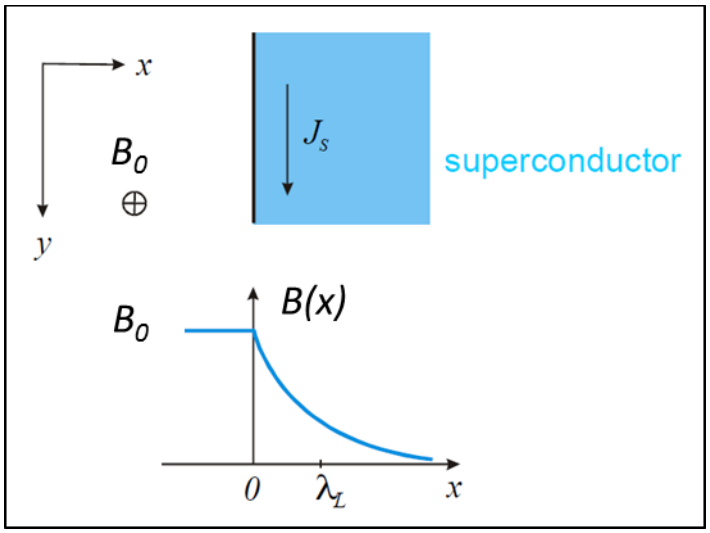

Figure 2.1 Magnetic field ***B*** distribution in a superconductive semi-infinite domain under uniform applied field B_0

In this case, London equation 1.10 can be written as:

$$\frac{\mathrm{d}^2 B_z}{\mathrm{d}x^2} - \frac{B_z}{\lambda^2} = 0 \qquad (2.1)$$

Given the symmetry of the problem we can impose the boundary conditions $B_z(x=0)=B_0$ to arrive at the solution for the magnetic field inside the superconductive domain:

$$B_z(x) = B_0 \exp\left[\frac{x}{\lambda}\right] \quad (2.2)$$

This simple case demonstrates how that the magnetic flux density B is exponentially attenuated within a distance comparable to λ, as it enters the superconducting domain, vanishing deep inside the bulk of the superconductor. The length λ is characteristic to each material and is a fundamental parameter in superconductors known as the London penetration depth.

The same attenuation is experienced by electric fields inside a superconductor. Making use of the Maxwell relation $\nabla \times \boldsymbol{B} = \mu_0 \boldsymbol{j}$ and the continuity equation for currents expressed by:

$$\nabla \cdot \boldsymbol{j} = \frac{d\rho}{dt} \quad (2.3)$$

Considering the conservation of electric charges, it is easy to show that, inside a superconductor, screening currents j perpendicular to the field are formed at the surface in order to shield the external applied magnetic field. For the case considered above, the supercurrent density has the following spatial dependence:

$$j(x) = -\frac{B_0}{\mu_0 \lambda} \exp\left[-\frac{x}{\lambda}\right] \quad (2.4)$$

The screening currents will generate a total magnetic moment, similar to the one created by the bound currents in magnetic materials. The induced magnetic moment has enough magnitude so that it produces a response magnetic field to cancel the applied field inside. The magnetic moment will also alter the $\boldsymbol{B}$ field distribution outside the superconductive material. This induced magnetic moment can be associated with a magnetization $\boldsymbol{M}$ (magnetic moment per unit volume) expressed by the relation:

$$\boldsymbol{j} = \nabla \times \boldsymbol{M} \quad (2.5)$$

where, as in the case of magnetic media, the total magnetic moment $\boldsymbol{m}$ can be calculated from:

$$\boldsymbol{m} = \int_V \boldsymbol{M}\, dV \quad (2.6)$$

In magnetic materials, considering a relation of the form:

$$\boldsymbol{M} = \frac{\boldsymbol{r} \times \boldsymbol{j}}{2} \quad (2.7)$$

will result in total magnetic moment created by the induced currents that can be expressed as:

$$\boldsymbol{m} = \frac{1}{2}\int_V \boldsymbol{r} \times \boldsymbol{j}\, dV \quad (2.8)$$

Although the relation described by Eq. 2.8 does not locally apply to supercurrents, considering that the only physically meaningful quantity is the total magnetic moment $\boldsymbol{m}$ (as we will show in Chapter III), both definitions will lead to the same result for $\boldsymbol{m}$ in superconductors. Introducing Eq. 2.5 in

London's second equation (Eq. 1.9) one arrives at the constitutive equation for the magnetization in a superconductor:

$$\nabla^2 \boldsymbol{M} = -\frac{\boldsymbol{B}}{\mu_0 \lambda^2} \tag{2.9}$$

If we consider the case of the semi-infinite superconductor described above, using the expression in Eq. 2.9 with the calculated field dependence in Eq. 2.2, the spatial variation of the magnetization $\boldsymbol{M}$ can be found to be:

$$M_z(x) = -\frac{B_0}{\mu_0}\left(1 - \exp\left[-\frac{x}{\lambda}\right]\right) \tag{2.10}$$

In the bulk of the superconductor ($x \gg \lambda$), the magnetization reaches its maximum value:

$$M_{bulk} = -\frac{B_0}{\mu_0} \tag{2.11}$$

Similar to the magnetic intensity H introduced in the case of magnetic media to account for the contribution of free current sources, an auxiliary magnetic field intensity $\boldsymbol{H}$ can be introduced for superconductors defined in the same manner:

$$\boldsymbol{H} = \frac{\mathbf{B}}{\mu_0} - \boldsymbol{M} \tag{2.12}$$

which satisfies the following relation, where $\boldsymbol{J_{ext}}$ is the free external current density,

$$\nabla \times \boldsymbol{H} = \boldsymbol{J_{ext}} \tag{2.13}$$

For the case of the semi-infinite superconductive domain, looking at Eq. 2.2 and Eq. 2.10, it is straightforward that

$$\frac{B_z(x)}{\mu_0} - M_z(x) = \frac{B_0}{\mu_0}\exp\left[\frac{x}{\lambda}\right] + \frac{B_0}{\mu_0}\left(1 - \exp\left[-\frac{x}{\lambda}\right]\right) = \frac{B_0}{\mu_0} = H_0 \tag{2.14}$$

We can thus see that the magnetic intensity $\boldsymbol{H}$ is uniform and has the same value, outside and inside the superconductor, equal to the applied field created by external currents. This is however not the case for finite size superconductive domains where demagnetizing effects will alter both the magnetic induction and intensity inside and outside the superconductor, as we will see later.

The magnetic susceptibility describes how a material behaves in an applied magnetic field and in its simplest form can be locally defined as

$$\chi = \frac{M}{H} \tag{2.15}$$

Considering the situation described above, one can easily integrate to find the total susceptibility of a superconductive domain. Since the domain is extended to infinity, the total magnetization will converge to its value in the bulk thus, considering $H = H_0 = H_{applied}$, the value of susceptibility will tend to the perfect diamagnetic value of $\chi = -1$. The same value is obtained if we consider that the penetration

depth is much smaller than the geometric dimensions of the domain. Consequently, perfect diamagnetism is a unique property of superconductors as evidentiated by the Meissner effect.

Fig. 2.2 illustrates the Meissner effect in a superconductive sphere of radius a obtained by solving the London equation with appropriate boundary conditions (uniform applied field). Although analytical solutions exist for a sphere, we show the results obtained through numerical simulations. The details of the simulations will be presented in the next section where the simple case of a sphere constitutes a straightforward way to corroborate the numerical results of our simulation method.

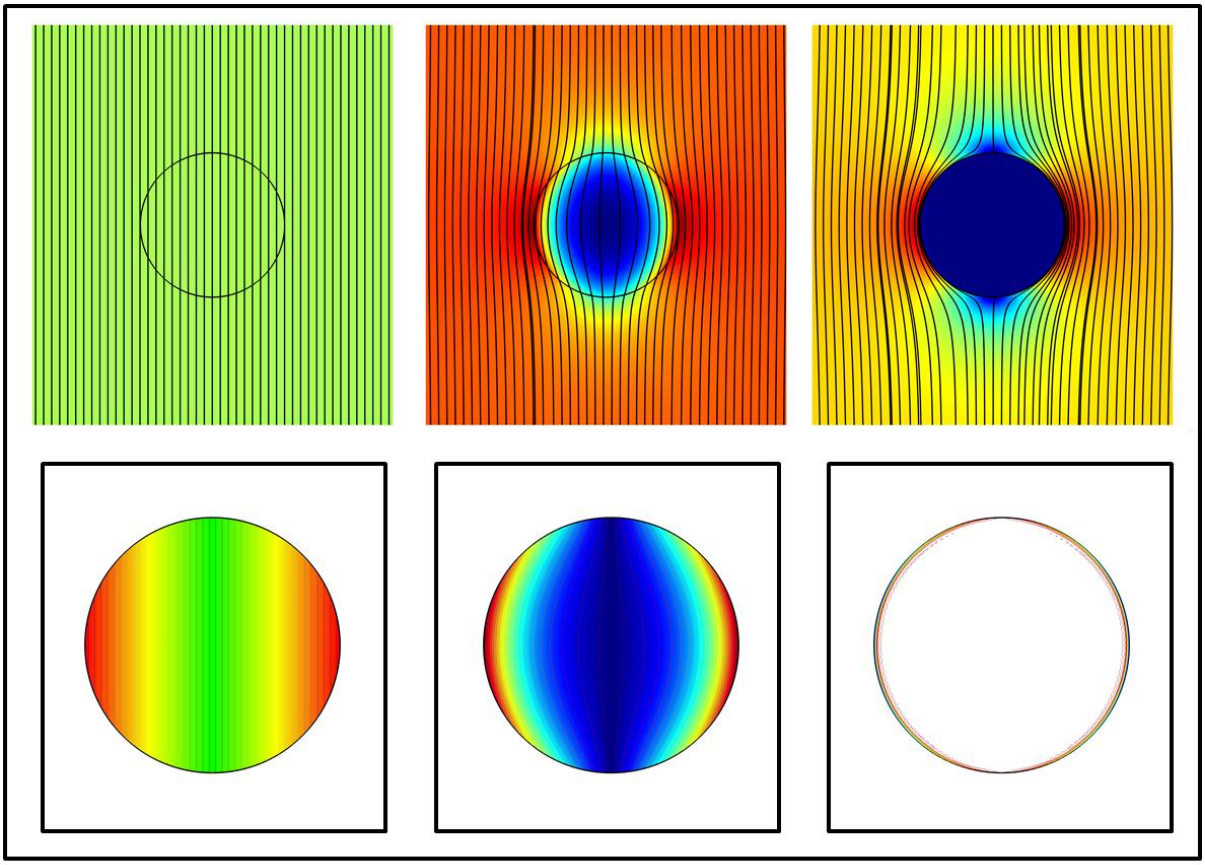

Figure 2.2 Meissner effect in a superconductive sphere. Calculated magnetic flux density and field lines (top) and supercurrent density (bottom) for $\lambda \gg a$ (left), $\lambda = a/5$ (middle) and $\lambda \ll a$ (right).

Above the critical temperature the sphere is in a normal state so the magnetic flux will penetrate its volume unhindered. As temperature is decreased, the sphere enters a superconductive state characterized by a gradual expulsion of magnetic flux lines. At the lowest temperature, the London penetration values become very small (typically in the micrometer to nanometer range) so the magnetic

field in completely expelled from the bulk of the superconductor. The supercurrent density is proportional to the vector potential according to London equation (Eq. 1.15). As we can see from the illustrated results, as the penetration depth decreases the current density becomes more concentered near the surface of the superconductor. At low penetration depth values, supercurrents exist only in a thin layer near the surface.

2.2. Magnetic penetration in rectangular slab shaped superconductors

London equations can be used to calculate the magnetic field configuration for any shape superconductor in Meissner state although, analytical solution are known for only a few geometries e.g. an infinite bar or cylinder in longitudinal field, a cylinder in perpendicular field, a sphere or a thin film in uniform field [98]. In Fig. 2.1 we illustrated the magnetic field distribution for a semi-infinite superconductive domain and the field expulsion from a sphere in a Meissner state in Fig 2.2. In practice however, one deals with finite size samples in a magnetic applied field which may or may not be uniform throughout the sample volume, in which case the London equations have to be solved numerically. With the tremendous advances in the area of computational physics and mathematical algorithms and the continuous increase in computing power, the numerical analysis of differential equation has become a trivial task. Nowadays, numerical solutions to complex equations can be easily obtained on personal computers in record times. A great tool that I have used over the course of my research time for quick and reliable results, amongst many others, has been the commercial COMSOL Multiphysics software, an interactive environment for modeling and simulating scientific and engineering problems which uses finite element analysis to solve for differential equations and boundary conditions [99]. Using such finite element solvers can greatly facilitate ones understanding of physical phenomena and provide an alternative test method for otherwise lengthy and costly experimental investigations. One example is the experimental investigation of the temperature dependence of London penetration depth from magnetic susceptibility measurements. In a finite size sample, the Meissner state susceptibility can have a complicated dependence on penetration depth as demagnetizing effects can strongly influence the magnetic field distribution. Solving the London equations for special sample geometry can provide the necessary information on the relation between susceptibility and magnetic penetration depth to be used in experimental investigations. A most common situation in practical arrangements involves the use of rectangular shape samples. Most high T_C superconductors are crystalline and samples are typically thin platelets with large aspect ratios. The same case applies for our FeSeTe single crystal samples for TDO measurements, with typical dimension of 2 x 2 x 0.1 mm. Since the TDO method is basically a magnetic susceptibility measuring technique, in order to obtain information about the penetration depth of our

samples, an expression relating susceptibility (which as we will later show is directly proportional to the measured resonant frequency shift) to the London penetration depth has to be known. Numerical methods, like the one developed by E. H. Brandt [100], can be used to find the flux penetration and magnetic susceptibility of plates however, applying them in the interpretation of experimental results is somewhat less practical. Consequently, R. Prozorov *et al.* [101] proposed an approximate analytical relation between measured susceptibly and magnetic penetration depth for rectangular slab like superconductive samples based on numerical solutions of London equations in rectangular cross section infinite slab in a perpendicular applied field. Since for our TDO measurements the $\chi(\lambda)$ relation proposed in [101] will be used in this work, it is important to mention its derivation and limitations.

Considering an isotropic superconducting slab of width $2w$ in the x direction, thickness $2d$ in the y direction and infinite in the z direction the London equation Eq.1.15 can be solved numerically for a uniform magnetic field H_0 is applied along the y direction. The situation is depicted in Fig. 2.3 below.

If we consider the applied field as derived from the vector potential A we can make use of the London equation

$$\nabla^2 \boldsymbol{A} = -\frac{\boldsymbol{A}}{\lambda^2} \qquad (2.16)$$

to solve for the x-y spatial distribution of the (only) z component of the potential A inside the slab and the Ampere's law $\nabla^2 \boldsymbol{A} = 0$ for the vector potential outside the sample. We consider that $A = H_0 x$ far from the sample i.e. $y \gg d$ and $x \gg w$ as well as the London gauge condition and continuity A on the sample boundary.

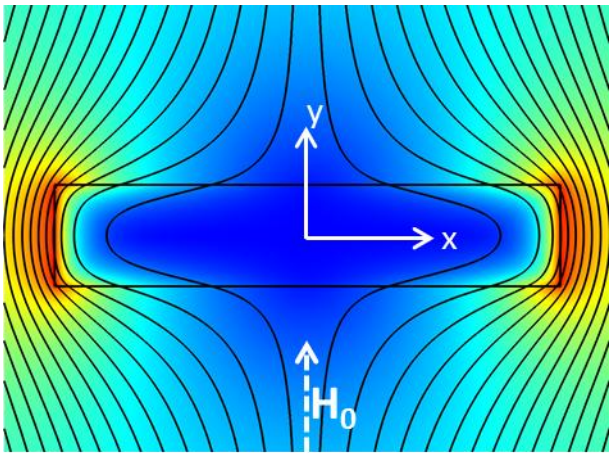

Figure 2.3 Magnetic flux density (low density: blue - high density: red) and magnetic field lines illustrating the Meissner effect in an infinite slab with rectangular cross section under H_0 perpendicular applied field.

Considering that $\boldsymbol{B} = \nabla \times \boldsymbol{A}$ the only two components of the magnetic field in this geometry can be calculated using:

$$B_x = \frac{\partial A_z}{\partial y}; B_y = \frac{\partial A_z}{\partial x}; \quad (2.17)$$

In Fig. 2.3 above we show the numerical results of the London equation for the magnetic flux density and magnetic field lines obtained using the COMSOL software for the 2D cross section for the infinite slab geometry with $\lambda = 2d/5$. The numerical analysis was performed using the Magnetic Fields Module assuming an external current density value coupled to the magnetic vector potential value by the London relation (Eq. 1.15) for the sample domain and solving for the z component of the vector potential within a sufficiently large integration domain.

Recalling the London relation from Eq. 1.15 and the definition of magnetic moment in Eq. 2.8 we can express the magnetic susceptibility per unit volume (unit of surface cross section in the 2D case) as:

$$\chi = \frac{M}{H_0} = \frac{m}{dwH_0} = \frac{1}{2\mu_0 dwH_0\lambda^2}\int_0^d dy \int_0^w A(x,y)xdx \quad (2.18)$$

Exact evaluation of the integral requires the knowledge of the vector potential values inside the sample. However, from the numerical results, R. Prozorov *et al.* [101] deduced a simple analytical approximation by calculating the ratio of the volume penetrated by magnetic field to the total volume of the sample. They found that the magnetic susceptibility can be obtained as:

$$\chi = -\frac{1}{1-N}\left[1 - \frac{\lambda}{R}\tanh\left(\frac{R}{\lambda}\right)\right] \quad (2.19)$$

where N is an effective demagnetizing factor and R an effective dimension, both depending of the aspect ratio w/d of the sample. **This simple expression relates the London penetration depth to the measurable effective susceptibility of superconductive rectangular slab shaped samples.**

The hyperbolic tangent term insures a correct limit as $\lambda \to \infty$. It is easy to see that, as $\lambda \to 0$, overlooking demagnetizing effects, the susceptibility $\chi \to -1$ which is the case of perfect diamagnetism. For not too large aspect ratios, the demagnetizing factor can be expressed as:

$$\frac{1}{1-N} \approx 1 + \frac{w}{d} \quad (2.20)$$

and consequently, the effective dimension R can be expressed, for the 2D case, as:

$$R_{2D} = \frac{w}{1 + \sin^{-1}\{[1 + (2d/w)^2]^{-1/2}\}} \quad (2.21)$$

The next step in [101] was the extension to the 3D case, namely a superconducting disk of radius w and thickness $2d$ in which case $1/(1-N) \approx 1 + w/2d$. The effective dimension R can now be expressed as:

$$R = \frac{w}{2 - 4d/w + 2[(1 + 4(d/w)^2)]arctan(w/2d)} \quad (2.22)$$

For a rectangular slab R. Prozorov *et al.* [101] suggested that the same expression for R in Eq. 2.22 can be used if we consider w as the geometric mean of its lateral dimensions.

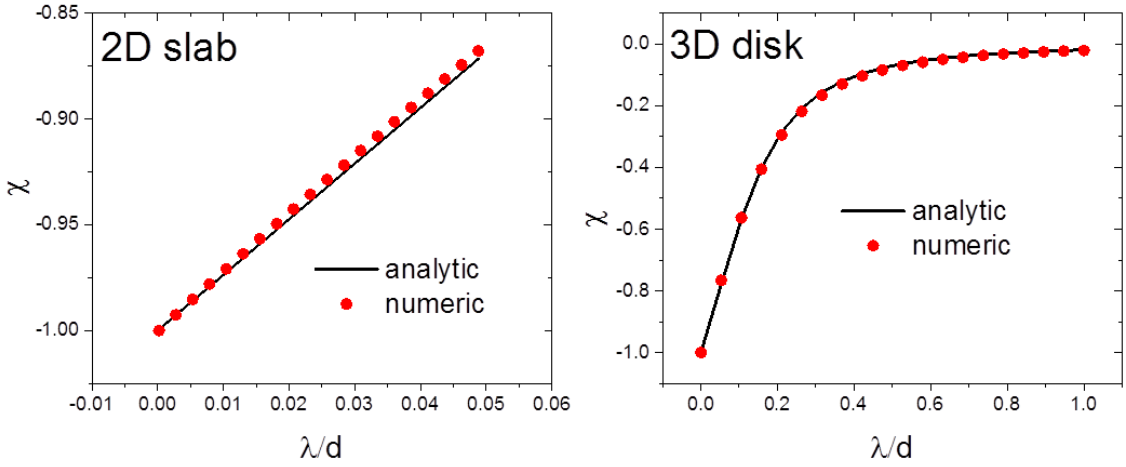

Figure 2.4 The magnetic susceptibility χ as a function of the reduced London penetration depth λ/d for two geometries i.e. 2D superconductive slab (left) and 3D disk (right). The analytical dependence is represented by continuous black lines while numerical results by red points. Note: for the 2D slab only the low values λ linear region of $\chi(\lambda/d)$ is shown.

We tested the analytical expression in Eq. 2.19 for two geometries i.e. infinite slab of rectangular cross section of width $2w$ and thickness $2d$ and disk of radius w and thickness $2d$. In both cases the aspect ratio $w/d = 5$ where R was calculated using Eq. 2.21 for the 2D slab and Eq. 2.22 for the 3D disk. We show in Fig. 2.4 our numerical results obtained for $\chi(\lambda/d)$ using London's equation (Eq. 2.19) for the two geometries and the comparison with the analytical dependence. For the 3D disk, a 2D axisymmetric geometry was used. It is easy to see that the numerical results agree well with the analytical expression on penetration depth and that at low values of magnetic penetration depth the susceptibility variation is almost linear as expected from Eq. 2.19.

Eq. 2.19 was derived for the case of isotropic superconductive samples. However, most superconductors of interest commonly have layered crystalline structures which make them highly anisotropic regarding their transport properties. In particular, magnetic field penetration in anisotropic superconductors will depend on the direction of the supercurrents created to cancel the field inside. Consequently, the London penetration depth has distinct values along different directions making the magnetic susceptibility strongly dependent on the orientation of applied field. Since most HTS materials

are layered structures, the penetration depth will have two distinct values namely λ_{ab} corresponding to induced currents in the *ab* plane (plane of the layers) and $\lambda_c$which corresponds to interplane transport currents, with typically larger value. The situation is illustrated in Fig. 2.5 where a magnetic field is applied both perpendicular and parallel to the *ab* plane of a layered superconductive rectangular slab. In the perpendicular field configuration, the applied magnetic field penetrates equally on all sides within a region characterized by the so called in-plane London penetration depth λ_{ab}. Consequently, the magnetic susceptibility can be calculated using Eq. 2.19 as in the case of isotropic media. In a parallel field, the magnetic susceptibility is the result of a mixture of in-plane and interplane transport currents and is a function of both λ_{ab} and λ_c.

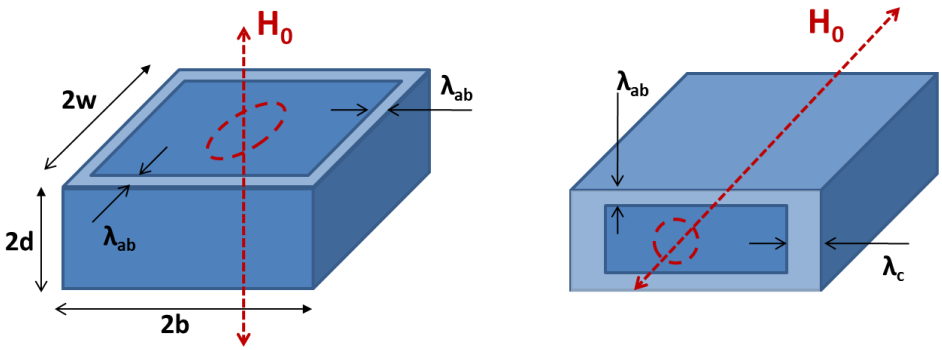

Figure 2.5 Anisotropic layered superconductive sample in a magnetic field H_0 applied perpendicular (left) and parallel (right) to the *ab* planes. In perpendicular field, supercurrents are induced in the *ab* plane only meaning the field will penetrate equally deep on all four lateral faces. For the parallel field configuration supercurrents are a mixture of in-plane and interplane transport resulting in a deeper field penetration on the lateral sides compared with the top and bottom surfaces [17].

The corresponding relation for magnetic susceptibility as a function of both components of London penetration depth can be found considering a generalized London equation for anisotropic media [73]. In the case of superconductive slab in parallel applied field (left side of Fig. 2.5) the resulting susceptibility can be determined by solving the full boundary generalized London problem. The solution was calculated by P. A. Mansky *et al.* [102] and the resulting dependence has the form [17]:

$$\chi = -1 + \frac{\lambda_{ab}}{d}\tanh\left(\frac{d}{\lambda_{ab}}\right) + 2\,\lambda_c b^2 \sum_{n=0}^{\infty} \frac{\tanh(p_n/\lambda_c) + 2}{{k_n}^2 {p_n}^3} \qquad (2.23)$$

where $k_n = \pi(0.5 + n)$ and $p_n = b\sqrt{1 + (k_n\lambda_{ab}/d)^2}$. Although, Eq. 2.23 can be sufficiently approximated considering only the first few terms in the sum, in practice this method is inconvenient. Moreover, the interplane penetration depth λ_c is somewhat complicated to interpret as it involves less

understood properties of interplane transport mechanism [73]. Nonetheless, in most cases λ_c is considerably larger than the in-plane penetration depth and for typical crystal dimensions, as $\lambda_c/d \gg \lambda_{ab}/b$, the susceptibility in Eq. 2.23 is predominantly influenced by λ_c.

Specifically, if one wants to investigate the in-plane penetration depth in highly anisotropic samples from susceptibility measurements, the thickness of the specimens has to be extremely small as to provide the condition $\lambda_c/d \ll \lambda_{ab}/b$. A more straightforward approach is to apply the magnetic field perpendicular to the *ab* plane. As a consequence, for a rectangular slab, considering that transport currents in the *ab* plane are isotropic, the $\chi(\lambda_{ab})$ dependence can be expressed as in the case of isotropic superconductors.

2.3. The structure of superconducting gap from λ(T) measurements

A major success of the BCS formalism was its ability to provide a microscopic derivation for the phenomenological equations proposed by the London brothers to explain the observed electromagnetic properties of superconductor. Moreover, the BCS theory shows that the Meissner effect is a clear proof that superconductivity is a manifestation of quantum mechanics.

If one considers the total magnetic field as derived from a vector potential $\boldsymbol{A}$ (Eq. 1.13), the effect of $\boldsymbol{A}$ on the expectation value of the current density $\boldsymbol{j}$ can be calculated using a perturbation Hamiltonian approach in the BCS formalism [103]. Although the following approach deals with stationary fields, the same calculations apply for time varying magnetic fields as long as the electromagnetic wavelength is larger than typical sample dimensions. The resulting perturbation term is:

$$H_P = \frac{ie\hbar}{2m}\sum_i \nabla_i \cdot \boldsymbol{A} + \boldsymbol{A} \cdot \nabla_i \qquad (2.24)$$

where the kinetic electron momentum is replaced by the associated quantum operator $\boldsymbol{p}_i \rightarrow -i\hbar\nabla_i$ and the sum is taken over all the particles. According to Bogoliubov canonical transformation [104, 105] we can write a set of operators responsible for creating quasi-particle excitations of two spin directions, from the ground state, in terms of creation operators $c_{\boldsymbol{k}}^*$:

$$\gamma_{\boldsymbol{k}0}^* = u_{\boldsymbol{k}}^* c_{\boldsymbol{k}\uparrow}^* - v_{\boldsymbol{k}}^* c_{-\boldsymbol{k}\downarrow}^* \; and \; \gamma_{\boldsymbol{k}1}^* = v_{\boldsymbol{k}}^* c_{\boldsymbol{k}\uparrow}^* + u_{\boldsymbol{k}}^* c_{-\boldsymbol{k}\downarrow}^* \qquad (2.25)$$

where $u_{\boldsymbol{k}}^*$ and $v_{\boldsymbol{k}}^*$ are numerical coefficients whose squared magnitude sum is unity. If the vector potential is expanded as a Fourier series given by:

$$\boldsymbol{A}(r) = \sum_{\boldsymbol{q}} \boldsymbol{a}(\boldsymbol{q}) e^{i\boldsymbol{q}\cdot\boldsymbol{r}} \qquad (2.26)$$

then the perturbation Hamiltonian can be expressed as:

$$H_P = -\frac{e\hbar}{m}\sum_i \boldsymbol{k}\cdot\boldsymbol{a}(\boldsymbol{q})c^*_{\boldsymbol{k}+\boldsymbol{q},\sigma}c^*_{\boldsymbol{k},\sigma} \quad (2.27)$$

The current density induced by this perturbation can now be calculated from the expectation value of the current density operator. The resulting expression, in Fourier space, has the form:

$$\boldsymbol{j} = \frac{e\hbar}{m}\sum_{\boldsymbol{k},\boldsymbol{q}} \boldsymbol{k}c^*_{\boldsymbol{k}-\boldsymbol{q}}c_{\boldsymbol{k}} - \frac{ne^2}{m}\boldsymbol{A} = \boldsymbol{j_{par}} - \boldsymbol{j_{dia}} \quad (2.28)$$

We can see that the current induced by the $\boldsymbol{A}$ perturbation has two components, a paramagnetic term and a diamagnetic component (as suggested by the negative sign) given by:

$$\boldsymbol{j_{dia}} = -\frac{ne^2}{m}\boldsymbol{A} \quad (2.29)$$

which corresponds exactly to the London equation Eq. 1.15 if n could be interpreted as the density of superconductive electrons. However, n is the total density so Eq. 2.29 applies to the normal state as well. Consequently, the paramagnetic component in the resulting current density is important, as it will be responsible for canceling the diamagnetic response in the normal state.

The paramagnetic term can be calculated considering the current response to various Fourier components of the vector potential via Kubo formula [106], in the linear form:

$$\boldsymbol{j}(\boldsymbol{q}) = K(\boldsymbol{q})\boldsymbol{a}(\boldsymbol{q}) \quad (2.30)$$

with

$$K(\boldsymbol{q}) = K + K_{par} = -\frac{ne^2}{m} + \langle \boldsymbol{j_{par}}, \boldsymbol{j_{par}} \rangle(\boldsymbol{q}) \quad (2.31)$$

being the response function. The simple product structure in Eq. 2.30 implies a non-local relationship between $\boldsymbol{j}$ and $\boldsymbol{A}$. Considering that $\boldsymbol{j}(\boldsymbol{r}) = \int K(\boldsymbol{r},\boldsymbol{r}')\,\boldsymbol{A}(\boldsymbol{r}')d\boldsymbol{r}'$, $\boldsymbol{j}(\boldsymbol{r})$ depends on $\boldsymbol{A}(\boldsymbol{r}')$ at many points around $\boldsymbol{r}'$. Recalling the discussion in Chapter I, the characteristic length of this is given by $\xi_0 = \hbar v_F/\pi\Delta_0$. Moreover, it can be shown that, as $|\boldsymbol{q}| \to \infty$, $K(q)/K(0) \to 3\pi/4q\xi_0$ [103].

Considering the relationship of London penetration depth of magnetic potential, as derived from the London theory (Eq. 1.15), it is easy to see that the Meissner effect can be explained assuming only a constant $K(\boldsymbol{q})$

$$K(\boldsymbol{q}) = K(0) = \frac{1}{\mu_0\lambda^2} \quad (2.32)$$

Thus, in London theory, the response is independent of $\boldsymbol{q}$. If we consider the temperature dependence of $K(\boldsymbol{q})$ and the definition of the penetration depth (Eq. 1.21) for the ideal limit $T = 0$ we can write the response function as:

$$K(\boldsymbol{q},T) = \frac{1 + \mu_0\lambda^2(0)K_{par}(\boldsymbol{q},T)}{\mu_0\lambda^2(0)} \quad (2.33)$$

For isotropic systems and transverse fields, $\boldsymbol{q}$ is a scalar quantity. If we consider infinite wavelengths of the applied field ($q = 0$) we can write the response function as:

$$K(0,T) = \frac{1 + \mu_0 \lambda^2(0) K_{par}(0,T)}{\mu_0 \lambda^2(0)} = \frac{1}{\mu_0 \lambda^2(T)} \quad (2.34)$$

which suggests that the temperature dependence of $K(0,T)$ is defined by density of superconductive electrons n_s as a function of temperature.

For $\boldsymbol{q} = 0$ we have from Eq. 2.25 and 2.27 that:

$$H_P = -\frac{e\hbar}{m} \sum_k \boldsymbol{k} \cdot \boldsymbol{a}(0) (\gamma^*_{\boldsymbol{k}0} \gamma_{\boldsymbol{k}0} - \gamma^*_{\boldsymbol{k}1} \gamma_{\boldsymbol{k}1}) \quad (2.35)$$

where the 0 and 1 indices correspond to the diamagnetic term and paramagnetic term, respectively. The perturbing BCS Hamiltonian simply shifts the quasi-particle energies:

$$E_{k0} \to E_{k0} - \frac{e\hbar}{m} \boldsymbol{k} \cdot \boldsymbol{a}(0) \; and \; E_{k1} \to E_{k1} - \frac{e\hbar}{m} \boldsymbol{k} \cdot \boldsymbol{a}(0) \quad (2.36)$$

Thus, the expected paramagnetic current density can be written as:

$$\boldsymbol{j_{par}} = \frac{e\hbar}{m} \sum_{\boldsymbol{k}} \boldsymbol{k} \big(f(E_{k0}) - f(E_{k1}) \big) \quad (2.37)$$

where $f(E_{k0})$ and $f(E_{k1})$ are the expectation values of the quasi-particle operators γ_{k0} and γ_{k1}, responsible for creating quasi-particle excitations from the superconductive ground state [107], with f being the Fermi function corresponding to the energy difference. In the limit of $\boldsymbol{a}(0) \to 0$ (linear response) we can expand in a Taylor series and take to first component to find:

$$\boldsymbol{j_{par}}(\boldsymbol{q} = 0) = 2 \left(\frac{e\hbar}{m} \right)^2 \sum_{\boldsymbol{k}} [\boldsymbol{k} \cdot \boldsymbol{a}(0)] \boldsymbol{k} \left(-\frac{\partial f}{\partial E_k} \right) \quad (2.38)$$

Considering that $N_0 = 3n/4E_F$ and that $\sum_{\boldsymbol{k}} \to N_0 \int (d\Omega/4\pi) d\,\xi_k$ with $\int (d\Omega/4\pi) \boldsymbol{k} \cdot \boldsymbol{k} = 1/3$ from symmetry, considering $\boldsymbol{j_{par}}$ is always parallel to $\boldsymbol{A}(0)$, we obtain the homogenous static response

$$K_{par}(0,T) = -\frac{ne^2}{m} \left(1 - \int_{-\infty}^{\infty} \left(-\frac{\partial f}{\partial E_k} \right) d\xi_k \right) = -\frac{n_s e^2}{m} \quad (2.39)$$

If n_n is considered as a normal fluid density with $n_n(T) = n - n_s(T)$ we then have the microscopic justification for the phenomenological two-fluid model of superconductivity, in which the superfluid is made up of Cooper pairs and the normal fluid consists of thermally excited quasi-particles. Inserting 2.29 in the expression from Eq. 2.34 and considering the definition from Eq. 1.28, the temperature dependence of the penetration depth can now be written as:

$$\frac{1}{\lambda^2(T)} = \frac{1}{\lambda^2(0)} \left[1 - 2 \int_{\Delta_k}^{\infty} \left(-\frac{\partial f(E_k)}{\partial E_k} \right) \frac{E_k}{\sqrt{{E_k}^2 - {\Delta_k}^2}} dE_k \right] \quad (2.40)$$

In the normal state, $\Delta_k = 0$ so the integral in Eq. 1.48 reduces to $f(0) = 0.5$ which corresponds to $n_s(T > T_C) = 0$ and a cancelation of the diamagnetic component of the current density by the paramagnetic term (no Meissner effect).

By using the solution of the self-consistent gap equation (Eq. 1.29) the full range temperature dependence of $\lambda(T)$ can be calculated from Eq. 2.40 in a straightforward way for any Fermi surface geometry and superconducting gap structure.

In the ideal clean limit (no scattering from impurities) all electrons should form Cooper pairs. Thus, at $T = 0$ the density of superconductive electrons n_s equals the total electronic density n. As the temperature is increased, bound pairs become thermally excited forming Bogoliubov quasiparticles which make up the normal fluid with density $n_n(T)$. The normalized superfluid density is defined as the ratio between the density of superconductive electrons and the total electron density:

$$\rho_s(T) = \frac{n_s(T)}{n_s(T) + n_n(T)} = \frac{n_s(T)}{n(T)} \qquad (2.41)$$

We can see that, as $T \to 0$, the superfluid density becomes $\rho_s(0) = 1$. Above the critical temperature the density of superconductive electrons vanishes i.e. $\rho_s(T > T_c) = 0$.

Considering the electron density connection to the London penetration depth (Eq. 1.28) the temperature dependence of the superfluid density can be expressed as:

$$\rho_s(T) = \frac{\lambda^2(0)}{\lambda^2(T)} = \frac{1}{\left[1 + \frac{\Delta\lambda(T)}{\lambda(0)}\right]^2} \qquad (2.42)$$

where $\Delta\lambda(T) = \lambda(T) - \lambda(0)$ is the relative penetration depth. The expression in Eq. 2.40 can now be written as:

$$\rho_s(T) = \frac{\lambda^2(0)}{\lambda^2(T)} = 1 - 2\int_{\Delta_k}^{\infty}\left(-\frac{\partial f(E_k)}{\partial E_k}\right)\frac{E_k}{\sqrt{{E_k}^2 - {\Delta_k}^2}}dE_k \qquad (2.43)$$

We showed in Chapter I how different pairing symmetries result in different temperature variation of the energy gap magnitude $|\Delta_k|$. However, from Fig. 1.8 we can see that, regardless of the symmetry of the order parameter, for low temperatures (typically $T < 0.3\ T_C$) the gap amplitude is roughly constant. Consequently, the low temperature dependence of the London penetration depth is dictated by the symmetry of the superconducting gap alone. **We thus have the connection between the London penetration depth and the pairing symmetry in superconductors.** By measuring the low temperature behavior of $\lambda(T)$ information about the pairing symmetry can be extracted.

In conventional superconductors, characterized by s-wave type symmetry of the order parameter, the energy gap Δ_k is isotropic. At low temperatures, the gap magnitude is constant and equal to its zero

temperature value $\Delta_k = \Delta_0$. By considering a spherical Fermi surface in Eq. 2.43 we arrive at the standard BCS results in the low temperature limit [108]:

$$\rho_s(T) \approx 1 - \sqrt{\frac{2\pi\Delta_0}{k_B T}} \exp\frac{-\Delta_0}{k_B T} \qquad (2.44)$$

As the temperature is decreased, considering the fast temperature increase of the gap, we expect that at low temperatures the penetration depth will exponentially reach its $T = 0$ value. Thus, the variations in $\Delta\lambda(T)$ at low temperatures are relatively small. Consequently, we can write:

$$\frac{1}{\left[1 + \frac{\Delta\lambda(T)}{\lambda(0)}\right]^2} \approx 1 - 2\frac{\Delta\lambda(T)}{\lambda(0)} \qquad (2.45)$$

which, used in Eq. 2.44, results in the temperature dependence of London penetration depth for a conventional s-wave superconductor [73]:

$$\Delta\lambda(T) \approx \lambda(0)\sqrt{\frac{\pi\Delta_0}{2k_B T}} \exp\frac{-\Delta_0}{k_B T} \qquad (2.46)$$

Therefore, in a fully gapped superconductor, approaching very low temperatures the relative London penetration depth $\Delta\lambda(T)$ is expected to be exponentially saturated. This can be understood considering that at $T = 0$, the Fermi surface represents the set of highest occupied energy states. For an s-wave superconductor, the energy levels are fully gapped with respects to unoccupied states. The unoccupied energy levels are just below the occupied ones and as the temperature is increased they are populated exponentially slow. If the superconductive gap is nodal, the zero magnitude points in k-space will cause quasiparticle states to become populated even at very low temperature. Consequently, fast $\Delta\lambda(T)$ variations at very low temperatures could indicate the presence of nodes in the structure of energy gap.

We show in the left side of Fig. 2.6 the exponential temperature dependence of the relative London penetration depth $\Delta\lambda(T)$ in pure niobium as measured by the TDO technique [109] including the low temperature fit using Eq. 2.46. It is worth mentioning that this temperature dependence in Eq. 2.46 is only valid at low temperatures for a local approximation (pure superconductors) and it is practically indistinguishable from the experimentally observed dependence (Eq. 1.48) obtained prior to the BCS theory.

So far we have treated the case of isotropic materials for which electronic conduction is homogenous in respect to spatial direction. As mentioned in the previous section, some materials, namely layered structures, can be highly anisotropic. In cuprates, the transport anisotropy ρ_c/ρ_{ab} can be as high

as 10^5 [110] which makes them highly two dimensional. Consequently, the penetration of magnetic fields is different depending on which directions of the supercurrents are involved.

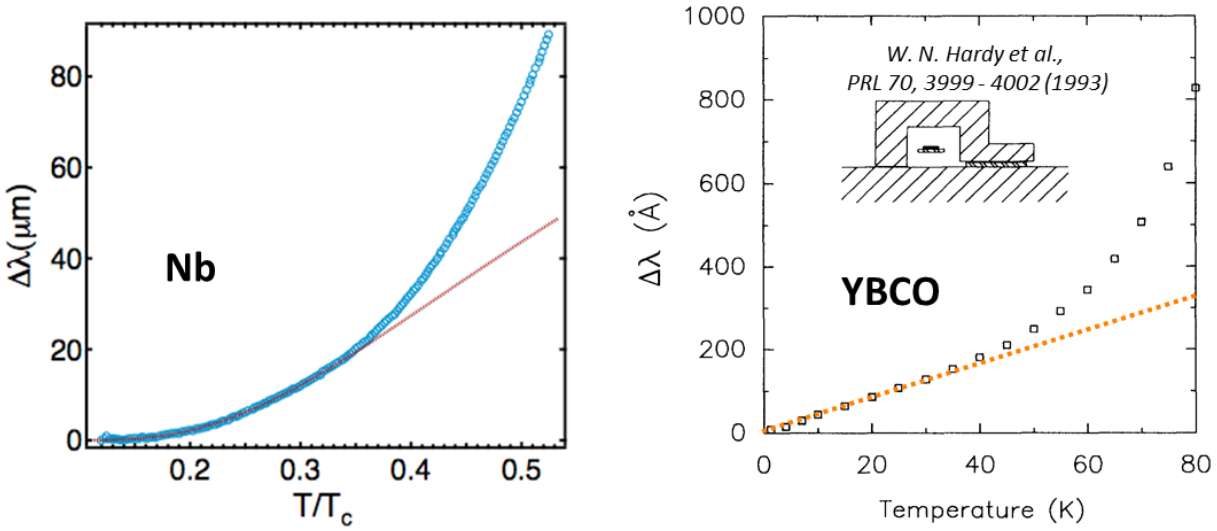

Figure 2.6 The temperature dependence of London penetration depth for conventional s-wave superconductors (Nb from [109]) (left) and unconventional d-wave (YBCO from [111]) (right) [x]

To account for the different components of the London penetration depth, B. S. Chandrasekhar and D. Einzel [112], based on a semi-classical model, provided a general method for calculating all spatial components of the London penetration depth given a Fermi surface and gap function. They suggested an effective electronic mass tensor dependent on Fermi surface ϵ_k as well as on the density of states:

$$m_{ij}^{-1} = \frac{\partial^2 \epsilon_k}{\hbar^2 \partial k_i \partial k_j} \qquad (2.47)$$

Consequently, different band masses will result in different components of the penetration depth. In the London approximation, the current density local relation to the vector potential can be written as:

$$\boldsymbol{j} = \overline{\overline{K}}_{ij} \boldsymbol{A} \qquad (2.48)$$

where $\overline{K}_{ij}$ is a symmetric response tensor whose expression is similar to Eq. 2.39 and is given by [73]:

$$\overline{\overline{K}}_{ij} = \frac{e^2}{\hbar 4\pi^3} \oint_{FS} dS_k \left[\frac{\boldsymbol{v}_F^i \boldsymbol{v}_F^j}{|\boldsymbol{v}_F|} \left(1 - 2 \int_{\Delta_k}^{\infty} \left(-\frac{\partial f(E_k)}{\partial E_k} \right) \frac{E_k}{\sqrt{{E_k}^2 - {\Delta_k}^2}} dE_k \right) \right] \qquad (2.49)$$

Here $\boldsymbol{v}_F^i$ are the components of the Fermi velocity and, as a reminder, $E_k/\sqrt{{E_k}^2-{\Delta_k}^2}$ is just the density of states $N(E_k)/N(0)$ normalized to its value at the Fermi level in normal state. Using a coordinate system defined by the principle axes of $\overline{K}_{ij}$, considering the London relation $\boldsymbol{j} = A/\mu_0\lambda_{ii}^2$, the different penetration depths correspond to the diagonal ii components i.e.

$$\lambda_{ii}^2 = \frac{1}{\mu_0 \overline{K}_{ij}} \tag{2.50}$$

The normalized superfluid density is thus given by:

$$\rho_{ii}(T) = \frac{\lambda_{ii}^2(0)}{\lambda_{ii}^2(T)} = \frac{\overline{K}_{ii}(T)}{\overline{K}_{ii}(0)} \tag{2.51}$$

For a spherical Fermi surface and an isotropic gap (s-wave) it is easy to show that the normalized superfluid density in Eq. 2.51 is isotropic and, from Eq. 2.49, its value can be calculated to give [17]:

$$\rho_s(T) = 1 - \frac{1}{2k_BT}\int_0^\infty \cosh^{-2}\left(\frac{\sqrt{\varepsilon^2+\Delta^2(T)}}{2k_BT}\right)d\varepsilon \tag{2.52}$$

which, for low temperatures, leads to the same BCS expression in Eq. 2.44.

If we now consider a cylindrical Fermi surface, which is the typical approximation for copper oxide superconductors, Eq. 2.49 and 2.51 result in the following expression for the in-plane components of $\rho_{ii}(T)$:

$$\rho_{\substack{aa\\bb}}(T) = 1 - \frac{1}{2\pi k_BT}\int_0^{2\pi}\begin{pmatrix}\cos^2\varphi\\ \sin^2\varphi\end{pmatrix}\int_0^\infty \cosh^{-2}\left(\frac{\sqrt{\varepsilon^2+\Delta^2(T,\varphi)}}{2k_BT}\right)d\varepsilon d\varphi \tag{2.53}$$

It is now widely believed that the pairing symmetry in cuprates is d-wave. In principle there are many gap functions consistent with a given symmetry. However, a common choice for the angle-dependent gap function $\Delta(T,\varphi)$ in $d_{x^2-y^2}$ symmetry is $\Delta(T,\varphi) = \Delta_0(T)\cos(2\varphi)$ (Eq. 1.47). Using this in the normalized superfluid density relation in Eq. 2.53 yields the following expression at low temperatures [17]:

$$\rho_s(T) = 1 - \frac{2\ln 2}{\Delta(0)}k_BT \tag{2.54}$$

Correspondingly, the London penetration depth behavior at low temperatures for d-wave is:

$$\Delta\lambda(T) \approx \lambda(0)\frac{\ln 2}{\Delta(0)}k_BT \tag{2.55}$$

The linear $\Delta\lambda(T)$ dependence can be understood considering the linear variation of the density of states $N(E) \propto E$ near the nodal points. Consequently, the nodal structure of the gap can be explored from the low temperature behavior of London penetration depth. We show in the right side of Fig. 2.6 the $\Delta\lambda(T)$

data for YBCO measured by W. N. Hardy *et al.* [111] and the low temperature linear fit consistent with d-wave symmetry.

By solving the full BCS equation for both s-wave and 2D d-wave symmetries the temperature dependence of London penetration depth can be calculated for the full temperature range. The obtained approximate expression for both symmetries are given in [73]:

$$\lambda_{s-wave}(T) = \lambda(0) \Big/ \sqrt{1 - \left(\frac{T}{T_c}\right)^2} \qquad (2.56)$$

and

$$\lambda_{d-wave}(T) = \lambda(0) \Big/ \sqrt{1 - \left(\frac{T}{T_c}\right)^{\frac{4}{3}}} \qquad (2.57)$$

At very low temperatures an exponential dependence of $\Delta\lambda(T)$ is consistent with an isotropic gap while a linear variation is indicative of nodes in the gap structure. However, magnetic as well as non-magnetic impurities in the superconductive material can drastically affect the low temperature behavior of $\Delta\lambda(T)$. In fact, before the microwave cavity penetration depth measurements of Hardy *et al.* [111], previous investigation in less pure crystals revealed a quadratic temperature dependence of $\Delta\lambda(T)$ in cuprate materials [17]. Hirschfeld and Goldenfeld [113] showed that scattering by non-magnetic impurities generates a non-zero density of quasiparticle states near $E = 0$. These states lead to a T^2 variation of the penetration depth below a crossover temperature T^*. In s-wave superconductors, the exponential low temperature behavior is less affected by non-magnetic contaminants.

Magnetic impurities will induce pair breaking effects with significant consequences of the superconductive properties, regardless of the symmetry. Besides lowering the critical temperature, magnetic impurities can directly affect $\Delta\lambda(T)$ measurements by introducing a finite permeability μ of the normal state. Recalling the relation between magnetic susceptibility and London penetration depth in Eq. 2.19 it can be shown that, at low temperatures, the effective measured penetration depth is given by [17]:

$$\lambda_{eff}(T) = \sqrt{\mu\lambda(T)} \qquad (2.58)$$

If the impurities are paramagnetic, at low temperatures $\mu \propto 1/T$ and the competing terms in Eq. 2.58 produce a minimum in $\Delta\lambda(T)$ measurements. This paramagnetic upturn was first observed by J. R. Cooper [114] in the NCCO copper oxide, who pointed out that the effect could mask the real temperature behavior of London penetration depth.

Thus far, we have shown that just by measuring relative changes in penetration depth $\Delta\lambda(T)$ at low temperatures, important information regarding the pairing symmetry of superconductors can be extracted. Fitting the experimental data with the corresponding $\Delta\lambda(T)$ temperature function, the magnitude of the gap $\Delta(0)$ as well as the value of London penetration depth at zero temperature $\lambda(0)$ can

in principle be calculated. If the value $\lambda(0)$ is known, $\Delta\lambda(T)$ measurements can be used to determine the temperature dependence of the normalized superfluid density which, as we have mentioned, can show effects associated with the structure of the gap over the entire range of temperatures $(0 - T_C)$.

The $\rho_s(T)$ dependence for a pure s-wave and a d-wave superconductor is shown in the left panel of Fig. 2.7. Deviations from such behavior can indicate effects originating from impurity scattering, admixtures of different symmetries or multigap superconductivity.

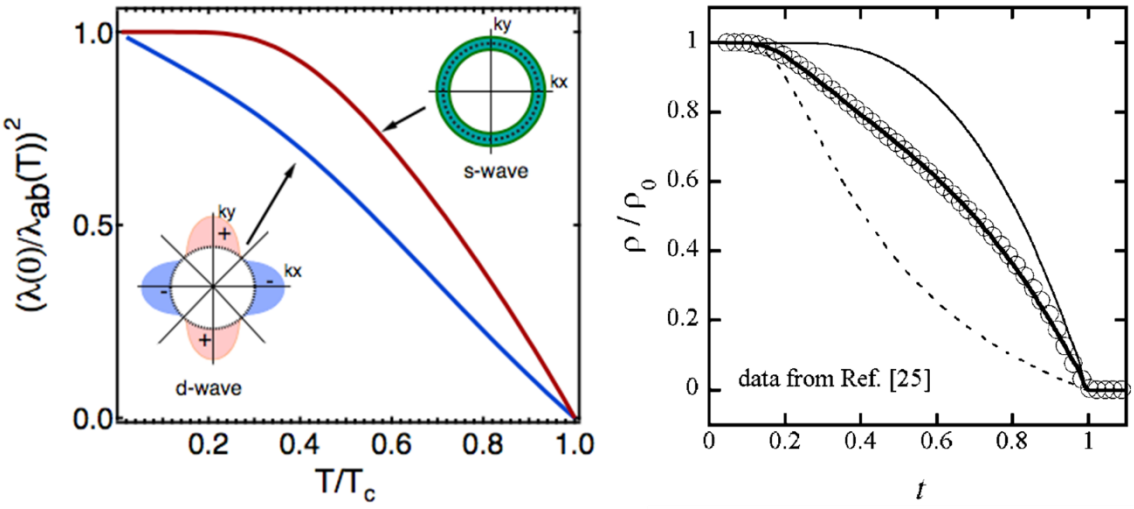

Figure 2.7 Normalized superfluid density as a function of reduced temperature for the s-wave and d-wave pairing symmetries (left) and multi-gap structure of MgB_2 (right). Images from [109] and [76].

The case of multigap superconductivity was made by F. Bouquet *et al.* [76] who proposed a phenomenological two-gap model for the superfluid density of the MgB_2 superconductor. They suggested that superconductivity in this material can be understood by considering two energy gaps with different magnitude and conventional BCS type temperature behavior. The total superfluid density can be fitted with a two-gap model (α model) of the form:

$$\rho(T) = x\rho_1(T) + (1 - x)\rho_2(T) \qquad (2.59)$$

where $\rho_1(T)$ and $\rho_2(T)$ are the superfluid densities evaluated using Eq. 2.43 assuming:

$$\Delta_{1,2}(T) = \frac{\alpha}{1.76}\,\Delta_{s-wave}(T) \qquad (2.60)$$

and x takes into account relative band contributions. The resulting α-model fit for the normalized superfluid density of MgB_2 is illustrated in the right panel of Fig. 2.7 and demonstrates the success of such a simple model in providing evidence for multigap superconductivity. A similar, more general model

(γ model) was suggested by V. G. Kogan *et al.* [115] which takes into account self-consistently all relevant coupling constants to evaluate temperature dependencies of the two gaps and of the superfluid density without making the a-priori assumption of a BCS gap temperature dependence.

In conclusion, temperature measurements of London penetration depth provide a useful tool in investigating the gap structure of superconductors. Many techniques have been developed to measure λ. Amongst the most common are the microwave cavity perturbation, muon spin relaxation, infrared spectroscopy, electron paramagnetic resonance, neutron diffraction and techniques based on magnetic susceptibility measurements including the TDO method described in the next chapter.

Chapter 3

The Tunnel Diode Oscillator Technique

3.1. Introduction

An ideal LC circuit consists of an ideal capacitor (infinite dc resistance) of capacitance C connected with an ideal inductor (zero dc resistance) of inductance L. If the capacitor is initially charged with a certain electric charge, upon connecting the inductor to its terminals, an alternative current (ac) will start flowing through the circuit. The resonance frequency of oscillations is dependent on the L and C values with an amplitude dictated by the total electric charge in the circuit. Considering that frequency measurements are amongst the most precise, with typical frequency counters nowadays being able to detect changes as small as 0.001 ppb in a second, having a measurement technique that can relate physical properties of materials to a frequency value is invaluable. In the practical implementation of LC circuits however, the finite resistance of the inductor and connections are responsible for energy losses in which case the amplitude of current oscillations will be exponentially damped with a time constant dependent of the resistance of the circuit. To keep a steady resonant state in an LC tank circuit, all the energy lost during each oscillation must be replaced and the amplitude of these oscillations must be mainianted at a constant level meaning that the amount of energy replaced must be equal to the energy lost during each cycle. One way of achieving this is taking a part of the output signal, amplifying it and feeding it back to the oscillator. Based on this principle there are a number of LC oscillator types like the Hartley oscillator or the Colpitts oscillator, each with its advantages and drawbacks. Another way of maintaining steady oscillations in a real LC circuit is by compensating for the lost energy using the negative resistance of a tunnel diode (Esaki diode).

A tunnel diode is a semiconductor device based on the quantum tunneling effect of electrons. Reona (Leo) Asaki working for Sony in 1958 discovered the effect in solids reporting that narrow (15 nm) p-n germanium junctions exhibit a region of negative differential resistance characterized by an increase in voltage as the current is decreased [116]. For his finding Asaki received the Nobel prize in Physics in 1973 together with Ivar Giaever "for their experimental discoveries regarding tunneling phenomena in semiconductors and superconductors, respectively" and with Brian David Josephson "for his theoretical predictions of the properties of a supercurrent through a tunnel barrier, in particular those phenomena which are generally known as the Josephson effects". At the time of its discovery, the tunnel diode was one of the most significant electronic devices to emerge since the transistor. Their simplicity,

high switching speeds and extremely low power consumption made them extremely advantageous compared to the transistors or electron tubes in high frequency applications. Tunnel diodes were first manufactured by Sony in 1957 followed by General Electric, Siemens and a number of other companies later. Today, however, are made in relatively low volumes as some of their qualities have been surpassed by other semiconducting devices for most technological application purposes. They are usually made from germanium, but can also be made from gallium arsenide and silicon materials. In a conventional normal junction semiconductor diode, conduction takes place while the lightly doped p-n junction is forward biased and blocks current flow when the junction is reverse biased. This occurs up to a point known as the "reverse breakdown voltage" when conduction begins (often accompanied by destruction of the device). In a tunnel diode, a very narrow p-n junction (nanometers) is heavily doped (thousands times greater than regular diodes) which results in a broken band gap where the electron conduction band on the n side is aligned with the hole valence band on the p side. The conduction and valence band electrons can then tunnel in both directions for zero applied voltage where the tunneling phenomenon is exponentially dependent on the electric field intensity across the barrier. The typical current-voltage (IV) curve of a forward biased tunnel diode is depicted in Fig. 3.1 below.

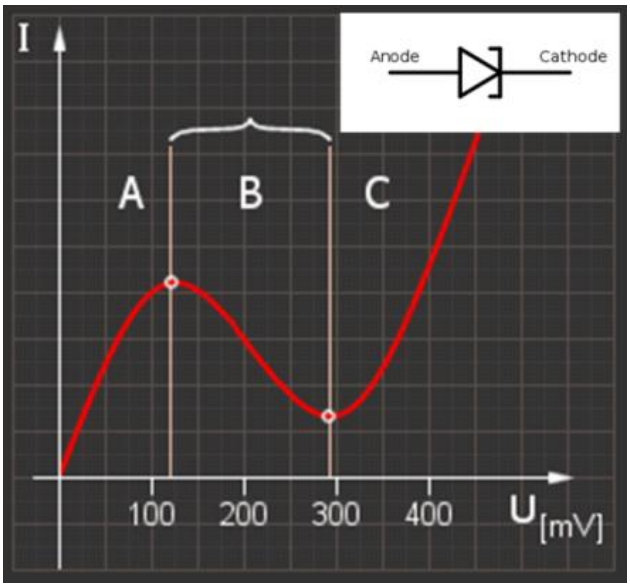

Figure 3.1 The characteristic I-V curve of a forward biased tunnel diode showing the negative differential resistance region B.

As a forward bias voltage is applied, the relative misalignment of the energy levels is increased and the tunneling of electrons for the n to the p type side creates a forward bias current (region A in Fig.

3.1). Increasing the forward bias voltage value will lead to a maximum tunneling current when the energy of the majority of electrons in the n-region is equal to that of the empty states (holes) in the valence band of p-region. As the forward bias continues to increase, the number of electrons in the n side that are directly opposite to the empty states in the valence band (in terms of their energy) decrease. Therefore decrease in the tunneling current will start (region B in Fig. 3.1). This current voltage relationship accounts for the negative differential resistance region of the I-V curve. As the voltage is further increased, tunneling stops and the junction behaves as for a regular diode (region C in Fig. 3.1).

3.2. Timeline of tunnel diode oscillator based experimental methods

If a tunnel diode is voltage biased to bring its current value in the negative differential resistance region, any small decrease in voltage will result in a corresponding increase in current. Connected to the oscillating voltage drop of an LC tank, the negative resistance can be used to compensate for the resistance losses of the LC circuit, the necessary condition for stable oscillations, provided that certain conditions are met, which we will detail later. The resulting circuit is called a tunnel diode oscillator (TDO) and is capable of resonating at frequencies from kilohertz to well into the microwave band. Since its frequency is always at resonance, very small value changes of its LC components will result in significant changes in frequency. This characteristic provides the foundation of using the TDO circuit as an experimental tool in investigating the physical properties of matter. The most common application consists in probing the magnetic susceptibility of materials. A magnetically active sample brought in close proximity of the inductor of a TDO circuit, will result in a change in the value of its inductance which, in turn, will generate a measurable corresponding resonant frequency shift. An analogous frequency shift can be induced by changes in the capacitance value due to a change in the electric permittivity however we will just mention this case without giving it any further consideration.

The first reported use of a TDO circuit operating at 15 MHz, occurred in 1969 when R. Meservey *et al.* [117] published their work detailing temperature measurements of kinetic inductance of superconducting structures. They used the TDO technique to determine the carrier concentration from penetration depth in films and wires of superconducting samples placed inside an LC tank at liquid helium temperature (with the tunnel diode and the rest of the components at room temperature).

R. B. Clover and W. P. Wolf [118] used a similar circuit a year later and reported on the successful use of the TDO method for paramagnetic susceptibility measurements at frequencies from 3 to 55 MHz, at temperatures from 1.2 to 77 K, and at magnetic fields up to 18 kG. They also proposed a semi-empirical formula for describing the frequency of TDO operation.

In 1971 Y. J. Kingma and V. Dvorak [119] proposed to use of a tunnel diode oscillator as a proximity switch based on a study of two mutually coupled resonant circuits. They found that, depending on the coupling strength of the two coils, the TDO can switch oscillation modes.

J. Aslam and W. Weyhmann published a paper in 1973 [120] presenting a tunnel diode oscillator used for NMR studies in ferromagnetic materials at VHF an UHF. Their circuit design included an electronic tuning of operating frequencies in a relatively broad range.

In 1975 C. T. Van Degrift [121] reported on the construction and the results of a systematic study of the design considerations of a tunnel diode oscillator for 0.001 ppm measurements at low temperatures Comprehensive calculations regarding the measured frequency, noise and dependence on bias voltage, magnetic field, and temperature of the TDO circuit are also presented in the paper. It also suggested that the TDO method can be used to detect extremely small changes in a number of material properties such as thermal expansion, surface impedance, and electric and magnetic permeability. Later, a number of publications reported the use of a TDO technique to study the temperature and magnetic field dependence of the rf susceptibility in insulators [122], organic compounds [123] and superconducting and magnetic thin films and surfaces [124] with the latter reporting that the device is capable to detect a change in susceptibility equal to that of a change in Fe thin film thickness of 0.03 atomic layers.

A paper published in 1986 by J. G. Brisson and I. F. Silvera [125] discusses the use of and theory behind a transmission-line tunnel diode oscillator with quick response times and immunity to stray reactance of the reentrant cavity.

G. J. Athas *et al.* [126] in 1993 reported on the first application of a tunnel diode circuit to investigate the de Haas–van Alphen effect and superconducting critical field values in small single crystal organic conductors.

The investigation of vortex dynamics and penetration depth in high Tc superconductors using a tunnel diode oscillator technique was reported by S. Patnaik *et al.* in 1999 [127].

In 1999 a paper by H. Srikanth *et al.* [128] describes the use of a TDO for precise measurements of relative magneto-impedance changes in materials directly from the measured shift in TDO resonance frequency.

In 2000 T. Coffey *et al.* [129] present the details of an apparatus that extended the tunnel diode techniques to measure the properties of materials in pulsed magnetic fields in a their paper. The sample is placed in the inductor of a small radio frequency (rf) tank circuit powered by a tunnel diode where the conductivity, magnetization, or penetration depth can be measured depending on the sample and configuration of the radio frequency field. A major innovation is reported regarding the stabilization of the tunnel diode oscillator during a magnet pulse by using compensated coils in the tank circuit.

In a series of papers spanning from 1997 to 2004, S. G. Gevorgyan *et al.* [130-138] make use of a flat coil based tunnel diode oscillator to increase the filling factor of thin films or plate like samples. They discuss the theory and modeling of tunnel diode oscillators and the use of their open flat coil magnetometer to study the superconductive properties of HTC materials with temperature and magnetic fields.

In 2000 L. Spinu *et al.* [139] suggested and implemented the use of the resonant TDO technique to prove the field response of dynamic transverse susceptibility in magnetic nanoparticle systems resulting in a precise mapping of fundamental parameters such as magnetic anisotropy and switching fields. The tunnel diode oscillator has proved to be a great tool in probing the transverse magnetic susceptibility of novel materials and structures such as magnetic nanostructures [140, 141], nanoparticle systems [139, 141, 142] and arrays [142, 143], magnetic multilayered structures [144, 145], and synthetic antiferromagnets [146, 147].

R. Prozorov *et al.* [101] in 2000 showed that the variations in London penetration depth of disk or rectangular slab shaped superconductors is directly proportional to the resonant frequency shift of the tunnel diode oscillator. The linear relation together with the great sensitivity of the TDO technique makes it an unparalleled tool in probing the temperature dependence of the magnetic penetration depth and consequently in investigating the pairing symmetry of unconventional superconductors.

Over the last decade a large amount of publications reported the use of the TDO method for the low temperature study of London penetration depth in novel superconductors. A more detailed overview of the TDO use in probing the low temperature penetration depth behavior of superconductors will be presented in Chapter V, however, some of the most active groups in the experimental field are the group from Ames Laboratory Iowa State University (R. Prozorov and A. Tanatar), University of Illinois at Urbana (E. M. Chia and M. B. Salamon) and the H. H. Wills Physics Laboratory at University of Bristol (A. Carrington).

3.3. Principle and theory of operation of a TDO circuit

Figure 3.2 illustrates the standard electrical diagram of the tunnel diode oscillator circuit used in our experimental setups. All the components are surface mount devices (SMD). The capacitors are ceramic while the resistors are thin film.

The LC tank is made up of capacitor C and inductor L. The small inductor resistance is represented by the series resistance r. In building our resonators we usually start with the inductor which is chosen based on the sample shape and size as well as the physical property that is to be measured.

Typically we deal with solenoids (5-30 turns) of either cylindrical shape or rectangular cross section with typical L values in the μH range. However, a large part of my research has focused on using flat coils in an either open or paired configuration. A more detailed description of the flat inductors used in our setup and the advantages over other geometries will be given in Section 3.5. The material of choice in building the coils is copper so, depending on the inductor geometry, the series resistance of our inductors can be anywhere between a few mΩ to hundreds of ohms.

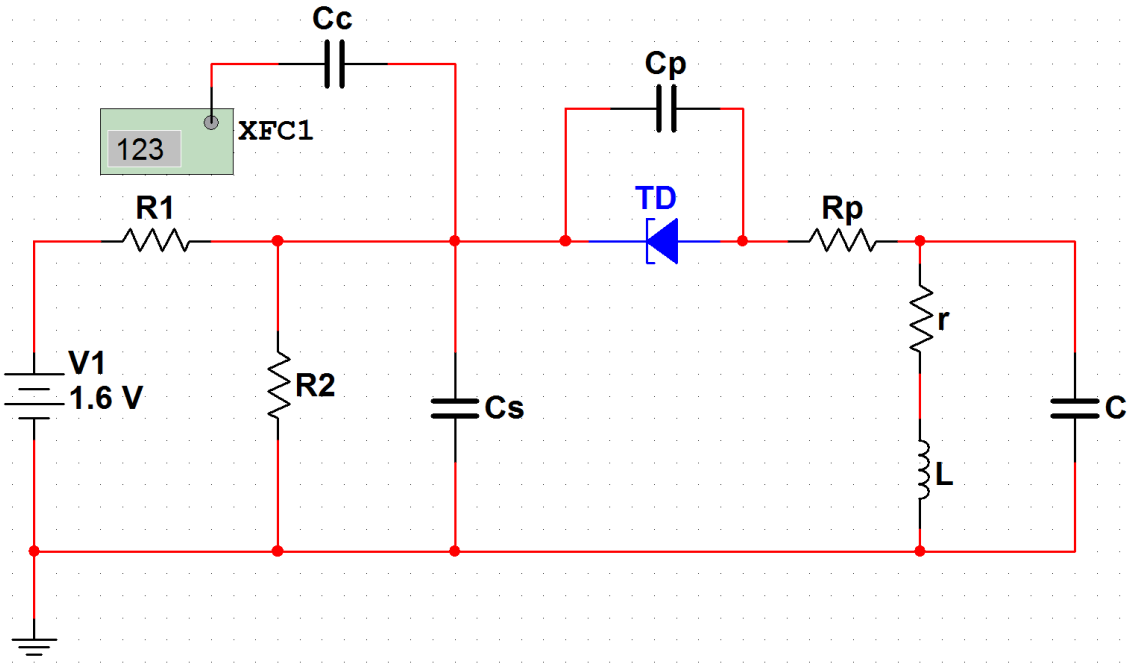

Figure 3.2 Schematic diagram of a tunnel diode oscillator (TDO) circuit used in our experiments

The capacitor C, with typical values ranging from 100 pF to 10 nF, is chosen based on the desired resonant frequency but, most importantly, its value must be in the range required for sustained oscillations. The impedance matching condition to be met for steady state oscillations will be presented in detail later, however, we will mention that the capacitance C value is strongly influenced by the choice of inductor and the tunnel diode used.

All of our TDO circuits use the MBD series germanium tunnel diodes manufactured by Aeroflex Metelics. The measured I-V curves for the four models in the MBD series most commonly used are illustrated in Fig. 3.3 below. It is easy to see that the measured I-V curves deviate considerably from the theoretical behavior suggested in Fig. 3.1 which can pose serious issues when trying to use theoretical models to describe the circuit behavior. Nonetheless, they all exhibit the region of negative differential resistance required for TDO resonance. The negative differential resistance $R_{nd} = dU/dI$ is a function of

voltage, however, we can define a total negative resistance $R_n = -(U_{max} - U_{min})/(I_{max} - I_{min})$ where U_{max} and I_{max} are the values of voltage and current at the maximum point of the I-V curve with U_{min} and I_{min} the values at the minimum point in the negative resistance region. The measured values of R_n for the MBD series are shown in the inset of Fig. 3.3. The impedance of the LC tank dictates the choice of the tunnel diode model. The steady state condition for oscillations is met when the average value per cycle of the power supplied by the tunnel diode equals the power dissipated by the rest of the circuit active components.

The parasitic suppression resistor R_p is used to prevent parasitic oscillation caused by the stray capacitance of the diode or by the inductance of the components. Typical resistance values for R_p in our circuits range from 50 Ω to 300 Ω.

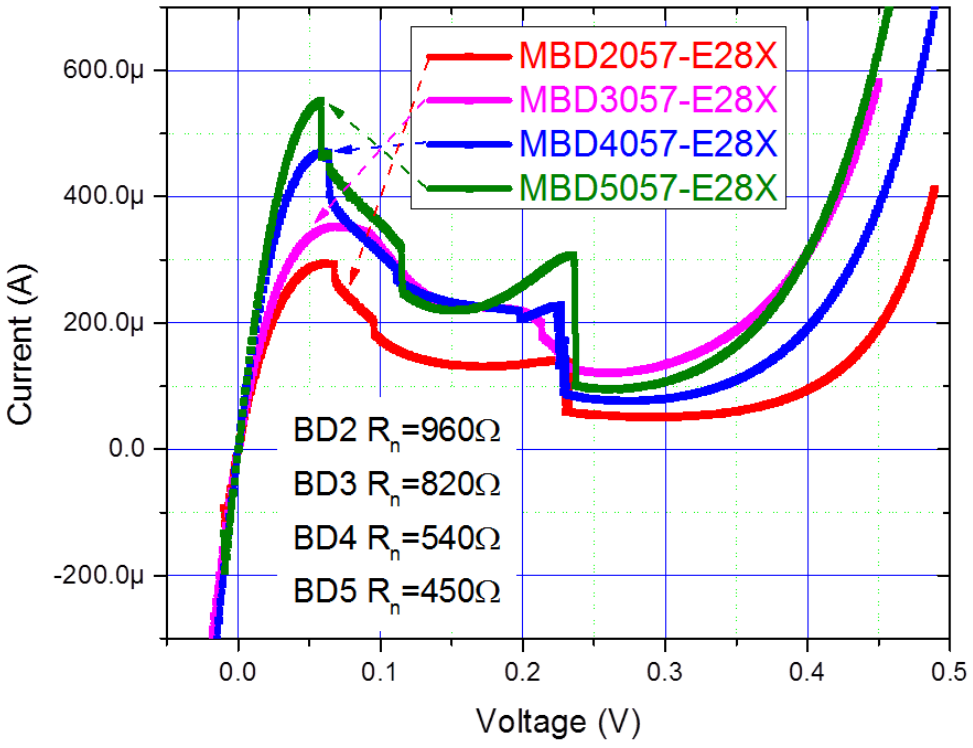

Figure 3.3 I-V curves for 4 models of the MBD series germanium tunnel diodes made by Aeroflex Metelics. Inset: absolute values of average negative resistance for each model

The bypass capacitor C_s value is chosen high enough to appear as a short circuit at the operating frequency value. Its purpose is to close the circuit thus separating the resonant side from the influence of external sources on the frequency (such as capacitance and inductance of the cables) as well as

minimizing external noise. The typical values for the capacitance of C_s in our setups are in the 500-3000 pF range. Although higher values would improve the decoupling from the external environment, the choice of C_s value is limited by the fact that the rf signal to be measured is extracted from the back of the tunnel diode meaning that high capacitance values of C_s would also drain a considerable amount of the signal to the ground. Consequently, the choice of C_s is a compromise between signal amplitude, external influence and noise.

From the anode terminal of the tunnel diode, the pure rf signal is separated from the dc component by the coupling capacitor C_c. It acts as a dc block for the signal which is then amplified and ultimately passed to the frequency counter. The high value of the coupling capacitance is in the order of μF although for most of our circuits, a dc block commerical circuit was used.

To push the diode in to the negative resistance region, a bias voltage (0.1-0.5 V) has to be applied to the tunnel diode but since the rf signal is extracted from the terminal of the diode, a constant voltage potential is detrimental. Consequently, a voltage divider made up of resistors R_1 and R_2 has to be used. The choice of resistance values is largely dictated by the available power supply maximum output voltage although other effects such as resistive heating and power dissipation, source voltage stability and diode characteristics have to be considered. Typically we use high values (order of a few kΩ) for $R_1$and an order of magnitude less for R_2 (50 Ω-500 Ω) with power supply voltages ranging from 3 to 25 volts. Choosing the value of R_2 is important as small values can diminish the rf signal and values larger than the negative resistance of the tunnel diode can result in absence of oscillations.

The capacitor C_p symbolizes the parallel capacitance of the tunnel diode which can be increased by adding a capacitor in parallel with the diode. This optional use of an additional capacitor can enhance the rf signal magnitude in the back of the diode and can also aid in adjusting the impedance of the diode to match the one of the LC tank.

What values for the components will make the circuit oscillate and what are the optimum values? For designing a reliable and precise TDO based experimental technique these are questions have to be addressed. Understanding the principles behind the tunnel diode resonator can greatly aid in the construction of a circuit with superior qualities. A thorough theoretical analysis of the TDO circuit is, despite its relative simplicity, very hard to realize as the electronic components are far from their ideal counterparts. However, a great deal can be understood about generation condition and oscillation frequency of a TDO by making a few assumptions about its constitutive elements.

There are a few studies in literature dealing with the theoretical investigation of the tunnel diode oscillator behavior. C. T. Van Degrift and D. P. Love [148] solved the differential equations system for electronic charge in a simplified version of the circuit and suggested the use of numerical modeling or the

use of an analytical approximation of the tunnel diode I-V curve. They arrived to an approximate expression for the frequency of harmonic oscillations of the form:

$$f = \frac{1}{2\pi\sqrt{LC}}[1 - F(C, C_P, R_P, L,)] \quad (3.1)$$

where the form of the function $F(C, C_P, R_P, L,)$ is given in [148] and

$$f_0 = \frac{1}{2\pi\sqrt{LC}} \quad (3.2)$$

is the resonant frequency of an ideal LC circuit.

S. G. Gevorgyan *et al.* [131] included the influence of the p-n junction capacitance C_j of the tunnel diode as well as its negative resistance value in the calculations and arrived at the following expression for the resonant frequency:

$$f = \frac{1}{2\pi\sqrt{LC}}\left[1 + \frac{1}{2}\frac{\omega_0 L}{Q}b_1 + \frac{1}{2}\frac{C_p + C_j}{C}(b_1 R_P - 1) - \frac{1}{2}\frac{\omega_0 R_P\left(C_p + C_j\right)}{Q} + \frac{1}{2}\frac{\omega_0 R_P L}{Q}{b_1}^2 + \cdots\right] \quad (3.3)$$

where $\omega_0 = 1/\sqrt{LC}$, $Q = (1/r)\sqrt{L/C}$ is the quality factor of the LC tank and $b_1 = 1/R_n$. They also showed that, in order to have sustained oscillations the following generation condition has to be met:

$$\frac{r}{L} + \frac{1}{R_P + R_n}\frac{1}{C} \leq 0 \quad (3.4)$$

Using the quality factor expression, the condition for stable oscillations can be written as:

$$|R_P + R_n| \leq Q\sqrt{\frac{L}{C}} = \frac{L}{rC} = Z_{res} \quad (3.5)$$

where Z_{res} is the resonance impedance of the LC circuit. We can see that, in order for sustained oscillations to exist, the impedance of the tank plus the contribution from the parasitic suppression resistance R_P has to be larger than the absolute value of the negative resistance of the tunnel diode. A value of Z_{res} too small, determined by either a large capacitance value or large resistance of the coil, will result in unbalanced energy losses thus damped oscillations. We can see from Eq. 3.5 that, depending on the component values of the LC tank, the oscillation generation condition can be met if the right tunnel diode type is chosen, based on its negative resistance. As an example, for the MBD series, the BD5 diodes have the smallest R_n, therefore they are best suited for inductors with high resistive losses.

As mentioned before, from a practical perspective, we are interested in the resonant frequency value of the TDO circuit. Frequency measurements are amongst the most precise types available, however frequency counters have a minimum input signal amplitude value requirement. Moreover, if the rf signal magnitude is comparable to external source signals, the frequency value will be distorted by noise effects. It is therefore meaningful to analyze in detail the oscillations amplitude in a TDO circuit. Following the approach in [131] we assume that the oscillations are harmonic with magnitude in the form $V =$

$V_a \cos \omega t$. In the steady oscillation mode of the TDO, from energy conservation considerations, the rf energy feeding of the tunnel diode must cancel out the rf energy losses in the circuit. These losses are mainly due to ohmic behavior of the inductor but are also caused by the overall resistive losses in the circuit, as well as by rf radiation. The average energy loss per unit cycle P_l can be written as:

$$P_l = \frac{1}{2\pi}\int_{-\pi}^{\pi} I(t)V(t)d(\omega t) = \frac{{V_a}^2}{2\pi R_{eff}}\int_{-\pi}^{\pi}\cos^2(\omega t)\, d(\omega t) = \frac{{V_a}^2 G_{eff}}{2} \quad (3.6)$$

where R_{eff} is an effective resistance of the circuit and $G_{eff} = 1/R_{eff}$ an effective loss conductance. The average energy feed per unit cycle P_f can be written in a similar form:

$$P_f = \frac{{V_a}^2 G_d}{2} \quad (3.7)$$

where G_d is the tunnel diode's oscillation period averaged differential conductance defined as [131]:

$$G_d = \frac{1}{2\pi}\int_{-\pi}^{\pi} \frac{dI_d(V_d + V)}{dV} d(\omega t) \quad (3.8)$$

The tunnel diode current I_d is dependent on the voltage drop across its terminals which is a sum of the bias voltage V_d and the harmonic voltage V. The oscillation condition is met when $P_l = P_f$, therefore the condition in Eq. 3.5 can also be expressed as:

$$|G_d(V_d, V_a)|R_{eff} = 1 \quad (3.9)$$

From Eq. 3.8 the oscillation amplitude dependence on diode bias voltage $V_a(V_d)$ can be derived if the I-V curve analytical expression of the tunnel diode is known. This can be achieved if we consider a polynomial fit for the measured I-V curve of our tunnel diodes. We show in Fig. 3.4 below an example of $G_d(V_a)$ curves for 50 different values of voltage bias ($V_d = 90 - 230\ mV$ in 50 steps) obtained using Eq. 3.8 by fitting the measured I-V curve of a MBD4 tunnel diode with an 8 degree polynomial function. One can see that a tunnel diode can accommodate a wide range of R_{eff} values and that the oscillation condition (Eq. 3.9) is satisfied for a large range of bias voltages and oscillation amplitude i.e. any horizontal straight line at vertical coordinate R_{eff} will satisfy Eq. 3.9 within an area delimited by the $G_d(V_a)$ curves.

On the right side of Fig. 3.4 we show the calculated oscillation amplitude dependence on the bias voltage $V_a(V_d)$ for $R_{eff} = 10k\Omega$. It is easy to see that there is an optimum value of V_d for which the oscillations have a maximum amplitude and that, at large enough bias voltage values (240mV in the case depicted in Fig. 3.4), the oscillations will die away. It is important to note that resonance causes the voltage drop on the diode to oscillate over a wide range of values which may include regions on the I-V curve not characterized by a negative differential resistance. However, by changing the bias voltage, the time averaging region can be modified to accommodate the total losses, providing the necessary condition for sustained oscillations.

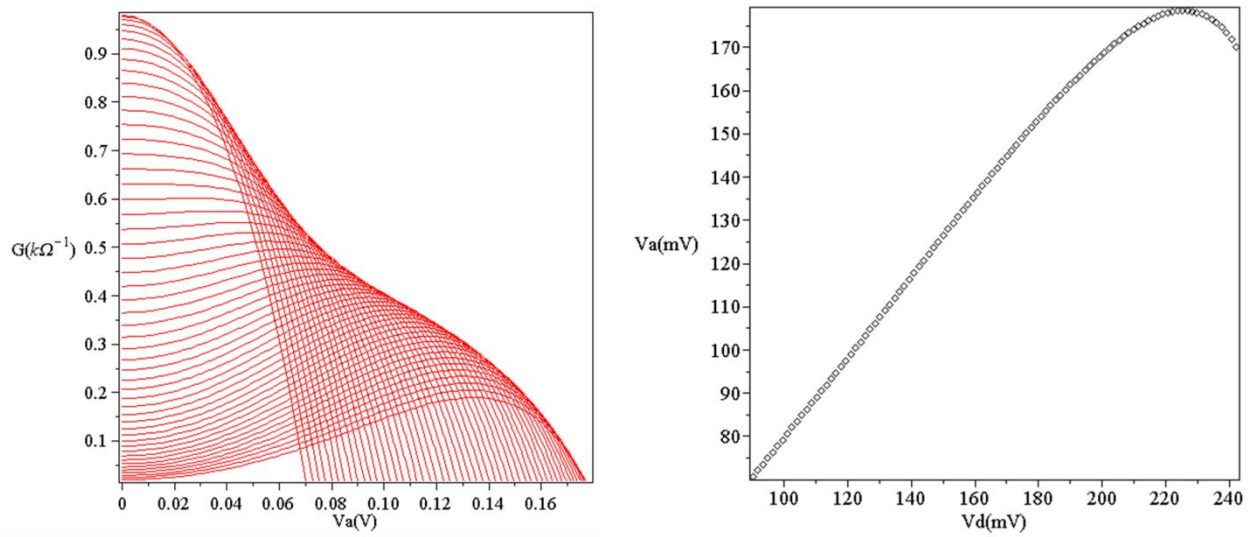

Figure 3.4 Left: Average period conductance vs. oscillation amplitude $G_d(V_a)$ curves for the MDB4 tunnel diode at 50 different values of bias voltage from 90 to 230 mV. Right: oscillations amplitude versus bias voltage $V_a(V_d)$ calculated for $G_d = 0.0001$.

Moreover, although the voltage drop across the LC circuit is harmonic, a large oscillation amplitude means that the voltage across the diode will be nonlinear. For small enough oscillation amplitudes, the negative region on the I-V curve can be approximated with a straight line. In practice, however, large amplitude values V_a are preferred, thus, the measured ac signal from the back of the diode will most likely be non-harmonic in nature. This was observed experimentally in a number of our TDO circuits. Nevertheless, this issue is of less practical concern in our measurements as the frequency counters require only a periodic signal regardless of its shape.

To test the predicted theoretical behavior of the tunnel diode oscillator circuit and to gain additional insight into its features, we also carried out numerical simulations for the TDO using the National Instruments Multisim commercial software [149], a SPICE based simulation environment used for circuit design and testing which provides a simple easy to use interface. The advantage of the software is its ability to simulate electronic circuits of great complexity and, most importantly, the option to use electronic components with realistic characteristics. The simulations confirmed the theoretical expectations for the TDO circuit performance and provided us with constructive information regarding the design and construction of our circuits. Simulations were carried out for the components of some of our TDO circuits and, as an example, we show the results for one of our circuits in Fig. 3.5 where we illustrate the electronic diagram of the TDO circuit together with numerical values and expected signals at different potential node points on the circuit. The tunnel diode used was MBD4 and its current-voltage

characteristic was simulated using a ABM current source with the I(V) dependence obtained from the 8 degree polynomial fit of the measured I-V curve.

From the numerical results, we notice that the ac current amplitude in the LC tank is in the order of mA (probe 1 in Fig. 3.5). Such high current values are expected considering that the LC tank is a parallel circuit at resonance. This information is particularly useful in estimating the magnetic field amplitude created by the coil and also in figuring the resistive power dissipated by the LC tank, which is essential if the TDO is to be used at low temperatures. As previously mentioned, the measured rf signal (oscilloscope curve on Fig. 3.5) is inharmonic due to the nonlinearity of the I-V curve of the tunnel diode. Also, the signal amplitude is of the order of a few mV at the point where the signal is extracted meaning that the small signal has to be amplified before being forwarded to the frequency counter.

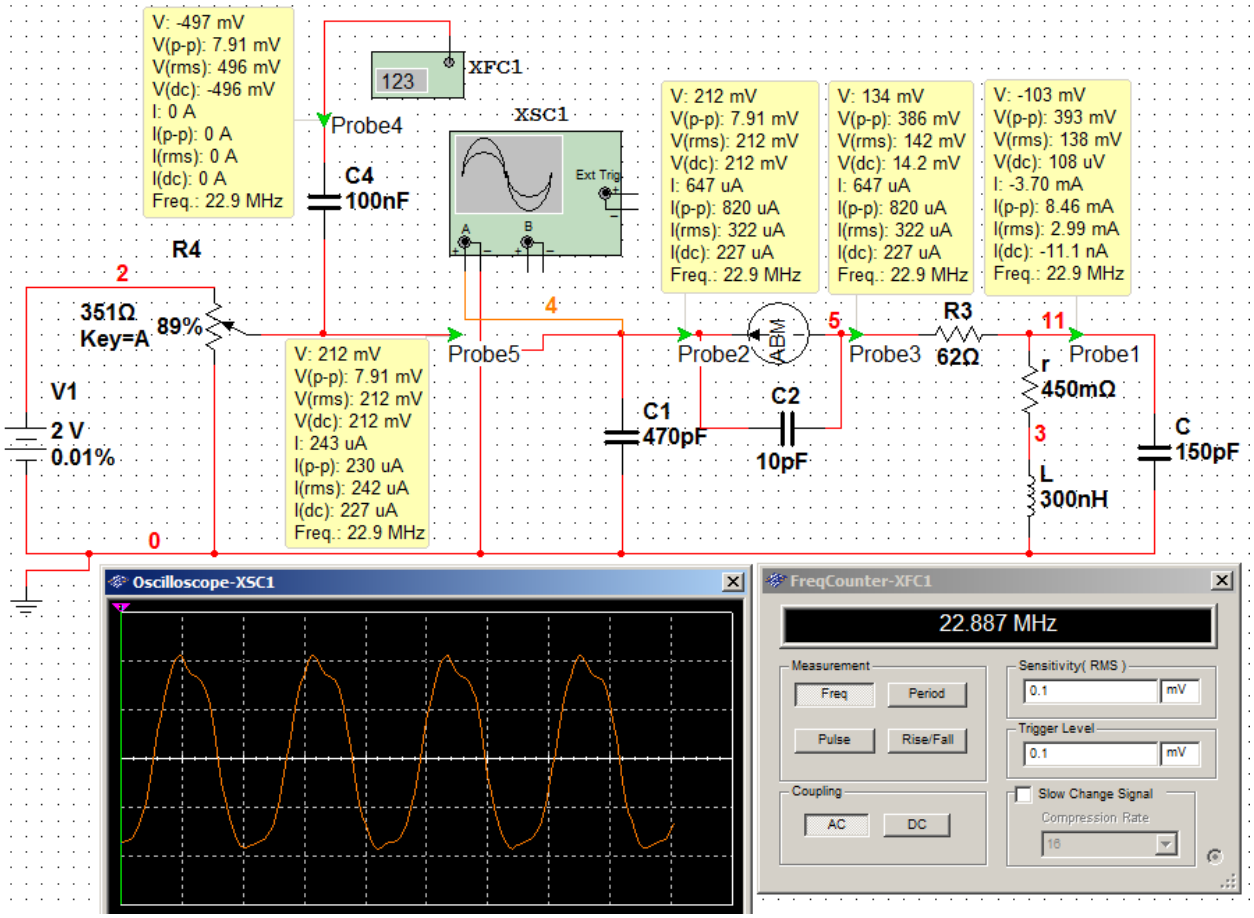

Figure 3.5 TDO circuit simulation using the NI Multisim commercial software.

Looking at the resonant frequency expression for a TDO circuit in Eq. 3.3 it is easy to see that it is considerably different than one expected for an ideal LC circuit (Eq. 3.2). Moreover, the expression is obtained considering that the impedance of the bypass capacitor C_s is low enough to act as a short and decouple the circuit from external sources. In practice however, a relatively low C_s capacitance value is needed to extract the rf signal to be measured. This capacitance can also influence the resonance frequency especially if its value is low enough to allow for a significant influence from the connecting cables inductance/capacitance. The obtained numerical results suggest that the influence on resonant frequency of the bypass capacitor C_s is negligible e.g. for the values in the TDO circuit tank of Fig. 3.5 doubling the capacitance value of C_s from 470 pF to 940 pF caused a frequency shift of only 2 kHz (10^{-5} %).

Ultimately, the resonant frequency of the TDO is dependent upon a large number of factors including all electronic components parameters and even the applied voltage. However, numerical simulations have shown that the major contribution to the deviation from the expected value f_0 for an ideal LC circuit (Eq. 3.2) is determined by the capacitance value of the tunnel diode (or the parallel capacitor C_p). This can also be observed by taking a closer look at the TDO frequency expression in Eq. 3.3. If we consider the component values from the TDO circuit diagram depicted in Fig. 3.5 we expect that $Z_{res} \sim R_n \approx 4.5$ kΩ. This suggests small values of $b_1$which lead to negligible values (~0.5e-3) for the term linear in $b_1$and more so for the last term which is quadratic in b_1. Also, $\omega_0/Q \approx 1.5 \times 10^6$, which for pF values of C_p, results in a negligible contribution from the 3rd term in Eq. 3.3. The only term of considerable weight is the 2nd term containing the ratio C_p/C thus, for the diode's parallel capacitance values comparable to the capacitance of the LC tank, the resonant frequency of the TDO will be considerably different than that of the ideal value. As an example, for the 10 pF value of the circuit in Fig. 3.5, the resonant frequency is ~ 22.9 MHz. The corresponding ideal LC circuit frequency value would be $f_0 \approx 23.7$ MHz. The TDO frequency will approach its ideal value if the parallel capacitance of the tunnel diode is considerably less than that of the LC tank. The MBD-E28X series has a relatively small junction capacitance ($C_j \approx 0.5$pF), however, a finite value is required for application purposes considering that the capacitance of the diode provides the necessary means for extracting the rf signal from the LC tank (the measured signal is picked up from the anode terminal of the diode).

In our practical application of the TDO circuit, in order to match the negative resistance of the diode with the impedance of the LC tank, we avoided the use of a large parallel capacitor C_p values with the tunnel diode. We choose a large enough (larger than C_j) LC tank capacitance and the proper diode to match the tank impedance Z_{res} and also found that the small junction capacitance C_j is sufficient for a

measurable signal in most cases. Consequently, the TDO resonant frequency can be approximated to the value of the ideal LC circuit for most practical applications.

3.4. The temperature dependence of TDO frequency

In practice, considering that most of the elements entering the expression of the resonant frequency of the TDO (Eq. 3.3) are susceptible to temperature, we expect that thermal effects will play an important role in the frequency stability of the circuit.

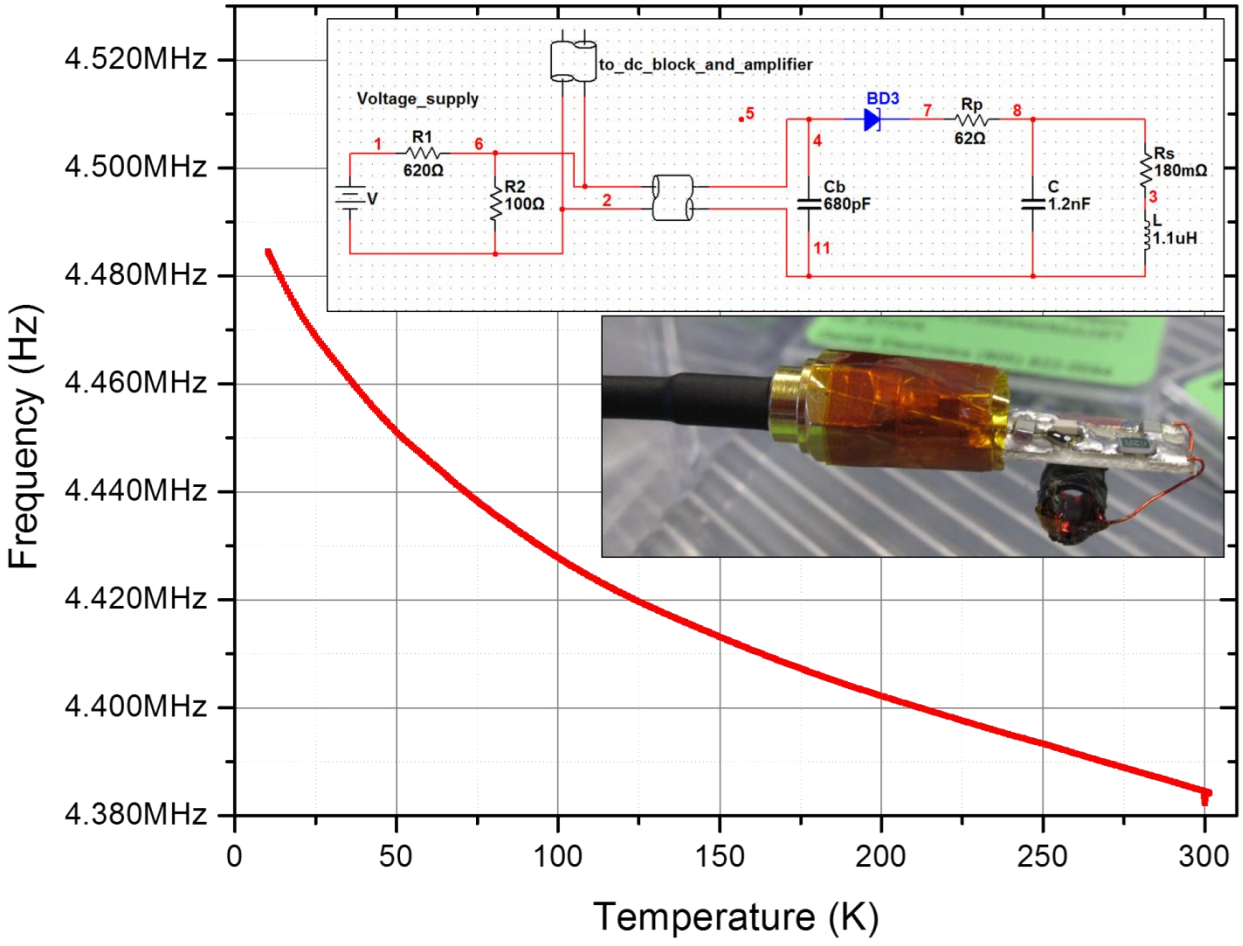

Figure 3.6 Resonant frequency versus temperature for a TDO circuit measured in the PPMS. Top inset: the circuit diagram and the component values used. Bottom inset: picture of a lab built TDO circuit and solenoid coil for PPMS measurements.

Moreover, since our interest is in the temperature investigation of magnetic properties of superconductors, the value of the TDO as a transducer for such measurements depends on the extent to which its frequency changes reflect only changes in the physical property to be studied. Consequently, the temperature dependence of the circuit characteristics should be minimized. In order to do so, we need to understand the thermal effects better and find ways to avoid them.

As an example, we illustrate in Fig. 3.6 the temperature dependence of the resonant frequency for a TDO circuit. The electronic components values are shown in the inset containing the schematic diagram of the circuit used. The measurements were performed in a commercial Quantum Design Physical Property Measurement System (PPMS) from room temperature down to 10 K. In order to avoid frequency variations that may arise from the temperature dependence of the resistors constituting the voltage divider, we built a separate enclosure for the divider which was kept at room temperature, outside the PPMS. The TDO circuit was lowered in the active thermal region of the PPMS with a coaxial cable, extending from the circuit to a top flange with vacuum sealed SMA feedthroughs, carrying both the supply dc voltage and the ac signal. The rf signal was extracted using a BLK-89-S+ dc block circuit, amplified using a ZFL -1000LN Mini-Circuits amplifier and measured with a Agilent 53131A Universal Frequency Counter. It is easy to see that, for the example given in Fig. 3.6, the temperature effects on resonant frequency are in no way negligible. The frequency decrease is about 25000 ppm in the 10-300 K interval. Most of our measurements require a frequency stability of 0.01 ppm thus, finding a way to eliminate the resonant frequency temperature dependence is imperative.

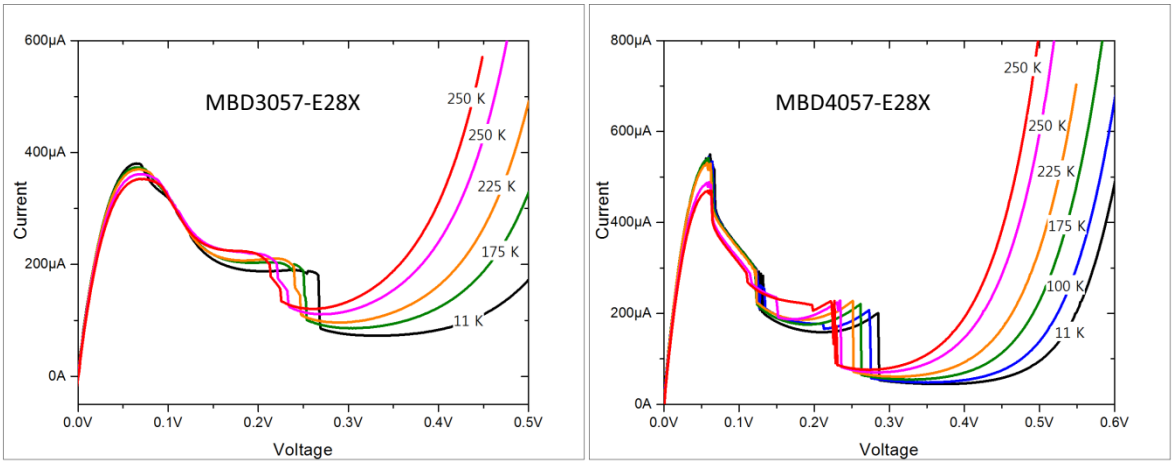

Figure 3.7 I-V curves for the MBD3057-E28X (left) and MBD4057-E28X (right) tunnel diodes at different temperatures.

An important contribution to the TDO's temperature dependence is expected to come from the characteristics of the tunnel diode. Fig. 3.7 shows the I-V curves of our BD3 and BD4 tunnel diodes measured at different temperatures in the PPMS. Although a significant temperature variation of the IV characteristic of our tunnel diodes can be observed, the temperature effects are more pronounced at higher temperature values. At lower values (below 30K), due to the heavy doping level of the junction, the IV curve is less dependent on temperature.

Another factor that can contribute to the temperature dependence of the TDO frequency is the temperature dependence of the capacitance value of the LC tank. This can be caused by either thermal contraction effects or by the temperature dependence of the dielectric material. For this reason Class I ceramic capacitors should be used, characterized by low temperature coefficients e.g. the C0G (NP0) type commercial capacitors have a zero temperature coefficient over a wide range of temperatures. Also, the inductor of the LC tank is susceptible to temperature effects as its geometric dimensions can change due to thermal expansion/contraction. Therefore, when constructing the inductor, materials, notably epoxies, with low expansion coefficients should be used.

Although all the above mentioned effects contribute to the temperature dependence of the resonant frequency, the most important contribution is arises from the resistivity variation with temperature of the parasitic suppression resistor R_n and the resistance of the LC tank inductor r. The most common material of choice in constructing inductors, which is also the case for our inductors, is copper. The resistivity of copper can decrease down to a few orders of magnitude lower values as the temperature is decreased from room temperature to cryogenic levels. Considering the substantial dependence of the TDO frequency on r (Eq. 3.3) and the change in negative resistance of the diode, necessary for sustained oscillations, associated with the increase in LC quality factor Q as the temperature is decreased, we can expect a significant contribution to arise from the temperature variation of resistance.

Regardless of the effects responsible for the temperature dependence of the TDO circuit frequency, maintaining the circuit components at a constant temperature ensures a temperature independent, stable frequency. This is necessary when the temperature investigations of physical properties are desired, where frequency variations are related only to the material property under study. A constant circuit temperature can also improve the performance of the TDO for non-temperature dependent measurement as most of the drift in the measured frequency of the circuit is caused by temperature fluctuations. Maintaining the TDO circuit at constant temperature in a practical setup is not a trivial task, however, great frequency stability can be achieved if special care is taken. We will discuss in more detail the practical aspects regarding frequency stability and temperature influence later, when we describe the setup for penetration depth measurements using the TDO technique in a dilution refrigerator.

3.5. The TDO as a London penetration depth measurement technique

The superior sensitivity of the TDO comes mostly from the fact that it is a resonant method. Since the LC circuit is always at resonance, minute changes in either L or C will cause significant changes in the resonant frequency. By measuring the TDO frequency as a function of the sample temperature, applied magnetic or electric field, based on induced changes in either capacitance or inductance, one can in principle extract different material properties, such as thermal expansion, surface impedance, electric and magnetic susceptibilities.

However, in our experiments we are only interested in using the TDO circuit as a measurement technique based on frequency changes induced by variations in inductance values caused by changes in the magnetic properties of samples. We showed that, in most cases, the TDO frequency can be approximated by the ideal LC circuit value:

$$f_0 = \frac{1}{2\pi\sqrt{L_0 C}} \qquad (3.10)$$

As the inductance value changes from an initial value L_0 to a value $L = L_0 + \Delta L$ (assuming constant capacitance) the frequency will shift to a value:

$$f = \frac{1}{2\pi\sqrt{LC}} = f_0 + \Delta f \qquad (3.11)$$

From Eq. 3.10 and Eq. 3.11 it is easy to show that the change in inductance ΔL can be obtained from:

$$\Delta L = L_0 \left[\left(\frac{f_0}{f} \right)^2 - 1 \right] \qquad (3.12)$$

Thus, from frequency measurements, the relative change in inductance can be estimated. If the frequency shift is small relative to the initial frequency value, meaning $\Delta f \ll f_0$, expanding the right side of Eq. 3.12 in power series around $\Delta f / f_0$ and keeping only the linear term, we can write the relative inductance change as:

$$\frac{\Delta L}{L_0} = -2\frac{\Delta f}{f_0} \Rightarrow \frac{\Delta f}{f_0} = -\frac{1}{2}\frac{\Delta L}{L_0} \qquad (3.13)$$

which suggests that for a small inductance variation ΔL, the corresponding relative frequency shift $\Delta f / f_0$ is directly proportional to the relative variation of the inductance value. Since in our practical application of the TDO we measure relatively small changes in frequency, using the approximate expression in Eq. 3.13 is sufficient.

A time varying electric current i passing through a conductor will create a time varying magnetic flux which, according to Faraday's law of induction, will generate a voltage drop across the conductor:

$$v = L\frac{di}{dt} \tag{3.14}$$

where L in the inductance of the conductor. In free space, the inductance L is just a geometrical factor depending solely on the shape of the conductor. However, in a magnetic permeable space, the magnetic flux magnitude created by the currents will be modified according to the permeability value. The most general definition for the inductance of any conductor can be given using an energy point of view:

$$L = 2\frac{W}{I^2} \tag{3.15}$$

where I is the current flowing through the inductor and W the magnetic energy produced by the current. The magnetic energy W is defined as:

$$W = \int_V \frac{(\boldsymbol{B}\cdot\boldsymbol{H})}{2} dV \tag{3.16}$$

where B and H are the magnetic flux density and magnetic field intensity, respectively, created by the current flowing through the inductor, at any point in space, with the integration carried over all space. In vacuum we have that $\boldsymbol{B} = \mu_0\boldsymbol{H}$ so the inductance can be calculated using:

$$L = \frac{\mu_0}{I^2}\int_V H^2 dV \tag{3.17}$$

From Biot-Savart law, the inductance of any shape conductor in vacuum can in principle be calculated using Eq. 3.17.

Let us consider an empty coil (conductor in vacuum) with inductance L_0 given by:

$$L_0 = \frac{\mu_0}{I^2}\int_{V_C} {H_0}^2 dV \tag{3.18}$$

where V_C is an effective coil volume (in most cases, a finite volume is sufficient for integration).
A magnetically active sample, placed in the field H_0 of coil, will develop a magnetization (magnetic moment per unit volume) M in response to H_0 expressed by:

$$M = \chi H_0 \tag{3.19}$$

where χ is the magnetic susceptibility, characteristic of the material. Strictly speaking, susceptibility is a tensorial quantity defined locally in a static form $\boldsymbol{M} = \chi\boldsymbol{H}$ or dynamic form $d\boldsymbol{M} = \chi d\boldsymbol{H}$. In linear magnetic materials (e.g. diamagnetic materials) the two forms are equivalent. Since the magnetic flux density $\boldsymbol{B} = \mu_0(\boldsymbol{H} + \boldsymbol{M})$ in the sample volume is different than the value in vacuum, the magnetic energy stored in the coil will change by an amount:

$$\Delta W = \int_{V_S} \frac{(\boldsymbol{B}\cdot\boldsymbol{H})}{2} dV \tag{3.20}$$

If we consider a uniform magnetization throughout the sample volume V_S induced by a uniform coil current field H_0, then the energy shift can be written as:

$$\Delta W = \int_{V_s} \frac{\mu_0 (H_0 + M) H_0}{2} dV - \int_{V_s} \frac{\mu_0 {H_0}^2}{2} dV = \int_{V_s} \frac{\mu_0 {H_0}^2 \chi}{2} dV \quad (3.21)$$

According to the definition for inductance (Eq. 3.15) the magnetic energy change ΔW will promote a corresponding inductance change:

$$\Delta L = \frac{2}{I^2} \Delta W = \int_{V_S} \frac{\mu_0 {H_0}^2 \chi}{I^2} dV \quad (3.22)$$

Considering the inductance value of the empty coil, expressed in Eq. 3.18, we can finally write the inductance of a coil producing a uniform field in a sample of magnetic susceptibility χ as:

$$L = L_0 + \Delta L = L_0 (1 + k\chi) \quad (3.23)$$

where $k = V_S / V_C$. This formula applies for samples where demagnetizing fields due to surface effects can be ignored e.g. elongated cylinder in parallel field. For finite size samples however, the demagnetizing effects can severely influence the magnitude of the field intensity and flux density in and around the sample and, consequently, the associated magnetic energy change and inductance shift. We can however find a similar expression for ΔL (Eq. 3.23) if we assume a constant demagnetizing factor N like is the case of ellipsoid shaped samples or thin films. Inside the sample, the magnetic intensity becomes:

$$H = H_0 + NM \quad (3.24)$$

Since the true internal magnetic susceptibility is defined in respect to the total field intensity H, the magnetization can be written as:

$$M = \frac{\chi H_0}{1 + N\chi} = \chi_{eff} H_0 \quad (3.25)$$

Here, χ_{eff} describes an effective magnetic susceptibility which defines the magnetic moment per unit volume induced by the applied field H_0. The magnetic flux density can now be written as:

$$B = \frac{\mu_0 H_0 (1 + \chi)}{1 + N\chi} \quad (3.26)$$

The field equations are also valid for non-linear materials (i.e. ferromagnetic and paramagnetic) since the field is uniform within the sample volume. Calculating the energy shift produced by a finite sample of effective susceptibility χ_{eff} we arrive at the corresponding expression for the relative inductance L change:

$$\frac{\Delta L}{L_0} = k\chi_{eff} \quad (3.27)$$

where χ_{eff} can be thought of as being:

$$\chi_{eff} = \frac{m}{V_S H_0} \quad (3.28)$$

Recalling the relation between the relative inductance change and TDO frequency shift (Eq. 3.13) we can finally write:

$$\frac{\Delta f}{f_0} = -\frac{1}{2}\frac{V_S}{V_C}\chi_{eff} \qquad (3.29)$$

Thus, the measurable frequency shift $\Delta \boldsymbol{f} = \boldsymbol{f} - \boldsymbol{f_0}$ of a tunnel diode oscillator circuit, upon placing a magnetic sample about its LC tank inductor, is directly proportional to the effective susceptibility of the material.

The proportionally relation between the relative inductance change was obtained considering a uniform field intensity produced by the coil currents as well as a uniform magnetization value throughout the sample volume. A uniform probing field from an inductor is however hard to achieve in practice. Long solenoid coils, which do have the advantage of generating a uniform field inside their core, have a correspondingly large volume, meaning low values of the relative inductance shift created by small size samples. Moreover, if the sample shape does not permit the assumption of a true demagnetizing factor (like in the case of long cylinders, ellipsoids or thin films), the magnetization value is not necessarily uniform throughout the sample volume.

In our study we are more interested in the diamagnetism of superconductors. We have shown in Chapter II that the constitutive equation for the magnetization in a superconductor (Eq. 2.9) is different from that of conventional magnetic media. Also, the superconductive samples used in practical setups are typically rectangular slab shaped where a true demagnetizing factor does not exist and magnetization is spatially dependent. Thus, the question that arises is: can we use a similar relation for the relative inductance variations (Eq. 3.27) in the case of diamagnetic susceptibility of superconductive samples of practical geometric shapes?

To answer this important question, we consider the magnetic energy change associated with placing a superconductive sample in an initial magnetic field $\boldsymbol{B_0} = \mu_0 \boldsymbol{H_0}$. If we neglect any magnetic effects of the normal state, this is equivalent to the energy difference between the Meissner state and normal state if the sources producing the field are fixed:

$$\Delta W = \int_V \frac{(\boldsymbol{B}\cdot\boldsymbol{H})}{2} dV - \int_V \frac{{B_0}^2}{2\mu_0} dV \qquad (3.30)$$

Considering that $\boldsymbol{B} = \mu_0(\boldsymbol{H} + \boldsymbol{M})$, the energy change can be expressed as:

$$\Delta W = \int_V \frac{\left(B^2 - {B_0}^2\right)}{2\mu_0} dV - \int_V \frac{\boldsymbol{M}\cdot\boldsymbol{B}}{2} dV \qquad (3.31)$$

The first term can be written as:

$$\int_V \frac{\left(B^2 - {B_0}^2\right)}{2\mu_0} dV = \int_V \frac{(\boldsymbol{B} - \boldsymbol{B_0})(\boldsymbol{B} + \boldsymbol{B_0})}{2\mu_0} dV \qquad (3.32)$$

If we consider the magnetic field as derived for the vector potential $\boldsymbol{A}$, it follows that

$$\boldsymbol{B} + \boldsymbol{B_0} = \boldsymbol{\nabla} \times (\boldsymbol{A} + \boldsymbol{A_0}) \qquad (3.33)$$

where $\boldsymbol{A_0}$ is the vector potential of the initial (applied) field. Considering that the sources are fixed we can write Ampere's law for the supercurrent density $\boldsymbol{j_s}$:

$$\boldsymbol{\nabla} \times (\boldsymbol{B} - \boldsymbol{B_0}) = \mu_0 \boldsymbol{j_s} \tag{3.34}$$

Consequently, the first term in the energy change expression (Eq. 3.31) can be expressed as [150]:

$$\int_V \frac{\left(B^2 - {B_0}^2\right)}{2\mu_0} dV = \int_S \frac{(\boldsymbol{A} + \boldsymbol{A_0}) \times (\boldsymbol{B} - \boldsymbol{B_0})}{2\mu_0} \cdot d\boldsymbol{S} + \int_V \frac{(\boldsymbol{A} + \boldsymbol{A_0}) \cdot \boldsymbol{j_s}}{2} dV \tag{3.35}$$

Here S is the surface enclosing the volume V. If the volume is extended to infinity (far from the source location), the surface integral vanishes since the integrand falls faster than inverse power law of distance. Thus, the energy change becomes:

$$\Delta W = \int_V \frac{(\boldsymbol{A} + \boldsymbol{A_0}) \cdot \boldsymbol{j_s}}{2} dV - \int_V \frac{\boldsymbol{M} \cdot \boldsymbol{B}}{2} dV \tag{3.36}$$

Recalling the London equation (Eq. 1.15) for superconductors we can write the second term as:

$$\int_V \frac{\boldsymbol{M} \cdot \boldsymbol{B}}{2} dV = \mu_0 \lambda^2 \int_V \frac{\boldsymbol{M} \cdot (\nabla \times \boldsymbol{j_s})}{2} dV \tag{3.37}$$

Making use of the vector identity $\boldsymbol{M} \cdot (\nabla \times \boldsymbol{j_s}) = \boldsymbol{\nabla} \cdot (\boldsymbol{j_s} \times \boldsymbol{M}) + \boldsymbol{j_s} \cdot \nabla \times \boldsymbol{M}$ and considering the magnetization expression in a superconductor $\boldsymbol{j_s} = \nabla \times \boldsymbol{M}$ as well as the London equation (Eq. 1.15) we arrive at the following expression for the second term in Eq. 3.31:

$$\int_V \frac{\boldsymbol{M} \cdot \boldsymbol{B}}{2} dV = \mu_0 \lambda^2 \int_V \frac{{\boldsymbol{j_s}}^2}{2} dV = \int_V \frac{\boldsymbol{A} \cdot \boldsymbol{j_s}}{2} dV \tag{3.38}$$

We can therefore write the expression for the energy change caused by a superconductor as:

$$\Delta W = \int_{V_S} \frac{\boldsymbol{A_0} \cdot \boldsymbol{j_s}}{2} dV \tag{3.39}$$

where the volume of integration is the sample volume, considering that the supercurrent vanishes outside the material. The expression in Eq. 3.39 involves the vector potential associated with the initial (external) field and the supercurrent density. Knowing the initial field configuration throughout the sample volume, using the London equation, the energy change can in principle be calculated for any geometry of a coil – sample configuration.

Making use of the relation $\boldsymbol{j_s} = \nabla \times \boldsymbol{M}$, the energy change can also be expressed as:

$$\Delta W = \int_{V_S} \frac{\boldsymbol{M} \cdot \boldsymbol{B_0}}{2} dV \tag{3.40}$$

which, for a uniform external field $\boldsymbol{B_0} = \mu_0 \boldsymbol{H_0}$, leads to a similar relation as in the case of magnetic media, where m is the total magnetic moment of the superconductor:

$$\Delta W = \frac{\mu_0 H_0}{2} \int_{V_S} \boldsymbol{M} dV = \frac{\mu_0 H_0}{2} m \tag{3.41}$$

If the uniform external field is produced by the current in the inductor, then, considering the initial inductance of the coil L_0 and the associated magnetic energy W_0 related by:

$$L_0 = 2\frac{W_0}{I^2} = \frac{2}{I^2}\frac{\mu_0 {H_0}^2}{2}V_C = \frac{\mu_0 {H_0}^2}{I^2}V_C \qquad (3.42)$$

a superconductive sample will cause a relative inductance change:

$$\frac{\Delta L}{L_0} = \frac{m}{V_C H_0} = k\chi_{eff} \qquad (3.43)$$

which is the same expression as in Eq. 3.29 where $k = V_S/V_C$. It is important to note that the relative inductance dependence on the effective susceptibility of a superconductor in Eq. 3.43 was obtained considering only a uniform excitation field in the sample volume which stands true regardless of the geometry of the coil producing the field with the only requirement being that the field is uniform in the sample region. This can be easily achieved by using long solenoids as inductors. However, due to their large volume compared to relatively small samples, the relative inductance changes case of solenoids may be harder to detect in practice. We can in principle increase the relative inductance shift by constructing coils with volumes close to the sample volume, however, the probing magnetic field of the coil might not be uniform anymore and the general expression in Eq. 3.39 has to be implemented. Calculating the supercurrent density for any applied field configuration can be done by making use of the London relation although, as previously mentioned, this is not a trivial task as for complex geometries numerical methods have to be implemented. To avoid such complications we will consider only the case when the probing field of the coil is uniform in the sample region in our further calculations.

Considering that the relative inductance changes caused by introducing a superconductive sample in the coil volume are proportional to the effective susceptibility of the sample (the total magnetic moment) (Eq. 3.43), if the coil is the tunnel diode oscillator LC tank inductor, we can relate this quantity to the relative resonant frequency shift in Eq. 3.13. Thus, a superconductive sample of effective susceptibility χ_{eff} will induce a proportional TDO frequency shift:

$$\frac{\Delta f}{f_0} = \frac{f - f_0}{f_0} = -\frac{1}{2}k\chi_{eff} \qquad (3.44)$$

where f_0 is the resonant frequency of the TDO circuit when the coil is empty.

If the sample is in a normal state of zero susceptibility, the resonant frequency has the same value as the empty LC tank frequency f_0. However, this might not be the case for all materials. Superconductors are metallic above the transition temperature so a radio frequency field will create finite diamagnetic susceptibility from the screening of the field due to skin effect in metals. The effective susceptibility has an additional diamagnetic term resulting from the skin depth δ of the field which is related to the resistivity of the material ρ by:

$$\delta = \sqrt{\frac{\rho}{2\pi\mu f}} \qquad (3.45)$$

where μ is the magnetic permeability of the material and f is the field frequency [151]. As an example, for an ellipsoid shaped sample, the skin effect susceptibility can be expressed as [111, 152]:

$$\chi_{skin} = -\left(1 - \frac{\delta}{2R}\tanh\frac{2R}{\delta}\right) \qquad (3.46)$$

where R is a characteristic dimension of the sample perpendicular to applied field. If necessary, the skin contribution to the effective susceptibility can be estimated if the resistivity of the material in normal state is known.

In our TDO experiments, the investigated superconductive samples have a rectangular slab shape with relatively small thickness compared to lateral dimensions. For this geometry (and disk geometry) , in Chapter II, we have shown that, the effective susceptibility in Meissner state for a perpendicular uniform applied magnetic field is related to the London penetration depth by:

$$\chi_{eff} = -\frac{1}{1-N}\left[1 - \frac{\lambda}{R}\tanh\left(\frac{R}{\lambda}\right)\right] \qquad (3.47)$$

where N is an effective demagnetizing factor and R an effective dimension, both depending of the aspect ratio w/d of the sample. Consequently, the relative frequency shift of a TDO can be expressed as:

$$\frac{\Delta f}{f_0} = \frac{V_S}{2V_C(1-N)}\left[1 - \frac{\lambda}{R}\tanh\left(\frac{R}{\lambda}\right)\right] \qquad (3.48)$$

If we consider small values of λ relative to the sample effective dimension $R \gg \lambda$, this can simply be written as:

$$\frac{\Delta f}{f_0} = \frac{V_S}{2V_C(1-N)}\left(1 - \frac{\lambda}{R}\right) \qquad (3.49)$$

The expression (3.49) relates a measurable relative frequency shift to the London penetration depth λ of a rectangular slab superconductive sample, in Meissner state, under a uniform perpendicular excitation field produced by the inductor of the TDO. In principle, it can be used to determine the absolute value of λ, however, the effective demagnetizing factor N or the coil volume V_C are difficult to estimate in practice. Nonetheless, we can use the TDO method to study relative changes in magnetic penetration depth such as the ones caused by temperature variations.

Let us consider the frequency values corresponding to two temperature values of London penetration depth. From Eq. 3.49 we can write:

$$f(T_1) - f_0 = \frac{f_0 V_S}{2V_C(1-N)}\left(1 - \frac{\lambda(T_1)}{R}\right) \qquad (3.50)$$

and

$$f(T_2) - f_0 = \frac{f_0 V_S}{2V_C(1-N)}\left(1 - \frac{\lambda(T_2)}{R}\right) \quad (3.51)$$

Subtracting the two equations we have that:

$$f(T_2) - f(T_1) = \frac{f_0 V_S}{2V_C(1-N)}\left(1 - \frac{\lambda(T_2) - \lambda(T_1)}{R}\right) \quad (3.52)$$

which can be expressed in the simple form:

$$\Delta f(T) = -\frac{G}{R}\Delta\lambda(T) \quad (3.53)$$

where

$$G = \frac{f_0 V_S}{2V_C(1-N)} \quad (3.54)$$

is a calibration factor depending on the sample-coil setup geometry. **We have thus shown that measurable temperature induced changes in the TDO frequency are directly proportional to the temperature variation of London penetration depth.**

At very low temperatures $\lambda(T \to 0) = \lambda_0 \ll R$ so, from Eq. 3.50, we can see that $f(T \to 0) - f_0 = G$. Therefore, the calibration factor G can be easily estimated by measuring the empty coil TDO frequency and the frequency with the sample at the lowest temperature. In practice, a straightforward way of estimating G is by the measuring TDO frequency shift resulting from extracting the sample from the coil at lowest temperature. If the susceptibility of the normal state of the sample is negligible, the empty coil frequency value is the same as the frequency for the sample above the superconductive transition temperature T_C. Consequently, an alternative determination of the calibration factor can be made by measuring the difference in frequency values corresponding to the sample close to base temperature and the sample in normal state, above T_C, respectively:

$$G = f(T \to 0) - f(T > T_C) \quad (3.55)$$

If, however, the normal state susceptibility has a finite value due to the electromagnetic skin depth contribution (Eq. 3.46), the frequency value for $T > T_C$ will be higher than the empty resonator value f_0. Considering that typical TDO frequencies are in the MHz region, the skin depth is expected to have small values compared to sample dimension, thus, for $\delta \ll R$, from Eq. 3.46 we can write:

$$\chi_{skin} \approx -\left(1 - \frac{\delta}{2R}\right) \quad (3.56)$$

Making use of Eq. 3.44, the difference in frequency value $f(T > T_C) - f_0$ caused by the skin effect can be estimated. Consequently, the alternative method of estimating the calibration factor can still be applied if the resistivity value of the normal state is known (Eq. 3.45).

3.6. Flat coils based TDO for measuring the in-plane penetration depth

In the previous section we have shown that the TDO method can conveniently be used to investigate the relative temperature variations in London penetration depth. The fact that it is a resonant method, combined with the great sensitivity of frequency counters, implies that minute changes in penetration depth can be detected with reported values as small as 1 Å [24, 101].

The resolution of the method is dependent of a number of factors. Looking at the expression in Eq. 3.53, we can see that larger values of the effective dimension R of the sample will results in larger frequency variations. Recalling the expression for R from Eq. 2.22, considerable increase in $\Delta\lambda(T)$ measurement resolution can be obtained considering large surface samples. Moreover, from the expression for G in Eq. 3.54, we can see that the same effect can be achieved by considering thinner samples which would increase the demagnetization factor. Consequently, the use of flat slab shaped samples can significantly improve the resolution of the technique. Just so it happens most HTC superconductors are layered structures which can be cleaved to result in thin specimens, which is also the case of our samples, as we will mention in more detail in Chapter IV. These layered superconductors are anisotropic meaning that the field penetration is dependent on orientation in respect to the sample's crystalline structure. We mentioned the effects of field orientation in Chapter II where we showed that, depending on the direction of the applied field, the effective susceptibility can be the result of a contribution from the in-plane London penetration depth and the out of plane correspondent. If the applied field is perpendicular to the surface of the sample (layer planes), the measured susceptibility changes are related only to the in-plane penetration depth λ_{ab}.

Apart from the sample geometry, we can we improve the resolution of the TDO technique for London penetration depth measurements in flat specimens by adapting the geometry of the inductor to increase the sample-coil filling factor $k = V_S/V_C$. Coils with volume close to the sample volume should promote larger measured frequency shifts. However, in relating the frequency variation to the in-plane penetration depth changes alone, the excitation field produced by the coil should be perpendicular to the sample surface. Moreover, simple analytical expressions like the one in Eq. 3.53 can only be used if the probing field of the coil is uniform in the sample region.

Solenoid inductors are most commonly used since they will accomplish these conditions however, for flat samples the filling factor is very small. An example is illustrated in Fig. 3.8(a) where we show the magnetic field density distribution for a disk shaped sample inside a solenoid inductor. The left side of Fig. 3.8 depicts the field distribution for the case when the sample has zero susceptibility (empty coil) while the right panel shows the case of a strong diamagnetic specimen.

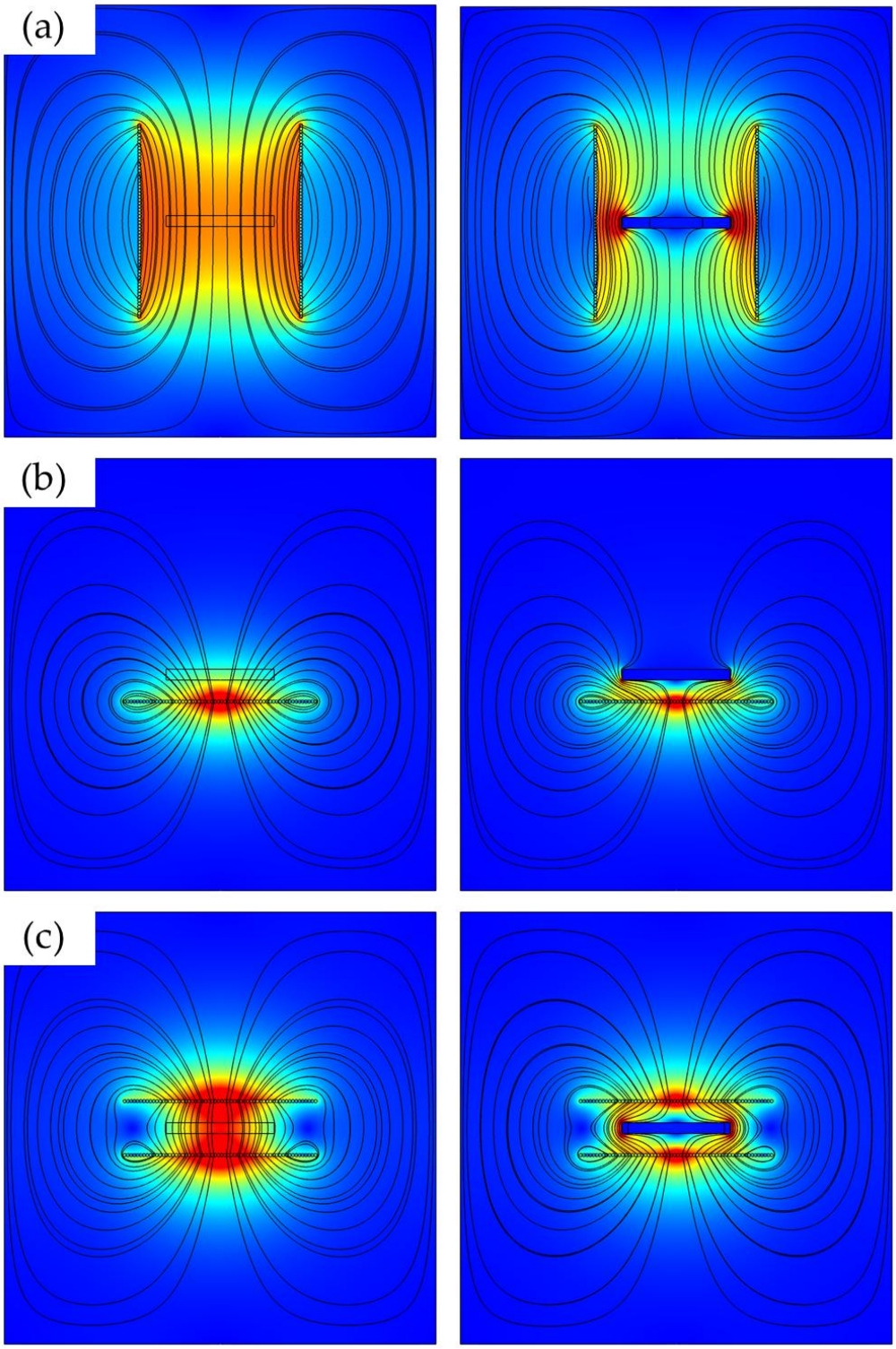

Figure 3.8 COMSOL simulations of magnetic field lines and flux density distribution in a cross section of an axially symmetric sample-coil geometry for the case of (a) solenoid inductor, (b) planar inductor, and (c) parallel pair of planar inductors. The disk shaped sample has zero susceptibility (left) and diamagnetic susceptibility close to unity (right).

It is easy to see that the field is indeed perpendicular to the surface of the sample; however, uniformity is achieved if the sample is constrained to a small central region of the coil or if long solenoids are used. In either case, the filling factor is considerably reduced for thin slab shaped samples.

A significant increase in TDO resolution for flat specimens can be achieved by making use of planar inductors like the ones suggested in [132, 133]. An example is illustrated in Fig. 3.8(b) where a disk shaped sample is placed near a flat spiral coil. We can see from the right panel of Fig. 3.8 (b) that, when the material is diamagnetic, the field distribution around the coil is significantly modified by the sample. Consequently, the inductance value shifts caused by the sample will be significant. Moreover, since spiral coils have significantly lower inductance values compared to solenoids, the relative inductance changes are higher. However, the complicated field distribution for an empty single flat coil makes it difficult to extract quantitative information. It is easy to see from the left side of Fig. 3.8 (b) that the field is neither uniform nor perpendicular to the sample. Moreover, for anisotropic superconductive samples, the resulting TDO frequency changes will be a result of both λ_{ab} and λ_c contributions to the susceptibility.

For measuring the in-plane London penetration depth λ_{ab} of our flat-like samples, we considered using pairs of planar inductors in a parallel configuration like in the case illustrated in Fig. 3.8(c). Looking at the left panel, we can see that, by using an additional flat circular coil, in a symmetric geometry with respect to reflection across the center plane of the sample, the field of the empty inductor is perpendicular to the sample surface and uniform within a significantly large central region of the coil volume.

We have shown in the previous section that the TDO frequency changes are directly proportional to the changes in the in-plane London penetration depth. For flat like specimens, the proportionality relation in Eq. 3.53 was obtained considering a uniform excitation field perpendicular to the sample surface in normal state which, as we have shown, stands true regardless of the geometry of the inductor creating the field. To make use of the increased filling factor provided by planar inductors, hence the sensitivity of our measurements, while providing a uniform and perpendicular field in the region of the sample in normal state, we used the pair configuration of planar inductors for our TDO setup.

Planar rectangular spiral coils, 8 x 8 mm^2 is size, were milled on a copper clad printed circuit board (PCB) with 1oz copper thickens (1.4 mils = 35μm). Using a LPKF Protomat S43 milling machine with a minimum milling tool diameter of 0.1 mm and 0.5μm translation resolution, we were able to build rectangular spiral coils with 3 turns/mm and a total of 12 turns. A magnified image of one such spiral coils is shown in Fig. 3.9. A 0.2 mm hole was drilled in the center pad of the coils to allow for lead attachment. A thin copper wire was soldered onto the center pad and the soldering joint (inset of Fig. 3.9) was trimmed to a minimum height. The coils were cleaned and covered with a thin layer of GE varnish to

prevent oxidation of the copper tracks. The typical series inductance and resistance values of the individual coils were 0.62 μH and 0.64 Ω respectively, as measured by an Agilent 4263B LCR meter. The coils were then connected in aiding parallel, in a geometry with reflection symmetry about the halfway plane, separated by a 2.7 mm gap (as measured from the copper track surface). The choice of parallel connection, as opposed to series, was made to provide a lower total inductance of the resulting coil which would boost the relative TDO frequency changes induced by a magnetic sample. The measured series inductance and resistance values for each resulting coil pair were around 0.39 μH and 0.32 Ω respectively.

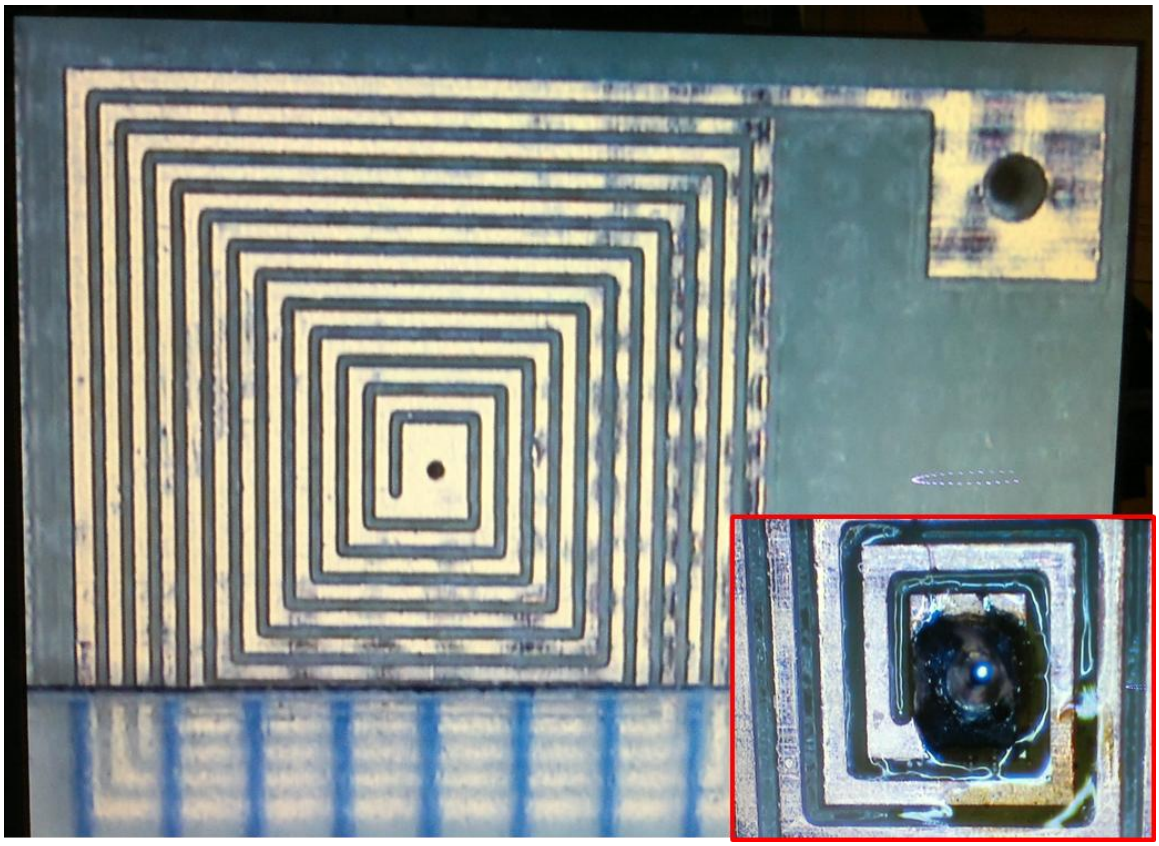

Figure 3.9 Picture of one of the 8 x 8 mm^2 flat spiral coils with 3 turns/mm milled on a copper-clad laminate 1oz PCB. Inset: soldering joint for the center lead.

Our superconductive samples for in-plane London penetration depth measurements (detailed in Chapter IV) are flat shaped single crystals with rectangular cross section and high aspect ratios (typical dimensions 2 x 2 x 0.1 mm). If the sample is positioned midway between the two planar inductors, with the *ab* crystallographic plane parallel to the surface of the flat coils (Fig. 3.10), considering the symmetry

of our setup and the small thickness of the samples relative to the coil gap, the probing ac field is expected to be parallel to the *c* axis of the crystal. Consequently, supercurrents are only induced in the *ab* plane, thus the measured changes in TDO resonant frequency are solely due to the variations in λ_{ab}.

To test for the perpendicularity as well as the uniformity of the field in the sample region, simulations were carried out for our specific coil-sample configuration, using the COMSOL Multiphysics software. The exact geometry used in the numerical simulations is depicted in Fig. 3.10. The coils geometry was directly imported from the Autodesk Autocad file used by the PCB milling machine for fabricating our planar inductors. The resulting 3D geometry was imported in COMSOL where the magnetic field distribution was calculated using the Magnetic Fields interface (right side of Fig. 3.10), assuming a uniform current density through the cross section of the coil tracks $j = 1/(0.2 \times 0.035)[mA/mm^2]$. The coil domain was assigned copper as the conductive material and air for the rest of the domains. We used the external current density approach to minimize the computational time. Since the current is oscillating at high frequencies, the current density is expected to be concentrated towards the surface of the conductor due to the skin effect. More precise calculations can be made using the frequency domain, however, the current density has to be computed before which, for 3D geometries, can take considerably more time. We have carried out simulations for both stationary and frequency domain studies and found that, for a 2D axially symmetric analog geometry, the differences in magnetic field values are negligible.

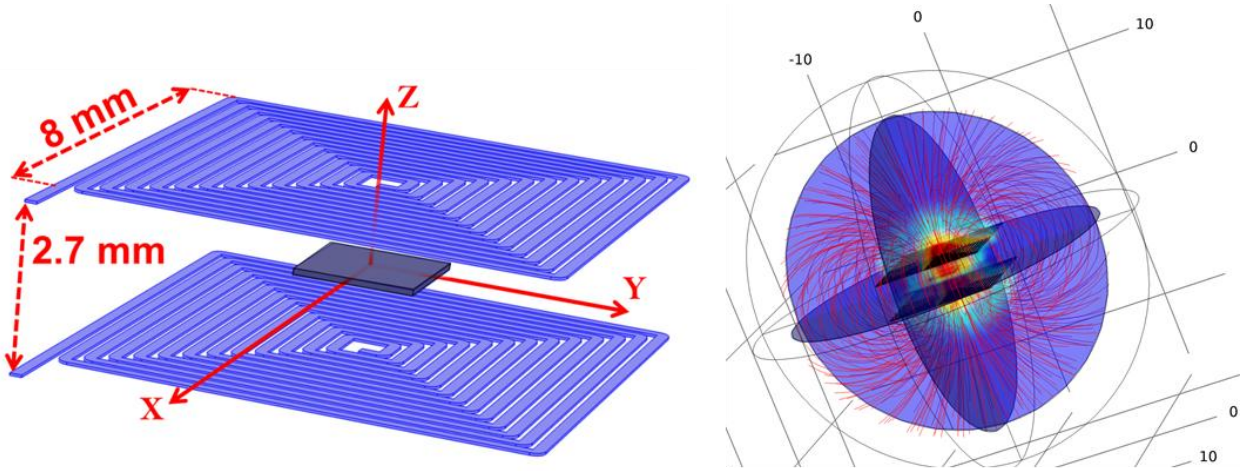

Figure 3.10 Left: Spatial arrangement of the coils and sample. The setup is symmetric with respect to reflection across the z = 0 plane. Right: COMSOL magnetic field simulations for the coil geometry

The simulated results obtained for the field lines and magnetic flux density distribution over the *y* = 0 and *z* = 0 cross sections of the setup for the normal state case of the sample (see left side of Fig. 3.10), are illustrated in Fig. 3.11.

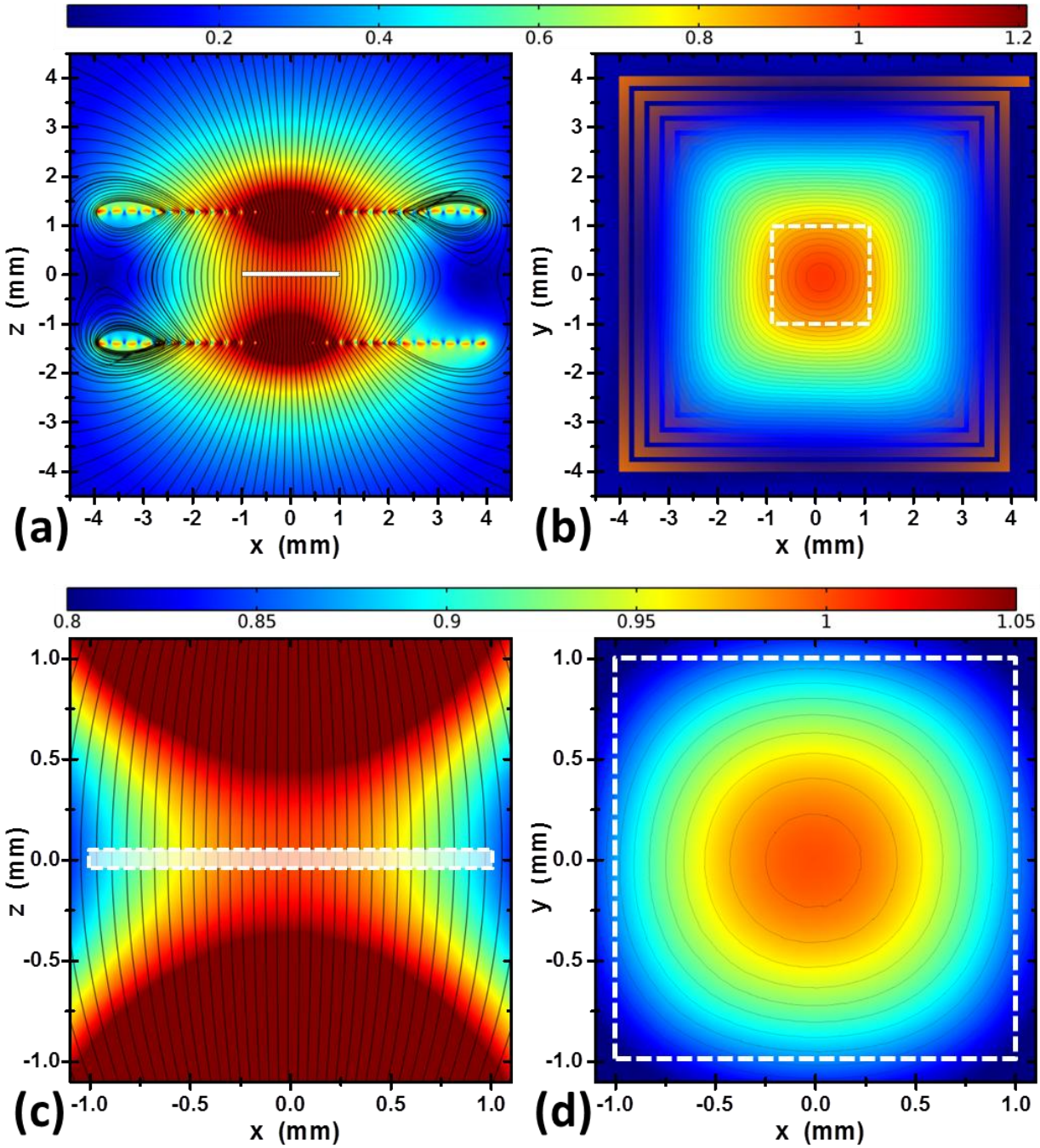

Figure 3.11 The simulated magnetic field distribution of our setup for the normal state of the sample. (a) Magnetic field lines and flux density distribution over the y=0 cross section of the setup (side view). (b) Flux density distribution over the z=0 cross section of the setup (top view). (c) Expanded view on the y=0 plane. (d) Expanded view on the z=0 plane. The white rectangles symbolize the domain of a 2*x*2*x*0.1 mm^3 sample. The color scale corresponds to the B field magnitude relative to its value in the center of the sample (0,0,0).

In panel (a) we show the magnetic field lines and flux density distribution over the $y = 0$ cross section of the sample-inductor setup (side view). In panel (b) the flux density distribution over the $z = 0$ cross section of the setup (top view). Panel (c) and (d) show an expanded view of the $y = 0$ plane and the $z = 0$ plane, respectively. The white rectangles symbolize the sections of a $2 \times 2 \times 0.1$ mm^3 sample. The color scale corresponds to the B field magnitude relative to its value in the center of the sample (x=0, y=0, z=0). The results confirm that the probing field from the coils is indeed perpendicular to the *ab* surface of the sample [Fig. 3.12(c)] and that in a central rectangular region of dimensions comparable to the sample size, the magnitude of the field is homogeneous with ~90% uniformity [Fig. 3.12(d)] i.e. the average value of the field across the surface relative to the center value is ~0.9. For the 1mA coil current used in the simulation, the calculated magnitude of the field in the center of the geometry is around 20 mOe.

3.7. Experimental TDO setup in a dilution refrigerator

To measure the temperature dependence of the in-plane London penetration depth of our samples we constructed four similar tunnel diode oscillator circuits using the flat coils in the parallel configuration described previously. The circuits were mounted in a Janis Model JDry-500 cryogen-free He_3 - He_4 Dilution Refrigerator System, capable of reaching a base temperature of 8mK with a cooling power of 450 µW at 100 mK. We describe next the experimental setup used for the measurements detailed in Chapter V.

The electronic diagram of our TDO circuits showing the values of the components used is illustrated in Fig. 3.12 below.

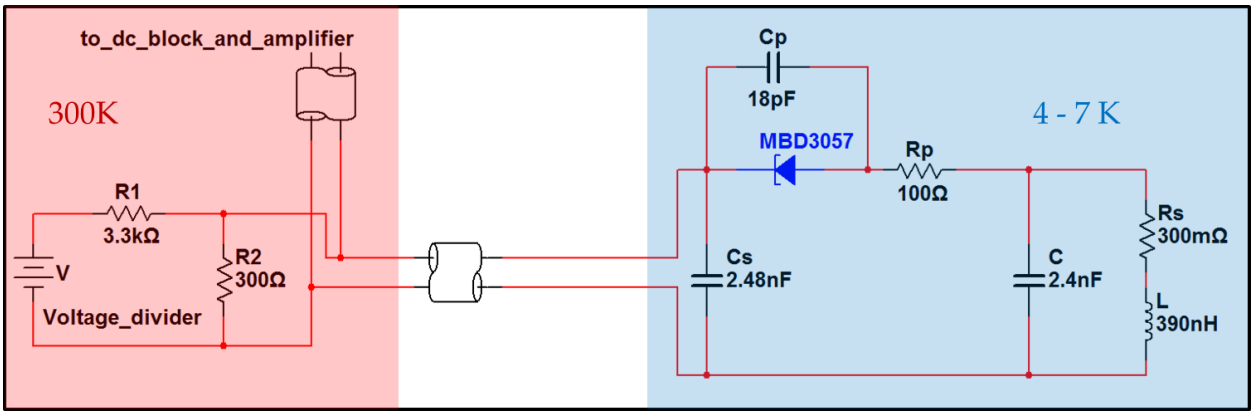

Figure 3.12 Electronic diagram for our TDO circuit used in the dilution refrigerator setup

The voltage divider was constructed inside a shielding metal enclosure with SMA connectors and was kept at room temperature, outside the dilution refrigerator (DR) system in order to prevent unnecessary heating of the system from ohmic losses. The power supply, a Keithley 2400 Source Meter, was connected to the voltage divider by coaxial cables with SMA connectors. The rf signal was extracted from an additional SMA port on the voltage divider enclosure, passed through a BLK-89-S+ 50Ω dc block circuit and amplified using a ZFL -1000LN Mini-Circuits amplifier. The frequency of the signal was measured with an Agilent 53131A Universal Frequency Counter. All the connecting cables are 50 Ω, high frequency coaxial cables, sharing the same common ground as the DR. No additional signal filtering systems were used. The output bias dc voltage to the tunnel diode is passed from room temperature to a separate TDO stage through a single path made up of a series of coaxial cables. The same path is used to carry out the rf signal from the TDO to the room temperature electronics.

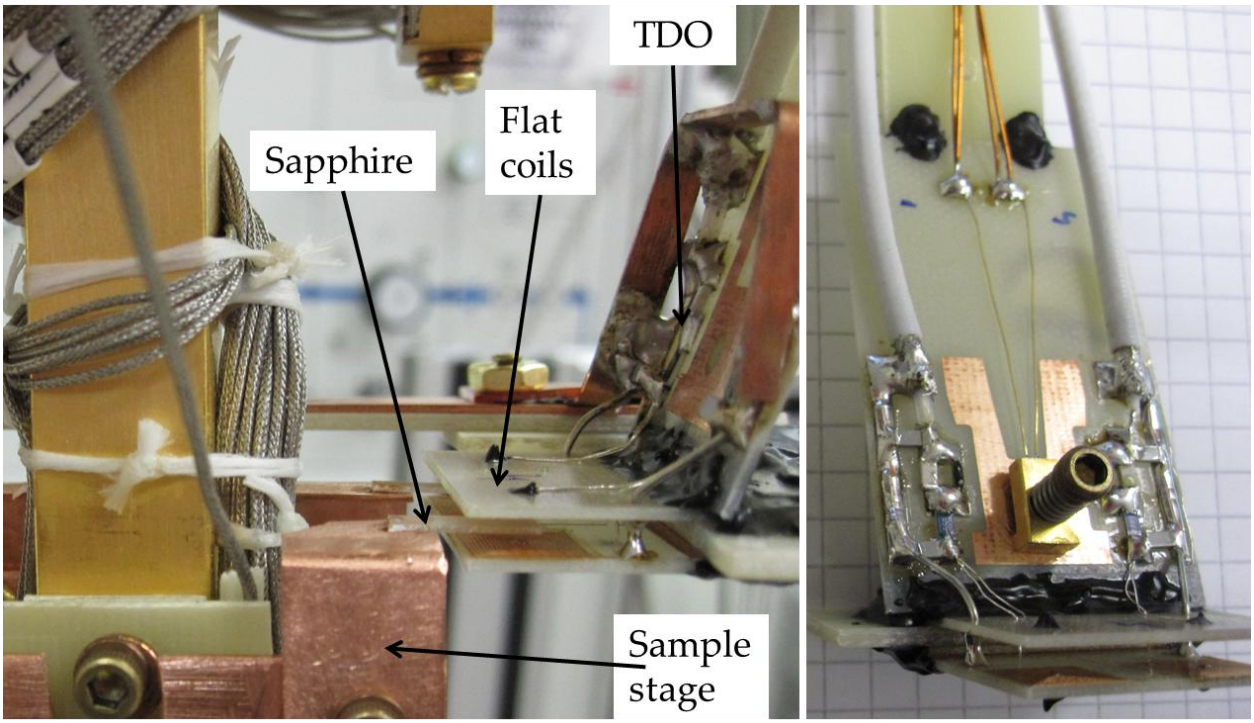

Figure 3.13 Left: Sample and TDO stage in our dilution refrigerator setup. Right: Picture of two flat inductor based TDO circuits used in our experiments. In the center we have a CERNOX thermometer to monitor the temperature of the circuits.

The rest of the TDO components, including the planar inductors, are mounted on a separate stage near the cold finger of the DR. A picture of the flat inductor based TDO circuits stage used in our

experiments is shown in the right panel of Fig. 3.13. Most commercial lead-tin solders become superconductive at relatively high temperatures (4-8 K) [114] meaning they lose thermal conductivity. S200 solder (96.5% Tin, 3.0% Silver, 0.5% Copper) is an alloy which is superconductive at lower temperatures than the TDO temperatures we are interested in (4-7 K).The SMD components are soldered onto a PCB board using S200 solder in order to ensure thermal contact between them. The coaxial cable providing the dc bias voltage and carrying the rf signal is also used as the cooling/heating source for TDO components while a Lakeshore Cryotronics CERNOX thermometer is used to monitor their temperature.

The left side of Fig. 3.13 shows a picture of the sample and TDO stages of our experimental setup in the dilution refrigerator. The sample stage is made out of Oxygen-free high thermal conductivity (OFHC) copper sheets and is thermally decoupled from the cold finger of the DR using G10 thermally insulating glass epoxy sheets. The samples are mounted using Apiezon N grease onto single crystal sapphire sheets, 1cm long, 2-3 mm wide and 0.5 mm thick. One end of the sapphire substrate is connected with GE varnish to the sample stage copper with the top surface of the crystals in the middle plane of the flat coils. At the other end the sample is placed in such a way that it is in the center of the TDO coils. A Lakeshore Cryotronics ruthenium oxide RX-102B-CB thermometer is used to monitor the temperature of the sample stage. A heater with nominal resistance of 100 Ω is connected to the sample stage which is used to increase the temperature of the samples. The cooling power is provided by a 10 cm long 30 AWG copper wire connecting the sample stage to the cold finger. When all the He_3 - He_4 mixture in the system is circulating, the base temperature of the cold finger is around 10 mK. Heating the cold finger directly causes the liquid mixture to boil around 0.8 K thus, in order to achieve higher temperatures most of the mixture has to be removed. The thermal decupling of the sample stage from the cold finger described above, allows us to heat up the samples to 5-8 K while maintaining the cold finger below 0.8 K. Moreover, when mixture is removed, it allows us to heat up the samples to temperatures as high as 20 K without significant heating of the upper stages.

We have shown is Section 3.4 how temperature variations can affect the stability of the resonant frequency. Under the circumstances, a great deal of care was taken to maintain the TDO circuit components at a constant temperature. Moreover, the temperature of the TDO must be independent of temperature of the sample. Consequently, the TDO stage is physically separated from the samples to achieve thermal decoupling.

In Figure 3.14 we show a schematic representation of the TDO setup in our dilution refrigerator. There are two TDO stages, each containing a pair of TDO circuits, on opposite sides of the cold finger. Half inch wide, 3/32 inch thick G10 plastic sheets are used to mechanically hold the TDO stages and at the same time minimize thermal transfer to the other DR stages. They also provide the mechanical support for the coaxial cables connecting the circuits.

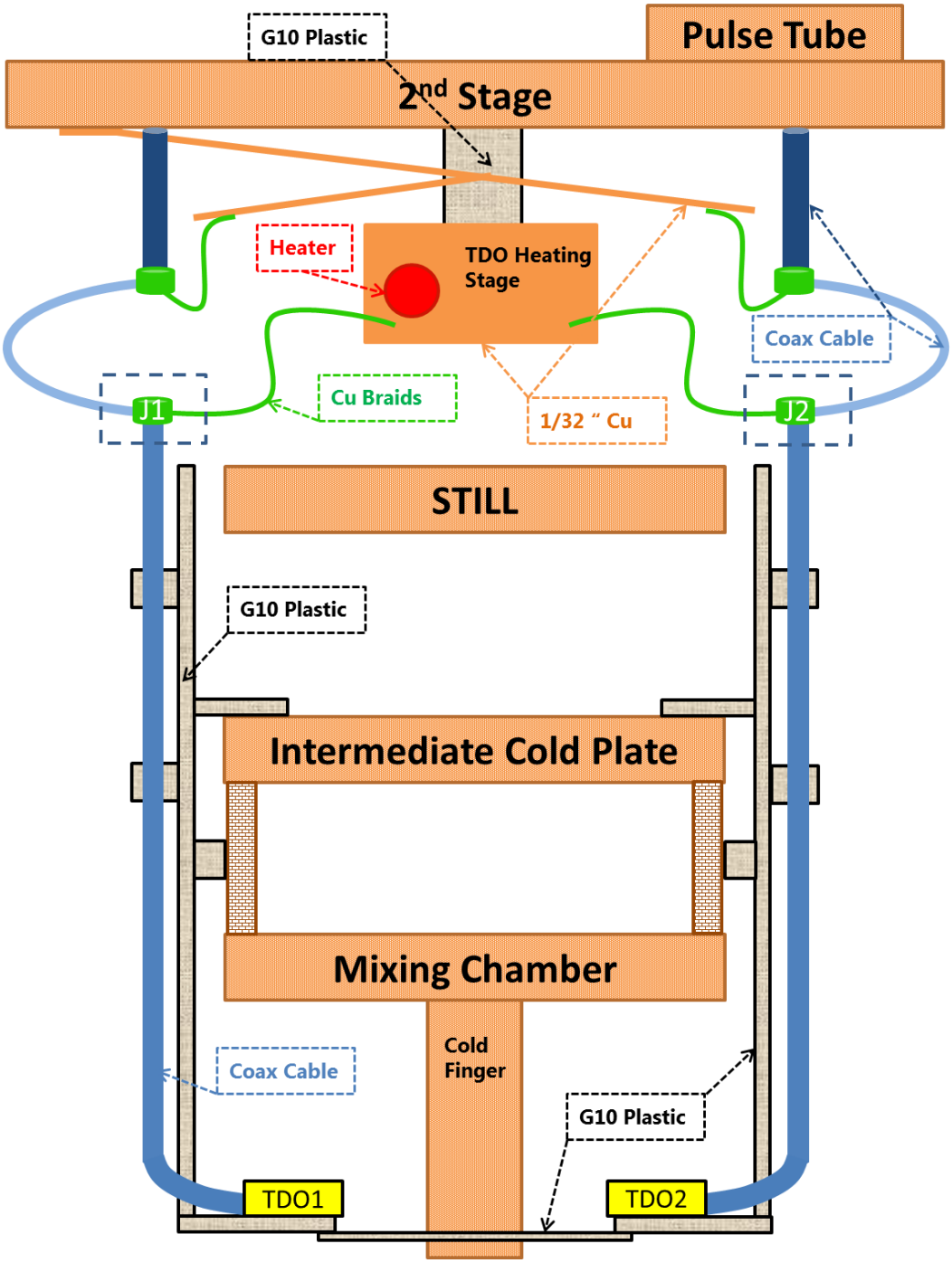

Figure 3.14 Schematic representation of our TDO experimental setup for penetration depth measurements in a dilution refrigerator

The G10 sheets are connected in two points above the mixing chamber, including an additional mechanical bridge between to two TDO stages to minimize vibrations of the coils about the sample position. The shielding of the four RG-316 DS coaxial cables connected to the TDO circuits is made from braided copper wire and it provides the cooling/heating path for the TDO stage i.e. the temperature of the

TDO components will be the same as the temperature of the cables. The only stage with relatively constant temperature in our system, invariant to changes in the temperature of the lower stages, is the 2nd stage which is cooled below 4K by a Pulse Tube cryo-cooler.

This makes our dry system different from liquid cryogen systems where a liquid helium bath is needed to cool the system down to 4K which also provides a constant temperature stage. Although more cost effective, using a pulse tube will cause the temperature of the 2nd stage to fluctuate. In our system the fluctuations can be as high as 0.1K while the temperature can vary between 2.7 K (when the cold finger is at base T) to 6K (when the cold finger is at 20 K). Thermalizing the TDO stages directly to the 2nd stage would cause the direct transfer of such thermal fluctuations to the TDO stage temperature and generate inconsistencies in measured frequency.

We control the temperature of the TDO circuits by controlling the temperature of the top ends of the coaxial cables (joints J1 and J2 in Fig. 3.14). The cooling power is provided by the second stage. To dampen temperature fluctuations originating from the pulse tube, 20 cm long copper sheets are used to connect one point (further from the pulse tube anchoring) on the 2nd stage, via a set of 10 cm copper braids, to four 6 inch thin RG-58 coaxial cables. The top end of the thin coaxial cables is connected (via SMA connectors) to the high frequency cables coming from room temperature through the 2nd stage. The bottom end of the thin coaxial cables is connected the top joints (top ends of the coaxial cables coming from the TDO) via SMA connectors. Thus, creating a long physical path from the cold point on the 2nd stage to the joints, the cooling power fluctuations are minimized.

The heating of the joints is obtained by thermally anchoring the joints to a TDO heating stage using 10 cm copper braids. The heating stage consists of a copper sheet attached right below the 2nd stage using thermally insulating G10 plastic in order to avoid heating the entire the 2nd stage when heating the joints (and consequently the TDO stages). The TDO heating stage contains a 50 Ω cartridge, which, together with the CERNOX thermometer used to monitor the temperature of the TDO components, is used to control the temperature of the circuits. Using the proportional derivative integral (closed PID loop) option of a Lakeshore Cryotronics LS370 Resistance Bridge, the same bridge used to measure all the resistive thermometers in our experiment, the temperature of the TDO can be stabilized anywhere between 3 K and 7 K with 0.2 mK accuracy.

The typical TDO frequency of our setup with empty coils is ~ 5.9 MHz. The resonant frequency versus temperature for our TDO circuits is plotted in the left panel of Fig 3.15. It is easy to see that a 3 K variation in TDO temperature corresponds to ~10 kHz variation in frequency, however, at lower temperatures the resonant frequency is less temperature dependent. In our measurements, the TDO temperature is maintained constant at 3.7 ± 0.0002 K making the changes in resonant frequency solely related to changes in susceptibility of the sample. In our London penetration depth measurements the

temperature of the sample is varied slowly in time (typical rates 0.02 K/min) and the frequency is measured within a 7 seconds time count frame. The typical noise in measured frequency is around 0.5 Hz with no detectable drift over the time period of our measurements (few hours).

Since the coils are in relative close proximity, to avoid inductive coupling of the frequencies, only one circuit is powered at a time. We have shown in Section 3.3 the TDO resonant frequency is strongly dependent on tunnel diode bias voltage. Consequently, fluctuations in dc voltage can generate additional noise in measured frequency value. However, we showed that the frequency dependence on applied voltage (bias voltage for the tunnel diode) reaches a maximum where the frequency becomes impervious to small fluctuations in bias voltage. By selecting the supply voltage corresponding to a maximum in frequency, the noise in frequency resulting from voltage fluctuations can be minimized.

In our practical application of the TDO however, there is no unique maximum frequency voltage. As the susceptibility of the sample changes, the maximum of the frequency vs. voltage curve changes as well. We illustrate such an example in the right panel of Fig. 3.15, where the resonant frequency of our TDO was measured as a function of applied dc voltage for the case of superconductive sample in Meissner state and normal state respectively.

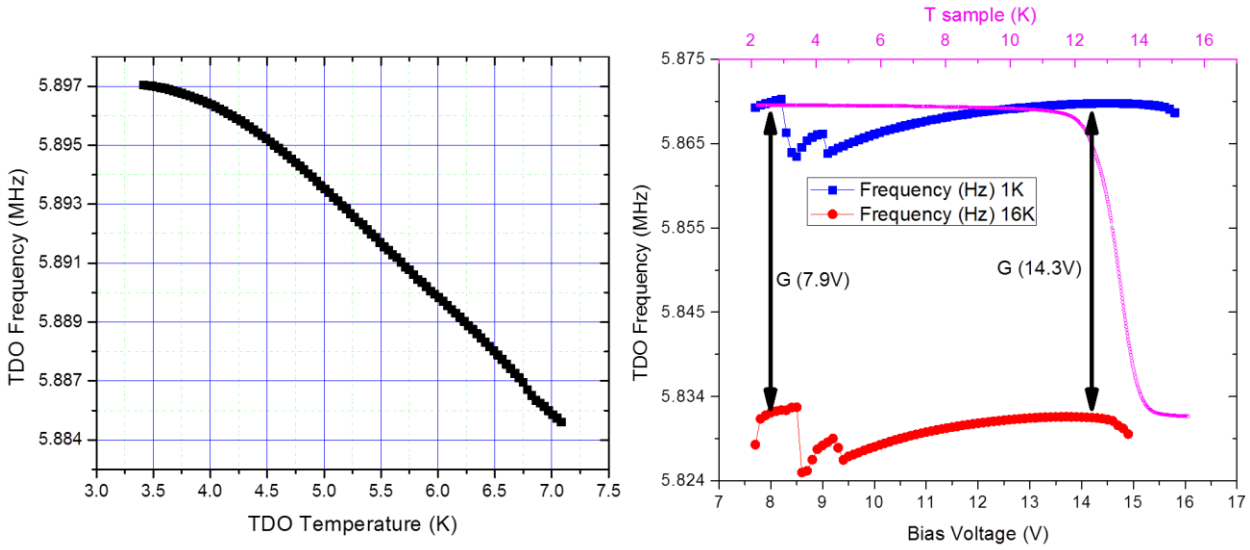

Figure 3.15 Left: Low temperature dependence of our TDO frequency. Right: TDO frequency versus bias voltage for a superconductive sample in Meissner state (blue curve) and normal state (red curve). The recorded superconductive transition $f(T)$ of the sample for 13 V applied dc voltage is superimposed.

It is easy to see that, the measured frequency exhibits a maximum for a certain applied dc voltage, however the maximum frequency voltage value corresponding to different inductance values (different

sample states) is slightly different. When measuring the temperature dependence of the frequency shift induced by changes in the susceptibility of our superconductive samples (we show an example of measured TDO frequency vs. sample temperature in the right panel Fig. 3.15), we selected the supply voltage corresponding to the maximum frequency of the empty coil (normal state of the sample). In this manner, by cooling the sample into a Meissner state, the bias voltage will always be less than the value for maximum frequency. This is necessary as larger bias voltages can cause oscillations to die out.

As previously detailed (Section 3.5) estimating the calibration factor G for London penetration depth investigation from TDO measurements, can be easily obtained by taking the difference between the frequency value at lowest temperature of the sample (Meissner state) and the frequency of the empty coil (or for normal state of the sample) (Eq. 3.55). This is obviously appropriate if the temperature effects and the influence of applied voltage are neglected. Keeping the bias voltage and temperature of the TDO constant is required for a precise estimation of G, however, slight unavoidable misestimations could arise from the difference in frequency vs. voltage dependence at the two distinct sample susceptibility values (Fig. 3.15).

Chapter 4

Iron Based Superconductors

4.1. Overview of iron based superconductors

The research for transparent semiconductors by the Tokyo Institute of Technology group of Hideo Hosono has led to the coincidental discovery of superconductivity at 4 K in LaFePO. Although the finding was reported in 2006 [55], the low transition temperature of the compound rendered the discovery generally unnoticed until 2008 when the same group, upon replacing phosphorous with arsenic and doping the oxygen site with fluorine, published a paper announcing superconductivity at 26 K in $LaFeAsO_{1-x}F_x$ [56]. Over the years scientists have avoided ferromagnetic compounds as building blocks for superconductive materials due to antagonistic relationship between ferromagnetism and superconductivity however, superconductive materials containing Fe were not unheard of. The 1.8 K superconductivity of Th_7Fe_3 [153], the heavy fermion U_6Fe with $T_C = 3.9$ K [154], the first the first molecular superconductor containing paramagnetic metal ions β″-(bedt ttf)$_4$ [$(H_2O)Fe(C_2O_4)_3$]·PhCN with a superconducting transition at 8.5 K [155] are just a few examples. Even Fe itself, the most known ferromagnetic element, is superconductive at 1.8 K albeit under high pressures [156].

What came as a surprise was the discovery of an iron-based superconductor with a high critical temperature. This seminal paper of Kamihara *et al.* [56] marked the starting point of a new era in superconductivity and triggered a renewed interest in superconductor physics community making it the most cited science topic of 2008 with over 5000 citations today. Soon following this discovery, an increasing number of Fe based superconductors with higher and higher transition temperatures have been reported on. The current T_C record was set in the same year when C. Wang *et al.* reported on the superconductivity at 56 K observed in $Gd_{1-x}Th_xFeAsO$ [157].

The tremendous interest in Fe based superconductors is based on a number of reasons. One, the story seems strikingly similar to the discovery and development of cuprates. Since the first report in 1986 on the superconductivity of Ba−La−Cu−O system at 35 K [3] the transition temperature has continuously increased with the cuprates holding the record for highest T_C. A similar development is now observed in Fe based superconductors and, in the hopes that history will repeat itself, iron based materials are perceived as the next generation of high temperature superconductors. Many of their characteristics seemed similar to the ones of cuprate superconductors leading researcher to believe that the mechanism behind superconductivity is similar. However, as further work has shown, there are important differences

between Fe based materials and cuprates [13]. Consequently, another reason for the interest in iron based superconductors stems from their basic physics. As a new class of unconventional superconductors they could hold the key to finally uncover the superconducting pairing mechanism responsible for high T_C and may lead the way to increase the critical temperature to the ultimate goal value of the field that is room temperature superconductors. Although the pairing mechanism behind their superconductivity is still elusive, as in the case of cuprates, a large amount of evidence points to magnetic spin fluctuations in iron based superconductors. Consequently, they may help shed some light on the interplay between magnetism and superconductivity.

There are over 50 different superconductive Fe based compounds discovered to date. These include two broad classes of materials, iron pnictides and chalcogenides. Despite exhibiting different behavior and properties, the iron chalcogenides and pnictides share common structural properties. They all exhibit a layered structure based upon a planar layer of Fe atoms joined by tetrahedral coordinated chemical element in group 15 of the periodic table known as pnictogens (P, As) or from group 16 chalcogens (S, Se, Te) anions arranged in a stacked sequence separated by alkali, alkaline earth or rare earth and oxygen/fluorine "blocking layers". There are six unique tetrahedral crystallographic structures shown to support superconductivity [13]. The six families are named based on the stoichiometry of their parental prototypes whose structures are illustrated in Fig. 4.1. I will briefly introduce each different crystalline structure of iron based materials in the order of their discovery.

The 1111-type family includes the first discovered iron based superconductors LaFePO [55] and $LaFeAsO_{1-x}F_x$ [56], whose structure is shown in Fig. 4.1(a), and it is the representative structure for the highest T_C members known today like $NdFeAsO_{1-y}$ (54 K) [158], $SmFeAsO_{1-x}F_x$ (55 K) [159] and $Gd_{0.8}Th_{0.2}FeAsO$ (56.3 K) [160]. The 122 family is the second type to be discovered and is represented by the $BaFe_2As_2$ parent structure in Fig. 4.1(b) which upon K hole doping exhibits a maximum transition temperature of 38 K [161] and upon electron doping $Ba(Fe_{1-x}Co_x)_2As_2$ with a T_C of 22 K [162]. The same family includes $EuFe_2(As_{1-x}P_x)_2$ with $T_C = 26$ K [163] and $Ba_{1-x}Na_xFe_2As_2$ with maximum $T_C = 34$ K [164]. The next family to be discovered is the 111-type represented by the LiFeAs structure in Fig. 4.1 (c) with $T_C = 18$ K [165] and includes NaFeAs which is superconductive below 9 K [166]. The 11-type family has the simplest structure and is represented by the iron chalcogenides FeSe (Fig. 4.1 (d)) and FeTe and their ternary combination $FeTe_{1-x}Se_x$ including $FeTe_{1-x}S_x$. The FeSe compound has been found to be superconductive at approximately 8 K [167] and up to 37 K under pressure [168] which upon Se substitution with Te the critical temperature T_C is increased to a maximum of about 15 K [169]. The fifth structure is the so-called 21311 (or 42622) structure with Sr_2ScO_3FeP exhibiting superconductivity at 17 K being the first member found [170] whose crystal structure is depicted in Fig. 4.1 (e). Replacing Sc with Cr or V, and P with As, T_C was increased up to 37 K in $Sr_2VOFeAs$ [171] and up to 39 K in

$Sr_2Mg_{0.2}Ti_{0.8}O_3FeAs$ [172]. The most recent structure discovered is represented in Fig. 4.1 (f) by $K_{0.8}Fe_{1.6}Se_2$ exhibiting superconductivity around 32 K [173] and is an ordered defect alteration of the 122 structure called the 122* structure [13]. The same structure applies to Rb, Cs and Tl replacing K materials with 32.5 K superconductivity in $Rb_{0.8}Fe_{1.6}Se_2$ single crystals reported by C.H. Li *et al.* (2011) in [174].

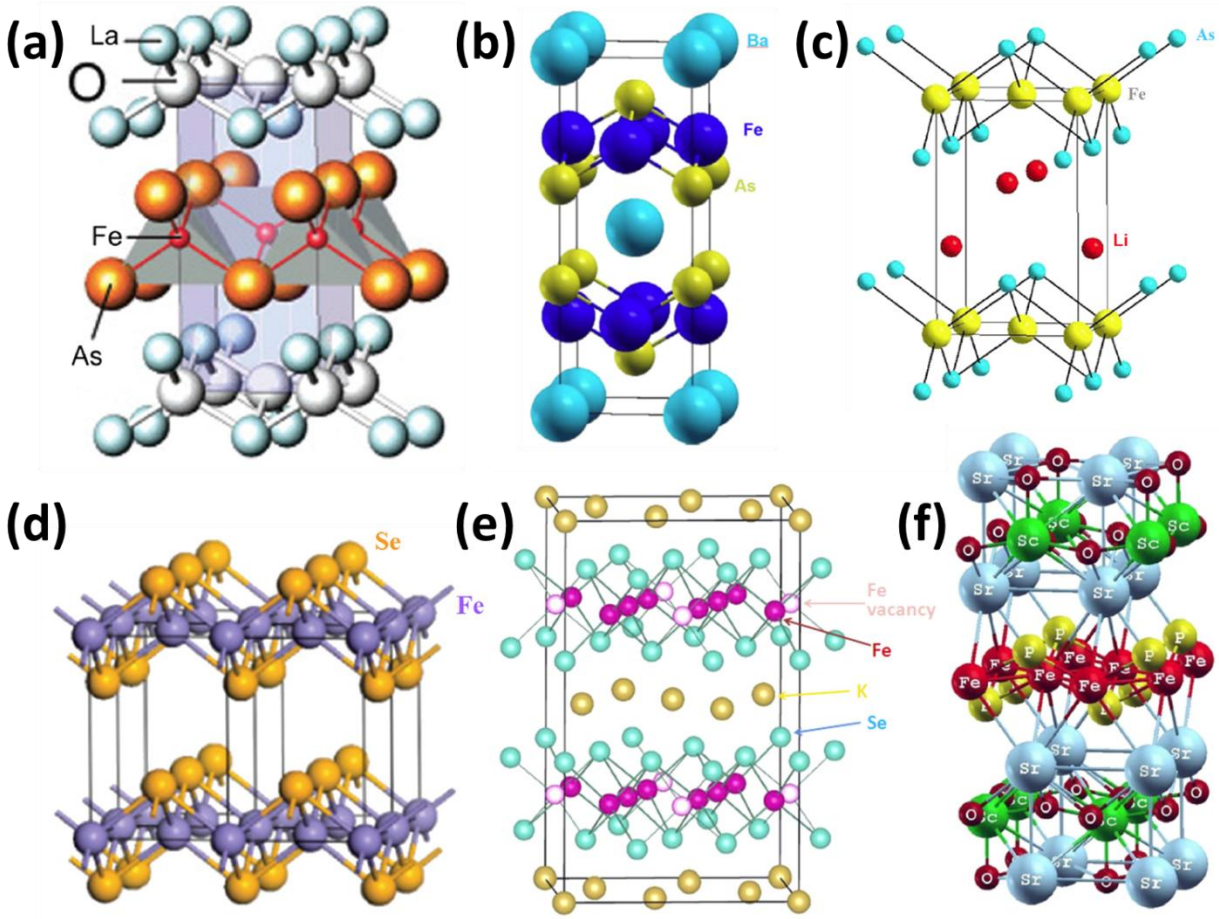

Figure 4.1 The six representative lattice structures known to support superconductivity in iron based materials: (a) 1111 structure of $LaFeAsO_{1-x}F_x$ from [56]; (b) 122 lattice structure of $BaFe_2As_2$ from [175]; (c) 111 lattice structure of LiFeAs from [176]; (d) 11 lattice structure of FeSe from [167]; (e) the 21311 lattice structure of Sr_2ScO_3FeP from [175]; (f) the 122* structure of $K_{0.8}Fe_{1.6}Se_2$ from [177].

All iron based superconductive compounds share similar electronic band structure in which the electronic states at the Fermi level are occupied predominantly by the 3d electrons of Fe. Since all iron based superconductors share a similar Fe lattice structure it is expected that the topology of the Fermi surface will have common features. Unlike the case of cuprates, the band structure from density

functional theory calculations for Fe based superconductors [178-181] and supported by angle resolved photoemission spectroscopy experiments [182-184] show that the Fermi topology consists of two small cylindrical hole pockets centered around the (0,0) point and two electron pockets centered around the (π,π) points in the folded Brillouin zone [185]. A simplified representation of the Fermi surface (FS) geometry that seems to be characteristic to iron based superconductors is illustrated in Fig. 4.2. The nearly perfect FS nesting between hole and electron pockets in many parent compounds suggests a static density wave with the nesting vector (π,π) as a way to lower the kinetic energy of the electrons [186] therefore, an antiferromagnetic spin density wave in those compounds is expected.

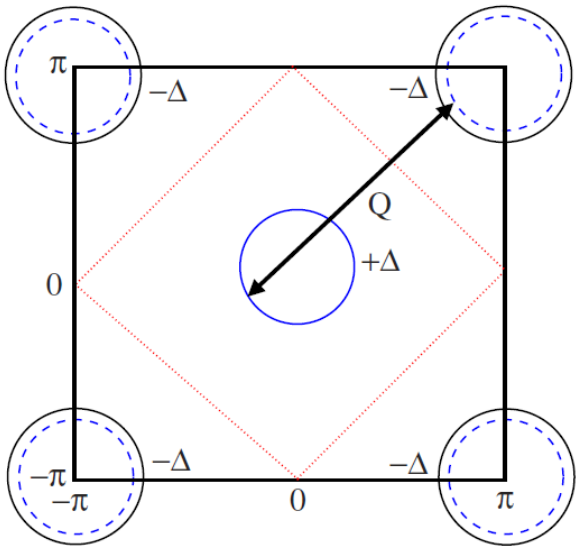

Figure 4.2 A simplified representation of the Fermi surface topology in iron based superconductors from [185]. For each (π,π) point the two cylinder like electron pockets are represented by the black curves while the hole pockets are represented by the blue curve centered around (0,0). Upon electron doping superconductive gaps Δ are formed at the two Fermi surfaces.

Upon electron doping, the size of the electron holes increases thus breaking the nesting resulting in the emergence of superconductivity and suppression of antiferromagnetic (AFM) order. This can be seen from the phase diagrams illustrated in Fig. 4.3 for a few representative iron based superconducting structures. Looking at the doping evolution of their magnetic and superconductive properties reflected in the phase diagrams, superconductivity seems to occur in close proximity of magnetic instabilities which lead to early speculations that Fe based materials are similar to the cuprate superconductors however, in contrast with the AFM Mott insulator behavior of the parent compounds of cuprates, the Fe

superconductors are spin density wave metals exhibiting itinerant AFM order where electrons appear to be more localized [187]. The nature of magnetism in the iron based parent compounds is a largely debated topic, mainly due to its implications in the superconductive pairing mechanism. The electronic structure suggests that the same magnetic interactions that support the AFM ordering may also be responsible for the pairing of electrons and superconductivity is most likely mediated by magnetic spin fluctuations [188].

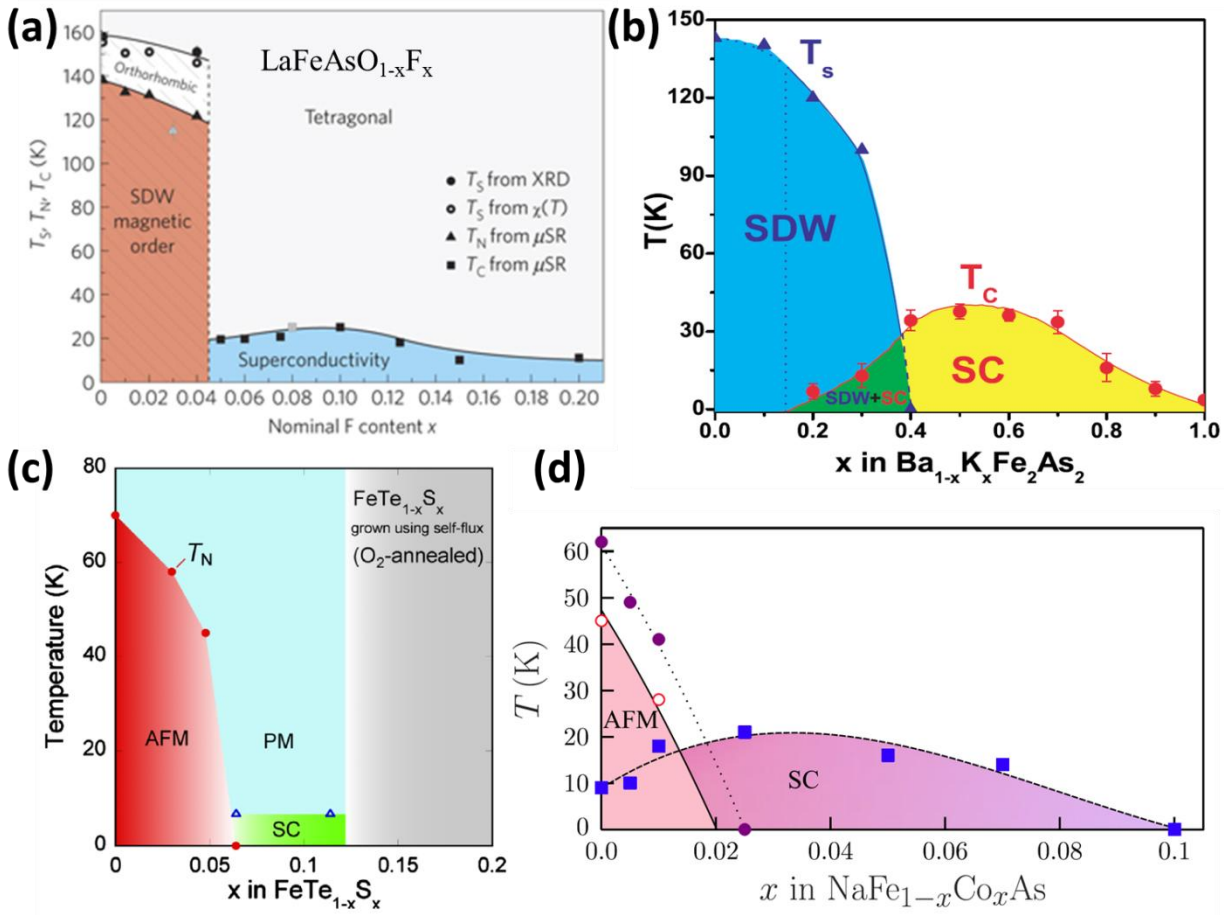

Figure 4.3 Composition-temperature phase diagrams containing the magnetic and superconductive properties of different families representative iron based superconductors: (a) $LaFeAsO_{1-x}F_x$ from [189]; (b) $Ba_{1-x}K_xFe_2As_2$ from [190]; (c) $FeTe_{1-x}S_x$ from [191]; (d) $NaFe_{1-x}Co_xAs$ from [192].

The pairing mechanism responsible with the high superconducting temperature of iron based materials is a highly controversial topic and like in the case of cuprates, its origin is still unknown. The conventional phonon mediated mechanism was quickly ruled out [12] although it is believed that phonon-electron coupling may play at least a partial role in the superconductivity of some iron based

superconductors [13, 14]. Most of the experimental evidence to date favors an unconventional pairing mechanism closely tied to magnetism. A variety of microscopic pairing models have been proposed [15, 16] most of them based on magnetic fluctuations. Thus an important step towards understanding the mechanism responsible for high T_C superconductors is investigating the superconductive order parameter symmetry from which different microscopic pairing models can be tested based on their association with different symmetry states. Although in cuprates the gap symmetry has been pin-pointed to d-wave type, the order parameter symmetry in iron based superconductors is a largely debated topic and presently under active research considering the experimental complexity of phase measurements and especially since there seems to be a non-universal symmetry describing iron based superconductors.

A large diversity of order parameters have been suggested including s-wave, d-wave, p-wave, and a variety of mixed symmetry states [193-196] but so far the leading candidates for gap symmetry in iron based superconductors seem to be the ones characterized by a change in sign of Δ at the Brillion zone e.g. an s-wave structure with isotropic gaps (s± symmetry) or anisotropic gaps and d-wave symmetry (Fig. 4.4).

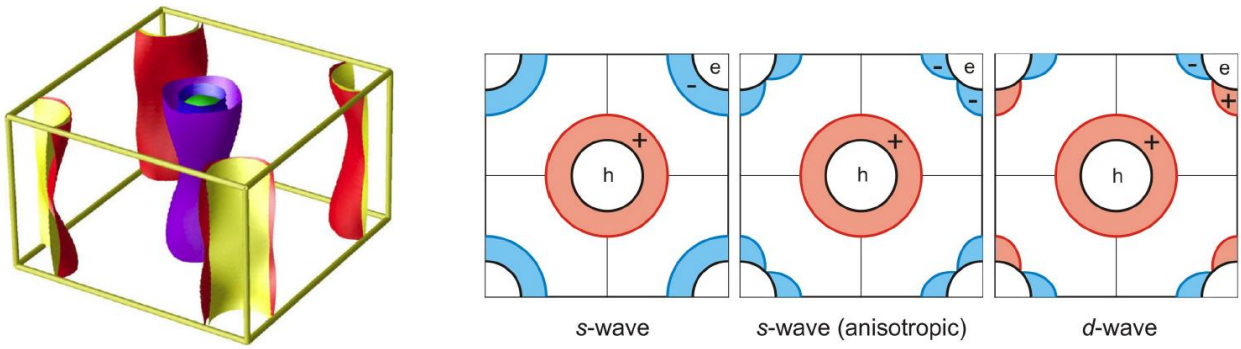

Figure 4.4 Left: Calculated Fermi surfaces of $BaFe_2As_2$. Right: Schematic picture of the two-dimensional momentum projection of the Brillouin zone of superconducting FeAs-based materials with multiple bands reduced to single hole (h) and electron (e) pockets. The proposed multi-band pairing gap symmetries, drawn as shaded regions on hole (red) and electron (blue) pockets, are shown for s± symmetry with isotropic gaps (left) and anisotropic gaps with accidental nodes on the electron pocket (middle), and for a d-wave symmetry (right). Image taken from [184].

A considerable amount of experimental results seem to support the s± symmetry as the leading candidate in iron based superconductors. In such a state, the superconductive order parameter (whose magnitude is proportional to the energy gap Δ) has one sign on the hole cylinders around the Γ point (zone center) of the Brillouin zone and opposite sign around the electron FS at the M points (zone

corners). This symmetry state can be very likely realized in a model where antiferromagnetic fluctuations are involved in the pairing interaction and implies that the pairing mechanism is repulsive at short distances and attractive at longer distances between electrons [197, 198]. Although the symmetry does not disclose the actual mechanism it can provide crucial information that would help determine its physical origin not only in Fe based materials but in all high temperature superconductors. As mentioned in Chapter I, the superconductive order parameter symmetry is directly involved in the temperature dependence of the London penetration depth. Measurements of $\lambda(T)$, constituting the main focus of my research, can provide valuable information about the superconducting symmetry of iron based materials.

Although the superconductive materials known as cuprates still hold the record for highest critical temperature (-139˚C) since their discovery in 1986, their ceramic texture and high manufacturing cost makes them impractical for a large number of technological applications [9]. As a consequence, superconductors for high-field application are still based on low-temperature superconductors. However, this year (2013) critical currents of an order of magnitude higher than typical superconductors have been reported in thin films of iron based superconductors [10]. Also, Fe based superconductors currently hold the record for highest critical field [11]. Their superior advantage over other materials makes them a genuine alternative in the production of high magnetic fields. From a theoretical perspective they could hold the key for the search of room temperature superconductors, an idea long believed to be impossible, which if brought to life, would revolutionize the technological world. The behavior in iron-based superconductors has still many open problems, as the distinct characteristics of these unconventional compounds introduce a new level of physical complexity. It is therefore essential to understand these materials better and to explore their unique properties.

4.2. The iron chalcogenide $Fe_{1+y}(Te_{1-x}Se_x)$

Amongst all iron based superconductors, the members of the 11-type family have the simplest layered structure. A schematic representation of the crystal lattice of $Fe_{1+y}(Te_{1-x}Se_x)$ is illustrated in Fig. 4.5. The crystal structure of this material series resembles that of iron arsenides [167] with Fe square planar sheets [Fe(1) in Fig. 4.5] forming from the edge-sharing iron chalcogen tetrahedral network and it exhibits an interesting feature: the interstitial sites of the (Te, Se) layers allow partial occupation of Fe, resulting in the nonstoichiometric composition $Fe_{1+y}(Te_{1-x}Se_x)$, where *y* represents the excess Fe at interstitial sites [Fe(2) in Fig. 4.5] [199, 200]. This structural characteristic is analogous to that of $Li_{1-x}FeAs$ in which Li occupies interstitial sites of As layers [165, 201].

The iron chalcogenide $Fe_{1+y}(Te_{1-x}Se_x)$ is an important ferrous superconducting system representing a special class of Fe based superconductors. Superconductivity of the end member with critical temperature $T_C = 8$ K was first reported in the PbO-type structure β-FeSe by F.C. Hsu *et al.* [202] Soon thereafter, T_C was increased to as high as 37 K under applied pressure [203]. Initially, this was directly linked to Se deficiencies [202] but later studies [204] also revealed the sensitivity of the critical temperature to the Fe non-stoichiometry. Band structure density functional theory calculations also show that the Fermi surface topology of FeSe is very similar to that of the FeAs-based compounds [180] which was later confirmed by photoemission studies [205]. The transition temperature of FeSe was raised to 14–15 K by partial Se substitution with Te [206, 207].

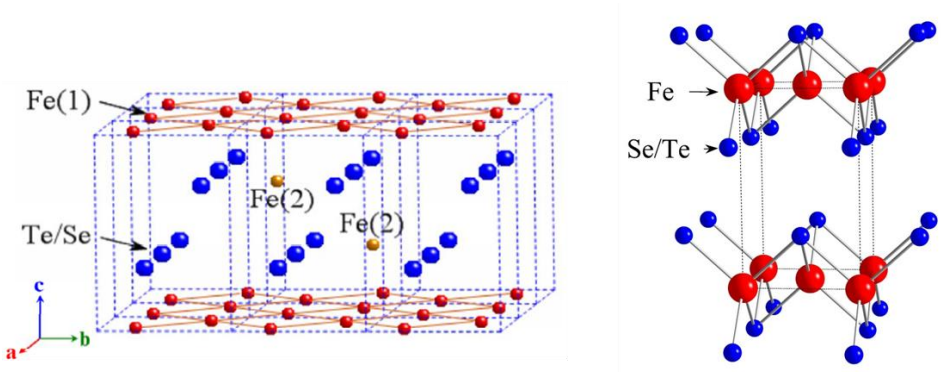

Figure 4.5 The schematic crystal structure of $Fe_{1+y}(Te_{1-x}Se_x)$. The iron on the square-planar sheets is denoted by Fe(1) while the excess Fe denoted by Fe(2) corresponds to iron partially occupying at the interstitial sites of the (Te,Se) layers

On the other end, the isostructural chalcogenide FeTe is a non-superconductive antiferromagnet with (π,0) magnetic wave vector whose AFM structure is distinct from that seen in undoped FeAs compounds [208, 209]. The AFM order in $Fe_{1+y}Te$ propagates along the diagonal direction of the Fe square lattice [200, 210] while in FeAs compounds the propagation direction of the spin-density wave (SDW)-type AFM order is along the edge of the Fe lattice [208, 209]. Moreover, W. Bao *et al.* showed that the AFM wave vector can be tuned by the excess iron [200] which suggests that the mechanism of magnetism in $Fe_{1+y}Te$ should be very different from that of the FS nesting driven SDW order in FeAs parent compounds which can result is unique superconductive characteristics.

The phase diagram of the $Fe_{1+y}(Te_{1-x}Se_x)$ system constructed by T.J. Liu *et al.* [211] following a comprehensive range of measurements on $Fe_{1.02}(Te_{1-x}Se_x)$ single crystals is depicted in Fig. 4.6.

Resistivity measurements were performed in a Quantum Design Physical Property Measurement System (PPMS) using a standard four terminal method, were gold leads were attached with silver epoxy to the gold coated contact area of the samples. Hall measurements were also performed in the PPMS using a five terminal method. Magnetic characterization was performed in a commercial Quantum Design Superconducting Quantum Interference Device (SQUID) were magnetization and magnetic susceptibility values were obtained for different temperatures in a 30 Gauss applied field. The magnetic structure of the iron chalcogenide $Fe_{1.02}(Te_{1-x}Se_x)$ was investigated using an elastic neutron scattering technique [211].

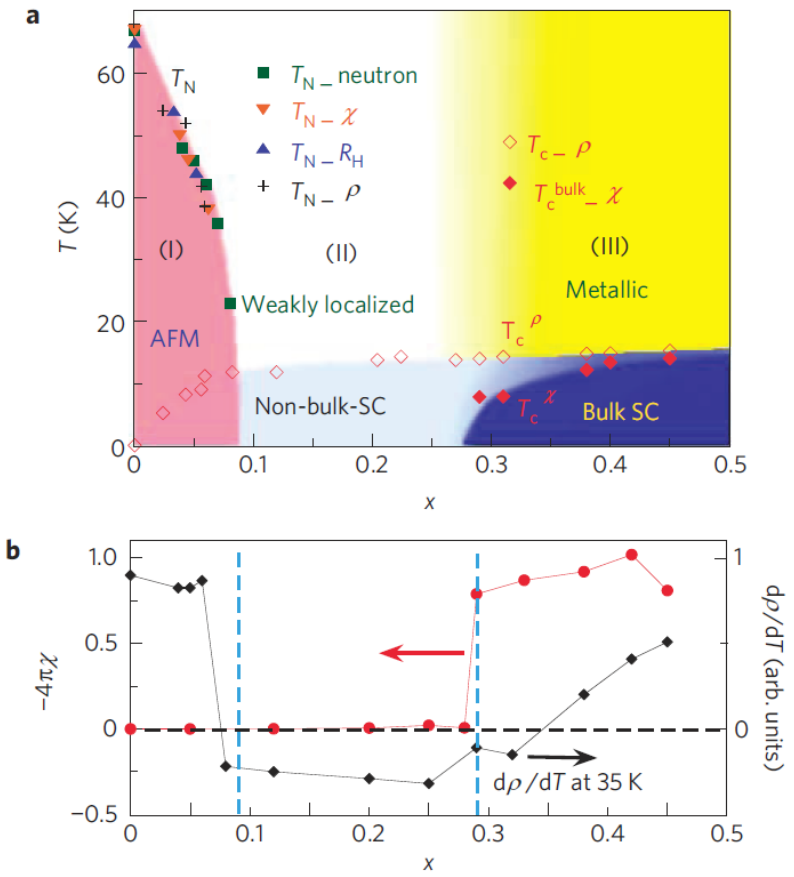

Figure 4.6 Magnetic and superconducting properties of $Fe_{1.02}(Te_{1-x}Se_x)$ for $0 < x < 0.5$. a: The phase diagram. The Néel temperature T_N, of the AFM phase, determined by neutron scattering (green squares), susceptibility (orange triangles), Hall coefficient (blue triangles) and resistivity (black crosses) measurements. T_C onset of the superconducting transition probed by resistivity (open diamonds); T_C bulk superconducting transition temperature (filled diamonds) probed by susceptibility. b: The superconducting volume fraction $(-4\pi\chi)$ and the derivative of normalized resistivity $(\rho_{ab}(T)/\rho_{ab}(300\ K)$ with respect to temperature as a function of Se content [211].

Fig. 4.7 shows the temperature dependence of (*ab* plane) resistivity (Fig. 4.7 a, b and c) susceptibility (Fig. 4.7 d), and specific heat (Fig. 4.7 e), for a wide range of Se concentrations. The phase diagram illustrated in Fig. 4.6 containing the magnetic and superconducting properties as a function of temperature over the 0% - 50% Se concentration range was obtained from a combination of the above mentioned measurements. Examining the doping phase diagram of the $Fe_{1.02}(Te_{1-x}Se_x)$ system it is clear that the material exhibits distinct physical properties for different Se doping levels.

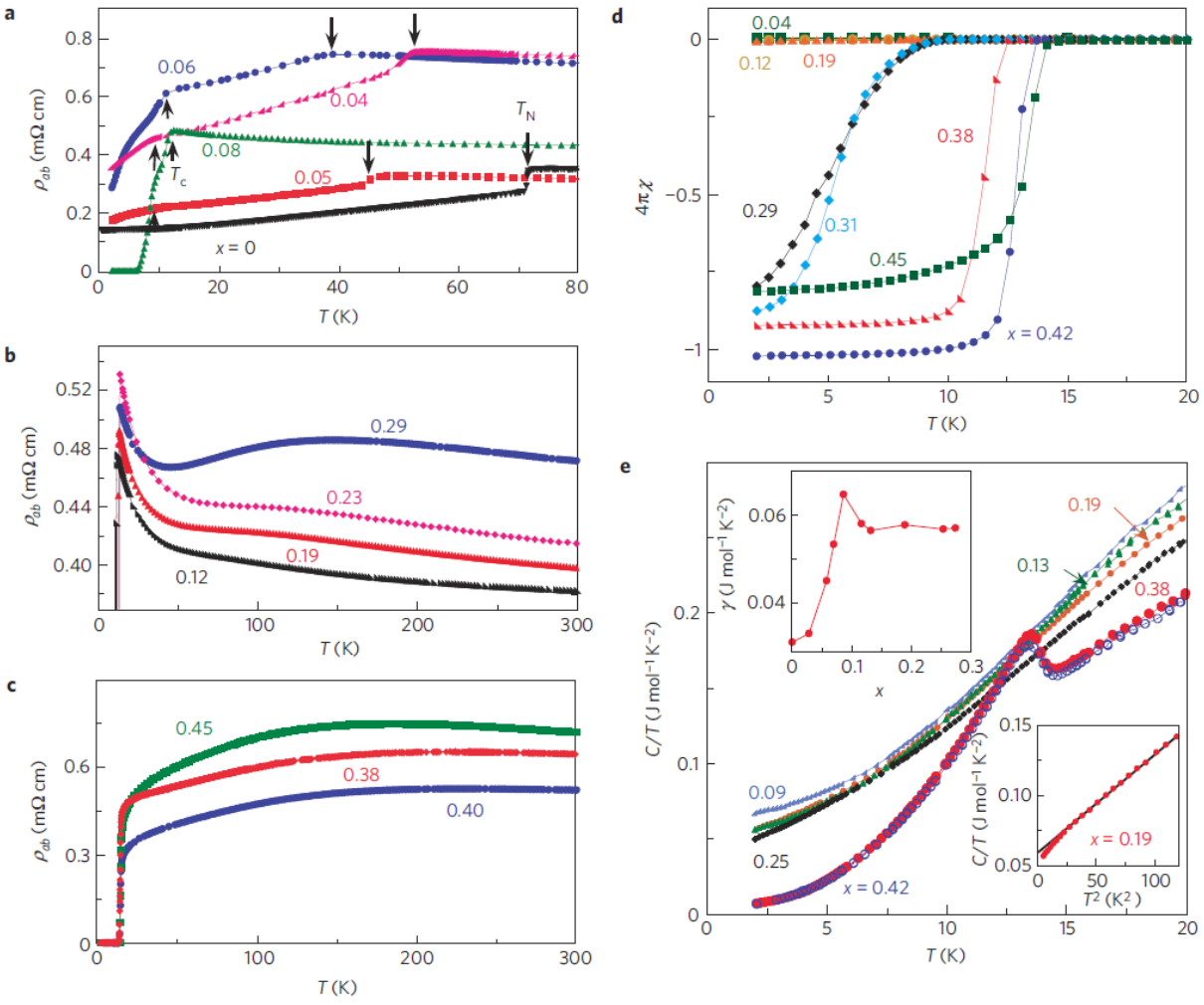

Figure 4.7 a: In-plane resistivity $\rho_{ab}(T)$ as a function of temperature for samples in the AFM region $(0 < x < 0.09)$. The downward arrows mark the AFM transition and the upward arrows mark the onset superconductivity. b: $\rho_{ab}(T)$ for samples with $0.09 < x < 0.29$. c: $\rho_{ab}(T)$ for samples with $x > 0.29$. d: Magnetic susceptibility data measured with a zero-field-cooling history and a field of 30 Oe for typical samples. e: Specific heat divided by temperature C/T as a function of temperature for various samples. The left inset is the electronic specific heat coefficient as a function of Se content x. The right inset is C/T as a function of T^2 for the $x = 0.19$ sample [211].

The isostructural chalcogenide $Fe_{1.02}Te$ parent compound is an antiferromagnet (AFM), with (π,0) magnetic wave-vector; upon Te substitution with Se it becomes superconductive with highest transition temperature at optimum Se doping level of 50%. Although zero transport resistance was observed for all Se concentrations, both specific heat and susceptibility measurements revealed that the bulk superconductivity does not occur until $x > 0.3$ and the maximum $T_C \approx 14\ K$ is obtained for $x \approx 0.5$.

The phase diagram delineates three distinct regions. Region I ($0 < x < 0.09$) shows long-range antiferromagnetic order with a wave vector (π,0) containing a trace of superconductivity as revealed by resistivity measurements. In region II ($0.09 < x < 0.29$) the long-range AFM order is completely suppressed although superconductivity remains a non-bulk phenomenon throughout the region i.e. superconductive sections within the sample volume will result in an overall to zero resistance but no detectable diamagnetism due to their relatively small volume compared to the bulk sample. In a sense, iron chalcogenides are similar to the cuprates and heavy-fermion unconventional superconductors where superconductivity occurs in close proximity to magnetic instabilities and seems to be mediated by spin fluctuations. By suppressing the long-range AFM order through charge carrier doping, superconductivity can be achieved in iron based superconductors as well however, in Fe pnictides bulk superconductivity occurs immediately after the antiferromagnetic phase, which gives the phase diagram of Fe chalcogenide distinction amongst other Fe based superconductors.

In region III ($x > 0.29$) bulk superconductivity is substantiated by the evidence of strong diamagnetism. Both susceptibility measurements and heat capacity tests seem to suggest large superconducting volume fractions below T_C with resistivity data suggesting evidence of metallic behavior in the normal state unlike region II where non-metallic temperature dependence in samples resistivity is observed (see Fig. 4.7 (b) and (c)). The substantial difference in properties of regions II and III is elucidated by neutron scattering measurements which show an absence of low-energy magnetic scattering at (π, π) but clearly defined magnetic short-range ordering at (π,0) which indicates that (π,0) magnetic correlations are antagonistic to superconductivity and contribute to weak charge carrier localization in region II. In region III the Se doping suppresses the (π,0) magnetic correlations and bulk superconductivity is observed in the samples coexisting with the (π, π) spin fluctuations. It is at the (π, π) magnetic wave vector that a spin gap and a magnetic resonance are formed, a result consistent with s± pairing symmetry [211, 212] and indicating a similar mechanism behind superconductivity of iron chalcogenide and iron pnictides.

Therefore, because iron pnictides also show superconductivity close to (π, π) magnetic instabilities, the pairing mechanism in $Fe_{1+y}(Te_{1-x}Se_x)$ may very likely be the same as in the FeAs-based compounds. However, the symmetry and the structure of the superconducting gap(s), which are intimately

related to the pairing mechanism, are still debated both in the FeAs and, perhaps even more so, in the Fe chalcogenide materials. Two independent reports of scanning tunneling microscopy (STM) seem to suggest a transition from a nodal superconducting gap in FeSe to a nodeless $s\pm$ gap symmetry in $Fe_{1+y}(Te_{1-x}Se_x)$ [213, 214]. However, specific-heat studies reveal isotropic gap behavior under zero magnetic field [215] but anisotropic/nodal gaps under magnetic field for optimally doped Fe(Se, Te) samples [216].

One of the most involved probes for studying $Fe_{1+y}(Te_{1-x}Se_x)$ superconductors is the London penetration depth. Measurements of $\lambda(T)$ are directly related to the density of states and provide a powerful tool for investigating low-lying quasiparticle energy and, for this very reason, can give valuable hints on superconducting gap function symmetry. Muon-spin rotation spectrometry (μ-SR) [18, 19] and microwave cavity studies [20] showed that superfluid density for $x = 0.50$ and 0.41, respectively, is consistent with two gaps with $s\pm$ symmetry. The microwave measurements also found that at low temperature, $\lambda(T)$ has a nearly quadratic behavior. Similar power-law temperature dependence T^n, with exponent $n \approx 2$, was also reported from radio-frequency tunnel diode oscillator (TDO) data by several groups [21-24].

In Chapter III we have shown the advantages of using the tunnel diode oscillator technique to study the superconducting properties of materials and specifically the temperature dependence of London penetration depth. For the $Fe_{1+y}(Te_{1-x}Se_x)$ system H. Kim *et al.* [21] used the TDO method to probe the temperature dependence of the in-plane penetration depth in $Fe_{1.03}(Te_{0.63}Se_{0.37})$ single crystals down to 0.5 K reporting a power law behavior of $\Delta\lambda_{ab}(T)$ at low temperatures with an exponent $n \approx 2.1$. A similar power law behavior with $n \approx 2.2$ was reported for $Fe_{1.0}(Te_{0.56}Se_{0.44})$ using the same method by A. Serafin *et al.* [22] down to a temperature of 0.2 K. T. Klein *et al.* [23] used a tunnel diode oscillator to measure the temperature dependence of λ_{ab} and λ_c in $Fe_{1.05}(Te_{0.55}Se_{0.44})$ and found the same quadratic temperature dependence for both crystallographic directions. K. Cho *et al.* [24] reported on TDO measurements of $\Delta\lambda_{ab}(T)$ in optimally-doped single crystals of $Fe_{1.0}(Te_{0.58}Se_{0.42})$ focusing on the effects of sample size, shape and surface roughness and reporting on a $n \approx 2.3$ power law variation for a number of different samples indicating an intrinsic behavior.

Most previous TDO studies, however, focus on one particular Se concentration, especially close to the optimal doping of the $Fe_{1+y}(Te_{1-x}Se_x)$ system, and there seem to be relatively large variations in the magnitude of $\lambda(T)$ between different measurements. Moreover, most reported penetration depth studies are limited to temperatures above 0.5 K with only one TDO study conducted at lower temperatures down to 0.2 K, performed on $Fe_{1.0}Te_{0.44(4)}Se_{0.56(4)}$ samples [22]. Since variations of $\lambda(T)$ represent the spectrum of the low-lying quasiparticles it is only at low temperatures that it is possible to have valuable hints on the gap function symmetry. Consequently, the temperature investigation of the London penetration depth

is appropriate in determining the pairing symmetry of iron based superconductors provided that low temperatures can be achieved. For higher temperatures thermal effects can make it difficult or even impossible to distinguish different symmetries.

In this work, we present a systematic study of the temperature dependence of the in-plane penetration depth $\lambda_{ab}(T)$ in $Fe_{1+y}(Te_{1-x}Se_x)$.We measured a significant number of single crystals, with different Se concentrations within the bulk superconductive region, and our measurements were extended down to 50mK in order to better understand the pairing symmetry of this system and its evolution with doping. We will also show the importance of extending the temperature range to the lowest possible value and the effect that ultra-low temperature region measurements can have on interpreting the results.

4.3. $Fe_{1+y}(Te_{1-x}Se_x)$ single crystals growth and characterization

The $Fe_{1+y}(Te_{1-x}Se_x)$ single crystal samples, with different Se concentrations, were synthesized using a solid state reaction method with self-flux at Tulane University by Dr. Z. Mao' research group. The high purity starting element powders are mixed and sealed in quartz tubes under high vacuum (pressure less than 10^{-4} torr). To reduce the slight iron oxidation several clean carbon pieces were also loaded into the quartz tubes however, they were not in physical contact with the powder. The sealed quartz tubes were placed in a furnace heated to 600 °C and kept in for 12 hours to allow the initial reaction of Se and other elements. The temperature was then increased to 930 °C and maintained for 24 hours for the complete reaction.

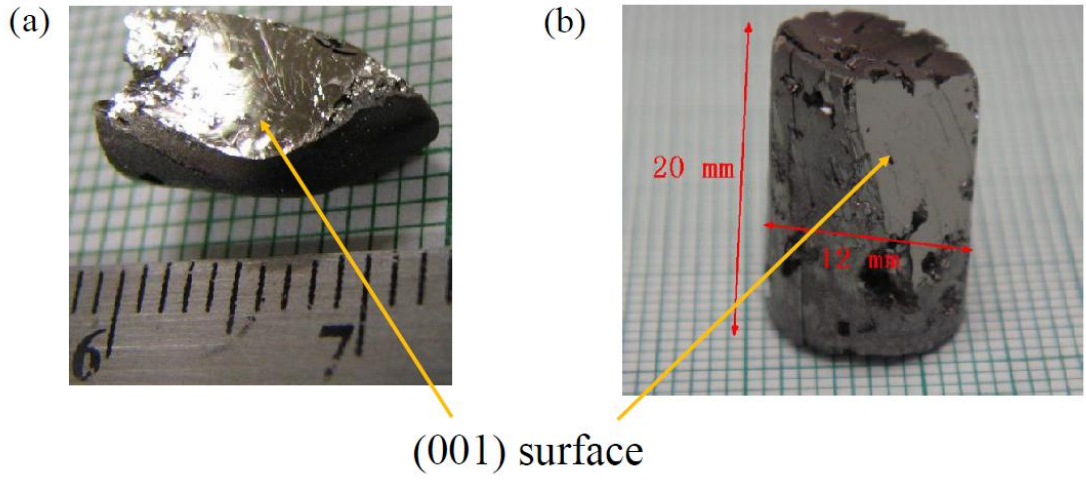

Figure 4.8 Pictures of $Fe_{1+y}(Te_{1-x}Se_x)$ bulk crystals as obtained with the flux method.

To obtain large single crystals, the temperature was slowly cooled down to 400 °C followed by the shutdown of furnace power. In this process Tellurium and Selenium act as flux and, during the cooling process, large single crystals can be obtained, as illustrated in Fig. 4.8.

High quality large $Fe_{1+y}(Te_{1-x}Se_x)$ single crystal, with Se concentration spanning from $x = 0$ to $x = 0.5$, can be obtained using the above mentioned flux method. However, this method is not viable for the growth of single crystals with Se concentrations above 60%. Pure $Fe_{1+y}Se$ crystallizes in two different phases with tetragonal (β phase, space group *P4/nmm*) and hexagonal structure (α phase, space group *P63/mmc*) respectively. A first order structural phase transition occurs around 457 °C which fractures the single crystal. Therefore the self-flux method does not allow the growth of the pure tetragonal superconducting $Fe_{1+y}Se$. Alternative methods, such as external KCl/NaCl flux growth [217-219] and vapor transport method [220, 221] have been reported. However, obtained crystals are small and involve intergrowth of both tetragonal and hexagonal phase as shown in the crystallographic XRD spectrum. Using large high quality single crystals is instrumental in obtaining pertinent experimental results, particularly in our penetration depth measurements where crystal purity is essential and large dimensions can significantly increase the sensitivity of the technique.

The chemical composition and crystalline structure of the $Fe_{1+y}(Te_{1-x}Se_x)$ samples were investigated using Energy-Dispersive X-Ray Spectroscopy (EDS) and X-Ray Diffraction (XRD) measurement respectively [204]. The EDS technique is an analytical tool widely used for elemental determination and it's usually in the form of an additional detector to an electron microscope. When a high energy electron beam is focused onto the surface of a solid sample, the electrons of inner atomic shells may be excited by the high energy electron beam and ejected from the shell leaving "holes" in their place. The higher energy electrons of the outer shells can then fill those "holes" thus occupying a lower energy state where the difference in energy can be released in the form of X-rays. Given that the emitted X-ray energy value is directly related to the unique electronic shell structure of individual atoms, the measured X-rays frequency is characteristic to individual elements where X-ray intensity is proportional to the amount of that element within the structure. Consequently, by analyzing the X-ray spectrum emitted by the sample quantitative information of the constitutive elements can be extracted.

An example of EDS spectra obtained for $Fe_{1+y}(Te_{1-x}Se_x)$ single crystals along with their electron microscope image is depicted in Fig. 4.9. The EDS results showed small deviations from the nominal concentrations and confirm the high purity of the crystals.

The crystal structure of $Fe_{1+y}(Te_{1-x}Se_x)$ was characterized using XRD measurements. The X-Ray Diffraction technique is one of the most powerful tools available to determine the lattice structure of a crystal. When a beam of X-rays is directed onto a crystal, the atoms in a periodic lattice will scatter the

incident X-rays. The scattered X-rays will interfere and constructive interference occurs when the distance between adjacent lattice planes and the incident beam angle satisfy the well-known Bragg's law.

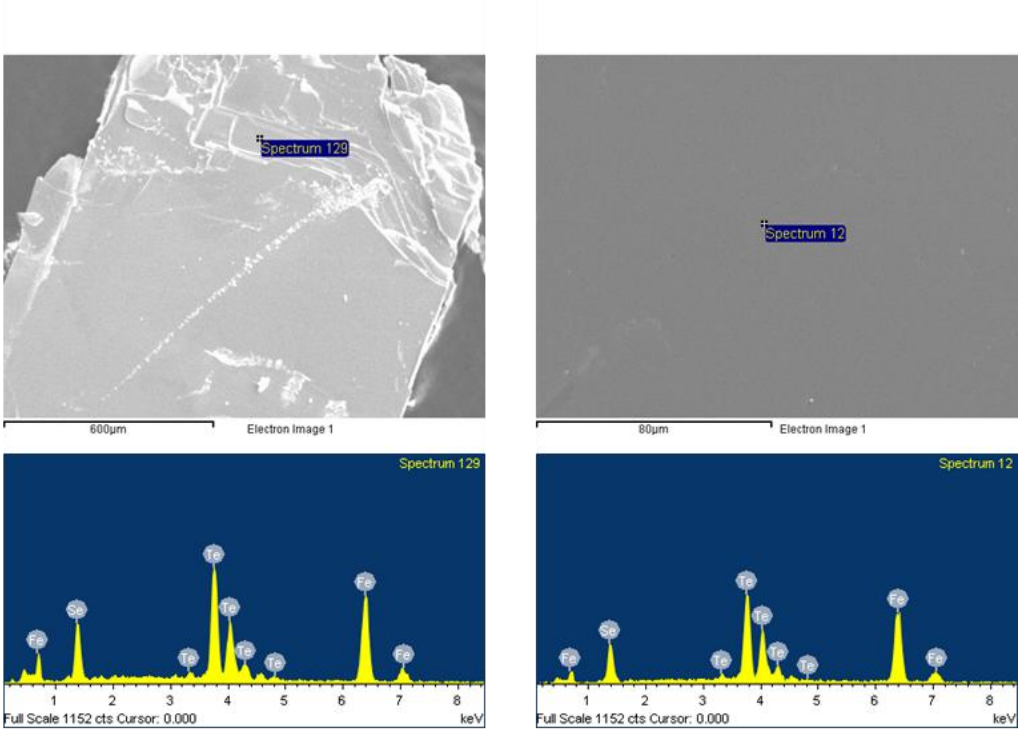

Element	Weight%	Atomic%
Fe K	33.39	49.63
Se L	17.55	18.45
Te L	49.07	31.92
Totals	100.00	

Element	Weight%	Atomic%
Fe K	36.88	53.95
Se L	14.26	14.75
Te L	48.87	31.29
Totals	100.00	

Figure 4.9 Typical electron microscopy images and Energy-Dispersive X-Ray Spectroscopy data for $Fe_{1+y}(Te_{1-x}Se_x)$ single crystals

An X-ray detector able to measure the intensity of the scattered radiations is then rotated simultaneously with the sample holder to provide an X-ray intensity versus angle spectrum. When Bragg's law is satisfied for an angle, a peak can be observed in XRD spectrum. Since different crystals are characterized by different sets of lattice planes, the XRD spectra can be used to check the phase of a sample (e.g., α-FeSe or β-FeSe). Furthermore, since the XRD spectra include the full set of structure information, the refinement of XRD spectra (Rietveld refinement) can resolve the atomic structure of the crystal. An example of the XRD spectra obtained for $Fe_{0.82}(Te_{1-x}Se_x)$ samples is shown in Fig. 4.10. The XRD measurements revealed that the synthesized crystals are indeed single phase with clear diffraction peaks consistent with expectations.

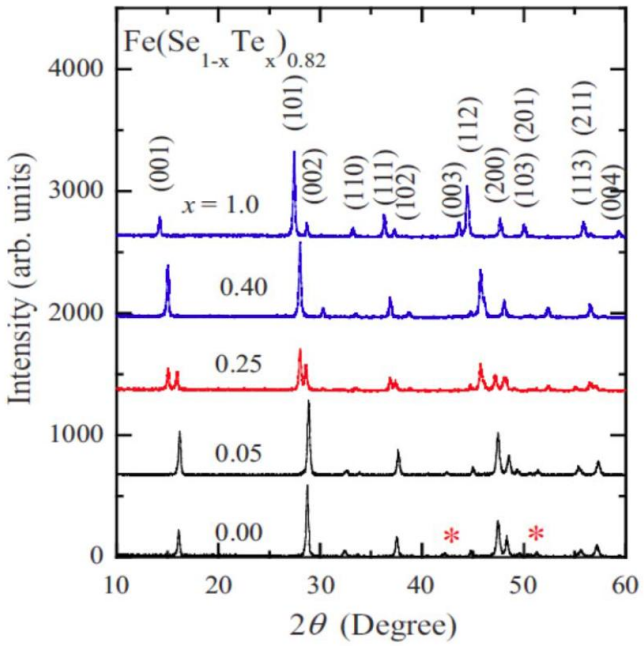

Figure 4.10 X-Ray Diffraction patterns of typical compositions in the $Fe_{0.82}$ ($Te_{1-x}Se_x$) series from [206].

Interstitial Fe can drastically affect the superconductive properties of the system as shown by T. J. Liu *et al.* [222]. One example is depicted in Fig. 4.11 where the superconductive transition was recorded using susceptibility and resistivity measurements for two samples i.e. $Fe_{1.03}(Te_{0.63}Se_{0.37})$ (SC1 in Fig. 4.11) and $Fe_{1.11}(Te_{0.64}Se_{0.36})$ (SC2 in Fig. 4.11). The excess Fe was found to lower the transition temperature value as well as superconductive volume fraction with increasing values of y leading to the total suppression of superconductivity.

The work presented in this dissertation focuses on further investigating the superconductive properties of $Fe_{1.02}(Te_{1-x}Se_x)$ single crystals as derived from temperature dependent London penetration depth measurements. The goal was to use a tunnel diode oscillator technique to probe the susceptibility of $Fe_{1.02}(Te_{1-x}Se_x)$ single crystals in order to investigate the Se doping influence on the magnetic penetration depth and subsequently on the physical properties that can be inferred from such measurements. London penetration depth studies have been reported for a number of iron based superconductors including the Fe_{1+y} ($Te_{1-x}Se_x$) system however, a comprehensive analysis of the iron chalcogenides was lacking at the time we started our investigation.

Since TDO measurements of London penetration depth require that certain conditions pertaining to the quality of the sample under investigation be met, an extensive sample selection process was implemented. Firstly, samples with minimum Fe excess were selected appertaining to their characterization by EDS analysis. The amount of excess iron y is hard to control in the synthesizing

technique described above. Consequently, careful EDS analysis was performed and used to select samples with minimum Fe excess. Since the resolution of the EDS technique is around 2%, we estimate that in the penetration depth samples referred to throughout this text, $y \sim 0.02$.

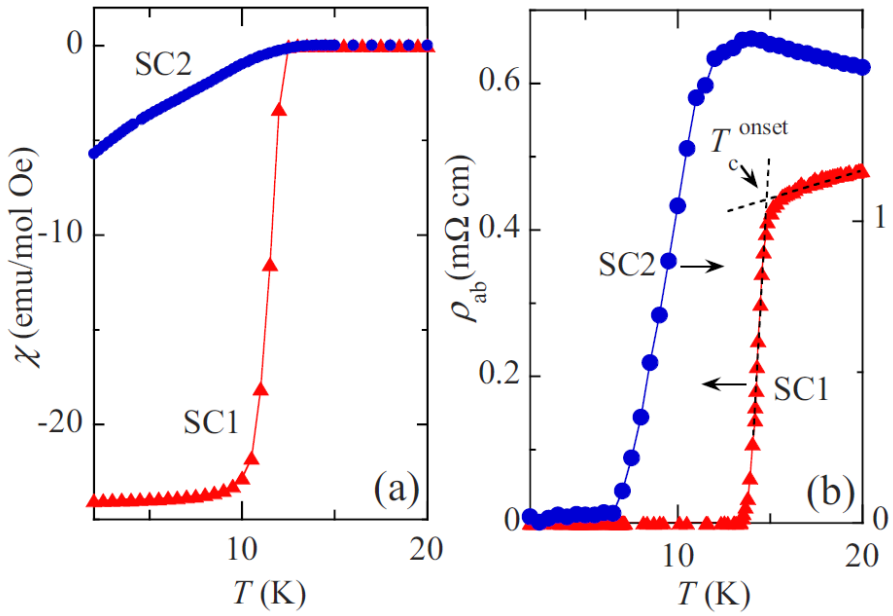

Figure 4.11 Left: Magnetic susceptibility as a function of temperature measured under a magnetic field of 30 Oe applied along the c axis. Right: In-plane resistivity as a function of temperatures. SC1 and SC2 represent two superconducting Fe_{1+y} ($Te_{0.6}Se_{0.34}$) samples with 3% and 11% excess iron [222].

In estimating the values of the relative penetration depth using a TDO technique, the physical dimensions of the sample have a direct involvement in relating the resonant frequency shift to the London penetration depth. If fractions of the sample volume are not superconductive, due to either impurities or defects, overestimations of the volume could lead to underestimations in $\Delta\lambda$. To minimize such effects, heat capacity measurements were performed to investigate the superconductive volume fraction V_{SC} and select the samples with highest homogeneity and superior characteristics. In addition, magnetic susceptibility of a large number of samples was examined using the AC Measurement System (ACMS susceptibility) option of a commercial Quantum Design PPMS at various excitation fields down to a minimum temperature of 2 K.

4.4. Heat capacity and magnetic susceptibility investigations

The specific heat determines the energy needed to change the temperature of a material by a specific amount. The Quantum Design Heat Capacity option measures the heat capacity at constant pressure by controlling the heat added to and removed from a sample while monitoring the resulting change in temperature. During a measurement, a known amount of heat is applied at constant power for a fixed time, and then this heating period is followed by a cooling period of the same duration. A platform heater and platform thermometer are attached to the bottom side of the sample platform. Small wires provide the electrical connection to the platform heater and platform thermometer and also provide the thermal connection and structural support for the platform. The sample is mounted to the platform by using a thin layer of Apiezon N grease, which provides the required thermal contact to the platform. The sample and platform are kept at high vacuum (0.01 mTorr) so that the thermal conductance between the sample platform and the thermal bath (puck) is totally dominated by the conductance of the wires. This gives a reproducible heat link to the bath with a corresponding time constant large enough to allow both the platform and sample to achieve sufficient thermal equilibrium during the measurement. For small size samples the amount of grease used to thermally anchor the sample is important as the heat capacity of the grease can be comparable to that of the sample under study. The amount of grease has to small enough to give negligible background but large enough to provide sufficient thermal contact. In order to probe the specific heat of the sample alone, an "addenda" was performed consisting in separately measuring the heat capacity of the grease which was later subtracted from the sample + grease HC signal. Considering that our PPMS Heat Capacity (HC) option can accommodate samples weighing at least 1 mg, an important factor in selected the size of the samples was the weight limit. Although larger samples would provide better accuracy in specific heat and, ultimately, TDO measurements, samples with corresponding sizes close to the PPMS HC weight limit were chosen in order to minimize inhomogeneity and inaccurate data due to crystal imperfections. Exact information about sample shape, dimensions and features is critical in correctly estimating the London penetration depth values from TDO susceptibility measurements. Single crystals of rectangular shape were carefully cut from the bulk material and investigated under an optical microscope to extract their dimensions and insure that the surfaces are flat and free of imperfections. The width and length of the rectangular crystals was estimated using a microscopic ruler while thickness was measured with a micrometer. We estimate the errors in the measured dimensions of the samples to be of the order of 0.01 mm.

In electric materials thermal energy is provided by crystal lattice vibration, leading to a phonon contribution to heat capacity, and electron kinetic energies which lead to an electron contribution to the specific heat (heat capacity per unit mass). In the Debye model approximation, i.e. $T \ll \Theta_D$ where Θ_D is

the Debye temperature (typically larger than room temperature for most elements), the phonon heat capacity has the following temperature dependence:

$$C_{ph} = \beta T^3 \quad (4.1)$$

where β is a material constant. The electronic component of the heat capacity of a Fermi gas has a linear temperature dependence given by:

$$C_{el} = \gamma T \quad (4.2)$$

where γ is the Sommerfeld parameter specific to each material. The total specific heat can thus be written as:

$$C = C_{el} + C_{ph} = \gamma T + \beta T^3 \quad (4.3)$$

or in a reduced linear form given by:

$$\frac{C}{T} = \gamma + \beta T^2 \quad (4.4)$$

By measuring C/T as a function of T^2, the material dependent coefficients can be extracted from the linear fit. This would be the expected temperature dependence of a superconductive material in normal state. As we have seen in Chapter I, upon entering the superconductive state the electronic specific heat exhibits a jump at T_C then exponentially decreases to a zero value as the temperature is decreased to zero. Consequently we can consider γ as a temperature dependent parameter in the superconductive state. If superconductivity is inhomogeneous, the non-superconducting fraction contributes to the electronic specific heat and leads to a residual finite value for C_{el} at lowest temperatures resulting in a total heat capacity expressed by:

$$C = C_{el}^{SC} + C_{el}^{res} + C_{ph} = C_{el}^{SC} + \gamma_{res} T + \beta T^3 \quad (4.5)$$

Considering that at low temperatures phonon contribution C_{ph} is negligible and the superconductive part of the electron specific heat C_{el}^{SC} is expected to vanish, the residual contribution γ_{res} can be obtained from the extrapolation of C/T data to zero temperature. Since the finite C_{el}^{res} is due to unpaired fraction of electrons, the superconductive volume fraction can be obtained as:

$$V_{SC} = \frac{\gamma - \gamma_{res}}{\gamma} \quad (4.6)$$

where γ can be extracted from the low temperature extrapolation of C/T data above T_C using the dependence in Eq. 4.4.

As previously mentioned, it is only in region III of the $Fe_{1.02}(Te_{1-x}Se_x)$ doping diagram that bulk superconductivity is achieved. Consequently, our measurements were only performed on samples with Se concentrations above 30%. Heat capacity measurements were performed on a large number of samples with doping levels spanning from 30% Se to optimum doping. As expected, considering previous reports on this system [211, 215], samples with Se concentration less than 36% did not exhibit a measurable

specific heat jump characteristic to superconductivity. It is for this reason that we focused our attention on samples with higher Se concentration namely $x = 0.36$, $x = 0.40$, $x = 0.43$ and $x = 0.45$.

Fig. 4.12 illustrates the heat capacity data down to 2 K obtained in three samples for each of the four different doping levels.

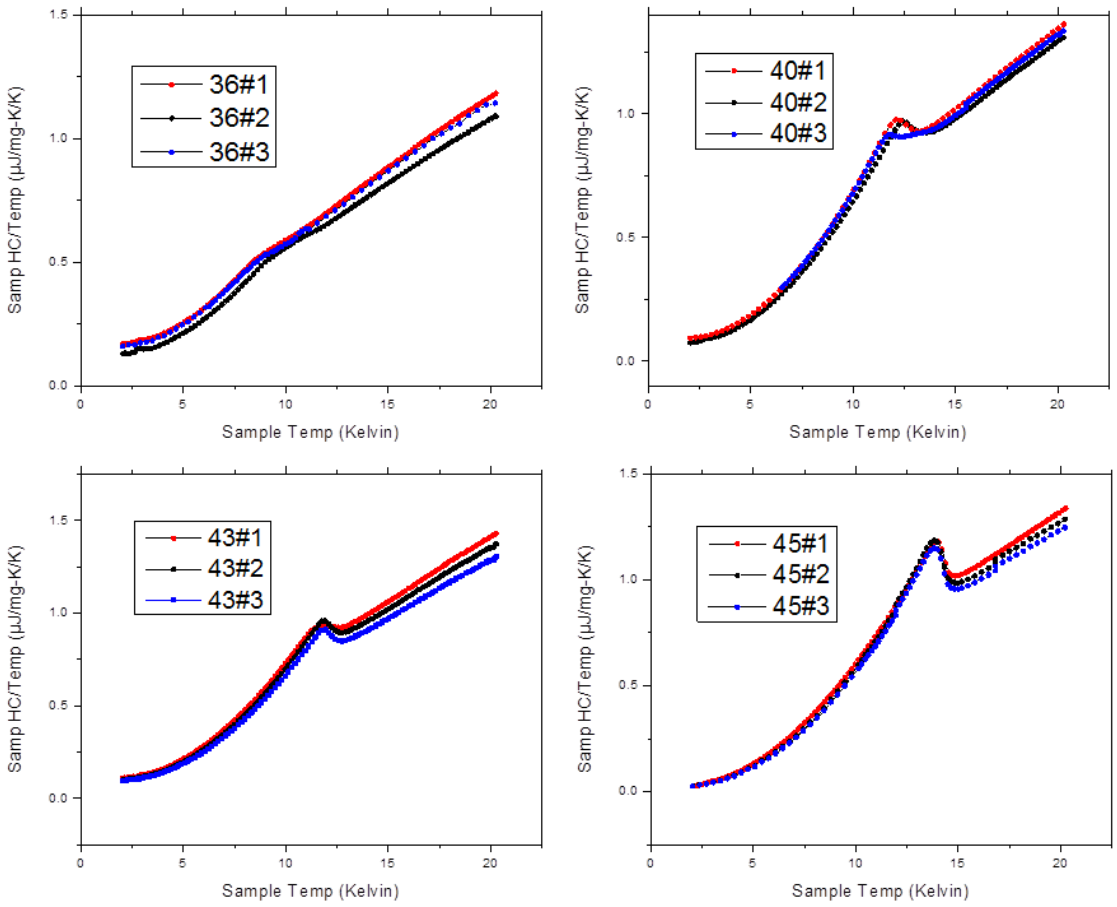

Figure 4.12 The reduced specific heat data $C/(m \cdot T)$ versus temperature obtained for the $Fe_{1.02}(Te_{1-x}Se_x)$ single crystals in the PPMS. Three samples for each of the four different Se concentrations within the bulk superconductivity region were chosen.

Although the actual number of samples investigated for each Se concentration is larger, we only show the reduced specific heat $C/m \cdot T$ data for three samples of each Se concentration specifically the samples that exhibited the best performance. As anticipated, the samples close to optimum doping showed the most pronounced characteristic jump in specific heat and lowest residual value in specific heat C_{el}^{res} evidence of strong homogeneity. As the doping level is decreased, the magnitude of the specific heat

discontinuity decreases together with the superconductive transition temperature. Moreover, the residual effects become significant as indicated by finite values of the specific heat at low temperatures which suggests that inhomogeneity becomes larger as Se concentration is decreased.

Using the above mentioned method, we also calculated the superconductive volume fraction for each sample. Table 4.1 contains the calculated values for V_{SC} together with other relevant information about the samples such as mass and physical dimensions. Temperature dependent specific heat investigation enabled us to select the samples with superior superconductive characteristics based on their volume fraction and magnitude of the specific heat discontinuity. Although the theoretical fitting for specific heat for $T > T_C$ using the Debye-Einstein model can in principle be used to make extrapolation to low temperatures, such estimations are only accurate for temperature well below the Debye temperature thus the fitting range is most reliable from T_C up to a limiting temperature well below the Debye value. For relatively high T_C , the range is considerably limited thus, such method could lead to overestimation of the volume fraction. Nevertheless, for the purpose of selecting the best samples for our TDO measurements the absolute values are less relevant. Compared to the rejected samples, the V_{SC} values are considerably higher.

Table 4.1 Geometric dimensions and calculated supercondcutive volume fraction for all 12 samples

Nominal Se %	Sample name	Mass	Thickness	Width	Length	Volume fraction V_{SC}
%		(mg)	(mm)	(mm)	(mm)	%
36	36#1	2.92	0.075	2.3	2.4	29
36	36#2	1.1	0.05	2.3	2.5	31
36	36#3	3.1	0.095	2.1	2.2	30
40	40#1	3.4	0.156	1.8	2	60
40	40#2	5.5	0.2	1.9	2.8	62
40	40#3	2.6	0.11	2.2	2.5	40
43	43#1	3.4	0.134	2.2	2.4	65
43	43#2	8.5	0.16	3.4	3.4	73
43	43#3	2.7	0.127	2.1	2.2	74
45	45#1	3.3	0.14	2	2.4	95
45	45#2	2.05	0.095	1.95	2.05	95
45	45#3	2.1	0.095	1.8	2.2	94

Our systematic specific heat measurements revealed that the superconductive volume fraction becomes considerably smaller as the Se concentration moves away from optimum doping. This could also be explained by the fact that the samples may include non-superconducting phases or voids. However, the superconducting phase may shield non-superconducting phases in diamagnetic response from magnetic

measurements which should prove beneficial for susceptibility measurements, as in the Meissner state the supercurrents are mostly present close to the surface of the bulk sample. To make sure that the low volume fraction of less doped sample is not due to such non-superconducting phases or voids we performed magnetic measurements to test the diamagnetic response of each sample.

The three samples for each of the aforementioned Se doping levels were further investigated using the ACMS option on the PPMS. Using this technique the absolute value of the "measured" magnetic susceptibility can be obtained. The ACMS contains an alternative current (AC)-drive coil set that provides an alternating excitation magnetic field and a detection coil set that inductively responds to the combined sample moment and excitation field. The drive coil is wound longitudinally around the detection coil set. The drive coil can generate alternating excitation fields of up to 10 *Oe* in a frequency range of 10 *Hz* to 10 *kHz*. The detection coils are arranged in a first-order gradiometer configuration to help isolate the sample's signal from uniform background sources. This configuration utilizes two sets of counter-wound copper coils connected in series and separated by several centimeters. During ac measurements, an alternating field is applied to the measurement region and the sample is positioned in the center of each detection coil. The detection coils indicate how the applied field is altered by the presence of the sample by measuring the induced voltage resulting from the alternating magnetic field created by the induced magnetic moment of the sample. The ac signal is then amplified by a lock-in amplifier and the resulting signal is accurately separated into the real and imaginary components proportional to the respective components of the ac moment response.

In principle, the technique is similar to the tunnel diode oscillator technique since both can be used to measure variations in magnetic susceptibility of the sample however, the ACMS can provide absolute values whereas the TDO only relative values of susceptibility. Nevertheless, the sensitivity of the ACMS is significantly lower than that of the TDO, as we will show later, although relatively quick information about the diamagnetism of superconductors can be obtained prior to the TDO investigations, which require considerably more time and effort. The samples are placed in the uniform excitation magnetic field of the drive coils with the *ab* crystallographic plane perpendicular to the direction of the field. This way the induced supercurrents travel exclusively in the *ab* plane of the rectangular samples.

A superconductive sample in Meissner state will exhibit near perfect diamagnetism characterized by $\chi = -1$ value of magnetic susceptibility at low enough temperatures. It is perhaps of use to note that in the CGS unit system magnetic susceptibility per unit volume in case of perfect diamagnetism is described by $4\pi\chi = -1$ where the unit is emu/cm^3/Oe. Therfore a perfectly diamagnetic sample of 1 cm^3 volume, under an applied field of 1 Oe will result in a measured magnetic moment of $-1/4\pi$ emu which is roughly 0.08 emu. As mentioned in Chapter III, demagnetizing effects due to the finite size of the sample can result in an enhanced value for the measured magnetic moment and for plate like samples the

measured signal will be considerably larger compared to the bulk value and is expected to increase as thickness of the samples is decreased. The increase from the 0.08 emu bulk value can be calculated based on the dimensions of the sample using the simple approximations given in Chapter II, Section 2.2 for rectangular samples. Based on the dimensions of our samples shown in Table 4.1, we can expect a minimum factor of 5 in amplification of measured signal. The measured magnetic moment as well as the resulting magnetic susceptibility per unit volume for our $Fe_{1.02}(Te_{1-x}Se_x)$ samples in a 10 kHz ac magnetic field of 1 Oe amplitude are illustrated in Fig. 4.13 and Fig. 4.14 respectively.

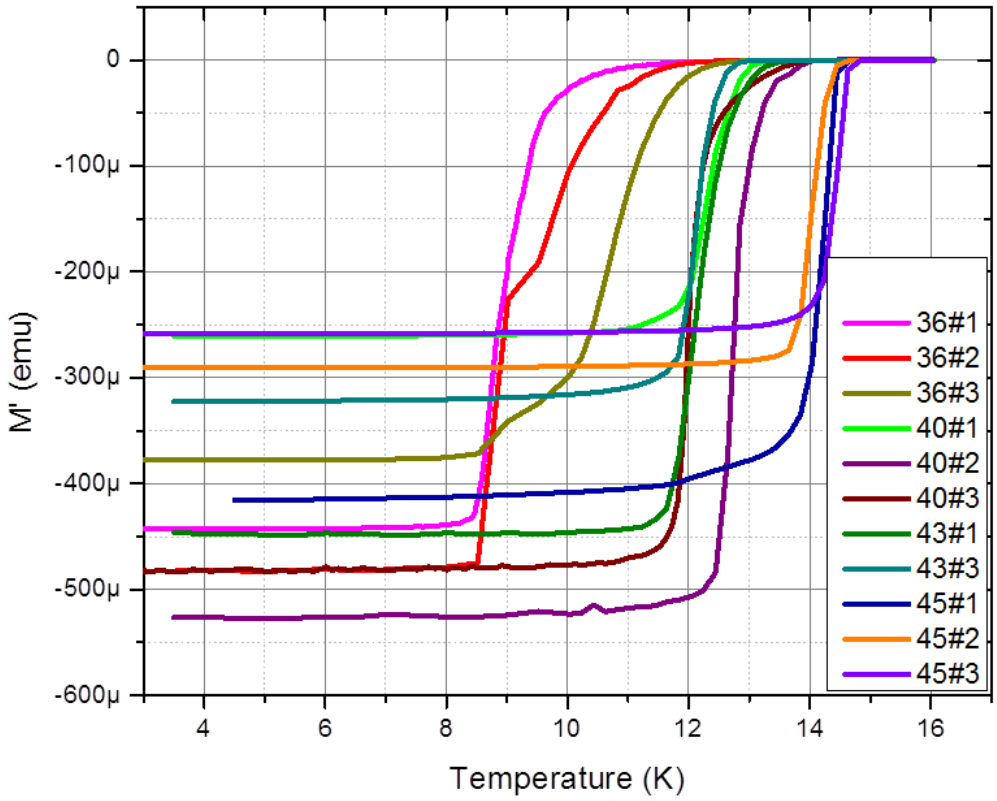

Figure 4.13 The magnetic moment of our $Fe_{1.02}(Te_{1-x}Se_x)$ samples as the real component of the susceptibility from ACMS measurements. The measurements were performed in a 10 kHz ac excitation magnetic field of 1Oe amplitude in the PPMS.

All the samples show pronounced diamagnetism consistent with perfect diamagnetism expected in the superconductive low temperature region. As expected, geometric factors play an important role in the strength of the measured signal. It can be seen that sample 40#2 has the largest volume yielding the strongest signal thus the largest magnetic moment value. Moreover the 36#2 sample has the smallest

thickness relative to its lateral dimensions and thus a large demagnetizing factor which leads to a large susceptibility value compared with all other samples. This information is particularly useful for TDO measurements, where resolution can be increased by choosing the right sample dimensions. Largest surface samples will yield the highest frequency shifts upon entering the Meissner state. At the same time, for close volume samples, the same amplification effect can be obtained by considering thinner samples thus increasing the demagnetizing factor.

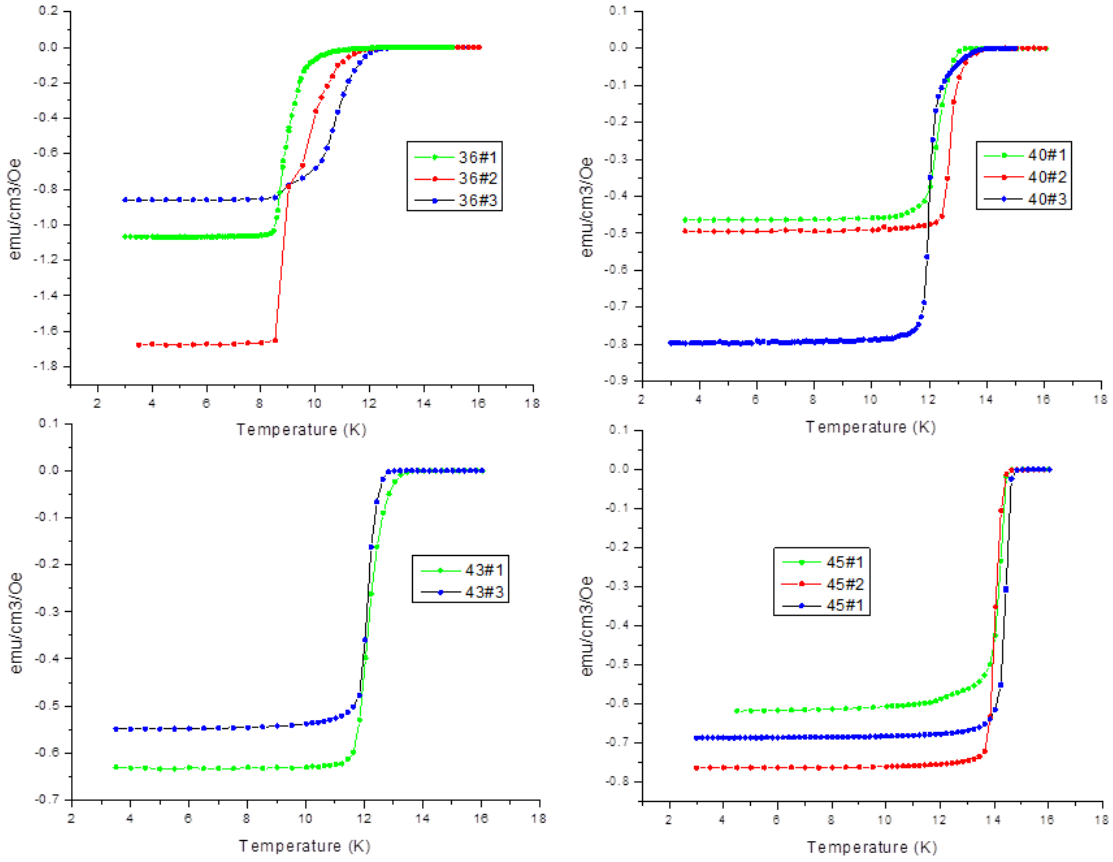

Figure 4.14 The volume susceptibility of our $Fe_{1.02}(Te_{1-x}Se_x)$ samples from ACMS measurements. The measurements were performed in a 10 kHz ac excitation magnetic field of 1Oe amplitude in the PPMS.

A second set of measurements performed consists in applying different excitation fields to the samples to study the effects of magnetic field magnitude on the superconductive properties of the $Fe_{1.02}(Te_{1-x}Se_x)$ samples. In a magnetic field, a superconductive sample goes normal at a lower temperature than in the absence of an applied field.

Although a higher value of applied magnetic field will result in an enhanced measured signal, thus increasing resolution, it can also influence the transition temperature value. In Fig. 4.15 we show the normalized susceptibility vs. temperature curves for all the samples at two different excitation fields, namely 1 Oe and 0.1 Oe. As it can be observed, the increase in applied magnetic field has a negligible influence on the transition of optimally doped samples however, as the Se concentration is decreased, the transition temperature shifts become more pronounced.

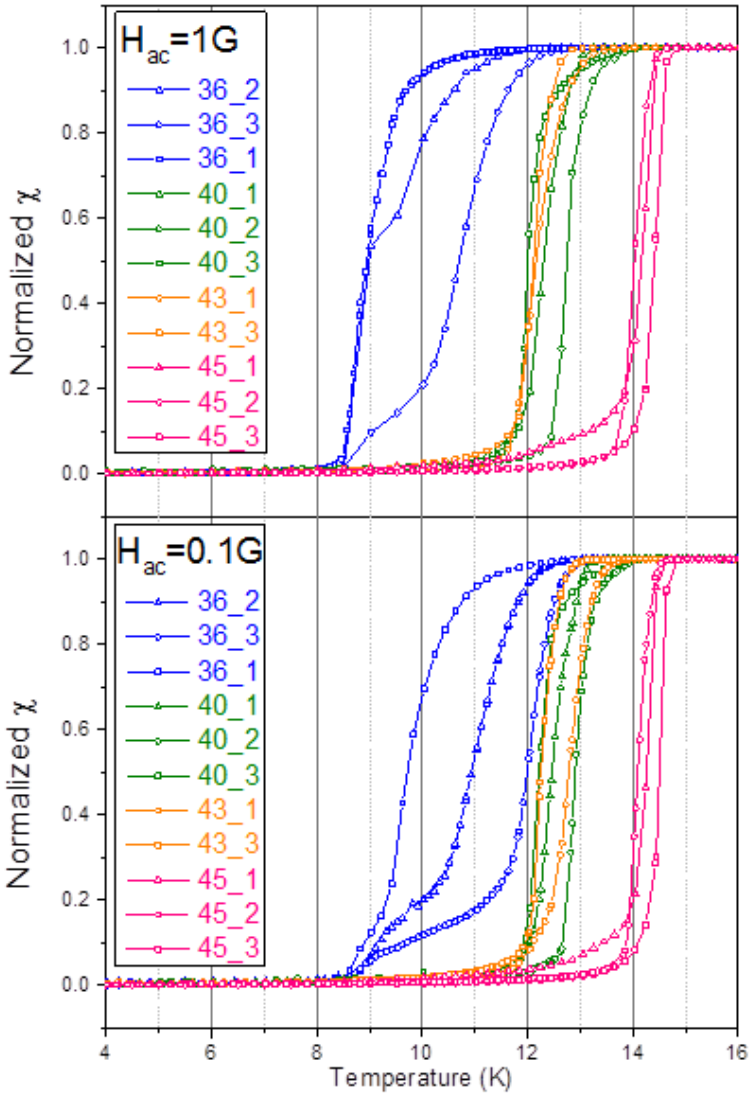

Figure 4.15 Normalized AC susceptibility data obtained in the PPMS for all for the $Fe_{1.02}(Te_{1-x}Se_x)$ samples. The upper and lower panel data was obtained for different values of the excitation field H_{ac} namely 1 Oe and 0.1 Oe

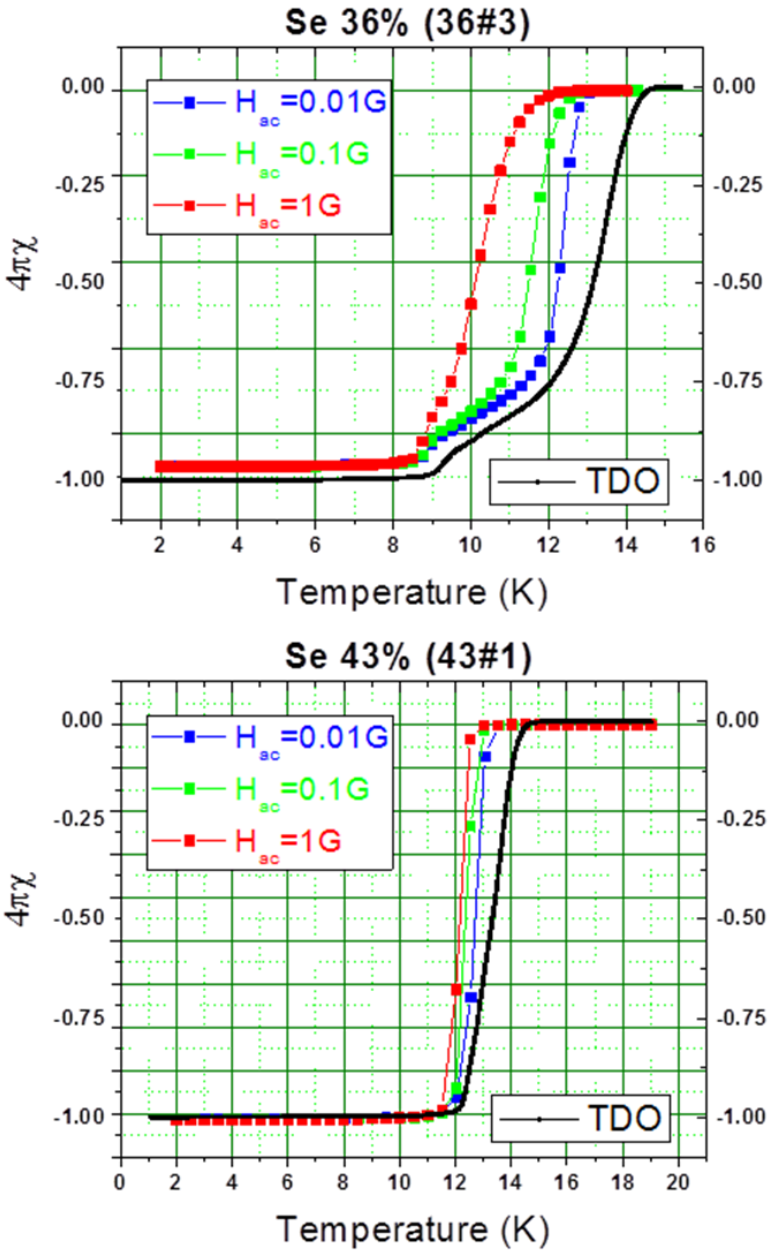

Figure 4.16 PPMS AC susceptibility data for different amplitudes of the magnetic excitation field (color points) for two $Fe_{1.02}(Te_{1-x}Se_x)$ samples with nominal Se concentrations of 36% (36#3) and 43%(43#1). The normalized TDO susceptibility data is represented by the black line. The TDO susceptibility data values were rescaled to match the ACMS limit values.

This is particularly relevant if one attempts to extract information about T_C values from magnetization measurement where relatively large magnetic fields have to be applied to magnetize the samples. Since the excitation field of a TDO coil is typically of the order of mOe, we do not expect any

influence on the transition temperature in TDO measurements which makes the TDO method all the more advantageous.

An example of comparison between susceptibility measurements obtained by the ACMS method and the TDO method is illustrated in Fig. 4.16 for the case of two samples i.e. 43#1 close to optimal doping and 36#2 for under doped. It can be seen that for the 43% Se sample, the magnitude of the applied field influence on the superconductive properties is negligible.

For the low Se doped $Fe_{1.02}(Te_{1-x}Se_x)$ sample, the influence is noticeable and as the excitation of the field is decreased, the ACMS data seems to approach the TDO data. Extrapolating ACMS values, it is apparent that the excitation field of the TDO setup is indeed very small with negligible effects on the temperature dependence of the superconductive transition.

Also, the data explains the difference in transition temperature values reported in [211] obtained by resistivity measurements as compared to the ones obtained from magnetic SQUID measurements. Another valuable information supplied by the ACMS investigations is the fact that, although the 36% samples data seems to suggest inhomogeneous properties of the under doped samples, the rest of the samples show narrow transition indicating pure specimens.

Chapter 5

London Penetration Depth in $Fe_{1+y}(Te_{1-x}Se_x)$ Single Crystals

5.1. Tunnel diode oscillator measurements

The temperature dependence of the London penetration depth in the $Fe_{1.02}(Te_{1-x}Se_x)$ single crystals was investigated in our dilution refrigerator using the tunnel diode oscillator radio-frequency setup described in Chapter III. As mentioned previously, the use of flat coil configuration ensures a uniform field in the sample region as well as a probing field parallel to the *c*-axis of the samples. Considering the fact that the $Fe_{1.02}(Te_{1-x}Se_x)$ system is anisotropic, the field configuration with respect to sample orientation ensures that supercurrents are induced in the *ab* crystallographic plane only thus, the measured changes in TDO frequency are solely due to in-plane London penetration depth λ_{ab} variations in temperature.

The resonant frequency variation as a function of temperature for all the samples is illustrated in Fig. 5.1. Considering the diamagnetism of the samples, the resonant frequency of the TDO is expected to increase as the temperature is decreased. Subtracting the resonant frequency value from the maximum frequency value measured at lowest temperatures, the relative frequency variation as a function of temperature in Fig. 5.1 was obtained considering $\Delta f(T) = f(T \to 0) - f(T)$. As anticipated, the total frequency shift from the normal state to the low temperature Meissner state is proportional to the diamagnetic moment and is strongly dependent on the geometry factor of the sample. The total frequency shift in the largest sample (43#2) is around 250 kHz while typical frequency shifts for the rest of the samples is around 70 kHz. Considering that the noise in measured frequency is around 0.5 Hz, the resolution of our TDO setup i.e. the smallest change we can detect can be estimated to be around 1 Hz. If we consider the magnetic moment values recorded by the PPMS ACMS option in Fig. 4.13 we can see that a the total magnetic moment value change from normal to superconductive state for most of our samples is around 0.5 memu.

From the TDO measurements results illustrated in Fig. 5.1 we can see that the corresponding frequency shift is as high as 250 kHz with typical values around 100 kHz. Considering the frequency resolution of the TDO setup, we can estimate the corresponding magnetic moment sensitivity for our samples is 0.2×10^{-8} emu.

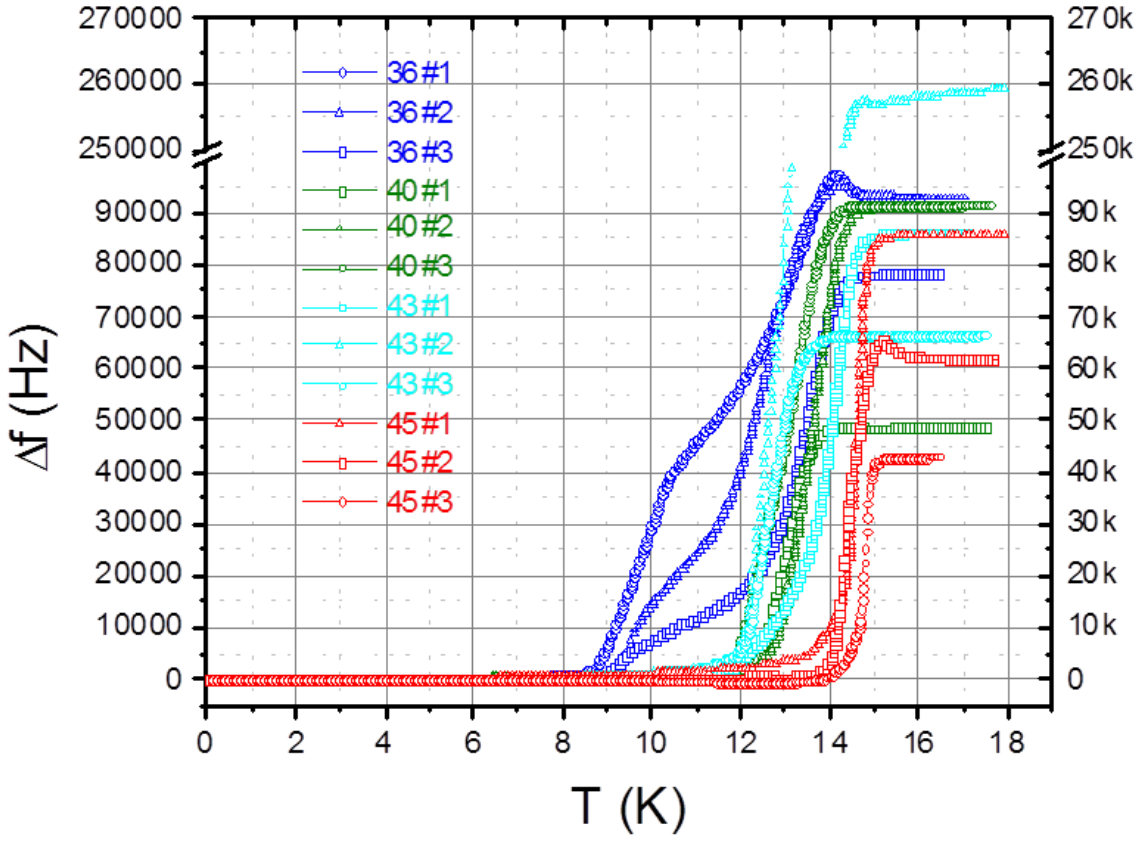

Figure 5.1 The resonant frequency shift values as a function of temperature for all $Fe_{1.02}(Te_{1-x}Se_x)$ sample as measured by our TDO setup.

Typical vibrating sample magnetometers (VSM) have a maximum sensitivity of 10^{-6} *emu* similar to the ACMS option of the PPMS while commercial SQUID magnetometers can go as high as 2 x 10^{-8} emu. Compared to other magnetometers it is easy to see that the precision of the TDO is superior. Moreover, considering that in other magnetometers the sensitivity is largely dictated by the intensity of the applied field, field which can greatly influence the properties of the samples, the remarkable precision of the TDO method while providing unaltered information about the sample properties, makes the TDO technique an unequalled tool in probing the magnetic properties of superconductors.

The superconducting transition temperature in can be sometimes hard to delineate. For this reason different methods are used in literature to define the transition temperature. Most commonly T_C is taken as the point at which the susceptibility starts to decrease which defines the onset transition temperature T_C^{onset}. A popular way of defining the onset temperature is depicted in Fig. 4.11 where T_C^{onset} is taken at the intersection of the linear extrapolation of the tangents to the normal state data with

the maximum slope data. Another method consists in taking T_C at the point at which the transition curve has a maximum derivative defining the maxim slope transition temperature T_C^{slope}.

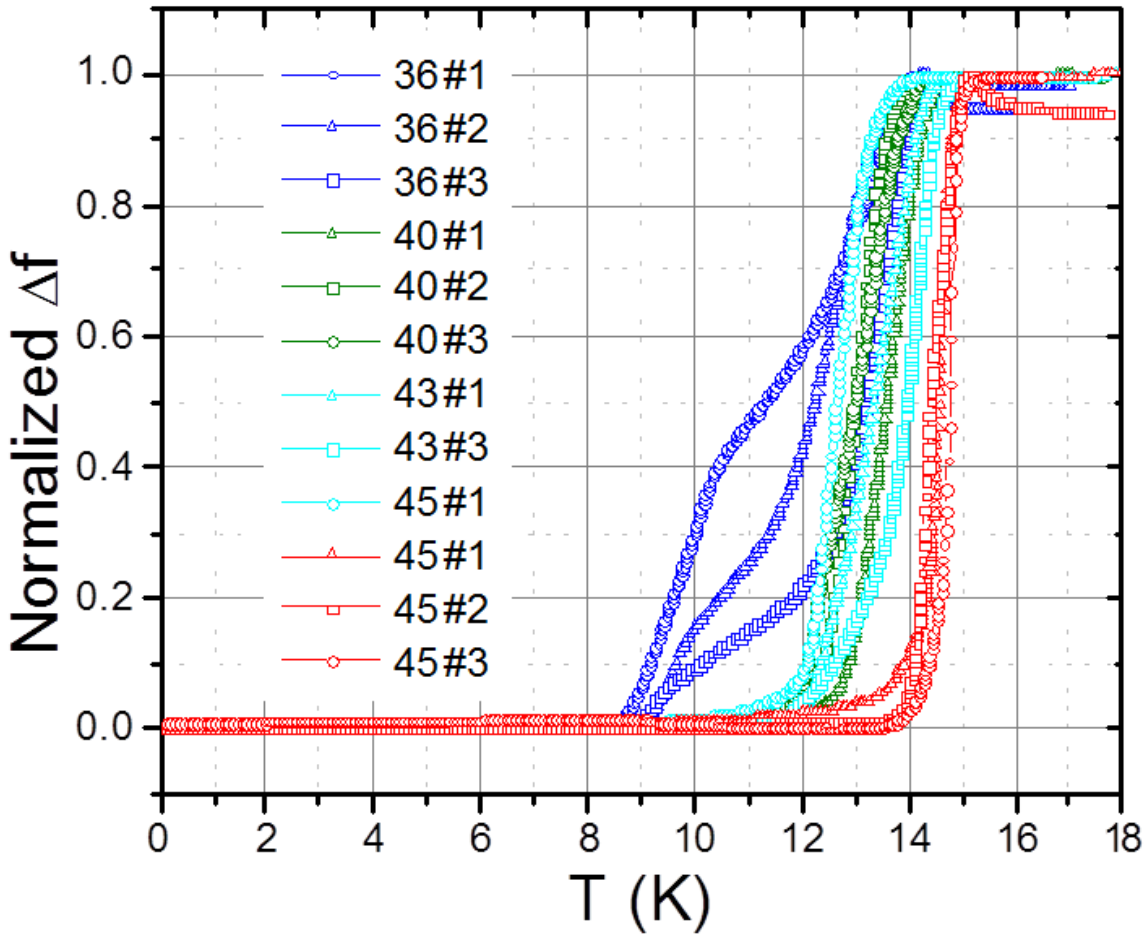

Figure 5.2 The normalized resonant frequency shift values as a function of temperature for all the sample as measured by our TDO setup. The curves for the $Fe_{1.02}(Te_{1-x}Se_x)$ samples are color grouped by their nominal Se concentration.

If we look at the normalized measured frequency shift values, illustrated in Fig. 5.2, it is easy to see that although the maximum slope seems to shift towards lower temperatures as the Se concentration is decreased (similar to critical temperature dependence observed by SQUID magnetic investigations), the onset temperature values are more or less the same for all samples consistent with the values obtained from resistivity measurements [211]. Broader transitions and additional humps can be observed in samples with 36% Se concentration which can be attributed to inhomogeneous superconducting transitions near the phase boundary where inhomogeneity is unavoidable [204, 211]. This behavior is also

observed in the ACMS data for the same samples in Fig. 4.15. Nevertheless, as we will later show, their low temperature behavior is very similar to that of the other concentrations, thus justifying their use in the current work regarding their penetration depth temperature dependence.

In Chapter III we have shown that the measured frequency shift for a plate like rectangular sample in Meissner state is directly related to the relative variation of the London penetration depth. Recalling the discussion in Section 3.5, the in-plane penetration depth variation can be calculated using:

$$\Delta f(T) = -\frac{G}{R}\Delta\lambda_{ab}(T) \qquad (5.1)$$

where G is a calibration factor depending on the dimensionality of the coil-sample setup and R is an effective dimension given by:

$$R = \frac{w}{2 - 4d/w + 2[(1 + 4(d/w)^2)]arctan(w/2d)} \qquad (2.22)$$

where w is the geometric mean of the two lateral dimensions of the rectangular shape and d is half the thickness [101].

The calibration factor G can be directly estimated by measuring the frequency change resulting from the removal of the sample from the coil at the lowest temperature as:

$$G = f(T_{min}) - f_0 \qquad (5.2)$$

where f_0 is the frequency of the empty resonator.

Our TDO setup does not include a mechanism that would allow for physical extraction of the sample *in situ*. In order to find the value for f_0 and also test the behavior of the empty TDO circuit a background run was performed prior the investigation of the $Fe_{1.02}(Te_{1-x}Se_x)$ samples. As mentioned in Chapter III, none of the 4 TDO circuits used showed any detectable temperature variation for the empty coils. A second background run was performed a couple of months apart from the first run, after all the samples have been measured. Although the conditions in which both tests were performed were similar, we observed that the empty resonator frequency values are different. There are a number of factors that will cause this drift and unfortunately this is beyond our control as the experimental condition in which two separate tests are performed can never be exactly the same. Using the background run value for f_0 in estimating the calibration factor can lead to over/under estimations.

To minimize potential over estimations in the value of G using the f_0 value from a separate run, we made use of the fact that the magnetic susceptibility of our samples in the normal state is negligible. This fact is evidentiated by the zero absolute values obtained from ACMS measurements as well as by the fact that the susceptibility of the $Fe_{1.02}(Te_{1-x}Se_x)$ samples does not show any temperature variation above T_C in both ACMS and TDO measurements (see Fig. 4.14 and 4.16). Thus, the normal state samples are not expected to change the empty resonant frequency value so, in principle, f_0 can be estimated within

the same run as the frequency of the TDO when the sample is above T_C. Consequently, we decided to use the second approach to estimate the calibration factor in our measurements. The values for G used in determining the relative penetration depth variations from Eq. 3.7 are calculated in the same run using

$$G = f(T_{min}) - f(T_{max}) \quad (5.3)$$

The estimated values for G using Eq. 5.3 together with the calculated values for the effective dimension R from Eq. 2.22 for each sample are included in Table 5.1 below. As detailed in Chapter III, our setup allows us to measure up to four samples in four separate TDO inductors within a single DR cool-down run. Consequently, our 12 different samples were measured in three separate runs over a period of approximately two weeks per run. We also included in Table 5.1 the minimum frequency value $f(T_{max})$ and maximum frequency value $f(T_{min})$ measured for each sample.

Table 5.1The effective dimension, minimum and maximum frequncy and claibration factor for all samples

sample#	TDO	R (mm)	Fmin (Hz)	Fmax (Hz)	G (Hz)	Run
40#1	3	0.18974	5.8193E6	5.86804E6	48737	1
45#1	4	0.21909	5.84952E6	5.93558E6	86060	1
36#3	4	0.21494	5.85129E6	5.92951E6	78217	1
43#2	2	0.34	5.8452E6	6.10428E6	259083	1
43#1	1	0.22978	5.90216E6	5.98856E6	86398	2
45#2	2	0.19994	5.83136E6	5.89672E6	65361	2
36#2	1	0.23979	5.89835E6	5.99314E6	94790	2
40#2	3	0.23065	5.81916E6	5.9106E6	91436	2
36#1	2	0.23495	5.82086E6	5.91841E6	97545	3
40#3	1	0.23452	5.8934E6	5.98499E6	91591	3
43#3	4	0.21494	5.84543E6	5.91189E6	66465	3
45#3	3	0.199	5.81338E6	5.85631E6	42928	3

Looking at the minimum frequency values measured with the same TDO (Table 5.1) we can see that, even though the samples in separate runs differ in size and structure, above T_C the $f(T_{max})$ values are very close together. However, in some cases, the difference is comparable to the frequency shift G which can lead to the overestimations discussed above if different run values are used. Also, considering values of G between 50 kHz and 250 kHz obtained for our specimens, from Eq. 5.1 we can estimate the sensitivity of our setup for $\Delta\lambda_{ab}$ measurements to be around 1 nm for the typical values of R of the samples shown in Table 5.1.

5.2. Temperature dependence of the in-plane London penetration depth

Using the linear dependence from Eq. 5.1 we can now plot the temperature dependence of the relative London penetration depth values in the $Fe_{1.02}(Te_{1-x}Se_x)$ single crystals measured in our TDO setup. Since $\Delta\lambda_{ab}$ has a linear dependence on the resonance frequency shift Δf, the temperature variation of the in-plane penetration depth is similar to that of the measured frequency as illustrated in Fig. 5.3 below.

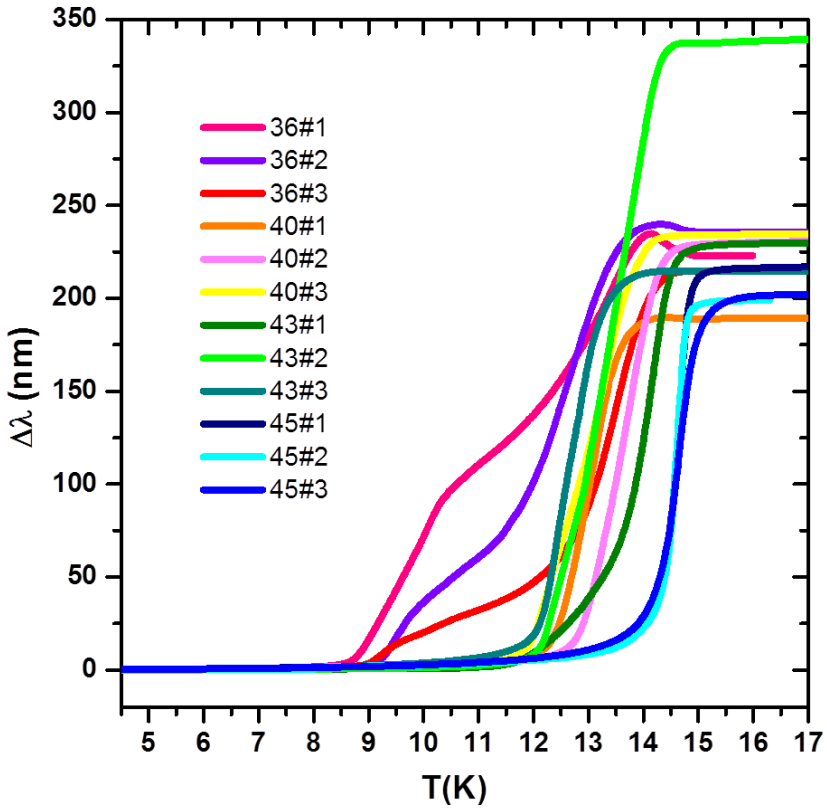

Figure 5.3 Relative temperature variation of the London penetration depth $\Delta\lambda_{ab}(T)$ in all samples

Regardless of the nominal Se concentration of the $Fe_{1.02}(Te_{1-x}Se_x)$ it is easy to see that below 8 K, the signal is more or less saturated indicating that all the sample are in a Meissner state. The temperature variation of London penetration depth represents the spectrum of the low-lying quasiparticles and only for low temperatures ($T < T_C/2$) it is possible to get meaningful information about the gap symmetry from its temperature dependence. For $T > T_C/2$ thermal effects make it difficult or even impossible to distinguish between different gap symmetries. A common choice in literature is $T < T_C/3$ which can be

explained recalling the discussion in Chapter I regarding the energy gap temperature variation for different symmetries illustrated in Fig. 1.8, where it can be seen that below $T_C/3$ the gap values are more or less saturated, regardless of the symmetry of the order parameter. We will start our analysis by focusing on the $T_{min} - T_C/3$ range. The choice of T_C is only relatively important to determine this range however, we will take the value of the transition temperatures as defined by T_C^{slope} discussed above.

The panels of Fig. 5.4 show the low temperature $\Delta\lambda_{ab}(T)$ data for the 12 samples discussed in this work, grouped by their nominal Se concentration with three samples for each.

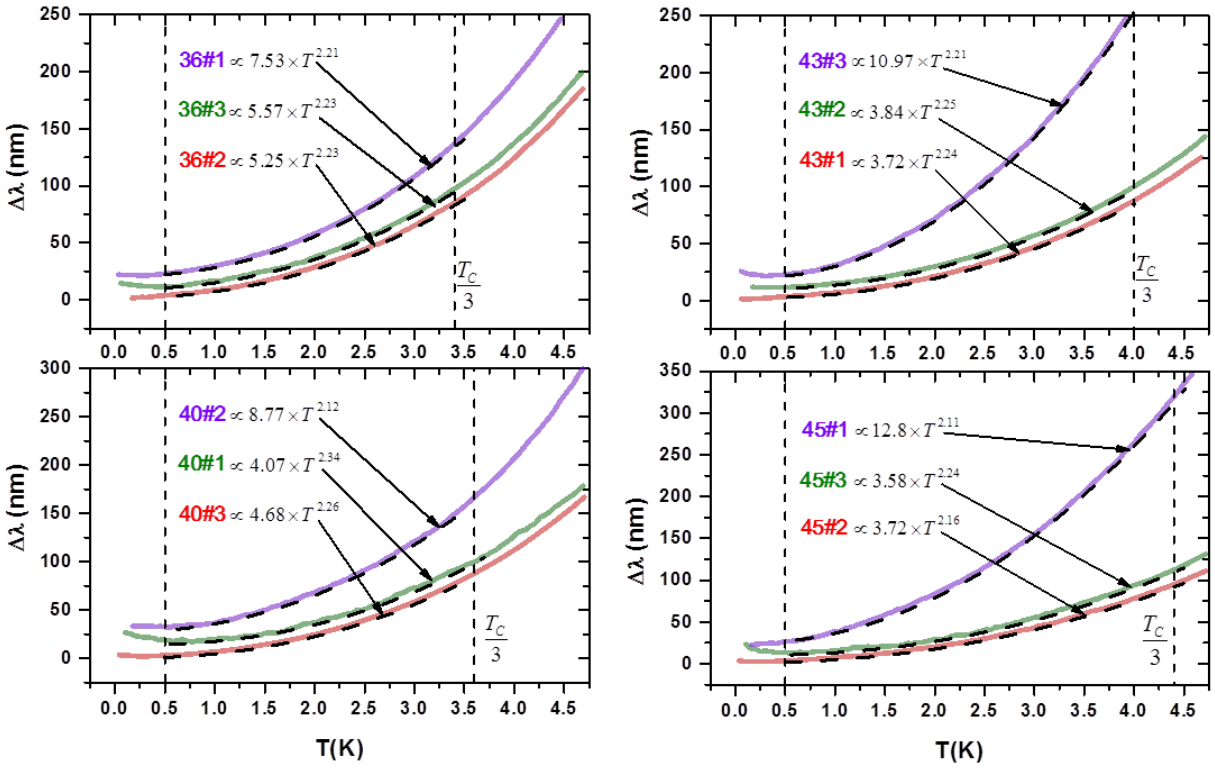

Figure 5.4 Relative variation of the in-plane London penetration depth $\Delta\lambda_{ab}(T)$ for the low temperature range for our $Fe_{1.02}(Te_{1-x}Se_x)$ samples (continuous color lines). Each panel contains the obtained data for each nominal Se concentration. The dashed black lines are allometric fits for each sample in the 0.5 K-$T_C/3$ range with the fitting parameters shown. The curves are offset by 10 nm for clarity.

Previous London penetration depth measurements using a microwave technique as well as from radio-frequency tunnel diode oscillator (TDO) measurements found that at low temperature, $\lambda(T)$ has a nearly quadratic power law behavior [21-24]. To test this we fitted our low temperature $\Delta\lambda_{ab}(T)$ data using an allometric type function of the form:

$$\Delta\lambda_{ab}(T) = \lambda_0 + A \cdot T^n \qquad (5.4)$$

where λ_0, A and n are used as fitting parameters. Since TDO measurements of $\lambda(T)$ are relative, the fitting parameter λ_0 (not to be confused with the absolute value of the London penetration depth at zero temperature) is required to make $\Delta\lambda_{ab}(T_{min})$ equal to zero i.e. $\lambda(T)$ data is relative to the minimum value. The pre-factor A and temperature exponent n can then be easily found from the relative penetration depth data. From the panels of Fig. 5.4 we can observe that, when a temperature range between 0.5 K and $T_C/3$ is used for analysis, like in most of the previous studies, $\Delta\lambda_{ab}(T)$ appears to have a well-behaved power-law dependence $\Delta\lambda_{ab}(T) = A \cdot T^n$, with the exponent n ranging from 2.16 to 2.34 for all the samples.

The $A \cdot T^n$ fit for our data is represented by dashed black lines in Fig. 5.4 together with the resulting fitting values. The pre-factor A values obtained from the fit seem to decrease as the nominal Se concentration of the sample approaches optimum doping although it can be seen that it value is considerably larger for some samples (2-3 times greater than the rest). The values we obtained for the fitting parameters in this temperature range shown in Fig. 5.4 are also summarized in Table 5.2. The value of A in most of our samples is close to those reported using TDO measurements for penetration depth in Fe chalcogenides. The deviations from the average value for some of our samples could also be caused by overestimations of the calibration factor G. Misestimations would directly affect the value of the pre-factor A however, considering the relatively small errors in estimating G for our setup, it is highly unlikely that the calibration procedure is responsible.

Moreover, most of the values are consistent with the previous reports of three different groups on TDO measurements of $\lambda_{ab}(T)$ in $Fe_{1+y}(Te_{1-x}Se_x)$ samples i.e. x = 0.37 [21] , x = 0.44 [22] and x = 0.45 [23]. They found similar power-law exponent n and some variation in the pre-factor A namely $n \sim 2.0$, $A \sim 3.7\ nm/K^n$ [21]; $n \sim 2.0$, $A \sim 0.9\ nm/K^n$ [22]; $n \sim 2.0$, $A \sim 4\ nm/K^n$ [23]. T. Klein *et al.* [22] reported on a mismatch between the pre-factor A values obtained from the $\lambda(T)$ fit of the TDO data and estimation from the first critical field using the Ginzburg-Landau theory. They suggested that the surface roughness of the samples, meaning that the volume penetrated by the magnetic field is much greater when the surface is rougher compared to the case of a perfectly flat surface, can lead to over estimation of the effective dimension R and consequently on the value of A, however, further TDO studies by K. Cho *et al.* [24] revealed that uncertainty in sample dimensions and the nature of surface roughness play only a minor role and that the calibration procedure used to obtain $\lambda(T)$ from the measured TDO frequency shift is robust.

Although the reason for the variations in the values of the pre-factor A is still unclear and we could disregard the large A samples from our investigations, the power law behavior is evident in all samples and a similar exponent can be observed, including the low Se concentration samples where inhomogeneity is unavoidable and the transition near T_C is not as abrupt as for the rest of the samples.

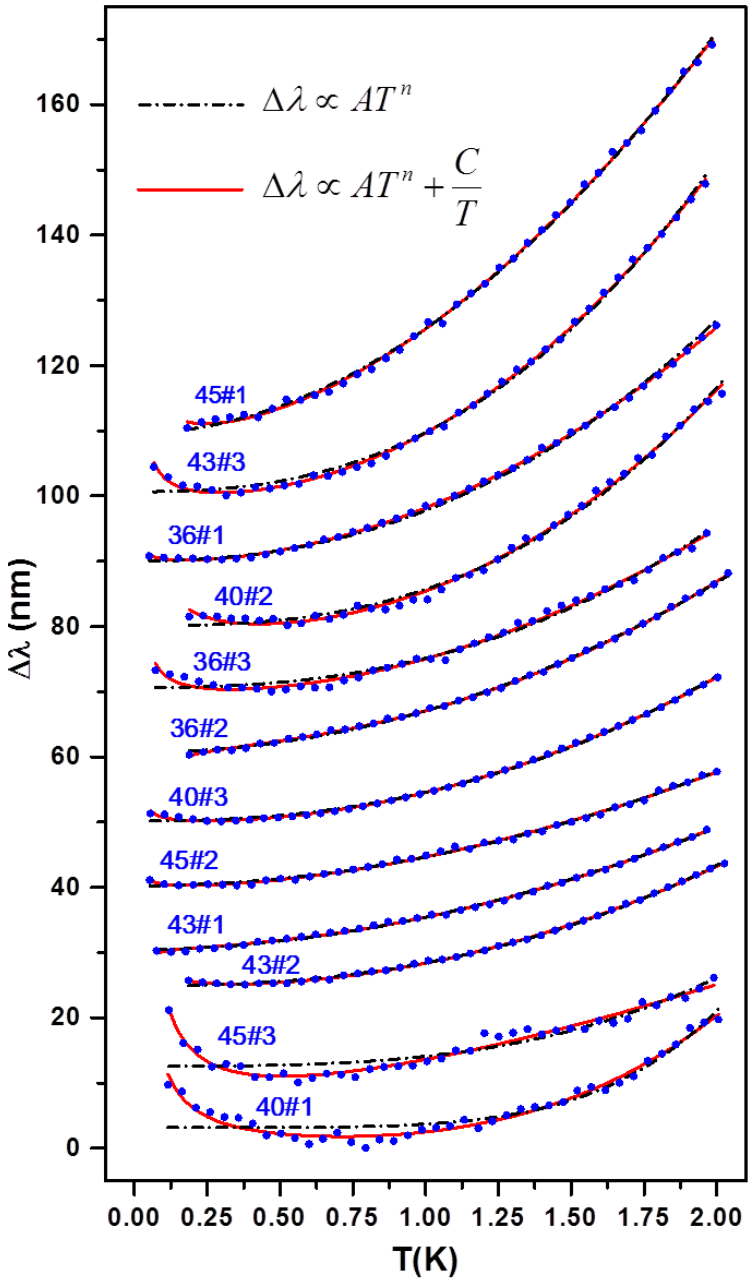

Figure 5.5 Relative variation of the in-plane London penetration depth $\Delta\lambda_{ab}(T)$ in the ultra-low temperature range for our $Fe_{1.02}(Te_{1-x}Se_x)$ samples (blue points). The power law fit $\Delta\lambda_{ab}(T) = A \cdot T^n$ from T_{min} to 2 K is represented by the black dashed lines. The red continuous lines represent the power law fit plus the additional paramagnetic contribution. The value of $\Delta\lambda_{ab}$ in each curve is shifted by 10 nm for clarity.

If we focus our attention at the London penetration depth data in the milliKelvin region, it can be observed from Fig. 5.4 that in the limit of $T \rightarrow 0$, most samples show an upturn of $\Delta\lambda_{ab}(T)$. This upturn can more easily be seen in Fig. 5.5 where we illustrated the results for all our samples in the T_{min} - 2 K low temperature range. A similar upturn at low temperatures was also reported in a previous TDO work on $Fe(Te_{0.56}Se_{0.44})$ single crystals by A. Serafin et al [22] and it was assigned to paramagnetic contribution from possible excess of Fe, occupying interstitial sites. As mentioned before, a minimum amount of excess iron is expected in all our samples and, although $y \sim 0.02$, this tiny amount can induce a significant effect on the London penetration depth measurements in $Fe_{1.02}(Te_{1-x}Se_x)$. If one were to limit the measurements to 0.5 K, as was the case for most previous TDO studies mentioned previously on similar compositions, the $\Delta\lambda_{ab}(T)$ data would seem to saturate approaching the minimum temperature. Recalling the discussion on penetration depth temperature variation from Chapter I, this would suggest a case corresponding to a symmetric fully gaped conventional BCS type behavior where, at low temperatures approaching zero, $\Delta\lambda(T)$ would saturate. However, taking data below 0.5 K it is clear from our measurements that this is not the case for the $Fe_{1.02}(Te_{1-x}Se_x)$ superconductors. The paramagnetic contribution observed in this system can cause serious issues as it can influence the observed magnetic behavior and consequently alter the diamagnetic response. Thus, it is important that measurements are performed in a complete range of temperatures even tough iron based materials are high temperature superconductors. Temperature measurements as close to zero Kelvin as possible are needed for a reliable determination of their pairing symmetry from magnetic investigations. Having taking data sufficiently low in temperature, the paramagnetic contribution in our samples can be easily subtracted if we consider a Curie type behavior for the magnetism of the excess Fe. Consequently, we fitted our low temperature data from T_{min} to 2 K with a power-law fit adding a Curie-type paramagnetic contribution of the form:

$$\Delta\lambda_{ab}(T) = A \cdot T^n + \frac{C}{T} \qquad (5.5)$$

where *C* is a paramagnetic Curie constant. The resulting fits using both dependencies from Eq. 5.4 and Eq. 5.5 are illustrated in Fig. 5.5. It is obvious that a simple power law of the form of Eq. 5.4 fails to explain the low temperature data and that, with the added paramagnetic term, Eq. 5.5 fits our very low temperature results well for all samples. The resulting values for the free parameters *A*, *n*, and *C*, respectively, are summarized in Table 5.2.

In general, the measured penetration depth λ_{meas} is related to the London penetration depth λ_L by:

$$\Delta\lambda_{meas}(T) = \Delta\lambda_L(T)\sqrt{1 + \chi_N(T)} \qquad (5.6)$$

where χ_N is the normal state magnetic susceptibility [223]. Assuming a simple Curie law of the form C/T for the normal state susceptibility, for $\chi_N(T) \ll 1$ the additional contribution to the low temperature $\Delta\lambda_{ab}(T)$ values can be estimated as being [22]:

$$\Delta\lambda_{para} = \frac{n_i \lambda_L(0) \mu_0 {\mu_e}^2}{6 k_B V_{cell} T} = \frac{C}{T} \qquad (5.7)$$

where n_i is the number of magnetic ions per unit cell, V_{cell} is the unit-cell volume (~86 Å^3), and μ_e is the effective magnetic moment of the paramagnetic ion. Using Eq. 3.13, the effective magnetic moment per unit cell can be calculated from the resulted *C* values for each sample (Table 5.2).

Table 5.2 The values of the fitting parameters of Eq. (2) for each sample and the corresponding magnetic moment.

Sample	$A(0.5K - T_c/3)$	$n(0.5K - T_c/3)$	$A(T_{min} - 2K)$	$n(T_{min} - 2K)$	$A(n = 2.15)$	$C(T_{min} - 2K)$	$\mu_{unitcell}$
36#1	7.53 ±0.1	2.21 ±0.01	8.67 ±0.13	2.07 ±0.02	8.22 ±0.03	0.079 ±0.015	$0.1\mu_B$
36#2	5.25 ±0.07	2.23 ±0.01	5.25 ±0.07	2.23 ±0.01	4.47 ±0.03	0	
36#3	5.57 ±0.1	2.23 ±0.01	6.11 ±0.39	2.1 ±0.08	5.93 ±0.7	0.41 ±0.06	$0.23\mu_B$
40#1	4.07 ±0.18	2.34 ±0.03	1.81 ±0.28	3.49 ±0.21	4.83 ±0.15	1.38 ±0.11	$0.43\mu_B$
40#2	8.77 ±0.18	2.12 ±0.02	7.38 ±0.51	2.39 ±0.09	8.71 ±0.1	1.02 ±0.21	$0.37\mu_B$
40#3	4.68 ±0.03	2.26 ±0.01	4.99 ±0.1	2.19 ±0.03	5.11 ±0.2	0.125 ±0.012	$0.13\mu_B$
43#1	3.72 ±0.04	2.24 ±0.01	3.72 ±0.04	2.24 ±0.01	4.25 ±0.04	0	
43#2	3.84 ±0.04	2.25 ±0.01	4.19 ±0.11	2.2 ±0.03	4.33 ±0.02	0.31 ±0.04	$0.2\mu_B$
43#3	10.97 ±0.16	2.21 ±0.01	10.9 ±0.26	2.26 ±0.03	11.7 ±0.07	0.45 ±0.04	$0.24\mu_B$
45#1	12.75 ±0.2	2.11 ±0.01	17.8 ±0.7	1.83 ±0.04	14.2 ±0.16	0.6 ±0.2	$0.28\mu_B$
45#2	3.72 ±0.05	2.16 ±0.01	4.86 ±0.18	1.88 ±0.05	4.05 ±0.05	0.07 ±0.02	$0.096\mu_B$
45#3	3.58 ±0.1	2.24 ±0.02	7.03 ±1.05	1.47 ±0.16	4.3 ±0.14	1.93 ±0.18	$0.5\mu_B$

The resulting values of *C*, for the samples revealing an upturn at low temperature, span between 0.07 and 1.9 nm·K, which would correspond to an average magnetic moment per unit-cell value between $0.09\mu_B$ and $0.5\mu_B$, respectively (see Table 5.2). We believe that the small excess iron *y* could account for these low values of the magnetic moment and explain the paramagnetic behavior observed in most samples at low temperatures. In reference [22] the data revealing a paramagnetic upturn in $Fe(Te_{0.56}Se_{0.44})$ single crystals at low temperature was found to be better fitted with a Curie-Weiss type equation for the magnetic contribution $C/(T - T_\Theta)$ where the Curie temperature T_Θ was found to be around 0.16 K. We considered a similar fit for our data although a Curie-Weiss type law did not significantly improve the quality of the fit in any of the samples. We will discuss this paramagnetic effect further after we focus our attention on the $\Delta\lambda_{ab}(T)$ temperature dependence and discuss possible implications on the structure of the superconducting gap Δ.

Knowing the values of *C*, the paramagnetic contribution can be subtracted from the $\Delta\lambda_{ab}(T)$ data over the full temperature range. It can be observed from the values of the fitting parameters A and n in the

50 mK - 2 K temperature interval from Table 5.2 that penetration depth still has a nearly quadratic temperature dependence for all Se concentrations.

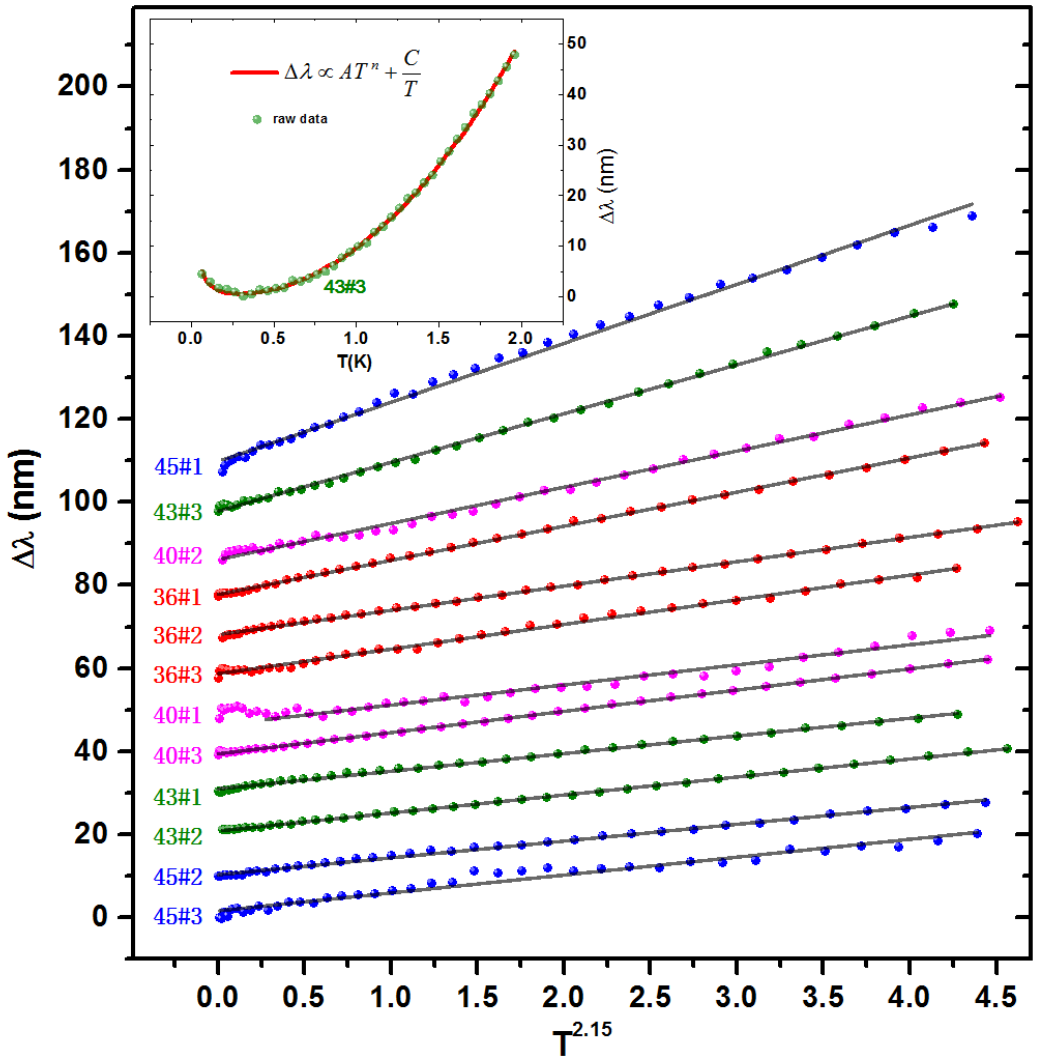

Figure 5.6 The relative variation of the in-plane penetration depth $\Delta\lambda_{ab}(T)$ data (points) at very low temperatures for all 12 samples, after subtracting the C/T paramagnetic contribution, as a function of $T^{2.15}$. The continuous lines are linear fits for the $T_{min} - 2$K temperature range with the slope values of A from Table 5.2. The data for each sample has been vertically shifted by 10nm. Inset: the raw $\Delta\lambda_{ab}(T)$ data (points) for the sample 43#3. The continuous red line represents the $A \cdot T^n + C/T$ fit of the upturn.

Except for two samples (labeled 40#1 and 45#3), where the exponent was either significantly larger ($n \approx 3.5$) or lower ($n \approx 1.5$) than the rest, we found an average value of $n = 2.15 \pm 0.25$. The experimental data was also more noisy for those two samples, therefore we may consider them as outliers,

rather than relevant for our results. Another important result of our measurements is the value of the pre-factor A which gives the magnitude of the change in penetration depth with temperature. In order to comment on the value of A and make a comparison between the samples, we considered the T^n variation of $\Delta\lambda_{ab}(T)$ with n having the value of the average exponent for all the samples i.e. $n = 2.15$. The main panel of Fig. 5.6 shows $\Delta\lambda_{ab}(T)$ after subtracting the magnetic contribution, as a function of $T^{2.15}$ where a well behaved linearity can be observed for the majority of our samples. The slope of the linear fit of the $\Delta\lambda_{ab}(T)$ vs. $T^{2.15}$ data yields the new values for the pre-factor *A* summarized in Table 5.2.

5.3. Evidence for s± symmetry in the $Fe_{1.02}(Te_{1-x}Se_x)$ system

We notice that, despite the effect of Se substitution on the critical temperature in $Fe_{1.02}(Te_{1-x}Se_x)$, we did not find a significant evolution with Se content in the exponent n. The quadratic behavior ($n \approx 2.15$) seems to be characteristic for the temperature variation of London penetration depth in all the samples. With one exception for each nominal Se concentration the results also show similar magnitudes of $\Delta\lambda_{ab}(T)$ suggested by the close values of the pre-factor $A \sim 4 - 5\ nm/K^n$ in the majority of the samples.

One possible explanation is that the scattering is strong enough that all samples are in the gapless regime. Magnetic impurities, like the excess Fe in our samples, can locally destroy the Cooper pairs. Even at $T = 0$ Cooper pairs will coexist with free electrons created in the partial breakup of the pairs. The Cooper pairs will still provide the zero resistance while the free electrons can absorb radiation at arbitrary low frequency values. Consequently, the energy gap in the elementary excitation spectrum vanishes, giving rise to gapless superconductivity. The possibility of gapless superconductivity in Fe-based superconductors is discussed in detail in [224-226]. Scattering by impurities, magnetic or non-magnetic, strongly affects the temperature dependence of London penetration depth. In the gapless limit, characterized by magnetic scattering time τ_m close to $2\hbar/\Delta_0$, where Δ_0 is the value of the gap magnitude at zero temperature, it was shown [225] that the penetration depth should have the following temperature dependence over almost the entire temperature range (from minimum T up to T_C):

$$\lambda(T) = \frac{\lambda_0}{\sqrt{1-(T/T_C)^2}} \qquad (5.8)$$

where the zero temperature value of penetration depth λ_0 is directly proportional to the scattering rate $1/\tau_m$. Considering that relative variation in penetration depth is $\Delta\lambda(T) = \lambda(T) - \lambda_0$ we have that:

$$\Delta\lambda_{ab}(T) = \lambda_0\left[\frac{1}{\sqrt{1-(T/T_C)^2}} - 1\right] \qquad (5.9)$$

To test our assumption regarding a gapless regime, we fitted our data using the temperature dependence in Eq. 5.9 using λ_0 and T_C as free fitting parameter. In Fig. 5.7 we show the result of such a fit for our $\Delta\lambda_{ab}(T)$ measurements in the $Fe_{1.02}(Te_{1-x}Se_x)$ samples with nominal Se concentrations $x = 0.36$ and $x = 40$.

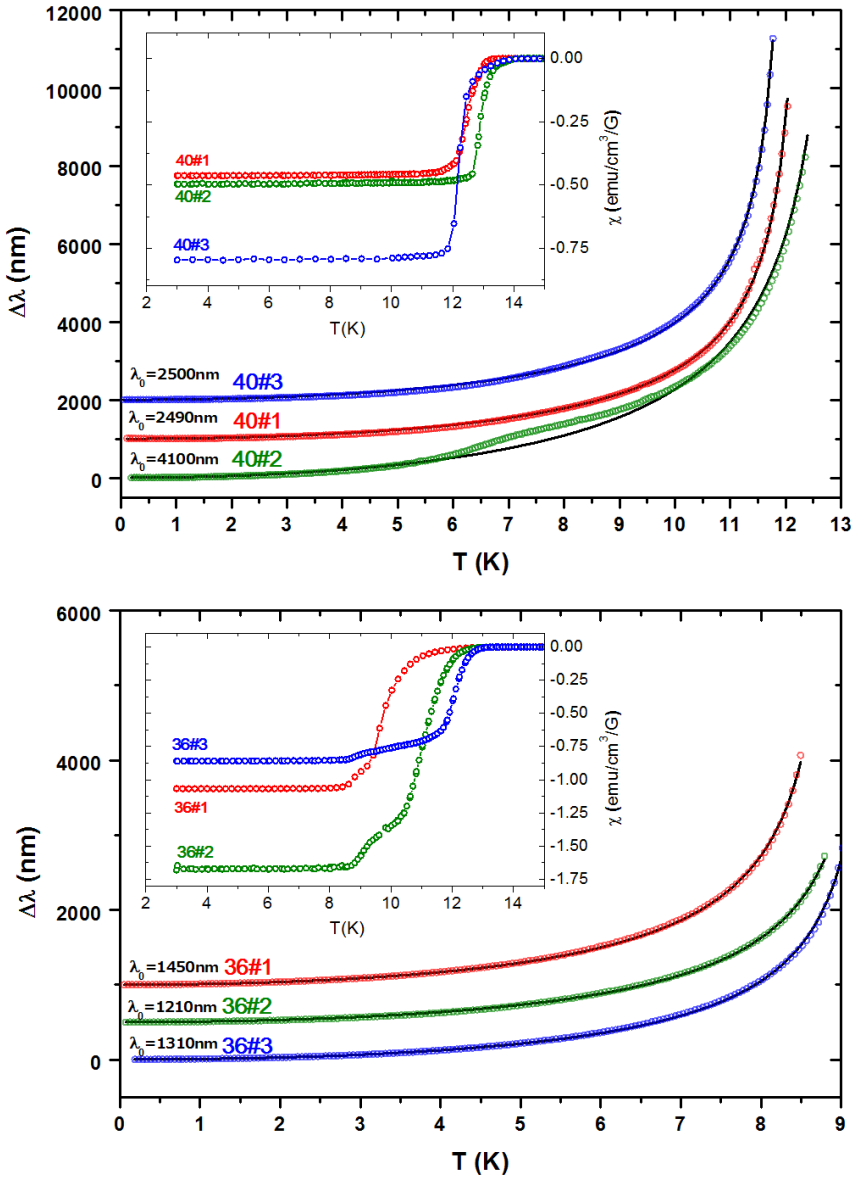

Figure 5.7 The relative temperature variation of the in-plane penetration depth $\Delta\lambda_{ab}(T)$ data (points) for the samples with x = 0.4 (top) and x=0.36 (bottom) and the $\lambda_0\left[1/\sqrt{1-(T/T_C)^2}-1\right]$ fit (continuous lines) for each sample. Inset: PPMS ACMS susceptibility per unit volume data.

Considering the large variations in T_C for different Se concentration as well as the differences in magnitude of the $\Delta\lambda_{ab}(T)$ values for different samples, in order to plot the data and corresponding fit for all the samples, we make use of the resulting fit values of λ_0 and T_C for all the samples to display our results in a linear fashion. From Eq. 5.9, the temperature can be expressed as:

$$T = T_C\sqrt{1-\left(\frac{\lambda_0}{\lambda}\right)^2} = T_C\sqrt{1-\left(\frac{\lambda_0}{\Delta\lambda+\lambda_0}\right)^2} \qquad (5.10)$$

We can thus plot the temperature value resulting from Eq. 5.10 (T_{fit}) using the resulting fit values of the free parameters λ_0 and T_C data versus the real temperature. A linear dependence of T_{fit} of temperature would suggest the penetration depth variation expressed in Eq. 5.9. In Fig. 5.8 we illustrate the resulting temperature dependence of T_{fit} for all our samples together with the resulting λ_0 and T_C values for each sample.

From figures 5.7 and 5.8 it can be seen that the equation 5.9 indeed fits very well the full temperature range for all samples regardless of Se concentration. A remarkably close value of the resulting T_C to the actual transition temperature T_C^{slope} is observed in most samples. Moreover, the fitting parameter λ_0 has very similar value for most samples, except for a few cases where it is almost twice as large. This would imply that the scattering rate $1/\tau_m$ is almost the same for all Se concentrations consistent with a close amount of excess Fe in all the samples. The value of λ_0 is however larger than the results previously reported in literature (around 500 nm) but considering that the resulting λ_0 parameter value is strongly dependent on the magnitude of $\Delta\lambda_{ab}(T)$, this could be related to the overestimation of the calibration factor.

It is however puzzling the large deviation that one sample in each batch has in the magnitude of $\Delta\lambda_{ab}(T)$ (Fig. 5.4), or in the value of λ_0 (inset of Fig. 5.8). In some of the Fe-based compounds it was proposed that electronic inhomogeneities may occur and if this were the case in our data, it would have been expected that samples with larger values of λ_0 to also have lower superconducting volume fraction or a smaller jump specific heat at T_C.

We have verified this possibility for all our samples by comparing with the specific heat data (Fig. 4.12) as well as with the magnetic susceptibility data obtained with the ACMS option in the PPMS (Fig 4.14 and insets of Fig. 5.7). We found that this is not necessarily the case as illustrated in Fig. 5.8. It can be seen for example that the sample labeled 40#2, although has the largest λ_0 i.e. temperature dependence of $\Delta\lambda_{ab}(T)$, has a superconducting volume fraction slightly larger than the sample labeled 40#1. Moreover, T_C is not smaller, nor the transition in broader in 40#2, comparing to the other samples (see Fig. 4.19).

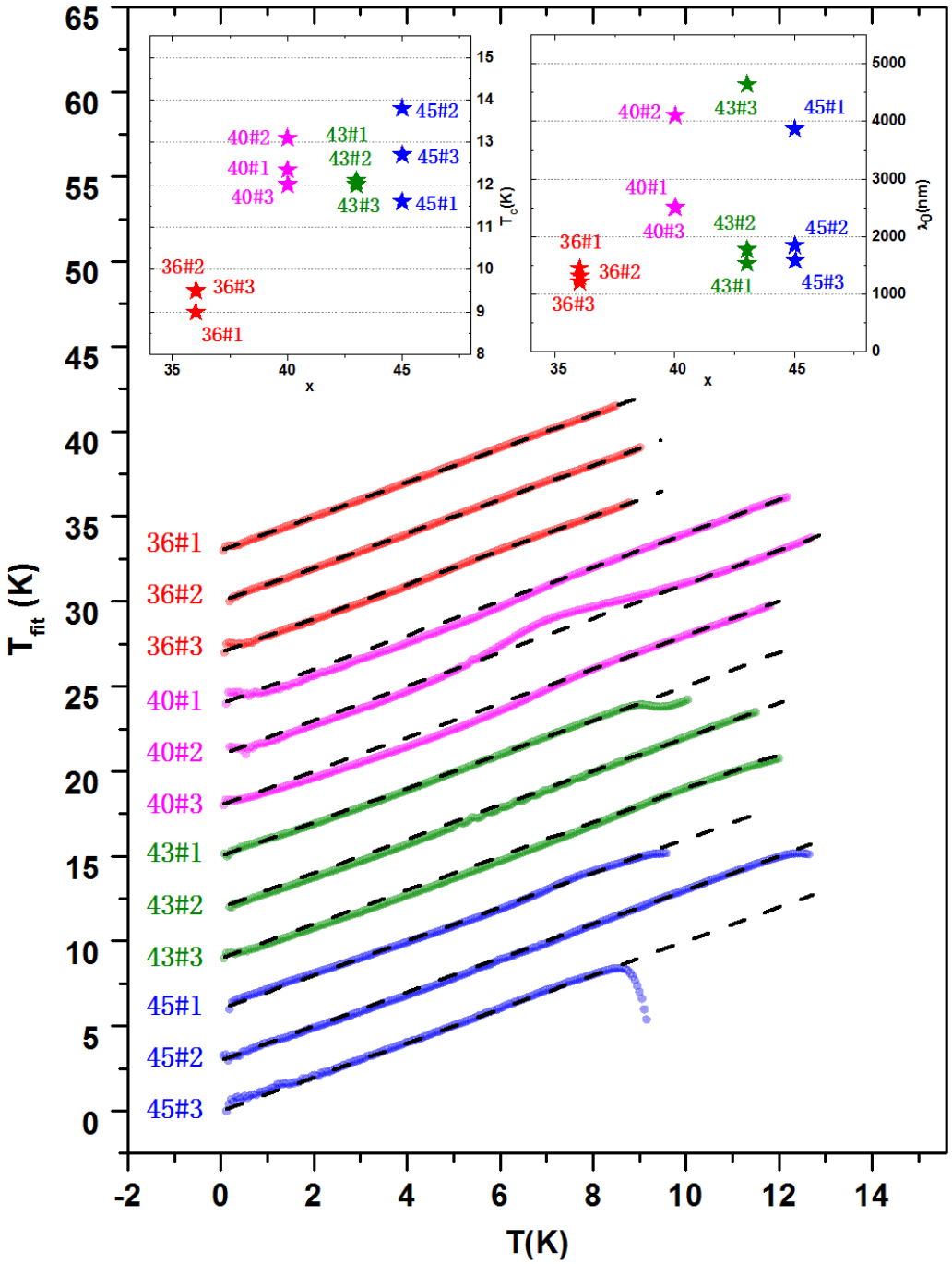

Figure 5.8 Representation of $T_{fit} = T_C\sqrt{1-(\lambda_0/\lambda)^2}$ versus T (points) for all the samples with λ_0 and T_C as the resulting fitting parameters derived from the $\Delta\lambda_{ab}(T)$ fit using Eq. 3.14. The dashed lines have unit slope and the data for each sample has been offset vertically. Left inset: The fitting parameter T_C as a function of Se concentration for all samples. Right inset: The fitting parameter λ_0 as a function of Se concentration for all samples.

The gapless regime of superconductivity was proposed by A. A. Abrikosov and L. P. Gor'kov for an s-wave superconductor with magnetic impurities in 1960 [227]. It was later shown that for a d-wave symmetry, both magnetic and non-magnetic impurities will have the same consequences [228]. However, for both symmetries, a strong dependence of the critical temperature on the scattering rate is expected in the gapless regime. Contrary, our data shows that T_C is not visibly suppressed for larger λ_0, hence larger scattering rates $1/\tau_m$. We can conclude that the most likely scenario for the large variation of λ_0 and of $\Delta\lambda_{ab}(T)$ for samples with almost same T_C is the presence of magnetic impurities in a superconductor with *s*± symmetry as proposed in Fe-based compounds [229]. Treating the $Fe_{1.02}(Te_{1-x}Se_x)$ system in the gapless regime seems to point to a *s*± wave symmetry however, a significant amount of experimental reports, which we will address next, concluded that superconductivity in $Fe_{1.02}(Te_{1-x}Se_x)$ is gapped. Consequently, we will set aside the idea of gapless superconductivity and try to understand the system and explain our results considering finite energy gap.

5.4. Evidence for nodal gap in the $Fe_{1.02}(Te_{1-x}Se_x)$ system

TDO measurements on $FeTe_{0.58}Se_{0.42}$ single crystals performed by K. Cho *et al.* [24] revealed that the average superfluid density of the system can be well described by a two-gap model where the zero temperature values of the energy gaps $\Delta_1(0)$ and $\Delta_2(0)$ are 2.5 meV $[\Delta_1(0) = 1.93k_BT_C]$ and 1.1 meV $\Delta_1(0) = 0.9k_BT_C]$, respectively. Their results suggest a nodeless two-gap pairing symmetry with strong pair breaking effects. Muon spin rotation (μSR) spectroscopy measurements [18, 19] and penetration depth TDO measurements [21] also suggest two isotropic gaps with similar zero energy magnitudes. The reported μSR studies in $FeTe_{0.5}Se_{0.5}$ [18, 19] revealed a larger gap of zero value $\Delta_1(0) \sim 2.6$ meV and a smaller magnitude gap $\Delta_2(0) \sim 0.5 - 0.87$ meV, while the penetration depth study [21] showed a 2.1 meV values for the larger gap and ~ 1.2 meV for the smaller gap. The scanning tunneling spectroscopy (STM) study on $FeTe_{0.6}Se_{0.4}$ crystals performed by T. Kato *et al.* [230] revealed a single *s*-wave gap of magnitude 2.3 meV corresponding to $\Delta(0) = 1.9k_BT_C$. Larger magnitude single or multi-gaps were reported from specific heat [215], optical conductivity [231], point-contact Andreev reflectivity [232] and angle-resolved photoemission spectroscopy (ARPES) [233] suggesting strong-coupling superconductivity.

The electronic specific heat measurements in $FeTe_{0.57}Se_{0.43}$ [215] revealed two energy gaps with $\Delta_1(0) \sim 7.4$ meV and $\Delta_2(0) \sim 5$ meV. The optical conductivity study of C. C. Homes *et al.* [231] in $FeTe_{0.55}Se_{0.45}$, two large energy gaps were also found with zero magnitudes $\Delta_1(0) \sim 5.1$ meV and $\Delta_2(0) \sim 2.5$ meV. The point-contact Andreev reflectivity in $FeTe_{0.55}Se_{0.45}$ study of W. K. Park *et al.* [232]

is consistent with single gap isotropic symmetry with $\Delta(1.7K) \sim 3.8$ meV. The ARPES instigations of K. Nakayama *et al.* [233] in $Fe_{1.03}(Te_{0.7}Se_{0.3})$ also point to an *s*-wave single gap of magnitude $\Delta(0) \sim 4$ meV. Overall, we can see that the pairing symmetry of the iron chalcogenide $Fe_{1+y}(Te_{1-x}Se_x)$ is a strongly controversial topic and the subject is still under debate. Below we will present our results and draw the conclusions resulting from our penetration depth measurements on this system.

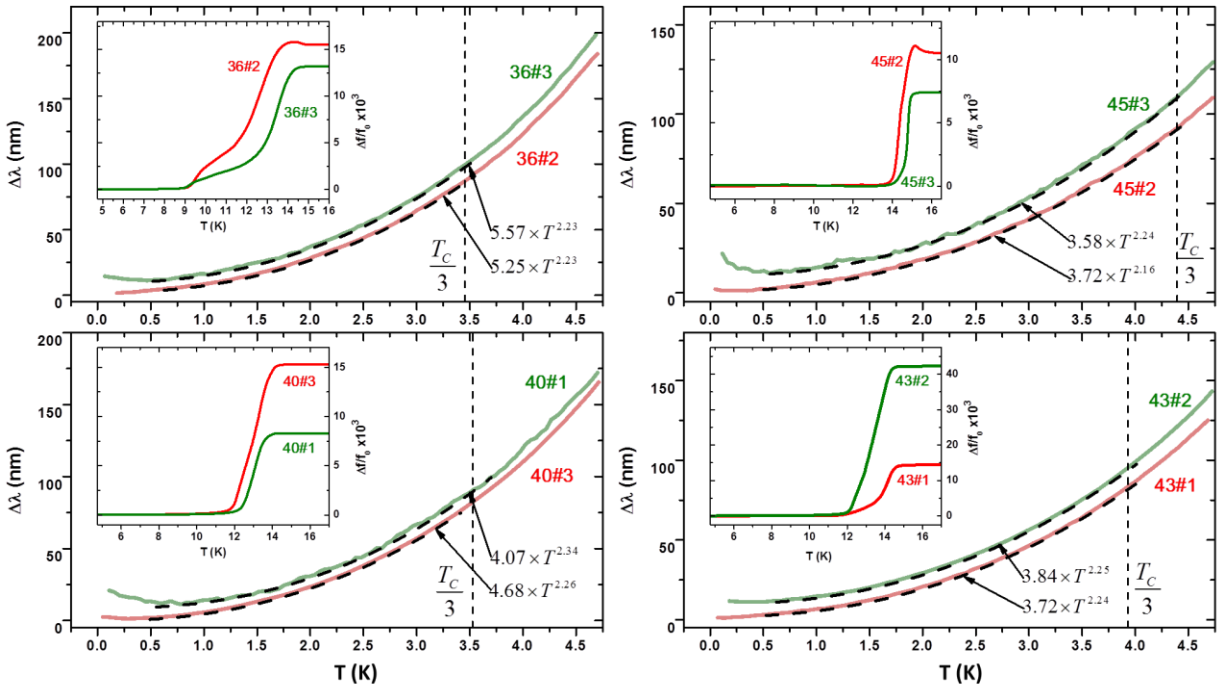

Figure 5.9 $\Delta\lambda_{ab}(T)$ (continuous lines) in $Fe_{1.02}(Te_{1-x}Se_x)$ single crystals for the low-temperature range in two different specimens for each nominal Se concentration, namely $x = 0.36$, $x = 0.40$, $x = 0.43$, and $x = 0.45$. The dashed black lines are the representative allometric fits for each sample in the 0.5 K–$Tc/3$ temperature range with the fitting parameters *A* and *n* shown. The curves have been offset by 10 nm vertically for clarity. Inset: Relative frequency variations from TDO measurements for each sample.

If we look at the $\Delta\lambda_{ab}(T)$ data in Fig. 5.9 obtained for all samples, we notice that for each nominal Se concentration, out of the three samples measured, one sample has a significantly larger magnitude i.e. value of A. Although there are a number of reasons that could cause the enhanced value of A, discussed in Section 5.2 above, we decided to disregard to higher magnitude samples from our further discussions.

We illustrate the temperature variation of the in-plane London penetration depth $\Delta\lambda_{ab}(T)$ data for the two selected samples for each doping level in Fig. 5.9. It can be seen that the two samples for each

doping level have a very similar temperature dependence even though their TDO signal over the full temperature range (see inset of each panel in Fig. 5.9) is considerably dissimilar which gives further evidence toward the robustness of the calibration method for the TDO technique. We recall that, after subtracting the paramagnetic contribution, the $\Delta\lambda_{ab}(T) = A \cdot T^n$ fit for the data below 2 K reveals that, except for two samples (labeled 40#1 and 45#3), where the exponent was either significantly larger ($n \approx 3.5$) or lower ($n \approx 1.5$) than the rest, the temperature dependence of $\Delta\lambda_{ab}$ is quadratic with average value of $n = 2.15 \pm 0.25$ (see Table 5.2).

Plotting the $\Delta\lambda_{ab}(T)$ data versus $T^{2.15}$, without the paramagnetic contribution (Fig. 5.6), a well behaved linearity is observed for all the samples. We can therefore claim that the nearly quadratic temperature dependence of penetration depth in $Fe_{1.02}(Te_{1-x}Se_x)$ is quite robust for all Se concentrations. On one hand, the power-law behavior of $\Delta\lambda(T)$ is very similar to that observed in some of the iron pnictides [234]. On the other hand though, the fact that it persists clearly at all doping levels, including optimally doped, sets them apart from pnictides, where the low-energy excitations generally show behavior consistent with isotropic gap for optimal doping and with the existence of nodes for underdoping/overdoping [235].

The values of the prefactor A for $n = 2.15$ (Table 5.2) in the pairs of close behavior samples also confirm the similarity between different Se concentrations. In each batch, the pre-factor has nearly the same value for most samples: $A = 4.7 \pm 1.2\ nm/K^n$. This result is also very different from pnictides, particularly the FeAs-122 family, where a much slower variation of penetration depth with temperature (i.e., lower value of A) was observed for optimally doped samples as reported in [226] and references therein. One possible implication is that unlike in FeAs materials, the superconducting gap in Fe chalcogenides may have the same structure for all Se concentrations, as we will discuss later.

Possible information about the superconducting gap(s) may be obtained by analyzing the temperature dependence of the superfluid density:

$$\rho_s(T) = [\lambda(0)/\lambda(T)]^2 \qquad (5.11)$$

where $\lambda(0)$ is the absolute value of London penetration depth at zero temperature. The superfluid density can be easily calculated from our $\Delta\lambda_{ab}(T)$ measurements provided that the values of $\lambda(0)$ are known. In general, the temperature dependence of ρ_s is strongly dependent on the value of $\lambda(0)$ and, as the critical temperature changes, the magnitude of $\lambda(0)$ is expected to change (Uemura scaling [236]). Most published absolute values for $\lambda_{ab}(0)$ are for the optimal (or close to) doped FeSeTe system i.e. 534(2) nm from μSR studies on $FeSe_{0.5}Te_{0.5}$ in [18], 491(8) nm from μSR studies on $FeSe_{0.4}Te_{0.6}$ in [19] and 430 ± 50 nm from Hc1 measurements on $FeSe_{0.5}Te_{0.5}$ in [23]. H. Kim *et al.* [21] report a value of 560 ± 20 nm for $FeSe_{0.37}Te_{0.43}$ from TDO measurements. From this we see that, contrary to other Fe-based

superconductors, previous reports of $\lambda(0)$ in the $Fe_{1+y}(Te_{1-x}Se_x)$ found very similar values for different values of *x* and do not suggest a systematic evolution with Se concentration. This is somewhat expected seeing how the Uemura scaling seems to be applicable only in the dirty limit and more and more deviations are being reported [73]. Seeing how our sample's Se concentrations range from 36% to 45% we expect similar values in $\lambda(0)$.

In Fig. 5.10, we show two examples, for *x* = 0.36 and 0.45, corresponding to samples 36#2 and 45#2, respectively. We calculated $\rho_s(T)$ for the two extreme values of $\lambda(0)$ reported in literature, i.e., 430 and 560 nm from Refs. [23] and [21], respectively. Similar to previous work [76] on MgB_2, we consider the popular two-gap fit:

$$\rho_s(T) = \alpha \cdot \rho_1(\Delta_1) + (1-\alpha) \cdot \rho_2(\Delta_2) \qquad (5.12)$$

where ρ_1 and ρ_2 are the superfluid density of the gap Δ_1 and Δ_2, respectively, and α represents the relative contribution of the gaps. As it can be observed from Fig. 5.10, apparently the fit reproduces well the experimental data, and we obtain very similar behavior for all doping levels: $\Delta_1/\Delta_2 \approx 3$ and $\alpha \approx 0.85$, i.e., the larger gap $\Delta_1$contributes about 85% to the superfluid density. We also found a systematic increase of $\Delta_1$with Se concentration, by about 40% at *x* = 0.45 comparing with *x* = 0.36, while Δ_2 remained almost the same. These results are valid irrespective of the choice of $\lambda(0)$, and while they may be qualitatively meaningful, there are serious issues with the fitting model. First, we mention that in all cases, both values of the gap resulted in lower than the BCS weak-coupling limit values of $1.76k_BT_C$ i.e. Δ_1 was about $1k_BT_C$ and Δ_2 about $0.3k_BT_C$.

As it was previously discussed, for the iron pnictide superconductors, this is clear indication that the model, which assumes that both gaps have BCS temperature dependence, with the same critical temperature, is not suitable for describing the superfluid density [115]. A second serious issue with this approach is that it fails to reproduce the experimental data at low temperature. We show two examples in the insets of Fig. 5.10 and further mention that this was the case for the majority of samples.

We return now to the low-temperature behavior of $\Delta\lambda_{ab}(T)$ and discuss possible implications on the structure of the superconducting gap(s). First, we recount that despite the effect of Se substitution on the critical temperature in $Fe_{1.02}(Te_{1-x}Se_x)$ we did not find a significant evolution with Se content, neither in the exponent nor in the magnitude of $\Delta\lambda_{ab}(T)$.

We proposed that the nearly quadratic temperature dependence of penetration depth in $Fe_{1.02}(Te_{1-x}Se_x)$ can be understood in terms of the pair breaking by magnetic fluctuations at (π,0). Previous neutron scattering study [237] on samples from the same growth found that the (π,0) antiferromagnetic fluctuations, originating from interstitial Fe, persist even at the optimal doping level and freeze into cluster spin-glass state at low temperature.

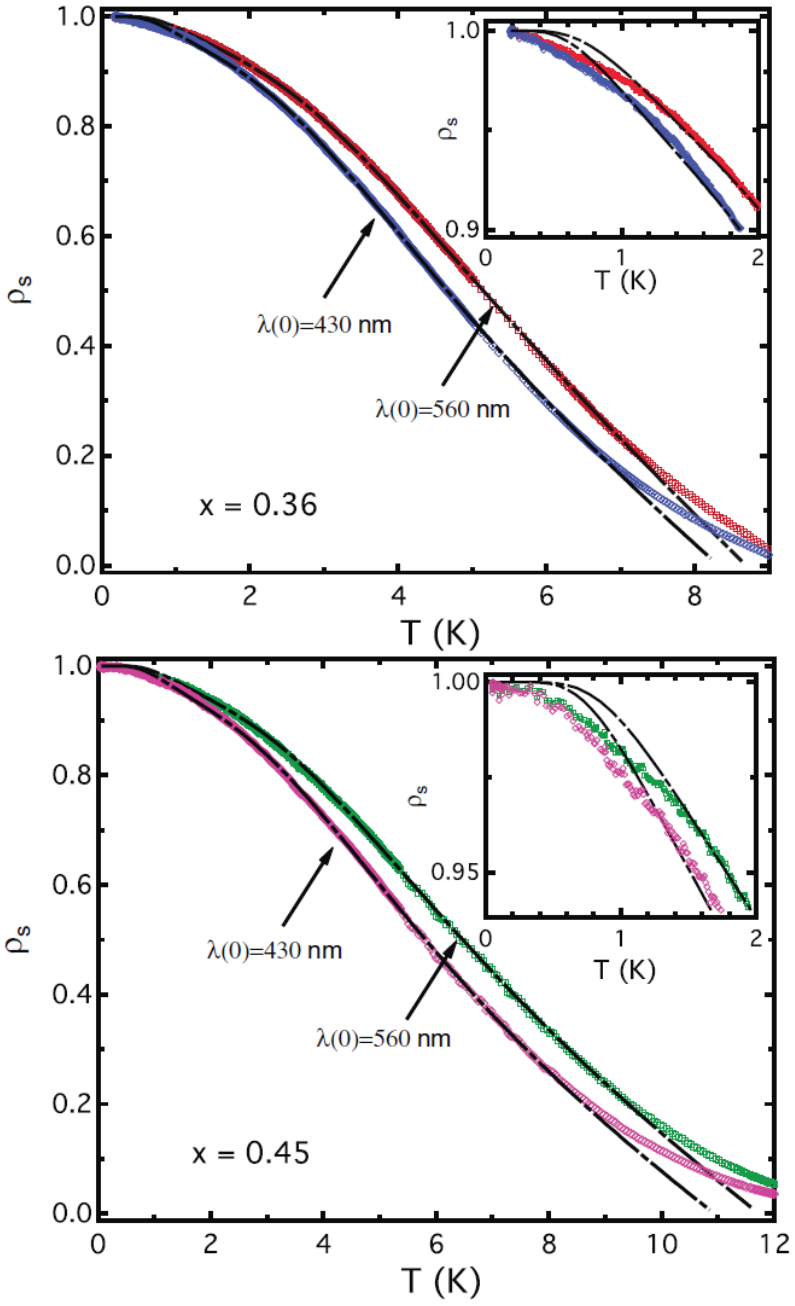

Figure 5.10 Superfluid density $\rho_s(T)$ in $Fe_{1.02}(Te_{1-x}Se_x)$ for the lowest Se doping x = 36 (sample 36#2, top) and highest Se doping x = 45 (sample 45#2, bottom) calculated from experimental data assuming two extreme values for $\lambda(0)$ reported in literature, i.e., 430 nm and 560 nm The dashed (black) lines illustrate the two-gap fit over the entire temperature range up to T_c. Inset: the low-temperature region.

Each spin cluster nucleates around interstitial Fe and involves more than 50 neighboring ions in the Fe plane. It was shown recently that such (π,0) magnetic correlations are sources of incoherent

magnetic scattering, which gives rise to charge carrier localization in the normal state and to pair breaking in the superconducting state [238]. Given that all our samples have almost the same Fe excess of about 2%, we believe that there are basically very similar sources of pair breaking for all concentrations, which produces low-energy excitations, hence power-law dependence of penetration depth as discussed in Ref. [239].

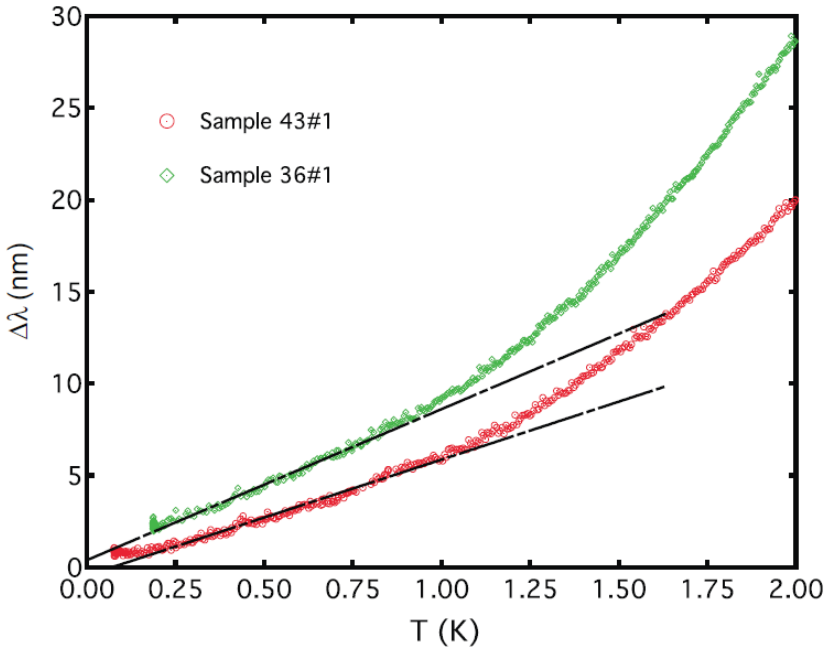

Figure 5.11 The relative variation of the in-plane penetration depth $\Delta\lambda_{ab}(T)$ raw experimental data (red points) for two samples with x = 0.36 (36#2) and x = 0.43 (43#1) at low temperatures revealing a linear region.

Additionally, we also suggest the possibility that at least one of the gaps is highly anisotropic, possibly nodal. It was shown theoretically [229] that for a superconducting gap with extended *s*-wave symmetry, without nodes, interband impurity scattering gives rise to a power-law temperature dependence of penetration depth $\Delta\lambda(T) \sim T^n$, with an exponent as low as $n \approx 1.6$. On the other hand, for an extended *s*-wave gap with nodes theory has shown [239] that ordinary disorder changes the otherwise linear behavior of $\Delta\lambda(T)$ into a power law with exponent $n \approx 2$. The situation is similar to that of the cuprate superconductors, with d-wave gap symmetry, where impurities give rise to a residual density of states [196]. Therefore, both theoretical studies may be consistent with our quadratic temperature dependence of penetration depth observed experimentally. However, we emphasize that when the fit is restricted to very low temperatures, below 1 K, $\Delta\lambda_{ab}(T)$ is almost linear in some of the samples. This can

be clearly observed from the superfluid density shown in the inset of Fig. 3.26, for 36% Se concentration. In addition, we plot in Fig. 5.11 the low-temperature region of $\Delta\lambda_{ab}(T)$ for this sample (36#2) and for another one with 43% Se (43#1), i.e., closer to optimal doping. In both cases, there is a clear linear region, albeit in a narrow temperature range.

We also emphasize that these are two samples that did not show an upturn at low temperature (Table 5.2), therefore ruling out possible artifacts due to the magnetic background subtraction. Given that for an $s\pm$ gap symmetry without nodes, theoretical studies [229] have concluded that impurity scattering cannot generate a linear $\Delta\lambda_{ab}(T)$ we believe that our data from Fig. 5.11 are rather consistent with a nodal gap. For the other samples, impurities turn the otherwise linear penetration depth into a power law, as discussed in Ref. [239]. Our finding appears to be consistent with the results from specific-heat measurements under magnetic fields [240] and with the theoretical model that predicts that gap on hole bands are fully gapped, while electron bands have nodal gaps or nodeless anisotropic gaps [241-244].

Conclusions

In the century since its discovery, superconductivity has been a field of continual development plentifully bestrewn with mystifying surprises, ground breaking theories and exciting new materials with intriguing properties. Today the abundant technological applications of superconductive materials cover a broad range of areas such as medicine, electronics, computing, energy generation and transport, nuclear fusion, particle accelerators and detectors, magnetometry and fast transportation vehicles. After 100 years of research, the scientific community agrees on one thing: the field of superconductivity is as much happenstance as it is science. Although immense progress has been made, a complete picture of the field is still being painted and a satisfactory microscopic explanation is lacking.

The discovery of high temperature cuprate superconductors in 1986 opened a new chapter in science. These new materials provided a legitimate prospect for practical applications of superconductivity but, at the same time, posed a serious challenge to the previous theoretical understanding of the field. Antecedently it was believed that phonons are responsible for the pairing of bound electron pairs causing the loss of resistance and the microscopic BCS theory successfully provided the necessary quantum mechanical explanation of superconductor properties. However, the growing experimental evidence made it clear that the conventional BCS theory, based on electron-phonon interactions, fails to describe the properties of cuprates. Their superconductivity seemed to be unconventional in nature and the picture of phonon mediated pairing had to be abandoned in favor of alternative scenarios. Considering that superconductivity in cuprates is achieved by suppressing a long-range antiferromagnetic (AFM) order of the parent compounds, through charge carrier doping or pressure, the attention focused on the interconnection between magnetism and superconductivity. The two phenomena were long thought to be antagonistic however it is now widely believed that magnetic spin fluctuations are the driving force responsible for the superconductive electron pairing in cuprates.

Investigations of the symmetry of the superconductive order parameter can be used to test the concept suggesting spin mediated pairing mechanism. By examining the symmetry of the energy gap (order parameter) in momentum space, which is related to the symmetry of the pairing wave function of the superconductive electrons, different pairing mechanisms can be tested. In conventional superconductors, the order parameter is isotropic and the pairing wave function exhibits s-wave symmetry, as expected from phonon mediated pairing. In cuprates is it now widely accepted that the wave function has a d-wave symmetry. However, some reports support the d-wave symmetry while some experimental results suggest different symmetries. Determining whether the pairing wave function has d-wave type symmetry is essential to test the spin fluctuation mechanism. If non d-wave symmetry is

involved then a spin mediated pairing mechanism can be ruled out. The ambiguity of reported experimental results regarding the pairing symmetry in cuprates makes the mechanism responsible for their superconductivity still under discussion.

A new level of complexity was introduced with the recent discovery of high transition temperature iron based superconductors. The conventional nature of superconductivity in these new materials has been quickly ruled out as experimental results revealed that phonons play a minor role in electron pairing. Similar to the case of cuprate superconductors, a large amount of evidence seems to point to a spin mediated pairing mechanism in iron based materials since the superconductivity in these systems occurs in close proximity to magnetic instabilities. The resemblance between the picture of cuprates and that of the iron-based superconductors points to a common underlying physical principle responsible for high temperature superconductivity in both. A popular concept is that the same spin fluctuations as in copper oxides are behind the mechanism responsible for their superconductivity, with a d-wave symmetry order parameter in cuprates and, the more recently proposed, s± wave type symmetry in the iron-based materials. Although a large number of experimental reports seem to point to the s± symmetry as a strong candidate, a consensus has yet to be reached in regards to the pairing symmetry of iron based superconductors. Consequently, the symmetry of the order parameter is still a largely debated topic under active research.

The mechanism responsible for high temperature superconductivity remains elusive and, as of 2010, it is considered one of the major unresolved problems in solid state physics. The newly discovered iron based superconductors could hold the key to finally elucidate the mystery around the microscopic origin of high temperature superconductivity. Consequently our research is focused on investigating the pairing symmetry of iron based superconductors.

With over 5000 publications today and 50 different superconductive iron based compounds discovered since 2008, branched into iron pnictides and iron chalcogenides, there is a wide disagreement in reported results regarding their characteristics. Moreover, the experimental evidence to date seems to point to a non-universal symmetry describing iron based superconductors. Our work wishes to contribute to a better understanding of these new materials by studying the superconductive properties of one special system, the iron chalcogenide $Fe_{1+y}(Te_{1-x}Se_x)$. With one of the simplest crystallographic structures and high quality single crystals readily available, we present a systematic study its superconductive properties focusing on the pairing symmetry as deduced from the temperature dependence of the in-plane London penetration depth in $Fe_{1+y}(Te_{1-x}Se_x)$ single crystals. Our results have been published recently in [245].

Measurements of $\Delta\lambda_{ab}(T)$ provide a powerful tool for investigating low-lying quasiparticle energy therefore they can give valuable hints on superconducting gap function symmetry. One of the most precise experimental methods for studying the low temperature dependence of London penetration depth

is the tunnel diode oscillator (TDO) technique. By measuring sample temperature induced changes in resonant frequency of a TDO circuit one can get direct information about $\Delta\lambda_{ab}(T)$. The fact that is it is a resonant method makes the TDO technique one of the most sensitive tools which can be used to measure relative changes in penetration depth as small as 1 Å.

In order to better understand the principles of a tunnel diode oscillator circuit we carried out a detailed theoretical analysis supported by additional numerical simulations. A great deal of experimental work was concentrated towards studying the susceptiveness of the TDO circuit to temperature effects and suggested means of improving technique performance in practical applications. We demonstrated the advantages of the technique in studying the magnetic susceptibility of materials as well as its limitations by means of rigorous mathematical analysis. We show how the TDO method can be used to study the susceptibility of superconductors in Meissner state and obtain direct information about the London penetration depth as well as suggest ways of improving resolution in such measurements.

Typical anisotropic crystalline superconductive samples are thin rectangular slabs. If such a specimen is placed in the uniform perpendicular excitation field of the TDO inductor the relative changes in measured frequency are directly proportional to the changes in in-plane London penetration depth. The vast majority of TDO studies make use of solenoid inductors to probe the Meissner state of superconductors. However, for flat slab like samples, the small filling factor of the coils can seriously depreciate the resolution of the method. Planar spiral inductors can be used to increase the filling factor although the complicated field distribution of the setup makes it difficult to extract quantitative results. Consequently, to increase the resolution of our TDO technique for our samples we implemented a novel coil configuration consisting of parallel planar inductors. A thorough mathematical analysis was performed to test for the appropriateness of using such geometry to extract quantitative values. We show that, regardless of the coil geometry, a proportional relation between TDO frequency changes induced by penetration depth variations stands true for flat slab like samples provided they are in a uniform perpendicular excitation field. We constructed pairs of rectangular spiral inductors for our TDO circuits and carried out numerical simulations to test for the magnetic field distribution of our coils. We showed that, using two parallel planar spiral coils, in mirror symmetry about a middle plane containing the sample, a large filling factor can be obtained while maintaining a uniform perpendicular field distribution in the sample space. As a result, the in-plane London penetration depth in rectangular flat slab shaped samples can easily be extracted and measured with great resolution.

At relatively high temperatures the thermal effects make it difficult to distinguish between different symmetries. Thus in appropriately determining the pairing symmetry from $\Delta\lambda_{ab}(T)$ measurements must be carried out at temperatures much lower than the critical temperature. Consequently, we implemented the TDO technique in a dilution refrigerator in order to study the

temperature dependence of the London penetration depth in an extensive range of temperatures, from ultra-low values of 50 mK to as high as 20K. A significant amount of effort was directed towards constructing the experimental setup for TDO measurements. Because the TDO circuit resonant frequency is extremely susceptible to temperature variations, considerable care has been taken to keep the circuit temperature constant. Moreover, to study the temperature induced sample properties exclusively, the TDO has to be thermally decoupled from the sample. This requires a solid, vibrations free structure while providing the necessary thermal separation. Considering the architecture of our dry dilution refrigerator, decoupling and stabilizing the TDO temperature, while being able to achieve a large sample temperature range, was not a trivial task. We disclose the practical details of our setup and expand on the steps taken to achieve the high frequency stability and increased performance of our TDO setup for ultra-low temperature measurements of the in-plane London penetration depth.

Most of the previously reported studies on the $Fe_{1+y}(Te_{1-x}Se_x)$ system focused on a particular Se concentration, especially close to the 50% Se optimal doping level. In our study we investigate the doping evolution of the superconductive properties of $Fe_{1+y}(Te_{1-x}Se_x)$ single crystals as derived from $\Delta\lambda_{ab}(T)$ measurements. We considered a comprehensive range of Se doping levels, spanning from 36% up to 45% optimum doping level. The high purity single crystal samples were obtained using a solid state reaction method with self-flux and carefully characterized using XRD and EDS techniques. Interstitial iron is very influential as excessive quantities can drastically alter the superconductive properties of the $Fe_{1+y}(Te_{1-x}Se_x)$ system. Consequently, the EDS analysis was used to select the minimum excess iron specimens (estimated 2% excess iron). A large number of samples were chosen and further investigated using heat capacity and ac susceptibility measurements. Based on the overall obtained results, a total of 12 samples with superior characteristics were selected, three samples for each Se doping level of 36%, 40%, 43% and 45%. All samples are thin rectangular single crystals with typical dimensions 2 x 2 x 0.1 mm,.

The TDO technique was used to study the temperature dependence of $\Delta\lambda_{ab}(T)$ in our $Fe_{1.02}(Te_{1-x}Se_x)$ samples and we found that at low temperatures (below 5 K), comparable to previous reports on the system, the London penetration depth exhibits a nearly quadratic temperature dependence. However, most reported TDO measurements are limited by a relatively high minimum temperature of 0.5 K. We found that, when extending to temperature range to ultra-low values, most samples exhibit a paramagnetic type upturn in $\Delta\lambda_{ab}(T)$ below 0.5 K. We believe the behavior is caused by the small amount of excess iron in the $Fe_{1+y}(Te_{1-x}Se_x)$ system and showed that it can have a significant influence on the higher temperature data. We also emphasize the necessity of extending the $\Delta\lambda_{ab}(T)$ measurements to ultra-low temperatures in order to extract the paramagnetic contribution from the results.

We found that, for low temperatures, our London penetration depth data can be appropriately fit with a temperature dependence of the form $\Delta\lambda_{ab}(T) = A \cdot T^n + C/T$. Upon subtracting the Curie

paramagnetic contribution, the resulting temperature dependence of $\Delta\lambda_{ab}$ is quadratic with average value of $n = 2.15 \pm 0.25$ in all of our samples. Moreover, the pre-factor has nearly the same value for most samples: $A = 4.7 \pm 1.2\, nm/K^n$, regardless of Se concentration.

Our results show that the properties of iron chalcogenides are very different from those of other iron based superconductors. The fact that the quadratic temperature dependence of $\Delta\lambda_{ab}$ in the $Fe_{1.02}(Te_{1-x}Se_x)$ system persists at all doping levels, including optimally doped, sets them apart from pnictides, where the low-energy excitations generally show behavior consistent with isotropic gap for optimal doping and with the existence of nodes for underdoping/overdoping. The similar observed magnitude in variation of penetration depth with temperature for all concentrations is also very different from pnictides, particularly the FeAs-122 family, where a much slower (i.e., lower value of A) was observed for optimally doped samples as reported in [226] and references therein. One possible implication is that unlike in FeAs materials, the superconducting gap in Fe chalcogenides may have the same structure for all Se concentrations.

Focusing on a broader temperature range (up to T_C), our $\Delta\lambda_{ab}(T)$ data seems to be consistent with the gapless regime resulting from the strong scattering induced by magnetic impurities in a superconductor with s± symmetry. However, given the fairly large amount of experimental evidence suggesting that superconductivity in the Fe_{1+y} $(Te_{1-x}Se_x)$ system is gapped, we abandoned the idea of gapless superconductivity in favor of a different scenario.

A significant amount of reported studies seem to suggest the multi gap scenario in iron based superconductors. Consequently, we aimed our attention at the temperature dependence of the superfluid density as obtained from or London penetration depth measurements. Fitting our data with the popular two gap α model, which assumes that both gaps have BCS temperature dependence, with the same critical temperature, revealed that the model is not suitable for describing the superfluid density in our samples. Moreover, we observe a linear dependence of $\Delta\lambda_{ab}(T)$ in two of our samples which did not exhibit a paramagnetic upturn at low temperatures.

Given that for an $s\pm$ gap symmetry without nodes, theoretical studies [229] have concluded that impurity scattering cannot generate a linear $\Delta\lambda_{ab}(T)$ we believe that our data is rather consistent with a nodal gap. We suggest that the power law behavior can be understood in terms of pair breaking by magnetic impurities (similar amount of excess iron for all Se concentrations) and that at least one of the gaps is highly anisotropic, possibly nodal. The impurities could be responsible for generating low-energy excitations turning an otherwise linear dependence of $\Delta\lambda_{ab}(T)$ into a quadratic power law. This may very well be the same scenario observed in cuprates more than 20 years ago when, many believed that the low temperature penetration depth was quadratic until, 7 years after their discovery, it was shown the dependence is linear and that the quadratic law was an artifact of impurity scattering.

Bibliography

[1] H. Rogalla and P. H. Kes, "100 Years of Superconductivity," ed: Taylor & Francis, 2011, pp. 145-232.

[2] C. P. Poole, "Superconductivity (Second Edition)," ed Amsterdam: Academic Press, 2007, pp. xvii-xix.

[3] J. G. Bednorz and K. A. Müller, "Possible highT c superconductivity in the Ba−La−Cu−O system," *Z. Physik B - Condensed Matter*, vol. 64, pp. 189-193, 1986/06/01 1986.

[4] C. W. Chu, L. Gao, F. Chen, Z. J. Huang, R. L. Meng, and Y. Y. Xue, "Superconductivity above 150 K in HgBa2Ca2Cu3O8+[delta] at high pressures," *Nature*, vol. 365, pp. 323-325, 09/23/print 1993.

[5] A. Schilling, M. Cantoni, J. D. Guo, and H. R. Ott, "Superconductivity above 130 K in the Hg-Ba-Ca-Cu-O system," *Nature*, vol. 363, pp. 56-58, 05/06/print 1993.

[6] L. Gao, Y. Xue, F. Chen, Q. Xiong, R. Meng, D. Ramirez, C. Chu, J. Eggert, and H. Mao, "Superconductivity up to 164 K in HgBa_ {2} Ca_ {m-1} Cu_ {m} O_ {2m+ 2+ δ}(m= 1, 2, and 3) under quasihydrostatic pressures," *Physical Review B*, vol. 50, p. 4260, 1994.

[7] S. Saxena, P. Agarwal, K. Ahilan, F. Grosche, R. Haselwimmer, M. Steiner, E. Pugh, I. Walker, S. Julian, and P. Monthoux, "Superconductivity on the border of itinerant-electron ferromagnetism in UGe2," *Nature*, vol. 406, pp. 587-592, 2000.

[8] Y. Kamihara, T. Watanabe, M. Hirano, and H. Hosono, "Iron-based layered superconductor La O1-xFx FeAs (x=0.05-0.12) with T-c=26 K," *Journal of the American Chemical Society*, vol. 130, pp. 3296-+, Mar 2008.

[9] S. R. Foltyn, L. Civale, J. L. MacManus-Driscoll, Q. X. Jia, B. Maiorov, H. Wang, and M. Maley, "Materials science challenges for high-temperature superconducting wire," *Nat Mater*, vol. 6, pp. 631-642, 09//print 2007.

[10] W. Si, S. J. Han, X. Shi, S. N. Ehrlich, J. Jaroszynski, A. Goyal, and Q. Li, "High current superconductivity in FeSe0.5Te0.5-coated conductors at 30 tesla," *Nat Commun*, vol. 4, p. 1347, 01/08/online 2013.

[11] F. Hunte, J. Jaroszynski, A. Gurevich, D. C. Larbalestier, R. Jin, A. S. Sefat, M. A. McGuire, B. C. Sales, D. K. Christen, and D. Mandrus, "Two-band superconductivity in LaFeAsO0.89F0.11 at very high magnetic fields," *Nature*, vol. 453, pp. 903-905, 06/12/print 2008.

[12] A. Subedi, L. Zhang, D. J. Singh, and M. H. Du, "Density functional study of FeS, FeSe, and FeTe: Electronic structure, magnetism, phonons, and superconductivity," *Physical Review B*, vol. 78, p. 134514, 10/13/ 2008.

[13] G. Stewart, "Superconductivity in iron compounds," *Reviews of Modern Physics*, vol. 83, p. 1589, 2011.

[14] P. M. Shirage, K. Kihou, K. Miyazawa, C.-H. Lee, H. Kito, H. Eisaki, T. Yanagisawa, Y. Tanaka, and A. Iyo, "Inverse Iron Isotope Effect on the Transition Temperature of the (Ba, K) Fe_ {2} As_ {2} Superconductor," *Physical review letters*, vol. 103, p. 257003, 2009.

[15] S. Raghu, X.-L. Qi, C.-X. Liu, D. Scalapino, and S.-C. Zhang, "Minimal two-band model of the superconducting iron oxypnictides," *Physical Review B*, vol. 77, p. 220503, 2008.

[16] C. Cao, P. Hirschfeld, and H.-P. Cheng, "Proximity of antiferromagnetism and superconductivity in LaFeAsO_ {1− x} F_ {x}: Effective Hamiltonian from ab initio studies," *Physical Review B*, vol. 77, p. 220506, 2008.

[17] R. Prozorov and R. W. Giannetta, "Magnetic penetration depth in unconventional superconductors," *Superconductor Science & Technology*, vol. 19, pp. R41-R67, Aug 2006.

[18] P. K. Biswas, G. Balakrishnan, D. M. Paul, C. V. Tomy, M. R. Lees, and A. D. Hillier, "Muon-spin-spectroscopy study of the penetration depth of FeTe0.5Se0.5," *Physical Review B,* vol. 81, Mar 2010.
[19] M. Bendele, S. Weyeneth, R. Puzniak, A. Maisuradze, E. Pomjakushina, K. Conder, V. Pomjakushin, H. Luetkens, S. Katrych, A. Wisniewski, R. Khasanov, and H. Keller, "Anisotropic superconducting properties of single-crystalline FeSe0.5Te0.5," *Physical Review B,* vol. 81, Jun 2010.
[20] H. Takahashi, Y. Imai, S. Komiya, I. Tsukada, and A. Maeda, "Anomalous temperature dependence of the superfluid density caused by a dirty-to-clean crossover in superconducting FeSe0.4Te0.6 single crystals," *Physical Review B,* vol. 84, Oct 2011.
[21] H. Kim, C. Martin, R. T. Gordon, M. A. Tanatar, J. Hu, B. Qian, Z. Q. Mao, R. W. Hu, C. Petrovic, N. Salovich, R. Giannetta, and R. Prozorov, "London penetration depth and superfluid density of single-crystalline Fe1+y(Te(1-x)Sex)and Fe1+y(Te(1-x)Sx)," *Physical Review B,* vol. 81, May 2010.
[22] A. Serafin, A. I. Coldea, A. Y. Ganin, M. J. Rosseinsky, K. Prassides, D. Vignolles, and A. Carrington, "Anisotropic fluctuations and quasiparticle excitations in FeSe0.5Te0.5," *Physical Review B,* vol. 82, Sep 2010.
[23] T. Klein, D. Braithwaite, A. Demuer, W. Knafo, G. Lapertot, C. Marcenat, P. Rodiere, I. Sheikin, P. Strobel, A. Sulpice, and P. Toulemonde, "Thermodynamic phase diagram of Fe(Se0.5Te0.5) single crystals in fields up to 28 tesla," *Physical Review B,* vol. 82, Nov 2010.
[24] K. Cho, H. Kim, M. A. Tanatar, J. Hu, B. Qian, Z. Q. Mao, and R. Prozorov, "Precision global measurements of London penetration depth in FeTe(0.58)Se(0.42)," *Physical Review B,* vol. 84, Nov 2011.
[25] F. London and H. London, "The electromagnetic equations of the supraconductor," *Proceedings of the Royal Society of London. Series A-Mathematical and Physical Sciences,* vol. 149, pp. 71-88, 1935.
[26] L. Landau and V. Ginzburg, "On the theory of superconductivity," *Journal of Experimental and Theoretical Physics (USSR),* vol. 20, p. 1064, 1950.
[27] J. Bardeen, L. N. Cooper, and J. R. Schrieffer, "Theory of superconductivity," *Physical Review,* vol. 108, p. 1175, 1957.
[28] J. Bardeen, L. N. Cooper, and J. R. Schrieffer, "Microscopic theory of superconductivity," *Physical Review,* vol. 106, pp. 162-164, 1957.
[29] H. Fröhlich, "Theory of the superconducting state. I. The ground state at the absolute zero of temperature," *Physical Review,* vol. 79, pp. 845-856, 1950.
[30] E. Maxwell, "Isotope effect in the superconductivity of mercury," *Physical Review,* vol. 78, pp. 477-477, 1950.
[31] C. Reynolds, B. Serin, W. Wright, and L. Nesbitt, "Superconductivity of isotopes of mercury," *Physical Review,* vol. 78, p. 487, 1950.
[32] L. N. Cooper, "Bound electron pairs in a degenerate Fermi gas," *Physical Review,* vol. 104, p. 1189, 1956.
[33] F. London, "On the problem of the molecular theory of superconductivity," *Physical Review,* vol. 74, p. 562, 1948.
[34] A. Pippard, "An experimental and theoretical study of the relation between magnetic field and current in a superconductor," *Proceedings of the Royal Society of London. Series A. Mathematical and Physical Sciences,* vol. 216, pp. 547-568, 1953.
[35] J. Bardeen, "Theory of superconductivity," in *Low Temperature Physics II/Kältephysik II*, ed: Springer, 1956, pp. 274-369.
[36] L. P. Gorkov, "Microscopic derivation of the Ginzburg-Landau equations in the theory of superconductivity," *Sov. Phys. JETP,* vol. 9, pp. 1364-1367, 1959.
[37] A. A. Abrikosov, "Magnetic properties of superconductors of the second group," *Sov. Phys.-JETP (Engl. Transl.);(United States),* vol. 5, 1957.

[38] U. Essmann and H. Träuble, "The direct observation of individual flux lines in type II superconductors," *Physics letters A*, vol. 24, pp. 526-527, 1967.
[39] N. Sarma, "Direct evidence for the laminar and flux line models of mixed state in type II superconductors," *Physics Letters A*, vol. 25, pp. 315-316, 1967.
[40] F. Steglich, J. Aarts, C. Bredl, W. Lieke, D. Meschede, W. Franz, and H. Schäfer, "Superconductivity in the Presence of Strong Pauli Paramagnetism: CeCu_ {2} Si_ {2}," *Physical Review Letters*, vol. 43, p. 1892, 1979.
[41] H. Ott, H. Rudigier, Z. Fisk, and J. Smith, "UBe_ {13}: An Unconventional Actinide Superconductor," *Physical review letters*, vol. 50, p. 1595, 1983.
[42] G. Stewart, "Heavy-fermion systems," *Reviews of Modern Physics*, vol. 56, p. 755, 1984.
[43] P. Morel and P. Anderson, "Calculation of the superconducting state parameters with retarded electron-phonon interaction," *Physical Review*, vol. 125, p. 1263, 1962.
[44] R. Balian and N. Werthamer, "Superconductivity with Pairs in a Relative p Wave," *Physical Review*, vol. 131, p. 1553, 1963.
[45] J. Bednorz, K. Muller, S. Uchida, H. Takagi, K. Kawasaki, and S. Tanaka, "Jap. JAP letters to appear," *z. Phys. B*, vol. 64, p. 188, 1986.
[46] C. Chu, P. Hor, R. Meng, L. Gao, Z. Huang, Wang, and YQ, "Evidence for superconductivity above 40 K in the La-Ba-Cu-O compound system," *Physical Review Letters*, vol. 58, pp. 405-407, 1987.
[47] M. K. Wu, J. Ashburn, C. Torng, P. Hor, R. Meng, L. Gao, Z. Huang, Y. Wang, and C. Chu, "Superconductivity at 93 K in a new mixed-phase Y-Ba-Cu-O compound system at ambient pressure," *Physical Review Letters*, vol. 58, pp. 908-910, 1987.
[48] H. Maeda, Y. Tanaka, M. Fukutomi, and T. Asano, "A new high-T (c) oxide superconductor without a rare earth element," *Japanese Journal of Applied Physics*, vol. 27, p. L209, 1988.
[49] R. Hazen, C. Prewitt, R. Angel, N. Ross, L. Finger, C. Hadidiacos, D. Veblen, P. Heaney, P. Hor, and R. Meng, "Superconductivity in the high-T_ {c} Bi-Ca-Sr-Cu-O system: Phase identification," *Physical review letters*, vol. 60, p. 1174, 1988.
[50] S. Putilin, E. Antipov, O. Chmaissem, and M. Marezio, "Superconductivity at 94 K in HgBa2Cu04+ δ," 1993.
[51] A. Schilling, M. Cantoni, J. Guo, and H. Ott, "Superconductivity above 130 K in the Hg-Ba-Ca-Cu-O system," *Nature*, vol. 363, pp. 56-58, 1993.
[52] D. Aoki, A. Huxley, E. Ressouche, D. Braithwaite, J. Flouquet, J.-P. Brison, E. Lhotel, and C. Paulsen, "Coexistence of superconductivity and ferromagnetism in URhGe," *Nature*, vol. 413, pp. 613-616, 2001.
[53] J. Nagamatsu, N. Nakagawa, T. Muranaka, Y. Zenitani, and J. Akimitsu, "Superconductivity at 39 K in magnesium diboride," *Nature*, vol. 410, pp. 63-64, 2001.
[54] S. Bud'Ko, G. Lapertot, C. Petrovic, C. Cunningham, N. Anderson, and P. Canfield, "Boron Isotope Effect in Superconducting MgB_ {2}," *Physical Review Letters*, vol. 86, p. 1877, 2001.
[55] Y. Kamihara, H. Hiramatsu, M. Hirano, R. Kawamura, H. Yanagi, T. Kamiya, and H. Hosono, "Iron-Based Layered Superconductor: LaOFeP," *Journal of the American Chemical Society*, vol. 128, pp. 10012-10013, 2006/08/01 2006.
[56] Y. Kamihara, T. Watanabe, M. Hirano, and H. Hosono, "Iron-Based Layered Superconductor La[O1-xFx]FeAs (x = 0.05−0.12) with Tc = 26 K," *Journal of the American Chemical Society*, vol. 130, pp. 3296-3297, 2008/03/01 2008.
[57] Z.-A. Ren, W. Lu, J. Yang, W. Yi, X.-L. Shen, Z.-C. Li, G.-C. Che, X.-L. Dong, L.-L. Sun, and F. Zhou, "Superconductivity at 55 K in iron-based F-doped layered quaternary compound Sm [O1-xFx] FeAs," *arXiv preprint arXiv:0804.2053*, 2008.
[58] A. B. Stambouli and H. Koinuma, "A primary study on a long-term vision and strategy for the realisation and the development of the Sahara Solar Breeder project in Algeria," *Renewable and Sustainable Energy Reviews*, vol. 16, pp. 591-598, 2012.

[59] J. Preskill, "Reliable quantum computers," *Proceedings of the Royal Society of London. Series A: Mathematical, Physical and Engineering Sciences,* vol. 454, pp. 385-410, 1998.
[60] G. M. Palma, K.-A. Suominen, and A. K. Ekert, "Quantum computers and dissipation," *Proceedings of the Royal Society of London. Series A: Mathematical, Physical and Engineering Sciences,* vol. 452, pp. 567-584, 1996.
[61] L. Landau, "A possible explanation of the field dependence of the susceptibility at low temperatures," *Phys. Z. Sowjet,* vol. 4, p. 675, 1933.
[62] R. Becker, G. Heller, and F. Sauter, "Über die Stromverteilung in einer supraleitenden Kugel," *Zeitschrift für Physik,* vol. 85, pp. 772-787, 1933.
[63] C. J. Gorter and H. Casimir, "On supraconductivity I," *Physica,* vol. 1, pp. 306-320, 1934.
[64] M. S. Morgan and M. Morrison, *Models as mediators: Perspectives on natural and social science* vol. 52: Cambridge University Press, 1999.
[65] W. McLean, "Superconducting Penetration Depth Measurements in Aluminium at 175 Mc/s," *Proceedings of the Physical Society,* vol. 79, p. 572, 1962.
[66] W. Heisenberg, *Two lectures*: CUP Archive, 1949.
[67] M. Born and K. C. Cheng, "Theory of superconductivity," *Nature,* vol. 161, pp. 968-9, 1948.
[68] B. Mühlschlegel, "Die thermodynamischen funktionen des supraleiters," *Zeitschrift für Physik,* vol. 155, pp. 313-327, 1959.
[69] P. Townsend and J. Sutton, "Investigation by electron tunneling of the superconducting energy gaps in Nb, Ta, Sn, and Pb," *Physical Review,* vol. 128, p. 591, 1962.
[70] G. Goll, "Unconventional superconductors: experimental investigation of the order-parameter symmetry," *Unconventional Superconductors: Experimental Investigation of the Order-Parameter Symmetry, by G. Goll. 2005 XII, 175 p. 67 illus. ISBN 3-540-28985-2. Berlin: Springer, 2005.*, vol. 1, 2005.
[71] F. Gross-Alltag, B. Chandrasekhar, D. Einzel, P. Hirschfeld, and K. Andres, "London field penetration in heavy fermion superconductors," *Z. Physik B - Condensed Matter,* vol. 82, pp. 243-255, 1991.
[72] I. Bonalde, B. D. Yanoff, M. Salamon, D. Van Harlingen, E. Chia, Z. Mao, and Y. Maeno, "Temperature Dependence of the Penetration Depth in Sr_ {2} RuO_ {4}: Evidence for Nodes in the Gap Function," *Physical Review Letters,* vol. 85, p. 4775, 2000.
[73] C. P. Poole. (2007). *Superconductivity*.
[74] J. Kortus, I. I. Mazin, K. D. Belashchenko, V. P. Antropov, and L. L. Boyer, "Superconductivity of Metallic Boron in MgB_{2}," *Physical Review Letters,* vol. 86, pp. 4656-4659, 05/14/ 2001.
[75] H. J. Choi, D. Roundy, H. Sun, M. L. Cohen, and S. G. Louie, "The origin of the anomalous superconducting properties of MgB2," *Nature,* vol. 418, pp. 758-760, 08/15/print 2002.
[76] F. Bouquet, Y. Wang, R. A. Fisher, D. G. Hinks, J. D. Jorgensen, A. Junod, and N. E. Phillips, "Phenomenological two-gap model for the specific heat of MgB," *Europhysics Letters,* vol. 56, pp. 856-862, Dec 2001.
[77] Y. A. Nefyodov, A. Shuvaev, and M. Trunin, "Microwave response of V3Si single crystals: Evidence for two-gap superconductivity," *EPL (Europhysics Letters),* vol. 72, p. 638, 2005.
[78] F. Groß-Alltag, B. S. Chandrasekhar, D. Einzel, P. J. Hirschfeld, and K. Andres, "London field penetration in heavy fermion superconductors," *Z. Physik B - Condensed Matter,* vol. 82, pp. 243-255, 1991/06/01 1991.
[79] V. P. Mineev and K. V. Samochin, *Introduction to unconventional superconductivity*: Taylor & Francis, 1999.
[80] G. Schatz, A. Weidinger, and J. A. Gardner, *Nuclear condensed matter physics: nuclear methods and applications*: John Wiley, 1996.
[81] Y. Kohori, Y. Yamato, Y. Iwamoto, T. Kohara, E. Bauer, M. Maple, and J. Sarrao, "NMR and NQR studies of the heavy fermion superconductors CeTIn_ {5}(T= Co and Ir)," *Physical Review B,* vol. 64, p. 134526, 2001.

[82] A. Amato, "Heavy-fermion systems studied by μSR technique," *Reviews of Modern Physics,* vol. 69, p. 1119, 1997.
[83] D. MacLaughlin, J. Sonier, R. Heffner, O. Bernal, B.-L. Young, M. Rose, G. Morris, E. Bauer, T. Do, and M. Maple, "Muon Spin Relaxation and Isotropic Pairing in Superconducting PrOs_ {4} Sb_ {12}," *Physical review letters,* vol. 89, p. 157001, 2002.
[84] L. Solymar, "SUPERCONDUCTIVE TUNNELLING AND APPLICATIONS," 1972.
[85] L. Greene, P. Hentges, H. Aubin, M. Aprili, E. Badica, M. Covington, M. Pafford, G. Westwood, W. Klemperer, and S. Jian, "Planar tunneling spectroscopy of high-temperature superconductors: Andreev bound states and broken symmetries," *Physica C: Superconductivity,* vol. 387, pp. 162-168, 2003.
[86] Ø. Fischer, M. Kugler, I. Maggio-Aprile, C. Berthod, and C. Renner, "Scanning tunneling spectroscopy of high-temperature superconductors," *Reviews of Modern Physics,* vol. 79, p. 353, 2007.
[87] Y. G. Naidyuk and I. I. K. Anson, *Point Contact Spectroscopy* vol. 145: Springer, 2005.
[88] R. Soulen Jr, J. Byers, M. Osofsky, B. Nadgorny, T. Ambrose, S. Cheng, P. R. Broussard, C. Tanaka, J. Nowak, and J. Moodera, "Measuring the spin polarization of a metal with a superconducting point contact," *Science,* vol. 282, pp. 85-88, 1998.
[89] A. Damascelli, Z. Hussain, and Z.-X. Shen, "Angle-resolved photoemission studies of the cuprate superconductors," *Reviews of Modern Physics,* vol. 75, pp. 473-541, 04/17/ 2003.
[90] H. Ding, M. R. Norman, J. C. Campuzano, M. Randeria, A. F. Bellman, T. Yokoya, T. Takahashi, T. Mochiku, and K. Kadowaki, "Angle-resolved photoemission spectroscopy study of the superconducting gap anisotropy in Bi_{2}Sr_{2}CaCu_{2}O_{8+x}," *Physical Review B,* vol. 54, pp. R9678-R9681, 10/01/ 1996.
[91] Z. X. Shen, D. S. Dessau, B. O. Wells, D. M. King, W. E. Spicer, A. J. Arko, D. Marshall, L. W. Lombardo, A. Kapitulnik, P. Dickinson, S. Doniach, J. DiCarlo, T. Loeser, and C. H. Park, "Anomalously large gap anisotropy in the a-b plane of Bi_{2}Sr_{2}CaCu_{2}O_{8+δ}," *Physical Review Letters,* vol. 70, pp. 1553-1556, 03/08/ 1993.
[92] A. Barone, G. Paterno, and J. Wiley, *Physics and applications of the Josephson effect* vol. 1: Wiley New York, 1982.
[93] T. Löfwander, V. Shumeiko, and G. Wendin, "Andreev bound states in high-Tc superconducting junctions," *Superconductor Science and Technology,* vol. 14, p. R53, 2001.
[94] J. Bardeen, G. Rickayzen, and L. Tewordt, "Theory of the thermal conductivity of superconductors," *Physical Review,* vol. 113, p. 982, 1959.
[95] S. Schmitt-Rink, K. Miyake, and C. Varma, "Transport and thermal properties of heavy-fermion superconductors: a unified picture," *Physical review letters,* vol. 57, p. 2575, 1986.
[96] L. F. DAVID, "Inhomogeneous d-wave Superconductors," McMaster University, 1997.
[97] H. Monien, K. Scharnberg, L. Tewordt, and D. Walker, "Specific heat, thermal conductivity, and ultrasound attenuation in d-wave superconductors," *Solid state communications,* vol. 61, pp. 581-585, 1987.
[98] D. Shoenberg, *Superconductivity, by D. Shoenberg,... [2nd edition.]*. Cambridge: University press, 1952.
[99] "http://www.comsol.com/."
[100] E. H. Brandt, "Superconductor disks and cylinders in an axial magnetic field. I. Flux penetration and magnetization curves," *Physical Review B,* vol. 58, pp. 6506-6522, 09/01/ 1998.
[101] R. Prozorov, R. W. Giannetta, A. Carrington, and F. M. Araujo-Moreira, "Meissner-London state in superconductors of rectangular cross section in a perpendicular magnetic field," *Physical Review B,* vol. 62, pp. 115-118, Jul 2000.
[102] P. A. Mansky, P. M. Chaikin, and R. C. Haddon, "Evidence for Josephson vortices in (BEDT-TTF)_{2}Cu(NCS)_{2}," *Physical Review B,* vol. 50, pp. 15929-15944, 12/01/ 1994.
[103] M. Tinkham, *Introduction to superconductivity*: DoverPublications. com, 2012.
[104] N. Bogoliubov, "On the theory of superfluidity," *J. phys.(UssR),* vol. 11, p. 4.2, 1947.

[105] N. Bogoliubov, "Nuovo Cimcnto 7, 794 (1958)," *Usp. Fiz. Nauk,* vol. 67, p. 549, 1959.
[106] R. Kubo, "Statistical-mechanical theory of irreversible processes. I. General theory and simple applications to magnetic and conduction problems," *Journal of the Physical Society of Japan,* vol. 12, pp. 570-586, 1957.
[107] N. Bogoliubov and O. Parasiuk, "On the Multiplication of the causal function in the quantum theory of fields," *Acta Math,* vol. 97, pp. 227-266, 1957.
[108] A. A. Abrikosov, "Fundamentals of the theory of metals, 1988," 1988.
[109] C. Martin, "London penetration depth in FeAs-1111 and FeAs-122 superconductors," *Oral presentation; University of New Orleans* 2009.
[110] A. Fiory, S. Martin, R. Fleming, L. Schneemeyer, J. Waszczak, A. Hebard, and S. Sunshine, "Transport, tunneling X-ray, and penetration depth studies of superconducting Bi< sub> 2+ x</sub> Sr< sub> 2− y</sub> CuO< sub> 6±δ</sub> crystals," *Physica C: Superconductivity,* vol. 162, pp. 1195-1196, 1989.
[111] W. Hardy, D. Bonn, D. Morgan, R. Liang, and K. Zhang, "Precision measurements of the temperature dependence of λ in YBa_ {2} Cu_ {3} O_ {6.95}: Strong evidence for nodes in the gap function," *Physical Review Letters,* vol. 70, p. 3999, 1993.
[112] B. Chandrasekhar and D. Einzel, "The superconducting penetration depth from the semiclassical model," *Annalen der Physik,* vol. 505, pp. 535-546, 1993.
[113] P. J. Hirschfeld and N. Goldenfeld, "EFFECT OF STRONG SCATTERING ON THE LOW-TEMPERATURE PENETRATION DEPTH OF A D-WAVE SUPERCONDUCTOR," *Physical Review B,* vol. 48, pp. 4219-4222, Aug 1993.
[114] J. R. Cooper, "Power-law dependence of the ab-plane penetration depth in Nd_{1.85}Ce_{0.15}CuO_{4-y}," *Physical Review B,* vol. 54, pp. R3753-R3755, 08/01/ 1996.
[115] V. G. Kogan, C. Martin, and R. Prozorov, "Superfluid density and specific heat within a self-consistent scheme for a two-band superconductor," *Physical Review B,* vol. 80, Jul 2009.
[116] L. Esaki, "New Phenomenon in Narrow Germanium p-n Junctions," *Physical Review,* vol. 109, pp. 603-604, 01/15/ 1958.
[117] R. Meservey and P. Tedrow, "Measurements of the kinetic inductance of superconducting linear structures," *Journal of Applied Physics,* vol. 40, pp. 2028-2034, 1969.
[118] R. Clover and W. Wolf, "Magnetic susceptibility measurements with a tunnel diode oscillator," *Review of Scientific Instruments,* vol. 41, pp. 617-621, 1970.
[119] Y. Kingma and V. Dvorak, "A negative resistance oscillator with two modes†," *International Journal of Electronics Theoretical and Experimental,* vol. 30, pp. 1-17, 1971.
[120] J. Aslam and W. Weyhmann, "A tunnel diode NMR spectrometer," *Review of Scientific Instruments,* vol. 44, p. 71, 1973.
[121] C. T. Van Degrift, "Tunnel diode oscillator for 0.001 ppm measurements at low temperatures," *Review of Scientific Instruments,* vol. 46, pp. 599-607, 1975.
[122] F. Habbal, G. Watson, and P. Elliston, "Simple cryostat for measuring rf susceptibility from 4.2 to 300 K," *Review of Scientific Instruments,* vol. 46, pp. 192-195, 1975.
[123] B. Van Riet and L. Van Gerven, "A cryogenic RE oscillator, the heart of a new NMR dispersion spectrometer," *Journal of Physics E: Scientific Instruments,* vol. 15, p. 558, 1982.
[124] R. Meservey and J. Moodera, "Performance of a magnetic susceptometer for thin films and surfaces," *Journal of applied physics,* vol. 60, pp. 3007-3014, 1986.
[125] J. G. Brisson and I. F. Silvera, "Transmission-line tunnel diode oscillator: A sensitive, fast, and flexible low-temperature detection system," *Review of scientific instruments,* vol. 57, pp. 2842-2847, 1986.
[126] G. Athas, J. Brooks, S. Klepper, S. Uji, and M. Tokumoto, "Tunnel diode oscillator application to high sensitivity de Haas–van Alphen and superconducting critical field studies of anisotropic organic conductors," *Review of scientific instruments,* vol. 64, pp. 3248-3251, 1993.

[127] S. Patnaik, K. Singh, and R. Budhani, "Apparatus for vortex dynamics studies in high< equation> T< sub> c</sub></equation> samples using close cycle refrigerator and rf oscillators," *Review of scientific instruments*, vol. 70, pp. 1494-1500, 1999.
[128] H. Srikanth, J. Wiggins, and H. Rees, "Radio-frequency impedance measurements using a tunnel-diode oscillator technique," *Review of scientific instruments*, vol. 70, pp. 3097-3101, 1999.
[129] T. Coffey, Z. Bayindir, J. DeCarolis, M. Bennett, G. Esper, and C. Agosta, "Measuring radio frequency properties of materials in pulsed magnetic fields with a tunnel diode oscillator," *Review of Scientific Instruments*, vol. 71, pp. 4600-4606, 2000.
[130] S. Gevorgyan, A. Movsisyan, G. Movsesyan, V. Shindyan, and H. Shirinyan, "On the Possibility of the Creation of Radically New Type Detectors of Particles and Radiation Based on High-T c Superconductors," *Modern Physics Letters B*, vol. 11, pp. 1123-1131, 1997.
[131] S. Gevorgyan, G. Movsesyan, A. Movsisyan, V. Tatoyan, and H. Shirinyan, "Modeling of tunnel diode oscillators and their use for some low temperature investigations," *Review of scientific instruments*, vol. 69, pp. 2550-2560, 1998.
[132] S. Gevorgyan, T. Kiss, A. Movsisyan, H. Shirinyan, Y. Hanayama, H. Katsube, T. Ohyama, M. Takeo, T. Matsushita, and K. Funaki, "Highly sensitive open-flat coil magnetometer for the λ (H, T) measurements in plate-like high-T c cuprates," *Review of Scientific Instruments*, vol. 71, pp. 1488-1494, 2000.
[133] S. Gevorgyan, H. Shirinyan, A. Manukyan, E. Sharoyan, M. Takeo, A. Polyanskii, A. Sarkisyan, and T. Matsushita, "Flat coil-based tunnel diode oscillator enabling to detect the real shape of the superconductive transition curve and capable of imaging the properties of HTSC films with high spatial resolution," *Nuclear Instruments and Methods in Physics Research Section A: Accelerators, Spectrometers, Detectors and Associated Equipment*, vol. 520, pp. 314-319, 2004.
[134] S. Gevorgyan, T. Kiss, T. Ohyama, A. Movsisyan, H. Shirinyan, V. Gevorgyan, T. Matsushita, M. Takeo, and K. Funaki, "Calibration of the open-flat coil-based tunnel diode oscillator technique (OFC magnetometer) for quantitative extraction of physical characteristics of superconductive state," *Physica C: Superconductivity*, vol. 366, pp. 6-12, 2001.
[135] S. Gevorgyan, T. Kiss, M. Inoue, T. Ohyama, M. Takeo, T. Matsushita, and K. Funaki, "Construction of the magnetic phase diagram in small-volume HTS by an OFC magnetometer," *Applied Superconductivity, IEEE Transactions on*, vol. 11, pp. 3931-3934, 2001.
[136] S. Gevorgyan, T. Kiss, M. Inoue, A. Movsisyan, H. Shirinyan, V. Gevorgyan, T. Matsushita, and M. Takeo, "Weakly expressed “paramagnetic” peculiarity of the superconductive transition detected in YBaCuO film by highly sensitive OFC-magnetometer," *Physica C: Superconductivity*, vol. 378, pp. 404-408, 2002.
[137] S. Gevorgyan, T. Kiss, M. Inoue, A. Movsisyan, H. Shirinyan, T. Harayama, T. Matsushita, T. Nishizaki, N. Kobayashi, and M. Takeo, "Peculiarities of the magnetic phase diagram in small-size untwinned YBa< sub> 2</sub> Cu< sub> 3</sub> O< sub> y</sub> crystal constructed by highly sensitive OFC-magnetometer," *Physica C: Superconductivity*, vol. 378, pp. 531-536, 2002.
[138] S. G. Gevorgyan, T. Kiss, T. Ohyama, M. Inoue, A. A. Movsisyan, H. G. Shirinyan, V. S. Gevorgyan, T. Matsushita, and M. Takeo, "New paramagnetic peculiarity of the superconductive transition detected by a highly sensitive OFC magnetometer," *Superconductor Science and Technology*, vol. 14, p. 1009, 2001.
[139] L. Spinu, H. Srikanth, E. Carpenter, and C. OConnor, "Dynamic radio-frequency transverse susceptibility in magnetic nanoparticle systems," *Journal of Applied Physics*, vol. 87, pp. 5490-5492, 2000.
[140] L. Spinu, C. O'Connor, and H. Srikanth, "Radio frequency probe studies of magnetic nanostructures," *Magnetics, IEEE Transactions on*, vol. 37, pp. 2188-2193, 2001.
[141] P. Poddar, Y. Sahoo, H. Srikanth, and P. Prasad, "Ferromagnetic ordering in nanostructured Mn-doped InP," *Applied Physics Letters*, vol. 87, pp. 062506-062506-3, 2005.

[142] L. Spinu, H. Srikanth, J. Wiemann, S. Li, J. Tang, and C. O'Connor, "Superparamagnetism and transverse susceptibility in magnetic nanoparticle systems," *Magnetics, IEEE Transactions on,* vol. 36, pp. 3032-3034, 2000.
[143] P. Poddar, J. Wilson, H. Srikanth, D. Farrell, and S. Majetich, "In-plane and out-of-plane transverse susceptibility in close-packed arrays of monodisperse Fe nanoparticles," *Physical Review B,* vol. 68, p. 214409, 2003.
[144] L. Spinu, A. Stancu, Y. Kubota, G. Ju, and D. Weller, "Vectorial mapping of exchange anisotropy in IrMn/FeCo multilayers using the reversible susceptibility tensor," *Physical Review B,* vol. 68, p. 220401, 2003.
[145] L. Spinu, H. Pham, C. Radu, J. Denardin, I. Dumitru, M. Knobel, L. Dorneles, L. Schelp, and A. Stancu, "Probing two-dimensional magnetic switching in Co⁄SiO multilayers using reversible susceptibility experiments," *Applied Physics Letters,* vol. 86, p. 012506, 2005.
[146] C. Radu, D. Cimpoesu, E. Girt, G. Ju, A. Stancu, and L. Spinu, "Reversible susceptibility studies of magnetization switching in FeCoB synthetic antiferromagnets," *Journal of applied physics,* vol. 101, pp. 09D109-09D109-3, 2007.
[147] H. Van den Berg, J. Altmann, L. Bar, G. Gieres, R. Kinder, R. Rupp, M. Vieth, and J. Wecker, "Magnetic tunnel sensors with Co-Cu artificial antiferromagnetic (AAF) hard subsystem," *Magnetics, IEEE Transactions on,* vol. 35, pp. 2892-2894, 1999.
[148] C. T. Van Degrift and D. P. Love, "Modeling of tunnel diode oscillators," *Review of Scientific Instruments,* vol. 52, pp. 712-723, 1981.
[149] "http://www.ni.com/multisim/."
[150] A. L. Dávalos, *Fundamentals of electromagnetism: vacuum electrodynamics, media, and relativity*: Springer, 1999.
[151] J. D. Jackson and R. F. Fox, "Classical electrodynamics," *American Journal of Physics,* vol. 67, p. 841, 1999.
[152] M. D. Vannette, A. S. Sefat, S. Jia, S. A. Law, G. Lapertot, S. L. Bud'ko, P. C. Canfield, J. Schmalian, and R. Prozorov, "Precise measurements of radio-frequency magnetic susceptibility in ferromagnetic and antiferromagnetic materials," *Journal of Magnetism and Magnetic Materials,* vol. 320, pp. 354-363, Feb 2008.
[153] B. T. Matthias, V. B. Compton, and E. Corenzwit, "Some new superconducting compounds," *Journal of Physics and Chemistry of Solids,* vol. 19, pp. 130-133, 4// 1961.
[154] B. S. Chandrasekhar and J. K. Hulm, "The electrical resistivity and super-conductivity of some uranium alloys and compounds," *Journal of Physics and Chemistry of Solids,* vol. 7, pp. 259-267, 11// 1958.
[155] A. W. Graham, M. Kurmoo, and P. Day, "[small beta][double prime]-(bedt-ttf)4[(H2O)Fe(C2O4)3][middle dot]PhCN: the first molecular superconductor containing paramagnetic metal ions," *Journal of the Chemical Society, Chemical Communications,* pp. 2061-2062, 1995.
[156] K. Shimizu, T. Kimura, S. Furomoto, K. Takeda, K. Kontani, Y. Onuki, and K. Amaya, "Superconductivity in the non-magnetic state of iron under pressure," *Nature,* vol. 412, pp. 316-318, 07/19/print 2001.
[157] W. Cao, L. Linjun, C. Shun, Z. Zengwei, R. Zhi, L. Yuke, W. Yuetao, L. Xiao, L. Yongkang, J. Shuai, X. Xiangfan, C. Guanghan, and X. Zhu'an, "Thorium-doping–induced superconductivity up to 56 K in Gd 1−x Th x FeAsO," *EPL (Europhysics Letters),* vol. 83, p. 67006, 2008.
[158] H. Kito, H. Eisaki, and A. Iyo, "Superconductivity at 54 K in F-Free NdFeAsO1-y," *Journal of the Physical Society of Japan,* vol. 77, p. 3707, 2008.
[159] Z. Gao, L. Wang, Y. Qi, D. Wang, X. Zhang, Y. Ma, H. Yang, and H. Wen, "Superconducting properties of granular SmFeAsO1− xFx wires with Tc= 52 K prepared by the powder-in-tube method," *Superconductor Science and Technology,* vol. 21, p. 112001, 2008.

[160] C. Wang, L. Li, S. Chi, Z. Zhu, Z. Ren, Y. Li, Y. Wang, X. Lin, Y. Luo, and S. Jiang, "Thorium-doping–induced superconductivity up to 56 K in Gd1− xThxFeAsO," *EPL (Europhysics Letters),* vol. 83, p. 67006, 2008.
[161] M. Rotter, M. Tegel, and D. Johrendt, "Superconductivity at 38 K in the Iron Arsenide (Ba_{1-x}K_{x})Fe_{2}As_{2}," *Physical Review Letters,* vol. 101, p. 107006, 09/05/ 2008.
[162] A. S. Sefat, R. Jin, M. A. McGuire, B. C. Sales, D. J. Singh, and D. Mandrus, "Superconductivity at 22 K in Co-Doped BaFe_{2}As_{2} Crystals," *Physical Review Letters,* vol. 101, p. 117004, 09/11/ 2008.
[163] Z. Ren, Q. Tao, S. Jiang, C. Feng, C. Wang, J. Dai, G. Cao, and Z. a. Xu, "Superconductivity Induced by Phosphorus Doping and Its Coexistence with Ferromagnetism in EuFe_{2}(As_{0.7}P_{0.3})_{2}," *Physical Review Letters,* vol. 102, p. 137002, 04/01/ 2009.
[164] R. Cortes-Gil, D. R. Parker, M. J. Pitcher, J. Hadermann, and S. J. Clarke, "Indifference of Superconductivity and Magnetism to Size-Mismatched Cations in the Layered Iron Arsenides Ba1−xNaxFe2As2," *Chemistry of Materials,* vol. 22, pp. 4304-4311, 2010/07/27 2010.
[165] X. C. Wang, Q. Q. Liu, Y. X. Lv, W. B. Gao, L. X. Yang, R. C. Yu, F. Y. Li, and C. Q. Jin, "The superconductivity at 18 K in LiFeAs system," *Solid State Communications,* vol. 148, pp. 538-540, 12// 2008.
[166] D. R. Parker, M. J. Pitcher, P. J. Baker, I. Franke, T. Lancaster, S. J. Blundell, and S. J. Clarke, "Structure, antiferromagnetism and superconductivity of the layered iron arsenide NaFeAs," *Chemical Communications,* pp. 2189-2191, 2009.
[167] F.-C. Hsu, J.-Y. Luo, K.-W. Yeh, T.-K. Chen, T.-W. Huang, P. M. Wu, Y.-C. Lee, Y.-L. Huang, Y.-Y. Chu, D.-C. Yan, and M.-K. Wu, "Superconductivity in the PbO-type structure α-FeSe," *Proceedings of the National Academy of Sciences,* vol. 105, pp. 14262-14264, September 23, 2008 2008.
[168] T. Imai, K. Ahilan, F. L. Ning, T. M. McQueen, and R. J. Cava, "Why Does Undoped FeSe Become a High-T_{c} Superconductor under Pressure?," *Physical Review Letters,* vol. 102, p. 177005, 04/29/ 2009.
[169] B. C. Sales, A. S. Sefat, M. A. McGuire, R. Y. Jin, D. Mandrus, and Y. Mozharivskyj, "Bulk superconductivity at 14 K in single crystals of Fe1+yTexSe1-x," *Physical Review B,* vol. 79, Mar 2009.
[170] H. Ogino, Y. Matsumura, Y. Katsura, K. Ushiyama, S. Horii, K. Kishio, and J.-i. Shimoyama, "Superconductivity at 17 K in (Fe2P2)(Sr4Sc2O6): a new superconducting layered pnictide oxide with a thick perovskite oxide layer," *Superconductor Science and Technology,* vol. 22, p. 075008, 2009.
[171] X. Zhu, F. Han, G. Mu, P. Cheng, B. Shen, B. Zeng, and H.-H. Wen, "Transition of stoichiometric Sr_{2}VO_{3}FeAs to a superconducting state at 37.2 K," *Physical Review B,* vol. 79, p. 220512, 06/22/ 2009.
[172] S. Sato, H. Ogino, N. Kawaguchi, Y. Katsura, K. Kishio, J.-i. Shimoyama, H. Kotegawa, and H. Tou, "Superconductivity in a new iron pnictide oxide (Fe2As2)(Sr4 (Mg, Ti) 2O6)," *Superconductor Science and Technology,* vol. 23, p. 045001, 2010.
[173] A. Ricci, N. Poccia, B. Joseph, G. Arrighetti, L. Barba, J. Plaisier, G. Campi, Y. Mizuguchi, H. Takeya, and Y. Takano, "Intrinsic phase separation in superconducting K0. 8Fe1. 6Se2 (Tc= 31.8 K) single crystals," *Superconductor Science and Technology,* vol. 24, p. 082002, 2011.
[174] C.-H. Li, B. Shen, F. Han, X. Zhu, and H.-H. Wen, "Transport properties and anisotropy of Rb_{1-x}Fe_{2-y}Se_{2} single crystals," *Physical Review B,* vol. 83, p. 184521, 05/26/ 2011.
[175] I. R. Shein and A. L. Ivanovskii, "Structural, electronic properties and intra-atomic bonding in new ThCr2Si2-like arsenides SrRu2As2, BaRu2As2, SrRh2As2 and BaRh2As2 from first principles calculations," *Solid State Communications,* vol. 149, pp. 1860-1865, 11// 2009.
[176] Z. Deng, X. Wang, Q. Liu, S. Zhang, Y. Lv, J. Zhu, R. Yu, and C. Jin, "A new," *EPL (Europhysics Letters),* vol. 87, p. 37004, 2009.

[177] W. Bao, Q. Huang, G. Chen, M. Green, D.-M. Wang, J.-B. He, X. Wang, and Y. Qiu, "A novel large moment antiferromagnetic order in K0. 8Fe1. 6Se2 superconductor," *Chin. Phys. Lett,* vol. 28, p. 2, 2011.
[178] S. Lebegue, "Electronic structure and properties of the Fermi surface of the superconductor LaOFeP," *Physical Review B,* vol. 75, p. 035110, 2007.
[179] D. J. Singh and M.-H. Du, "Density Functional Study of LaFeAsO_ {1-x} F_ {x}: A Low Carrier Density Superconductor Near Itinerant Magnetism," *Physical Review Letters,* vol. 100, p. 237003, 2008.
[180] A. Subedi, L. Zhang, D. J. Singh, and M.-H. Du, "Density functional study of FeS, FeSe, and FeTe: Electronic structure, magnetism, phonons, and superconductivity," *Physical Review B,* vol. 78, p. 134514, 2008.
[181] I. Mazin, D. J. Singh, M. Johannes, and M.-H. Du, "Unconventional Superconductivity with a Sign Reversal in the Order Parameter of LaFeAsO_ {1-x} F_ {x}," *Physical Review Letters,* vol. 101, p. 057003, 2008.
[182] D. Lu, M. Yi, S.-K. Mo, A. Erickson, J. Analytis, J.-H. Chu, D. Singh, Z. Hussain, T. Geballe, and I. Fisher, "Electronic structure of the iron-based superconductor LaOFeP," *Nature,* vol. 455, pp. 81-84, 2008.
[183] K. Terashima, Y. Sekiba, J. Bowen, K. Nakayama, T. Kawahara, T. Sato, P. Richard, Y.-M. Xu, L. Li, and G. Cao, "Fermi surface nesting induced strong pairing in iron-based superconductors," *Proceedings of the National Academy of Sciences,* vol. 106, pp. 7330-7333, 2009.
[184] J. Paglione and R. L. Greene, "High-temperature superconductivity in iron-based materials," *Nature Physics,* vol. 6, pp. 645-658, 2010.
[185] A. V. Chubukov, D. Efremov, and I. Eremin, "Magnetism, superconductivity, and pairing symmetry in iron-based superconductors," *Physical Review B,* vol. 78, p. 134512, 2008.
[186] A. Kordyuk, "Iron-based superconductors: Magnetism, superconductivity, and electronic structure (Review Article)," *Low Temperature Physics,* vol. 38, p. 888, 2012.
[187] M. R. Norman, "High-temperature superconductivity in the iron pnictides," *Physics,* vol. 1, p. 21, 2008.
[188] C. Day, "Iron-based superconductors," *Physics today,* vol. 62, pp. 36-40, 2009.
[189] H. Luetkens, H. H. Klauss, M. Kraken, F. J. Litterst, T. Dellmann, R. Klingeler, C. Hess, R. Khasanov, A. Amato, C. Baines, M. Kosmala, O. J. Schumann, M. Braden, J. Hamann-Borrero, N. Leps, A. Kondrat, G. Behr, J. Werner, and B. Buchner, "The electronic phase diagram of the LaO1-xFxFeAs superconductor," *Nat Mater,* vol. 8, pp. 305-309, 04//print 2009.
[190] H. Chen, Y. Ren, Y. Qiu, W. Bao, R. Liu, G. Wu, T. Wu, Y. Xie, X. Wang, and Q. Huang, "Coexistence of the spin-density wave and superconductivity in Ba1− xKxFe2As2," *EPL (Europhysics Letters),* vol. 85, p. 17006, 2009.
[191] Y. Mizuguchi, K. Deguchi, Y. Kawasaki, T. Ozaki, M. Nagao, S. Tsuda, T. Yamaguchi, and Y. Takano, "Superconductivity in oxygen-annealed< equation>< font face='verdana'> FeTe< sub> 1-x</sub>< font face='verdana'> S< sub> x</sub></equation> single crystal," *Journal of Applied Physics,* vol. 109, pp. 013914-013914-4, 2011.
[192] D. R. Parker, M. J. Smith, T. Lancaster, A. J. Steele, I. Franke, P. J. Baker, F. L. Pratt, M. J. Pitcher, S. J. Blundell, and S. J. Clarke, "Control of the competition between a magnetic phase and a superconducting phase in cobalt-doped and nickel-doped NaFeAs using electron count," *Physical review letters,* vol. 104, p. 057007, 2010.
[193] L. Boeri, O. V. Dolgov, and A. A. Golubov, "Electron–phonon properties of pnictide superconductors," *Physica C: Superconductivity,* vol. 469, pp. 628-634, //1.
[194] A. V. Chubukov, "Renormalization group analysis of competing orders and the pairing symmetry in Fe-based superconductors," *Physica C: Superconductivity,* vol. 469, pp. 640-650, //1.
[195] K. Kuroki and H. Aoki, "Unconventional pairing originating from disconnected Fermi surfaces in the iron-based superconductor," *Physica C: Superconductivity,* vol. 469, pp. 635-639, //1.

[196] P. J. Hirschfeld, M. M. Korshunov, and I. I. Mazin, "Gap symmetry and structure of Fe-based superconductors," *Reports on Progress in Physics*, vol. 74, p. 124508, 2011.
[197] A. Christianson, E. Goremychkin, R. Osborn, S. Rosenkranz, M. Lumsden, C. Malliakas, I. Todorov, H. Claus, D. Chung, and M. Kanatzidis, "Unconventional superconductivity in Ba0. 6K0. 4Fe2As2 from inelastic neutron scattering," *Nature*, vol. 456, pp. 930-932, 2008.
[198] M. Korshunov and I. Eremin, "Theory of magnetic excitations in iron-based layered superconductors," *Physical Review B*, vol. 78, p. 140509, 2008.
[199] D. Fruchart, "Antiferromagnetic Structure of Fe 1. 125 Te Along With a Monoclinic Deformation," *Materials Research Bulletin*, vol. 10, pp. 169-174, 1975.
[200] W. Bao, Y. Qiu, Q. Huang, M. Green, P. Zajdel, M. Fitzsimmons, M. Zhernenkov, S. Chang, M. Fang, and B. Qian, "Tunable ($\delta\pi$, $\delta\pi$)-type antiferromagnetic order in α-Fe (Te, Se) superconductors," *Physical review letters*, vol. 102, p. 247001, 2009.
[201] M. J. Pitcher, D. R. Parker, P. Adamson, S. J. Herkelrath, A. T. Boothroyd, R. M. Ibberson, M. Brunelli, and S. J. Clarke, "Structure and superconductivity of LiFeAs," *Chemical Communications*, pp. 5918-5920, 2008.
[202] F. C. Hsu, J. Y. Luo, K. W. Yeh, T. K. Chen, T. W. Huang, P. M. Wu, Y. C. Lee, Y. L. Huang, Y. Y. Chu, D. C. Yan, and M. K. Wu, "Superconductivity in the PbO-type structure alpha-FeSe," *Proceedings of the National Academy of Sciences of the United States of America*, vol. 105, pp. 14262-14264, Sep 2008.
[203] S. Medvedev, T. M. McQueen, I. A. Troyan, T. Palasyuk, M. I. Eremets, R. J. Cava, S. Naghavi, F. Casper, V. Ksenofontov, G. Wortmann, and C. Felser, "Electronic and magnetic phase diagram of beta-Fe1.01Se with superconductivity at 36.7 K under pressure," *Nature Materials*, vol. 8, pp. 630-633, Aug 2009.
[204] J. Hu, G. C. Wang, B. Qian, and Z. Q. Mao, "Inhomogeneous superconductivity induced by interstitial Fe deintercalation in oxidizing-agent-annealed and HNO3-treated Fe1+y(Te1-xSex)," *Superconductor Science & Technology*, vol. 25, Aug 2012.
[205] Y. Xia, D. Qian, L. Wray, D. Hsieh, G. Chen, J. Luo, N. Wang, and M. Hasan, "Fermi Surface Topology and Low-Lying Quasiparticle Dynamics of Parent Fe_ {1+ x} Te/Se Superconductor," *Physical review letters*, vol. 103, p. 037002, 2009.
[206] M. H. Fang, H. M. Pham, B. Qian, T. J. Liu, E. K. Vehstedt, Y. Liu, L. Spinu, and Z. Q. Mao, "Superconductivity close to magnetic instability in Fe(Se1-xTex)(0.82)," *Physical Review B*, vol. 78, Dec 2008.
[207] K. W. Yeh, T. W. Huang, Y. L. Huang, T. K. Chen, F. C. Hsu, P. M. Wu, Y. C. Lee, Y. Y. Chu, C. L. Chen, J. Y. Luo, D. C. Yan, and M. K. Wu, "Tellurium substitution effect on superconductivity of the alpha-phase iron selenide," *Epl*, vol. 84, Nov 2008.
[208] C. de la Cruz, Q. Huang, J. W. Lynn, J. Li, W. R. Ii, J. L. Zarestky, H. A. Mook, G. F. Chen, J. L. Luo, N. L. Wang, and P. Dai, "Magnetic order close to superconductivity in the iron-based layered LaO1-xFxFeAs systems," *Nature*, vol. 453, pp. 899-902, 06/12/print 2008.
[209] J. Zhao, D.-X. Yao, S. Li, T. Hong, Y. Chen, S. Chang, I. W Ratcliff, J. Lynn, H. Mook, and G. Chen, "Low Energy Spin Waves and Magnetic Interactions in SrFe_ {2} As_ {2}," *Physical review letters*, vol. 101, p. 167203, 2008.
[210] S. Li, C. de La Cruz, Q. Huang, Y. Chen, J. Lynn, J. Hu, Y.-L. Huang, F.-C. Hsu, K.-W. Yeh, and M.-K. Wu, "First-order magnetic and structural phase transitions in Fe_ {1+ y} Se_ {x} Te_ {1− x}," *Physical Review B*, vol. 79, p. 054503, 2009.
[211] T. J. Liu, J. Hu, B. Qian, D. Fobes, Z. Q. Mao, W. Bao, M. Reehuis, S. A. Kimber, K. Prokes, S. Matas, D. N. Argyriou, A. Hiess, A. Rotaru, H. Pham, L. Spinu, Y. Qiu, V. Thampy, A. T. Savici, J. A. Rodriguez, and C. Broholm, "From (pi,0) magnetic order to superconductivity with (pi,pi) magnetic resonance in Fe(1.02)Te(1-x)Se(x)," *Nat Mater*, vol. 9, pp. 716-20, Sep 2010.
[212] Y. Qiu, W. Bao, Y. Zhao, C. Broholm, V. Stanev, Z. Tesanovic, Y. Gasparovic, S. Chang, J. Hu, and B. Qian, "Spin Gap and Resonance at the Nesting Wave Vector in Superconducting FeSe_ {0.4} Te_ {0.6}," *Physical review letters*, vol. 103, p. 067008, 2009.

[213] T. Hanaguri, S. Niitaka, K. Kuroki, and H. Takagi, "Unconventional s-Wave Superconductivity in Fe(Se,Te)," *Science,* vol. 328, pp. 474-476, Apr 2010.
[214] C. L. Song, Y. L. Wang, P. Cheng, Y. P. Jiang, W. Li, T. Zhang, Z. Li, K. He, L. L. Wang, J. F. Jia, H. H. Hung, C. J. Wu, X. C. Ma, X. Chen, and Q. K. Xue, "Direct Observation of Nodes and Twofold Symmetry in FeSe Superconductor," *Science,* vol. 332, pp. 1410-1413, Jun 2011.
[215] J. Hu, T. J. Liu, B. Qian, A. Rotaru, L. Spinu, and Z. Q. Mao, "Calorimetric evidence of strong-coupling multiband superconductivity in Fe(Te0.57Se0.43) single crystal," *Physical Review B,* vol. 83, Apr 2011.
[216] B. Zeng, G. Mu, H. Luo, T. Xiang, I. Mazin, H. Yang, L. Shan, C. Ren, P. Dai, and H.-H. Wen, "Anisotropic structure of the order parameter in FeSe0. 45Te0. 55 revealed by angle-resolved specific heat," *Nature communications,* vol. 1, p. 112, 2010.
[217] Y. Zhang, J. Wei, H. Ou, J. Zhao, B. Zhou, F. Chen, M. Xu, C. He, G. Wu, and H. Chen, "Unusual Doping Dependence of the Electronic Structure and Coexistence of Spin-Density-Wave and Superconductor Phases in Single Crystalline Sr_ {1-x} K_ {x} Fe_ {2} As_ {2}," *Physical review letters,* vol. 102, p. 127003, 2009.
[218] B. Mok, S. Rao, M. Ling, K. Wang, C. Ke, P. Wu, C. Chen, F. Hsu, T. Huang, and J. Luo, "Growth and investigation of crystals of the new superconductor α-FeSe from KCl solutions," *Crystal Growth and Design,* vol. 9, pp. 3260-3264, 2009.
[219] D. Braithwaite, B. Salce, G. Lapertot, F. Bourdarot, C. Marin, D. Aoki, and M. Hanfland, "Superconducting and normal phases of FeSe single crystals at high pressure," *Journal of Physics: Condensed Matter,* vol. 21, p. 232202, 2009.
[220] U. Patel, J. Hua, S. Yu, S. Avci, Z. Xiao, H. Claus, J. Schlueter, V. Vlasko-Vlasov, U. Welp, and W. Kwok, "Growth and superconductivity of< equation>< font face='verdana'> FeSe< sub> x</sub></equation> crystals," *Applied Physics Letters,* vol. 94, pp. 082508-082508-3, 2009.
[221] J. Wen, G. Xu, Z. Xu, Z. W. Lin, Q. Li, W. Ratcliff, G. Gu, and J. Tranquada, "Short-range incommensurate magnetic order near the superconducting phase boundary in Fe_ {1+ δ} Te_ {1− x} Se_ {x}," *Physical Review B,* vol. 80, p. 104506, 2009.
[222] T. J. Liu, X. Ke, B. Qian, J. Hu, D. Fobes, E. K. Vehstedt, H. Pham, J. H. Yang, M. H. Fang, L. Spinu, P. Schiffer, Y. Liu, and Z. Q. Mao, "Charge-carrier localization induced by excess Fe in the superconductor Fe1+yTe1-xSex," *Physical Review B,* vol. 80, p. 174509, Nov 2009.
[223] K. Hashimoto, A. Serafin, S. Tonegawa, R. Katsumata, R. Okazaki, T. Saito, H. Fukazawa, Y. Kohori, K. Kihou, C. H. Lee, A. Iyo, H. Eisaki, H. Ikeda, Y. Matsuda, A. Carrington, and T. Shibauchi, "Evidence for superconducting gap nodes in the zone-centered hole bands of KFe_{2}As_{2} from magnetic penetration-depth measurements," *Physical Review B,* vol. 82, p. 014526, 07/19/ 2010.
[224] R. T. Gordon, H. Kim, M. A. Tanatar, R. Prozorov, and V. G. Kogan, "London penetration depth and strong pair breaking in iron-based superconductors," *Physical Review B,* vol. 81, p. 180501, 05/05/ 2010.
[225] V. G. Kogan, "Pair breaking in iron pnictides," *Physical Review B,* vol. 80, p. 214532, 12/28/ 2009.
[226] R. Prozorov and V. G. Kogan, "London penetration depth in iron-based superconductors," *Reports on Progress in Physics,* vol. 74, Dec 2011.
[227] A. Abrikosov, "Nobel lecture: Type-II superconductors and the vortex lattice," *Reviews of modern physics,* vol. 76, pp. 975-979, 2004.
[228] V. G. Kogan, R. Prozorov, and C. Petrovic, "Superfluid density in gapless superconductor CeCoIn(5)," *Journal of Physics-Condensed Matter,* vol. 21, Mar 2009.
[229] A. B. Vorontsov, M. G. Vavilov, and A. V. Chubukov, "Superfluid density and penetration depth in the iron pnictides," *Physical Review B,* vol. 79, Apr 2009.
[230] T. Kato, Y. Mizuguchi, H. Nakamura, T. Machida, H. Sakata, and Y. Takano, "Local density of states and superconducting gap in the iron chalcogenide superconductor

Fe_{1+δ}Se_{1−x}Te_{x} observed by scanning tunneling spectroscopy," *Physical Review B,* vol. 80, p. 180507, 11/17/ 2009.
[231] C. C. Homes, A. Akrap, J. S. Wen, Z. J. Xu, Z. W. Lin, Q. Li, and G. D. Gu, "Electronic correlations and unusual superconducting response in the optical properties of the iron chalcogenide FeTe_{0.55}Se_{0.45}," *Physical Review B,* vol. 81, p. 180508, 05/17/ 2010.
[232] W. Park, C. Hunt, H. Arham, Z. Xu, J. Wen, Z. Lin, Q. Li, G. Gu, and L. Greene, "Strong Coupling Superconductivity in Iron-Chalcogenide FeTe $ _ {0.55} $ Se $ _ {0.45} $," *arXiv preprint arXiv:1005.0190,* 2010.
[233] K. Nakayama, T. Sato, P. Richard, T. Kawahara, Y. Sekiba, T. Qian, G. F. Chen, J. L. Luo, N. L. Wang, H. Ding, and T. Takahashi, "Angle-Resolved Photoemission Spectroscopy of the Iron-Chalcogenide Superconductor Fe_{1.03}Te_{0.7}Se_{0.3}: Strong Coupling Behavior and the Universality of Interband Scattering," *Physical Review Letters,* vol. 105, p. 197001, 11/02/ 2010.
[234] R. T. Gordon, H. Kim, N. Salovich, R. W. Giannetta, R. M. Fernandes, V. G. Kogan, T. Prozorov, S. L. Bud'ko, P. C. Canfield, M. A. Tanatar, and R. Prozorov, "Doping evolution of the absolute value of the London penetration depth and superfluid density in single crystals of Ba(Fe1-xCox)(2)As-2," *Physical Review B,* vol. 82, Aug 2010.
[235] J. P. Reid, M. A. Tanatar, X. G. Luo, H. Shakeripour, N. Doiron-Leyraud, N. Ni, S. L. Bud'ko, P. C. Canfield, R. Prozorov, and L. Taillefer, "Nodes in the gap structure of the iron arsenide superconductor Ba(Fe(1-x)Cox)(2)As-2 from c-axis heat transport measurements," *Physical Review B,* vol. 82, Aug 2010.
[236] Y. Uemura, G. Luke, B. Sternlieb, J. Brewer, J. Carolan, W. Hardy, R. Kadono, J. Kempton, R. Kiefl, and S. Kreitzman, "Universal Correlations between T_ {c} and n_ {s}/m^{*}(Carrier Density over Effective Mass) in High-T_ {c} Cuprate Superconductors," *Physical review letters,* vol. 62, p. 2317, 1989.
[237] V. Thampy, J. Kang, J. A. Rodriguez-Rivera, W. Bao, A. T. Savici, J. Hu, T. J. Liu, B. Qian, D. Fobes, Z. Q. Mao, C. B. Fu, W. C. Chen, Q. Ye, R. W. Erwin, T. R. Gentile, Z. Tesanovic, and C. Broholm, "Friedel-Like Oscillations from Interstitial Iron in Superconducting Fe1+yTe0.62Se0.38," *Physical Review Letters,* vol. 108, Mar 2012.
[238] J. Hu, G. Wang, B. Qian, and Z. Mao, "Inhomogeneous superconductivity induced by interstitial Fe deintercalation in oxidizing-agent-annealed and HNO3-treated Fe1+ y (Te1− xSex)," *Superconductor Science and Technology,* vol. 25, p. 084011, 2012.
[239] V. Mishra, G. Boyd, S. Graser, T. Maier, P. J. Hirschfeld, and D. J. Scalapino, "Lifting of nodes by disorder in extended-s-state superconductors: Application to ferropnictides," *Physical Review B,* vol. 79, Mar 2009.
[240] B. Zeng, G. Mu, H. Q. Luo, T. Xiang, Mazin, II, H. Yang, L. Shan, C. Ren, P. C. Dai, and H. H. Wen, "Anisotropic structure of the order parameter in FeSe0.45Te0.55 revealed by angle-resolved specific heat," *Nature Communications,* vol. 1, Nov 2010.
[241] T. A. Maier, S. Graser, D. J. Scalapino, and P. J. Hirschfeld, "Origin of gap anisotropy in spin fluctuation models of the iron pnictides," *Physical Review B,* vol. 79, Jun 2009.
[242] K. Kuroki, H. Usui, S. Onari, R. Arita, and H. Aoki, "Pnictogen height as a possible switch between high-T-c nodeless and low-T-c nodal pairings in the iron-based superconductors," *Physical Review B,* vol. 79, Jun 2009.
[243] A. V. Chubukov, M. G. Vavilov, and A. B. Vorontsov, "Momentum dependence and nodes of the superconducting gap in the iron pnictides," *Physical Review B,* vol. 80, Oct 2009.
[244] F. Wang, H. Zhai, and D. H. Lee, "Antiferromagnetic correlation and the pairing mechanism of the cuprates and iron pnictides: A view from the functional renormalization group studies," *Epl,* vol. 85, Feb 2009.
[245] A. Diaconu, C. Martin, J. Hu, T. J. Liu, B. Qian, Z. Q. Mao, and L. Spinu, "Possible nodal superconducting gap in Fe1+y(Te1-xSex) single crystals from ultralow temperature penetration depth measurements," *Physical Review B,* vol. 88, Sep 2013.

Vita

The author, Andrei Diaconu, was born in 1983 in Radauti, Romania. He enrolled in the Physics Department at "Alexandru Ioan Cuza" University in Iasi, Romania in 2002 from which he received his B.Sc. in Physics in 2006. He then pursued a Master degree in Modeling and Simulations under the supervision of Prof. Dr. Alexandru Stancu, at the same university, receiving a M.Sc. in 2008. In January of 2009, he joined the group of Dr. Leonard Spinu at University of New Orleans focusing on Magnetism, Cryogenics, Computational Science and Superconductivity.